The Effect of Disorder in Crystalline Materials on Structural and Spectroscopic Properties of Ln^{3+}-Doped Alkali Yttrium Fluorides

Quantum Chemical & Experimental Assessment

Dissertation

der Mathematisch-Naturwissenschaftlichen Fakultät

der Eberhard Karls Universität Tübingen

zur Erlangung des Grades eines

Doktors der Naturwissenschaften

(Dr. rer. nat.)

vorgelegt von

M. Sc. Chris Steve Conrad

aus Jena

Tübingen

2025

Gedruckt mit Genehmigung der Mathematisch-Naturwissenschaftlichen Fakultät der Eberhard Karls Universität Tübingen.

Tag der mündlichen Qualifikation:	20.03.2026
Dekan:	Prof. Dr. Thilo Stehle
1. Berichterstatter/-in:	Prof. Dr. Reinhold F. Fink
2. Berichterstatter/-in:	Prof. Dr. Marcus Scheele

I would like to thank everybody who has supported me in the last five years and helped me get to where I am now, personally and professionally.

"Lanthanum has only one important oxidation state in aqueous solution, the +3 state. With few exceptions, this tells the whole boring story about the other 14 elements."

Pimentel, G. C. & Spratley, R. D. Understanding Chemistry (Holden-Day, 1971)

At least for the three lanthanides assessed in this work,

the story is indeed much more interesting.

Für Helgo

Table of Contents

Abstract

Because of their unique optical properties, the lanthanides (Ln) are employed as dopants in a large manifold of optoelectronic applications. The optical properties of the Ln are influenced by the local coordination environment at an atomistic level. This local environment, in turn, is linked to the (crystallographic) order or disorder present in the lattice of the host material. Energy levels, oscillator strengths, and emission spectra of lanthanides doped into either ordered or disordered host materials may, therefore, vary noticeably. For other effects, such as photon upconversion, that depend on these properties, different responses are also to be expected for ordered and disordered systems.

In this work, a combined theoretical and experimental investigation of the optical properties of three Ln (Er, Tm, and Yb) doped into two typical upconverting host materials, ordered $LiYF_4$ and intrinsically disordered β-$NaYF_4$, is presented. The objectives of this study were to establish how crystallographic disorder influences the structure of the host material, the local symmetry of doping sites, and the optical response of Ln doped into such sites. In the first part of the study, periodic density functional theory was applied to optimise the examined structures and systematically characterise the consequences of cation disorder in β-$NaYF_4$. The model was benchmarked by comparing its predictions with data from the literature for both $LiYF_4$ and β-$NaYF_4$. In the second part, the optimised structures served as the basis for embedded cluster calculations to predict crystal field splitting, energies, and oscillator strengths via a wavefunction-based approach for the three Ln. Results were compared to values available in the literature and showed very good agreement. In both studies, the disorder experienced by β-$NaYF_4$ was considered through a custom weighting scheme of the available disordered structures.

Finally, emission spectra from specifically prepared Ln-doped upconverting nanoparticles were recorded and compared to those generated from the computational data sets. Great overlap between the spectra compared was observed, highlighting the validity of the computational approach and the disordered nature of β-$NaYF_4$. The study demonstrated that β-$NaYF_4$ cannot be adequately described by a single representative structure. Remaining challenges are connecting the observed changes in the emission profiles to the enhanced upconversion yield observed for disordered host materials.

Zusammenfassung

Aufgrund ihrer einzigartigen optischen Eigenschaften werden Lanthanoide (Ln) als Dotierstoffe in einer Vielzahl von optoelektronischen Anwendungen eingesetzt. Die optischen Eigenschaften der Ln werden durch die lokale Koordinationsumgebung auf atomarer Ebene beeinflusst. Diese lokale Umgebung hängt wiederum mit der (kristallographischen) Ordnung oder Unordnung im Gitter des Wirtsmaterials zusammen. Die Energieniveaus, Oszillatorstärken und Emissionsspektren von Lanthanoiden, die entweder in geordnete oder ungeordnete Wirtsmaterialien dotiert sind, können daher erheblich variieren. Für andere Effekte, wie zum Beispiel die Photonenhochkonversion, die von diesen Eigenschaften abhängen, sind ebenfalls unterschiedliche Reaktionen für geordnete und ungeordnete Systeme zu erwarten.

In dieser Arbeit wird eine kombinierte theoretische und experimentelle Untersuchung der optischen Eigenschaften von drei Ln (Er, Tm und Yb) vorgestellt, die in zwei typische Wirtsmaterialien zur Hochkonvertierung, geordnetes $LiYF_4$ und intrinsisch ungeordnetes β-$NaYF_4$, dotiert wurden. Ziel dieser Studie war es, festzustellen, wie kristallographische Unordnung die Struktur des Wirtsmaterials, die lokale Symmetrie der Dotierungsstellen und die optische Reaktion, der in solche Stellen dotierten Ln, beeinflusst. Im ersten Teil der Studie wurde die periodische Dichtefunktionaltheorie angewendet, um die untersuchten Strukturen zu optimieren und die Folgen der Kationenunordnung in β-$NaYF_4$ systematisch zu charakterisieren. Das Modell wurde durch einen Vergleich seiner Vorhersagen mit Daten aus der Literatur für $LiYF_4$ und β-$NaYF_4$ validiert. Im zweiten Teil dienten die optimierten Strukturen als Grundlage für eingebettete Clusterberechnungen, um die Kristallfeldaufspaltung, Energien und Oszillatorstärken für die drei Ln mittels eines wellenfunktionsbasierten Ansatzes vorherzusagen. Die Ergebnisse wurden mit den in der Literatur verfügbaren Werten verglichen und zeigten eine sehr gute Übereinstimmung. In beiden Studien wurde die Unordnung von β-$NaYF_4$ durch ein maßgeschneidertes Gewichtungsschema der verfügbaren ungeordneten Strukturen berücksichtigt.

Schließlich wurden Emissionsspektren von speziell hergestellten Ln-dotierten Hochkonvertierungs-Nanopartikeln aufgezeichnet und mit den Spektren verglichen, die aus den rechnerischen Datensätzen generiert wurden. Es wurde eine große

Übereinstimmung zwischen den verglichenen Spektren festgestellt, was die Gültigkeit des rechnerischen Ansatzes und die ungeordnete Struktur von β-$NaYF_4$ unterstreicht. Die Studie zeigte, dass β-$NaYF_4$ nicht durch eine einzige repräsentative Struktur angemessen beschrieben werden kann. Die verbleibende Herausforderung besteht darin, die beobachteten Veränderungen in den Emissionsprofilen mit der erhöhten Effizienz der Hochkonvertierung in Verbindung zu bringen, die für ungeordnete Wirtsmaterialien beobachtet wurde.

1. List of Publications

1) The True Atomistic Structure of a Disordered Crystal: A Computational Study on the Photon Upconverting Material β-$NaYF_4$ and its Er^{3+}-, Tm^{3+}-, and Yb^{3+}-Doped Derivates. Chris Steve Conrad, Holger Euchner, Eva Hemmer, and Reinhold F. Fink, ***Nanoscale***, 2025,**17**, 8599–8613. Reproduced from Ref. 1 with permission from the Royal Society of Chemistry, 2025.

The manuscript is referenced as Conrad (I) *et al.* in this dissertation.

2) Effect of Disorder on the Emission Spectra of Er^{3+}, Tm^{3+}, and Yb^{3+}-Doped β-$NaYF_4$: Quantum Chemical and Experimental Results. Chris Steve Conrad, Stefan Behnle, Eva Hemmer, and Reinhold F. Fink, ***Journal of Physical Chemistry*** *C*, 2025, **129**, 45, 20446–20464. Reproduced with permission from Ref. 2. Copyright 2025 American Chemical Society.

The manuscript is referenced as Conrad (II) *et al.* in this dissertation.

1.1. Contributions to Collaborative Publications

Nr.	Accepted manuscript (peer-reviewed) yes/no	№ of authors	Position of candidate in list of authors	Scientific ideas by the candidate (%)	Data generation or/and programming by the candidate (if applicable) (%)	Analysis/ interpretation/ technical work by the candidate (if applicable) (%)	Paper writing done by the candidate (%)
1	yes	4	1	50	90	90	85
2	yes	4	1	50	80	90	85

2. Introduction

This introduction aims at conveying relevant concepts necessary for understanding the later discussed research questions, but also for providing a motivation at large for the subject of this dissertation. In this first chapter, fundamental principles regarding the lanthanides and rare earths in general, the electronic fine structure of the lanthanides in particular, basic knowledge about disordered crystal structures, and an overview for the upconversion phenomenon are presented.

2.1. Lanthanides and Rare Earths

The lanthanides (Ln) cover 14 elements of the 6th period in the periodic system of the elements (PSE), from lanthanum (atomic number 57) to ytterbium (70). Together with scandium, yttrium, and lutetium (all of which are d-block transition metals), they are also referred to as rare earths elements (RE).[3, 4] The 14 lanthanides and lutetium form a large chemically very coherent group in the PSE, and this similar chemical behaviour explains why the designation "lanthanides" commonly also encompasses lutetium.[3] The same grouping will be upheld in this text from here on, so that there are 15 elements in the lanthanide series. While showing mostly alike bonding behaviour, the optical properties of individual lanthanides differ significantly and are often unique compared to those of other elements of the PSE.[5] Indeed, the optical properties of several of the lanthanides enable a distinct optical process called 'upconversion', as explained at the end of this chapter.[6-8]

2.1.1. Overview

The lanthanides share several mutual characteristics, though, the single most outstanding one is indeed the almost identical chemical behaviour when it comes to bonding in ionic compounds.[3, 4] All lanthanides exhibit the +III oxidation state as their most common one, although, for several lanthanides two other oxidation states are readily available.[3, 4, 9] These are the +II and +IV oxidation states, observed for lanthanides where they represent favourable electronic configurations (*i.e.*, half or fully filled subshells).[10, 11] Given that the lanthanides share a common oxidation state and very similar ionic radii (from La^{3+} = 103.0 pm to Lu^{3+} = 86.1 pm), it comes as no surprise that their bonding behaviour

and, therefore, their formation of ionic compounds can often be regarded as near identical.[3, 4, 12] Since the two earlier group 3 elements, *i.e.*, scandium and yttrium, also primarily feature the +III oxidation state and have comparable ionic radii, *i.e.*, Sc^{3+} = 74.5 pm and Y^{3+} = 90.0 pm, especially yttrium but also scandium is also found in the same minerals as the lanthanides.[3, 4, 12]

Reflecting these similarities is the name given to the *lanthanides*. When lanthanum was first discovered, it was thought to hide behind other elements in the same minerals.[13] The word 'lanthanide' originates from the Greek word λανθανειν (lanthanein*)*, translating to "to lurk" (as in the sense of staying hidden).[14] Subsequently, the 4f elements were referred to as lanthanides altogether, as all of them seemed to behaving like lanthanum.[13] Given their almost identical (geo)chemical behaviour, during the early years of their discovery many *pure* samples of a lanthanide would actually contain two or even more lanthanides.[3, 15] The history of the discovery of the lanthanides therefore is comprised of some truly new findings but also many false ones, and it took considerable time and effort to understand which findings belonged to a new and unique element.[16, 17]

2.1.2. A Short History of Discovery

In the late 18th century, two so far unknown oxides in newly found minerals were discovered: 1) Yttria in the mineral gadolinite from a mine in Ytterby. 2) Ceria in the mineral bastnäsite from a mine in Bastnä. Both Ytterby and Bastnä are located in Sweden.[3] Approximately forty years after the initial discoveries, it was realised that both yttria (in 1842) and ceria (in 1839) were not individual oxides but contained additional oxides of until then unknown elements.[3] Yttrium oxide, erbia, and terbia formed yttria, while cerium oxide and lanthana were found to make up ceria. Only a few years later, it became clear that lanthana was not a pure oxide but again a mixture of several lanthanides: lanthanum oxide and didymia, another mixed compound. Subsequently, the same happened with erbia in 1878, then terbia, and again didymia, leading to the discovery of more and more elements.[3]

With the emergence of new spectroscopic techniques at the end of the 19th century, researchers kept identifying unknown spectral lines besides the ones previously assigned and argued from this that more than one element was present in a *pure* sample. This also

led to the discovery of false elements as spectral lines of two (un)known elements were thought to be a single new element, among many other sources or error.[17] The process of chemically separating and spectroscopically identifying new, presumably new, or ultimately false lanthanides continued for almost 120 years until 1907, when, finally, 14 lanthanides, missing promethium, plus scandium and yttrium were separated and characterised.[18] The order in which these 16 elements were discovered is shown in Figure 1. Because of the radiative nature of promethium and its short half-life time of about 18 years, this element was not discovered until 1945.[3]

2.1.3. Natural Occurrence

The lanthanides, as part of the rare earth elements, are relatively abundant in Earth's crust and not scarce as the name 'rare earths' invokes.[4, 19] Compared to more common elements, *i.e.*, oxygen ($0.5 \cdot 10^6$ ppm), silicon ($0.3 \cdot 10^6$ ppm), or iron ($0.1 \cdot 10^6$ ppm), their concentrations seems indeed to be rather low, *e.g.*, cerium (66 ppm), gadolinium (6 ppm), or erbium (4 ppm).[20] On the other hand, relative to the noble metals, *e.g.*, silver ($75 \cdot 10^{-3}$ ppm), gold ($4 \cdot 10^{-3}$ ppm),[20] there appears to be an excess of rare earths. Overall, the concentration of the rare earths is comparable to that of elements such as copper (60 ppm) or slightly lower.[20] However, contrary to transition or noble metals, minerals that contain high amounts of the rare earths are actually rare.[21] Instead, their concentration within Earth crust's is relatively consistent. The concentration is, therefore, often lower compared to the concentrations of on average rarer elements that accumulated at certain sites within the crust.[4] Deposits with higher concentrations of these rarer elements are usually easier to mine. The economical exploitation of deposits containing rare earth bearing minerals is instead often much more difficult.[22]

2.1.4. Geology and Mining

Concentration of the lanthanides in minerals is highest in the fluorocarbonate bastnäsite, $(La, Ce, Y)CO_3F$, the phosphates monazite, $LnPO_4$, and xenotime, YPO_4, and the silicate gadolinite, $(Ce, La, Nd, Y)_2FeBe_2Si_2O_{10}$.[3, 4] Additionally, ion-absorption clays are also an important source for mining, especially in Southern China.[21] While the rare earth oxide content is rather low in this silicate, *i.e.*, < 1 %, ion-absorption clays are easily extractable from the source rock.[3, 4] Notably, in most rare earth bearing minerals a wide range or even all

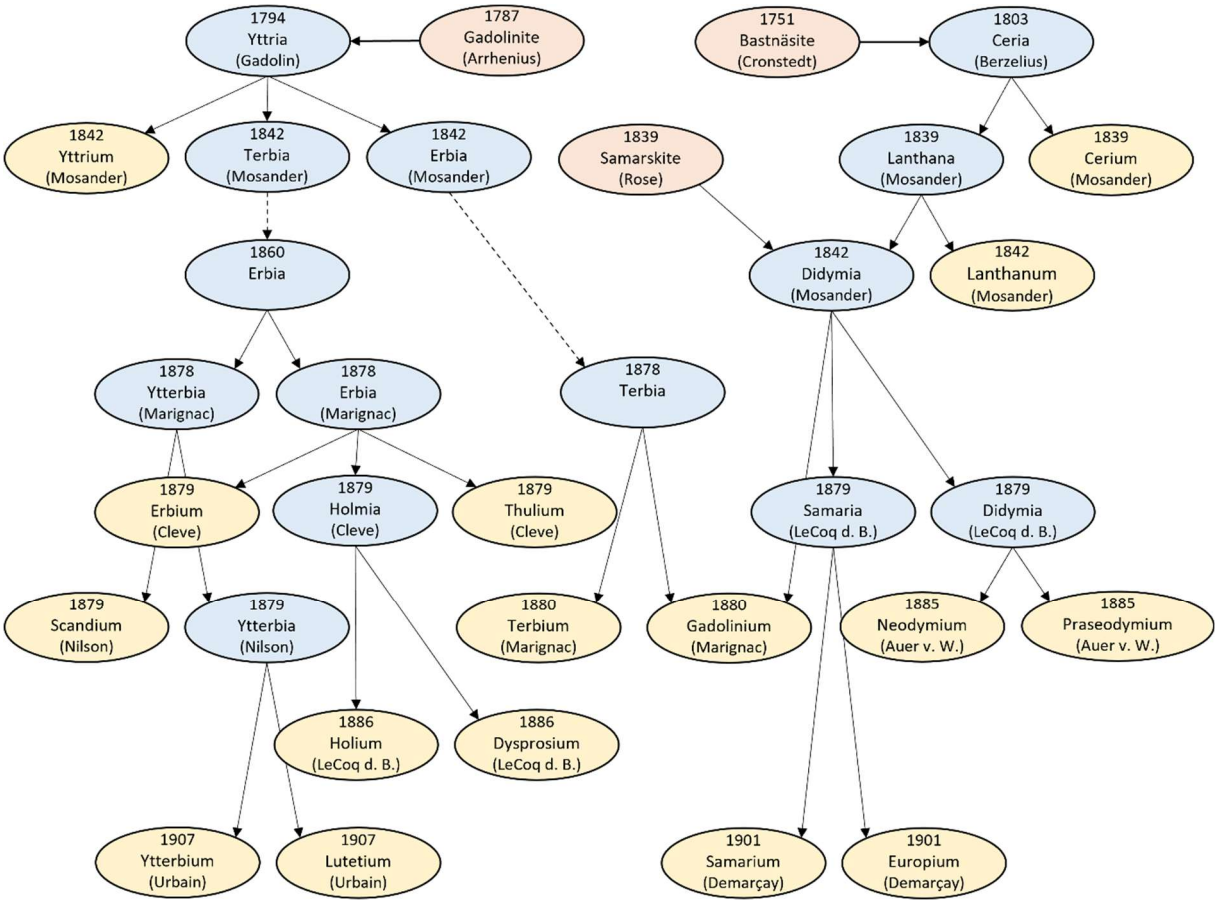

Figure 1: Flow chart showing the timeline of rare earth discovery by separation of the corresponding minerals and oxides. The red balloons represent the three minerals from where the separation started. The blue balloons show the impure/mixed rare earth oxides that were obtained from these minerals. Balloons in yellow at the very end of each separation process showcase the final pristine elements. Each balloon shows the year of discovery, the name of the element, and the person discovering it (from top to bottom). All years of discovery refer to the oxide or a salt of the element, the metallic elements were isolated (much) later.[4] Not included in this flow chart are the numerous false findings, (in)dependent discoveries by several people, and disputes of priority over a discovery. Flow chart inspired by Peter van der Krogt, Elementymology & Elements Multidict, 2010, elements.vanderkrogt.net/rareearths.php.[16] Last accessed: 09.09.2025.

---

rare earths can be found.[3, 4] For example, bastnäsite from the Mountain Pass mine in California features about 50 % CeO_2, 33 % La_2O_3, 12 % Nd_2O_3, 4 % Pr_6O_{11}, 1 % Sm_2O_3, and smaller quantities (< 0.2 %) of most other rare earth oxides (percentages are given relative to the overall rare earth oxide concentration).[21] Actually, the maximum rare earth oxide content in the minerals listed above can reach up to 75 %.[3, 4] While that sounds rather high, it needs to be kept in mind that these minerals themselves are often rather scarce

within the source rock. Typical values of the rare earth oxide content within the source rock are less than 5 %,[23] although historically more abundant mineral deposits did exist.[4, 24] To give an example, at the beginning of its exploitation, rare earth concentrations at the Mountain Pass mine were exceeding 10 % of the source rock, making the extraction highly profitable and thereby becoming the paramount source of rare earths from 1964 to approximately 1984.[22] Afterwards, Chinese rare earth mines (and processing) started dominating international markets.[19, 21, 25-28]

2.1.5. Modern-Day Usage

While the lanthanide's geochemistry is almost identical, their opto-electronic properties are everything but the same (as discussed in the next chapter). Their electric, electronic, optic, optoelectronic, and magnetic properties are mostly determined by the number of (unpaired) electrons in the 4f subshell, which differs immensely across the series.[3, 4] When determining their properties, important factors are also their increasing spin-orbit coupling and the special relationship the lanthanides have with their surroundings. Unique combinations of properties such as ladder-like energetic states, long lifetimes, sharp emission profiles, and low toxicity have allowed the lanthanides to find application in a variety of research fields.[29-31] For example, lanthanides are employed in materials science, biomedicine, or sensing applications.[4, 32-35] In industry, lanthanides are used in magnets, the glass industry, catalysis, or as phosphorescent substances in optoelectronic devices.[4, 28] To give an example, 0.1 weight% of a modern smartphone are made up by around eight different lanthanides and yttrium.[4] While this appears to be an insignificant amount, the lanthanides fulfil niche requirements for which finding a substitute can be quite challenging or is connected with reduced performance.[28]

2.2. Electronic Properties of the Lanthanides

2.2.1. Electronic Configuration

All lanthanides possess the electron configuration of xenon plus additional electrons in the 6s, 5d, and 4f subshells.[3, 4] Figure 2 provides an overview of the different available subshells for the elements in the PSE and their energetic ordering. In their elemental form, the 6s subshell is filled with two electrons for all lanthanides and the 5d subshell with one or none.[3, 4] The occupation of the 4f subshell differs for most lanthanides and increases from lanthanum to lutetium: $[Ln] = [Xe]\,6s^2\,5d^M\,4f^N$, where $M = 0 - 1$ and $N = 0 - 14$.[9] The electronic configuration of three lanthanides except for three elements follows the Aufbau principle or Madelung's rule. [3] For the three exceptions, the 5d subshell 'grabs' one electron as this energetically more favourable for their specific configurations.[36]

Although the orbitals of the 4f subshell are filled with electrons last for the lanthanides, these electrons usually do not participate in bonding or chemical reactions.[29] The electrons in the 4f subshell are shielded from the environment by the electrons of other subshells, specifically, by the electrons of the 5s and 5p subshells.[9, 37] This is shown in Figure 3 and Figure 4 and discussed further below. The 4f electrons are, thereby, rendered almost inert to outside influences.[3, 4] Emphasise is placed on the word *almost*, since the electrons are still susceptible to their environment although to a lesser extent than, for example, the d electrons of the transition metals.[37] Upon cation formation, the two 6s electrons and one 5d electron (if available, alternatively one 4f electron) are removed, giving rise to the typical +III oxidation state of the (trivalent) lanthanides: $[Ln^{3+}] = [Xe]\,6s^0\,5d^0\,4f^N$, where $N = 0 - 14$.[29, 38] The removal of two electrons from the highest s subshell and one electron from the highest d subshell is also observed when cations of scandium and yttrium are formed.[4]

The (opto)electronic properties of the trivalent lanthanides are mostly determined by their number of (unpaired) electrons in the 4f subshell.[3] This number gradually increases from zero for lanthanum and one for cerium to seven for gadolinium. Beyond gadolinium, the number of electrons in the seven orbitals still increases, but the number of unpaired electrons starts decreasing. To better understand why the number of (unpaired) electrons in the 4f subshell is so important and how it shapes the electronic properties of

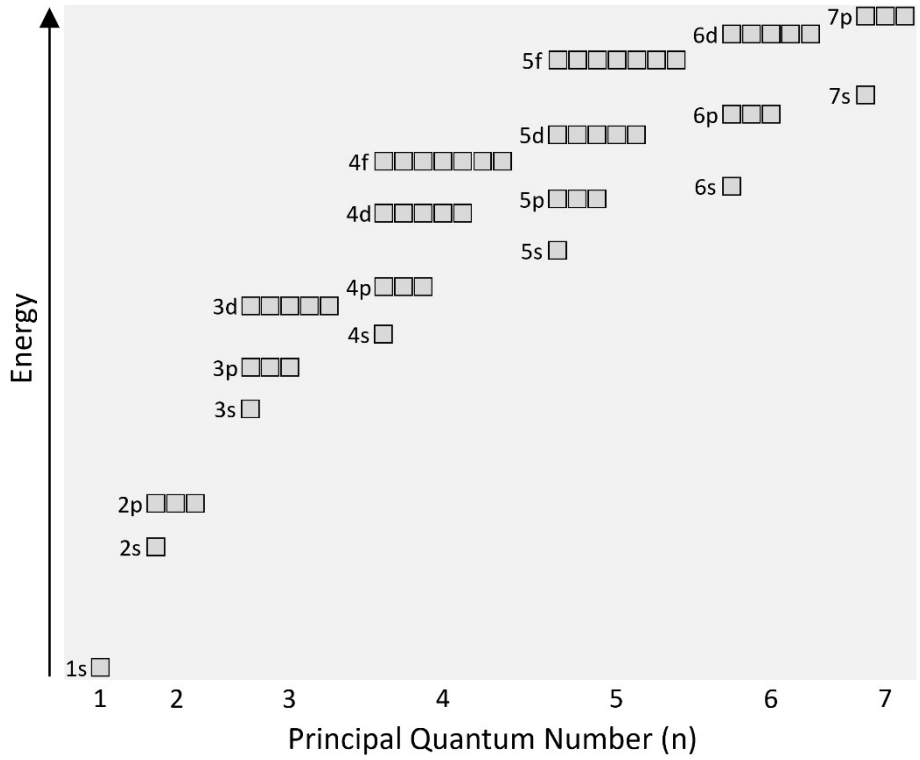

Figure 2: Energetic ordering of the subshells from 1s to 7p, including their respective number of orbitals. The energy of a subshell increases with increasing principal quantum number (QN), $n = 1-7$, and increasing azimuthal QN, $l = 0$ (s), 1 (p), 2 (d), 3 (f), ... The principal QN describes which period (shell) a subshell belongs to and the azimuthal QN expresses the orbital angular momentum of the subshell and its orbitals. Electrons are filled into the respective orbitals according to energetic ordering of the subshells, the filling process is known as Aufbau principle. Diagram inspired by several similar depictions.[39]

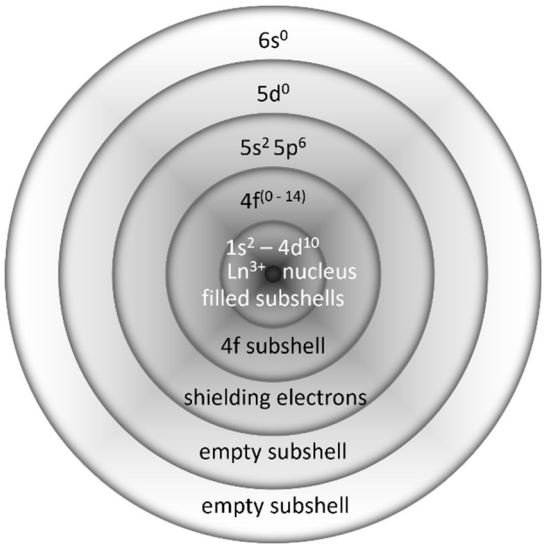

Figure 3: Generic electron occupation scheme for the trivalent lanthanide ions. The spatial positioning of the individual subshells is simplified but correctly depicts the shielding of the 4f electrons by electrons of other subshells. The drawing is not true to scale. Inspired by Walsh, B.M. (2006). Judd-Ofelt Theory: Principles and Practices. In: Di Bartolo, B., Forte, O. (eds) *Advances in Spectroscopy for Lasers and Sensing*. Springer, Dordrecht, 406.[37]

the lanthanides, despite these electrons being buried by electrons of energetically lower subshells, the basic properties of the 4f subshell are elucidated.

2.2.2. 4f Subshell

Especially the 5s and 5p subshells, but to a certain extent also the 6s subshell, lie energetically lower than the 4f subshell and are filled with electrons first (refer to Figure 2).[3, 39] However, the spread of the electron density around the core is determined by the radial distribution function of a subshell and is based on its principal quantum number (QN). [3, 29] For the 4f subshell, the principal QN is equal to 4. Therefore, the radial distribution of the 4f subshell decays faster than those of subshells with higher principal QN. Its electrons are, on average, closer to the nucleus than the electrons of the energetically lower 5s, 5p, and 6s subshells (Figure 4).[3, 29, 40] The result of this is that the electrons of the 4f subshells are less exposed to the environment of the lanthanide than their counterparts in the 5s and 5p subshells.[3, 4] In this regard, the term *lanthanide* (from *staying hidden*) applies not only to the geochemical behaviour of the lanthanides, but also extends to the positioning of the 4f subshell and its electrons. Overall, the energetic positioning of the 4f subshell and its radial distribution explain why the electrons in the orbitals of the 4f subshell are considered chemically inert and generally do not participate in bonding or chemical reactions (with exceptions).[3, 4, 29]

2.2.3. Influence of the Crystal Field

While it is true that the 4f electrons of the lanthanides are not interacting massively with the surroundings, it is also true that they are not completely unresponsive to changes in the environment of the respective lanthanide.[4, 9] In order to explore the influence and magnitude the crystal field of an (inorganic) crystal has onto a lanthanide doped into such a crystal, several factors must be considered in conjunction. These are, in order from strongest to weakest, the interaction between the electrons and the nucleus of the ion, the repulsion between the electrons within the subshell, their spin-orbit coupling, and, finally, the influence of the crystal field. All these factors combined generate the electronic fine structure of a lanthanide.[37]

Starting with the most influential factor, the attraction between electrons surrounding the core and the protons within. The number of negatively charged electrons and their attraction by the positively charged protons determine the *configuration* of a lanthanide.[9] For all trivalent lanthanides, the ground state configuration is equal to [Xe] $4f^N$, where

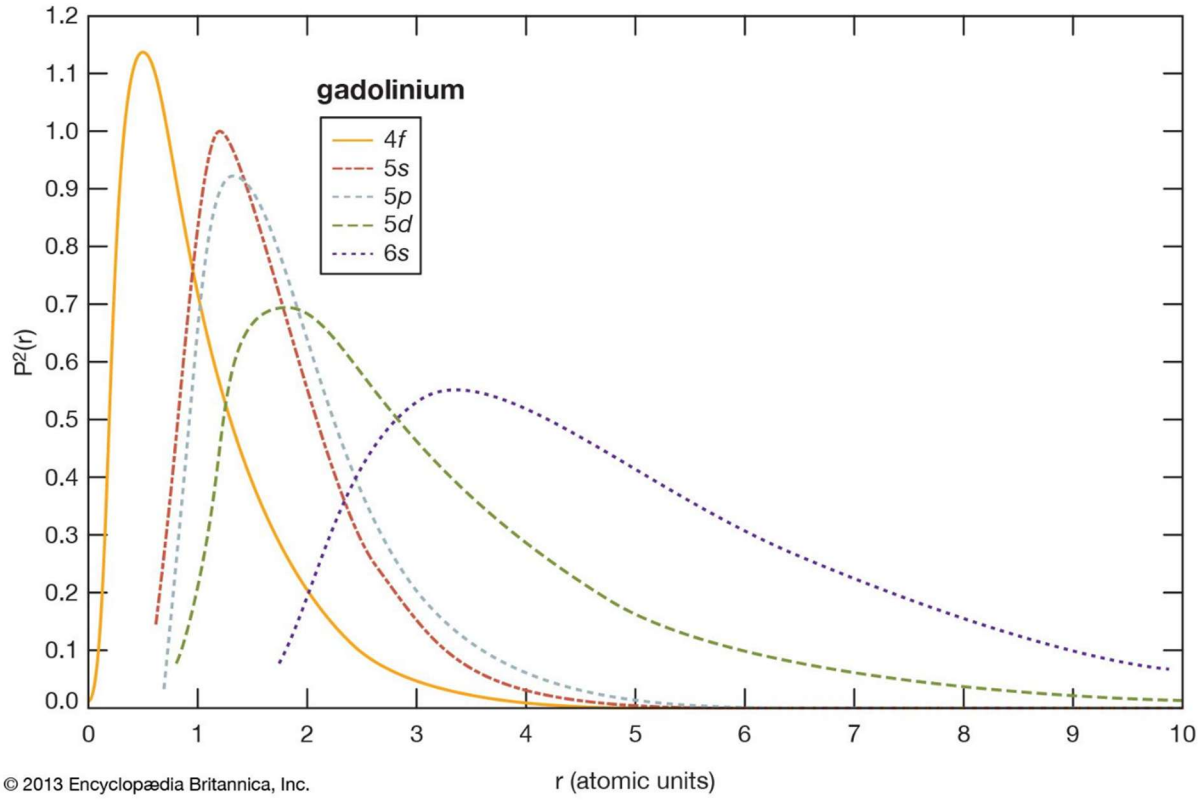

Figure 4: Radial distribution functions of gadolinium for the 4f, 5s, 5p, 5d, and 6s subshells. *r* is the distance from the core in atomic units, $P^2(r)$ is the square of the wave function for each of the subshells depicted and equals its electron probability density. On average, electrons in the 4f subshell are situated closer to the nucleus than those in the 5s, 5p, 5d, and 6s subshells, with the 5s and 5p subshells being fully filled even for the trivalent lanthanides. The electrons in the 5s and 5p subshell therefore shield those in the 4f subshell from interactions with the environment. The graphic was taken from Britannica.com. Rare-Earth Element - Electronic Structure and Ionic Radius. 2013. https://www.britannica.com/science/rare-earth-element/Electronic-structure-and-ionic-radius. Last accessed: 15.09.2025.[41]

$N = 0-14$.[3] The next higher configuration is $[Xe]\,4f^{N-1}\,5d^1$, if enough energy is provided to the lanthanide so that a 4f electron (if available) can be promoted to the 5d subshell.[4, 29]

Subsequently, each configuration splits further into *terms* under the influence of the Coulomb interaction (or rather the contributions of the exchange integrals).[9, 38] This interaction represents the mutual repulsion of the electrons. Different terms arise for each configuration under the Coulomb/exchange interaction, depending on two factors: 1) the orientation of the spins of the electrons and 2) the distribution of the electrons in the available orbitals and the orientation of the angular momentum of these occupied orbitals.[29]

To easily differentiate the available terms of a configuration from each other, the notation ^{2S+1}L was introduced.[29] Here S is the total spin QN and $2S+1$ is called the spin multiplicity of the respective term (*i.e.*, singlet, doublet, triplet, *etc.*). L instead is the total orbital QN.

The created terms are split in turn by the third contribution to the energetic fine structure of a lanthanide, that is, the spin-orbit coupling. This interaction results in the formation of *multiplets*, which is short for *J*-multiplets, also called levels.[9, 38] Both the rotation of the electron around itself (its spin) and the electron around the core (its orbital momentum) cause a magnetic momentum. These magnetic momenta couple with each other and result in a combined angular momentum, represented by the total angular momentum QN (J).[29] In *LS* (or Russel-Sanders) coupling, it is assumed that the spin-orbit coupling is much weaker than the Coulomb/exchange interaction.[3, 29] This allows to first calculate the total spin QN (S) and the total orbital QN (L), and then calculate the total angular momentum QN (J), with possible values $|L-S|$, $|L-S|+1$, ..., $L+S-1$, $L+S$.[3] For the lanthanides, with their larger number of protons and neutrons in the core and, thereby, increased electron speed, the assumption that the Coulomb/exchange interaction is much stronger than spin-orbit coupling is no longer fully valid.[29] Other schemes, such as j-j coupling or a combination of LS and j-j coupling, called intermediate coupling, are often better suited to give an accurate description of the corresponding multiplet.[29] Specifically, LS and j-j coupling are specific cases of intermediate coupling that, though more complex, provides the most appropriate description of any real system.

As long as at least one unpaired electron is available in an atom or ion, several multiplets are formed within one term through spin-orbit coupling. It is important to note that usually the S, L, and J values of the predominantly contributing multiplet are used to construct the spectroscopic term symbol of a multiplets, *i.e.*, $^{2S+1}L_J$.[29, 42] For example, the ground state multiplet of Eu^{3+} has the spectroscopic term symbol $^7F_0$, as shown in Figure 5. However, it should be kept in mind that these multiplets often are a combination of several different multiplets with the same total angular momentum QN that, for example, can differ in their total spin QN or total orbital QN.[42] A result of the stronger spin-orbit coupling and, therefore, more influential total angular moment of the lanthanides. This also explains why transitions between multiplets with differing total spin QNs can be observed for the lanthanides, even though these transitions are forbidden by the spin

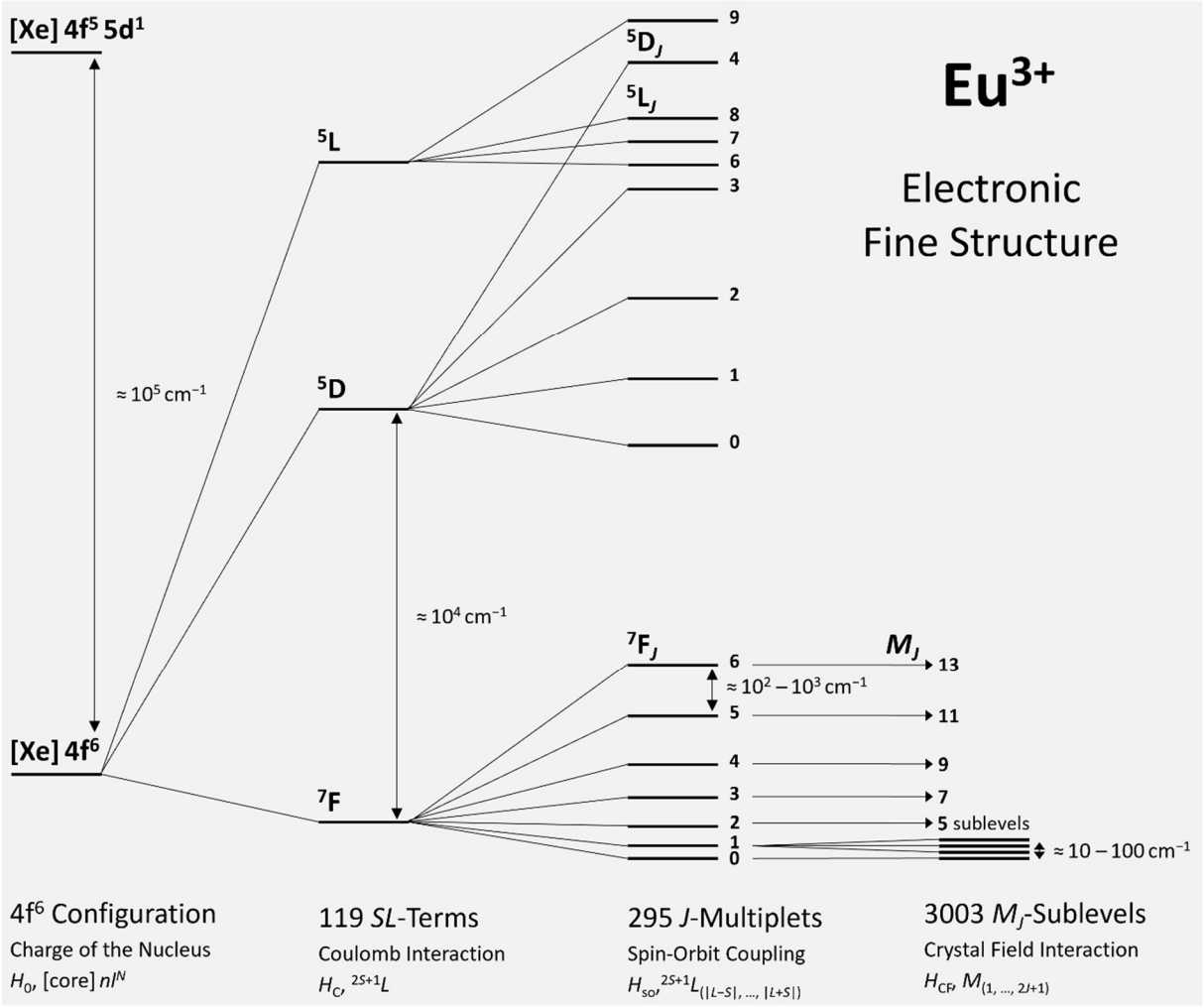

Figure 5: Partial energy level diagram showing the electronic fine structure of Eu^{3+} in an arbitrary but low-symmetry host material. Initially degenerate energy levels split because of the interaction between the nucleus and the electrons (H_0), the Coulomb interaction (H_C), spin-orbit coupling (H_{SO}), and the crystal field interaction (H_{CF}).[9] For the lanthanides, the magnitude of these influences is approximately $H_0 > H_C \approx H_{SO} > H_{CF}$.[9, 37] While the sublevels of different multiplets usually are clearly separated, overlap is observed between multiplets of different terms and terms of different configurations.[42-44] This is especially true where terms are densely packed and for the energetically higher terms. The energetic separation of the different energy levels is not drawn true to scale and only selected energy levels are depicted, irrespective of their ordering. Depiction inspired by Binnemans, K. Interpretation of Europium(III) Spectra. *Coordination Chemistry Reviews* **2015**, *295*, 3 and Baur, F.; Jüstel, T. Eu^{3+} Activated Molybdates – Structure Property Relations. *Optical Materials: X* **2019**, *1*, 3.[45, 46]

---

selection rule ($\Delta S = 0$).[29, 38, 46] The involved wavefunctions are not spin-pure but a combination of wavefunctions of multiplets with different total spin QNs.[42]

The three interactions discussed so far determine the electronic structure of the lanthanides in an environment that does not induce any additional distortions (in the gas phase or rather vacuum).[3, 4, 29] So far missing is the final and least influential, in terms of magnitude, contribution to the electronic fine structure of the lanthanides: the crystal field interaction.[3, 37] It originates, as the name suggests, from the interaction between the electrons of the lanthanides and the surrounding electrons from the ions of an inorganic crystal. Once subjected to such a crystal field (or electrical field in general), the previously degenerate *J*-multiplets split into *sublevels*, short for M_J*-sublevels*, also called states or Stark levels.[9, 29, 38] The maximum number of sublevels generated through the interaction with the crystal field depends on the total angular momentum of the respective *J*-multiplet and the symmetry of the crystal field. There are $2J+1$ possible values for M_J, representing the available projections of the total angular momentum QN (*J*) along the z-axis.[9, 29, 44] However, the degeneracy of the multiplet and separation into all possible sublevels is fully lifted only under the following conditions: 1) For integer values of *J*, that is, for a lanthanide with an even number of electrons, the point group of the position the lanthanide is doped into must be rather low, *i.e.*, $C_{2h/v}$ and D_{2h} or lower.[29] 2) For half-integer values of *J*, that is, an odd number of electrons, the point group cannot be one of the highly symmetric groups, *i.e.*, $T_{d/h}$ and O_h or higher, and an additional magnetic field is required (Zeeman effect).[29, 46] Tables listing the number of sublevels per multiplet in each point group for both integer and half-integer values can be found in the literature. [9, 38] A detailed discussion of the underlying concept, called crystal field theory, and its application to the lanthanides is also available in the literature.[42, 47]

While the influence of the Coulomb/exchange interaction and spin-orbit coupling can have similar magnitude for the lanthanides, the crystal field interaction is much weaker (refer to Figure 5).[3, 29, 37] This is different to, for example, the d-metals, where the spin-orbit coupling is much less significant than the influence of the crystal field.[3, 37] The result of the reduced influence of the crystal field for the lanthanides is that the sublevels of one multiplet usually do not overlap with the sublevels of another multiplet. Indeed, their energetic separation is often so small (few hundred wavenumbers) that normally all sublevels are grouped together under their corresponding multiplet. Similar to how they are grouped for most multiplets in the Dieke-Diagram, partially shown in Figure 6.[44-46] Furthermore, the exact energetic separation of the individual sublevels of one multiplet

depends on the total angular momentum QN of the multiplet, the point group of the lanthanide, and the strength of the corresponding crystal field.[9, 29] Finally, it should be noted that the crystal field does not meaningfully shift the energetic positioning of the multiplets, meaning the energetic barycentre of the multiplet stays almost the same.[48] Because of this it is possible to refer to one (the Dieke-) diagram when inquiring about the positioning of the multiplets of lanthanides in often very different host materials.[44]

2.2.4. 4f – 4f Transitions

Despite the weak interaction of the lanthanides with the surrounding crystal field, the influence of the crystal field has very important consequences when it comes to the electronic properties of the lanthanides.[4, 9] According to Laporte's rule, electronic transitions during which parity is conserved are forbidden (if an inversion centre is present).[3, 29] Put differently, Laporte's rule states that an electronic transition for an atom or ion in a centrosymmetric environment will only be possible if during the transition the change of the azimuthal QN is equal to an odd integer, *i.e.*, $\Delta l = \pm 1, \pm 3 \ldots$.[37] Therefore, no transitions within the same configuration, in general, and between terms, multiplets, and sublevels within the 4f subshell, in particular, should be possible.[9, 38] Δl will always be equal to 0 for these transitions. It is noteworthy that also many transitions for the d metals violate Laporte's rule. However, for these elements (and for some lanthanides complexes) vibronic coupling between the metal and its ligands lifts their inversion symmetry and enables the transitions.[3, 37] Having explained this, vibronic coupling is of little relevance for the 4f electrons of the lanthanides as interaction with the crystal field is very weak.[3] However, electronic transitions between the multiplets and sublevels of the 4f configuration, though weak, can still be observed.[4, 29, 38] Instead, the lanthanide's violation of Laporte's rule is explained by the influence of the crystal field.[9] It is argued that the crystal field interaction not only splits the multiplets into sublevels but also mixes the sublevels of different configurations, particularly those of the $4f^N$ and $4f^{N-1}\,5d^1$ configurations.[9, 29, 37] This introduces the azimuthal QN of the d subshell, *i.e.*, 2, to the transition. An alternative formulation is that through this mixing even parity character is introduces into the otherwise odd parity 4f configuration.[9, 29, 38] Thereby making the transitions comply with Laporte's rule. It should be noted that these restrictions apply to electronic dipole transitions only, while other rules are valid for magnetic dipole and electric quadrupole transitions.[29, 37, 38]

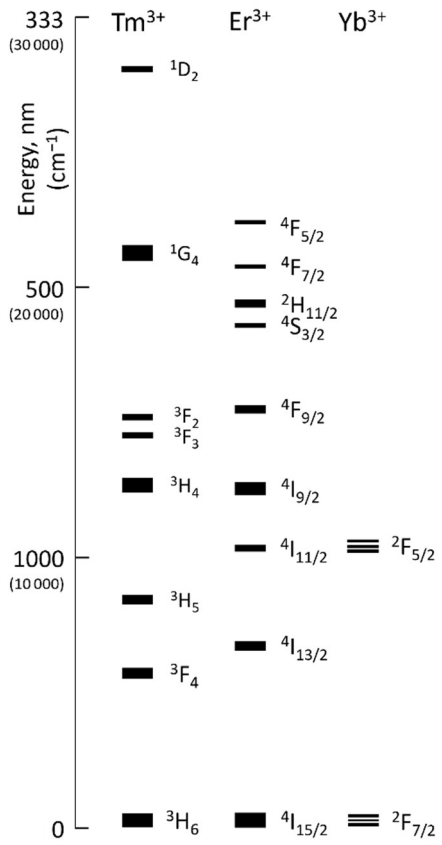

Figure 6: Partial energy level diagram for Tm^{3+}, Er^{3+}, and Yb^{3+} in LaF_3. These lanthanides are commonly used in upconverting systems, and their properties have been assessed in the two studies that form the basis for this dissertation. The full diagram involving all Ln^{3+} and including more energy levels over a wider energetic range is commonly known as Dieke-Diagram.[48] Diagram adapted from Reid, M. F. Theory of Rare-Earth Electronic Structure and Spectroscopy. In *Handbook on the Physics and Chemistry of Rare Earths*, Bünzli, J.-C. G., Pecharsky, V. K. Eds.; Vol. 50; Elsevier, 2016; p 51.[44]

Having said the above, even though no longer forbidden, transition intensities for the lanthanides are still particularly low, even in non-centrosymmetric environments.[3, 29, 37] Also, the absorption and emission lines that result from these transitions are quite sharp and narrow.[9, 29] Again a result of the missing vibronic coupling with the surrounding, which otherwise would make the transitions more likely but also more diffuse.[3] An important consequence of all of these effects is that individual multiplets and sublevels of the Ln^{3+} are rather localised. Together with the many available multiplets and sublevels (crystal field energy levels), the energetic fine structure of the lanthanides is often described as "ladder-like".[49] Each multiplet represents one step of the ladder. Indeed, the low probability of promoting a lanthanide from its ground into an excited state results in particularly long lifetimes of the excited state (µs – ms range), since relaxation back to the ground state is equally (un)likely.[4, 38] This effect plays an important role for the upconversion process (see below). To overcome the weak emission intensities, the lanthanides are often doped into low-symmetry host lattices with an irregular crystal field.[9, 50-53] Many examples of suitable low-symmetry host exist, *e.g.*, $LiYF_4$ or cubic (α-) and hexagonal (β-) $NaYF_4$ and $NaGdF_4$. Among them are those that are highly irregular because of their inherent disorder, *i.e.*, β-$NaYF_4$ and β-$NaGdF_4$ plus, to a lesser extent, the cubic versions of these crystals.

2.3. Disorder (in Crystal Lattices)

A variety of reasons exist why an inorganic crystal can be disordered, many of these reasons are considered defects to the crystal lattice and are often invoked by external effects and influences.[54] Among such defects are point defects like vacancies, interstitial atoms, or dopants, but also line defects, planar, and bulk defects. However, there is also a substantive number of crystal structures for which disorder is a feature, not a bug. To explain this phenomenon further, a crystal with a cubic unit cell as shown in the two depictions of Figure 7 is considered. The unit cell of that crystal is made up by 1000 (10^3) lattice positions, evenly spaced along all three lattice directions. These positions are occupied by each 500 ions of two different types. In this example, the two types of ions are called purple and white, and the two ions are assumed to be identical except for the colour. Finally, all lattice position of the cube must be occupied by one of the two ions, and no interstitial positions are available. Therefore, the possible number of arranging the 500 ions of one type onto the 1000 lattice positions can be calculated with the binomial coefficient (1000 choose 500). This results in more than 10^{299} different possibilities / configurations of the lattice. The ions of the other type will fill the remaining positions, and no additional configurations are thereby generated. The corresponding crystal structure is considered inherently disordered, since no outside influence is necessary for creating this large number of configurations. To describe such a lattice accurately, the occupation of each lattice position must be provided individually. Two of the possible configurations of this crystal are shown in Figure 7. While both configurations have the same probability of occurrence, $1/10^{299}$, the probability of occurrence for the *more ordered* configuration on the left seems to be deemed, incorrectly, higher.[55-59]

In reality, of course, the two different types of ions must have a charge associated with them, for example, +1 for purple and −1 for white. In this case, the two ions might create a configuration as shown in the depiction on the left of Figure 7 (depending on their relative ionic radii). The two types of ions strictly alternate, thereby creating a configuration with a highly regular pattern. Such an ordered crystal can be described by a single and much smaller unit cell, only containing one ion of each type, and additional symmetry information.[9] When taking a closer look at such a crystal, however, it is possible that the purple ion is a placeholder ion for two different types of ions. For example, P_1 and P_2, each

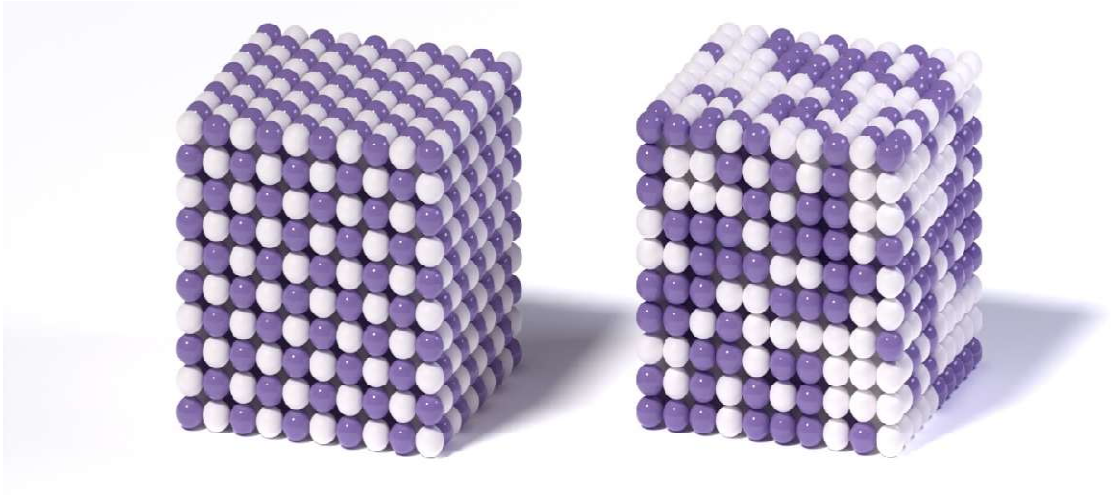

Figure 7: Depiction showing two cubes with different arrangements of purple and white spheres (ions) at the available lattice positions of the cube (crystal). The arrangement on the right is an example for a possible configuration of a disordered structure. The cube on the left can represent both the single configuration of an ordered structure or a second configuration of the disordered structure shown on the right. Depiction taken from Simonov, A. Order and Disorder in Crystals. ETH Zürich, Department of Materials, 2025. https://disorder.mat.ethz.ch/research.html. Last accessed: 19.09.2025.[60]

---

of them with charge +1 and similar ionic radii. Moreover, there are each 250 ions of type P_1 and P_2 available. The 10 x 10 x 10 crystal still offers each 500 fixed positions for the white anions and the purple cations. However, now that the cationic positions can be occupied by either P_1 or P_2, the crystal lattice becomes inherently disordered once more. For arranging the cations P_1 and P_2 onto the 500 positions available, (500 choose 250 ≈) 10^{149} possibilities exist. Significantly less than in the previously example, but still larger than even one googol, which is equal to 10^{100}, and almost twice as large as the assumed number of elementary particles in the universe (10^{80}).[61]

When trying to depict a crystal lattice in which the exact distribution of two types of ions at the same lattice position is unknown, but there is a 50 % chance of finding one or the other on average, often half-half ions as shown in Figure 8 are utilised. While this is a convenient way of displaying this type of disorder, it might invoke the notion that the crystal, that it represents, will look more like the ordered configuration on the left (strictly alternating occupation) than the disordered configuration on the right of Figure 7 (purely random occupation). This is even though both configurations have an equal probability of

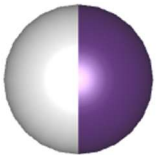

Figure 8: Lattice position that is occupied by a white or a purple ion with a probability of 50 % each. Depiction created with the VESTA crystal visualization program by Momma and Izumi.[62]

being realised in such a crystal (not accounting for second-order or long-range effects that might induce the creation of local clusters). Also, when only one single configuration of that crystal must be chosen, *e.g.*, for a theoretical study, usually the ordered configuration is picked.[55-59] This may, however, be a severe shortcoming of the calculation, as the properties of the single ordered configuration will not necessarily be an accurate representation of the properties of the disordered structure overall.[1, 2]

Assuming a lanthanide (or any other ion) is doped into a (disordered) crystal, its exact electronic fine structure and properties such as 4f-4f transitions rates depend on the precise arrangement of the other ions around the lanthanide.[2, 37, 63] In an ordered structure, all positions the lanthanide can be doped into are equivalent or a limited number of non-equivalent positions exist.[1, 2] On the other hand, in a disordered structure a large variety of non-equivalent positions are available. Doping the lanthanide in any of them can lead to slightly different properties of the lanthanide, creating a larger variety of these properties for an ensemble of lanthanides.[1, 2, 64-68] Problematically, the number of all possible non-equivalent positions might be hard to account for, even for very small disordered systems. Therefore, the questions arises whether the ordered configuration or any one of the disordered configurations is a good approximation to the environment the lanthanide doped into the lattices is experiencing. Indeed, when trying to predict certain properties, it might be insufficient to assume that for probing these properties a single configuration suffices. Instead, it might be necessary to account for all or a large number of configurations individually. This could be especially relevant when processes are probed that might benefit from a larger variety of the properties in question.

2.4. Upconversion

One process that might be influenced meaningfully by the lattice disorder is photon upconversion. In the upconversion process, two or more photons, typically from the near infrared (NIR) region, are absorbed, their energy combined, and then a single, higher-energy photon is emitted.[8] The emitted photon is often from the ultraviolet (UV) or visual (Vis) part of the electromagnetic spectrum but can also be a higher-energy NIR photon.[8] If the specific upconversion process involves more than one ion, which is usually the case, (non-radiative) energy transfer from one ion to the other is required. The specific term for this type of upconversion is energy transfer upconversion (ETU) and is depicted in Figure 9 in detail.[8] In general, energy transfer is most efficient if the energy available by the relaxation of the donor (sensitiser) is matching or is slightly higher than the energy required for the excitation of the acceptor (activator).[9, 65-67, 69]

For the activator, that is responsible for the actual upconversion, Figure 9, often Er^{3+} or Tm^{3+} are employed. However, because of their low absorption cross-section, they are a poor choice for the sensitiser, for which instead mostly Yb^{3+} is used as a copodant.[70] Importantly, the full sensitiser-activator system consist of two hetero-ions for this kind of ETU. The energy provided by Yb^{3+} should ideally match exactly the energy required by Er^{3+} or Tm^{3+}. However, for many transfers this not the case.[43] Especially for the second transfer in the Er^{3+}-Yb^{3+} system, step 4 in Figure 9, more energy is required by Er^{3+} (activator) than is available through the relaxation to the ground state by Yb^{3+} (sensitiser).[2] This energy mismatch negatively impacts the rate of energy transfer between these two ions, which reduces upconversion efficiency (quantum yield). In fact, typical upconversion system suffer from very low quantum yields, although the energy mismatch between sensitisers and activators is only part of the problem.[71-77]

For many potential applications of the upconversion process, sensitisers and activators are doped into nanoparticles.[70] Such upconverting nanoparticles (UCNPs) then can be employed in photo-induced drug delivery, photodynamic and photothermal therapies, plant cultivation, and for enhancing photovoltaics, especially if their currently still low quantum yields are improved significantly.[34, 35, 78] A disordered host material could help getting closer to this goal for the following reason: In a co-doped system, an Yb^{3+} in an excited state often has more than one Er^{3+} in its proximity. For an ordered crystal, all of

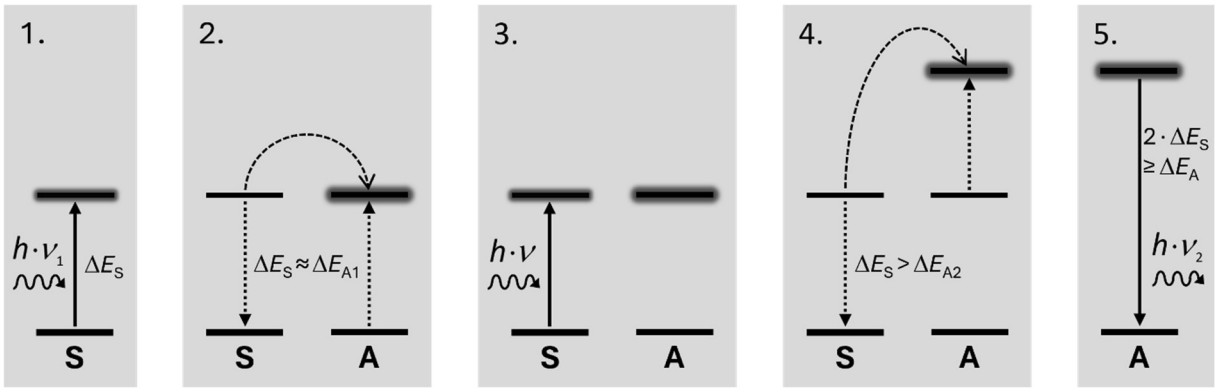

Figure 9: Required steps for energy transfer upconversion. **1:** A photon is absorbed by the sensitiser (S), and the energy of the absorbed photon is used to promote the sensitiser to an excited state. **2:** The sensitiser transfers the energy non-radiatively to a neighbouring activator (A) and simultaneously relaxes back to the ground state. The activator reaches an excited state. The energy differences between the ground and excited states of the sensitiser and activator should be similar or slightly favour the sensitiser transition. **3:** The sensitiser absorbs another photon and reaches its excited state once more. **4:** The obtained energy is again transferred to the neighbouring activator. Since the lanthanides have long excited state lifetimes, this activator has a high chance of still being in its excited state and, therefore, for using the received energy to reach an ever higher excited state. At the same time, the sensitiser relaxes back to the ground state. Upconverting systems often feature energy transfers steps in which the acceptor (activator) requires less energy for its transition than the donor (sensitiser) provides. However, also the other way round is possible. **5:** The energy stored in the higher excited state of the activator is released radiatively through emitting a photon when the activator relaxes to the ground state. The energy of the emitted photon is at most the combined energy of the (two) absorbed photons, however, for many upconverting systems it is (significantly) lower. A frequently used sensitiser is ytterbium, for the activator typically erbium and terbium are utilised, with other combinations of lanthanides also being possible.[79-81]

---

these Er^{3+} have the same environment, or a limited number of different environments exist. In a disordered system, however, every Er^{3+} will find itself doped into a slightly different environment and, thereby, will exhibit slightly adjusted properties. If one of the many available Er^{3+} has a reduced separation for the relevant energy levels, the energy required for the transition is also reduced. This results in an increased transition rate between the excited Yb^{3+} and this specific Er^{3+}, potentially leading to a more efficient upconversion process and increased upconversion quantum yield for the system overall.[2, 63]

3. Objectives

Initially, the goal of this research project was to create a computational model that could simulate the ETU process for a chosen combination of host crystal and co-doped lanthanides in its entirety. With such a model at hand, it would be possible to computationally predict (relative) upconversion yields of different dopant-host combinations. Once established which of the assessed combinations appear to be particularly efficient upconverters, synthesising them in a laboratory would be the next logical step. Such an approach circumvents a tedious trial-and-error approach for finding UCNPs with higher quantum yield by synthesising and characterising all possible candidates.

Previously, Shyichuk *et al*. created such a model for Er^{3+} and Yb^{3+} doped into YVO_4, employing a semi-empirical setup.[69] However, in order to make the approach more flexible, easier adjustable, to obtain information about the structure of the lattices on an atomic level, and to calculate optical properties based on the exact atomic arrangements, a purely *ab initio* approach was favoured by us. Indeed, if simulations of several dopant-host system are to be compared, the chosen model should be easily transferable from one system to another. Therefore, it was decided to design an adapted model that relies on *ab initio* calculations to the largest extent possible.

For creating and testing such a model, a choice on the initial host material had to be made. Very popular hosts for UCNPs among experimentalists are the cubic (α) and hexagonal (β) versions of $NaYF_4$ and $NaGdF_4$.[50-53, 82-84] Also, record upconverting quantum yield has often been reported for systems using these crystals as host lattices.[85-89] Interestingly, all four of these crystals are inherently disordered.[1, 50, 66, 90, 91] The unit cell of β-$NaYF_4$, with its two disordered sites, is shown in Figure 10. The other three structures feature similar disordered sites within their unit cells. When setting up the *ab initio* computational model for the structural optimisation of the crystal lattice, the question arose how to deal with these disordered sites and the lattice structure overall. Computational chemistry programmes require exactly defined lattice positions as inputs and not occupation probabilities for several ions at the same lattice position. Shyichuk *et al*. choose an ordered crystal structure for their semi-empirical study, therefore, no insights into this question were provided by them.[69]

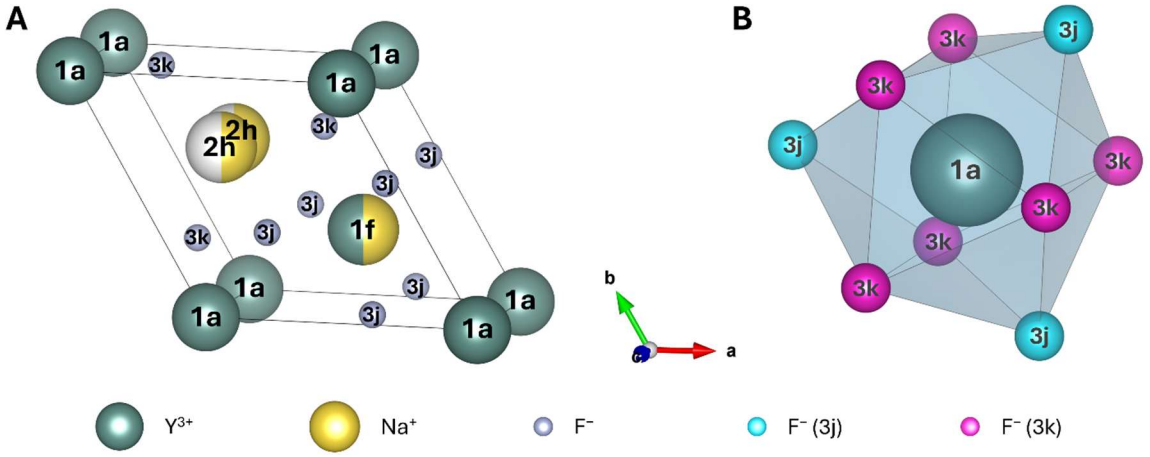

Figure 10: (A) Unit cell of β-$NaYF_4$, space group $P\bar{6}$, with the composition $Na_{1.5}Y_{1.5}F_6$. Dark green spheres represent Y^{3+}, yellow spheres Na^+, white spheres are unoccupied sites, and small grey spheres represent F^-. Half spheres indicate a 50 % occupation. The unit cell of β-$NaYF_4$ features two disordered sites, the 1f and 2h site. In every unit cell, the 1f site is either occupied by Na^+ or Y^{3+} and of the two 2h sites only one is occupied by Na^+. The exact arrangement of Na^+ and Y^{3+} at these sites influences the position of the F^- at the 3k and 3j sites. The rearrangement of the F^- in turn changes the optical properties of lanthanides doped into the structure at 1a or 1f sites, replacing Y^{3+}.[9] **(B)** Potential 1a Ln^{3+}-doping site, coordinated in a tricapped trigonal prismatic geometry by nine F^-. For clarity, the three 3j (caps) and the six 3k (trigonal prism) F^- are coloured in cyan and in pink, respectively. The respective prism for the 1f site is generated by rotating the coordination polyhedron shown in (B) by ca. 90° around the c-axis and by swapping the Wyckoff symbols for all F^-. Reproduced from Ref. 1 with permission from the Royal Society of Chemistry, 2025.

Interestingly, among experimentalists the disordered nature of these four structures is widely discussed and reviewed. [50, 66, 91-98] However, most computational studies focussing on β-$NaYF_4$ treat its lattice structure as ordered, seemingly ignoring the 2h disordered site and assuming a strictly regular alternation of Na^+ and Y^{3+} at the 1f disordered site.[55-59] Admittedly, the choice is understandable. Even for a very small system, consisting of eight unit cells combined into a larger supercell, hundreds of thousands if not a million configurations of the supercell are possible for this structure when fully accounting for its disorder.[1] This being said, instead of following this pathway of least resistance and reducing the complexity of the crystal structure, it was decided that a way had to be found of working with the disorder β-$NaYF_4$ and similar crystal exhibit.

Therefore, the task was set to first establish whether it was possible to structurally optimise the (disordered) lattice. Secondly, it was then to be assessed whether the lattice

structure of β-$NaYF_4$ was truly disordered or whether locally ordered configurations were formed. An earlier study based on experimental measurements and Monte-Carlo simulations tended to imply the latter.[50] Additionally, if the structure was disordered, it should be established whether the disorder meaningfully influences the (optical) properties of three different lanthanides, *i.e.*, Er^{3+}, Tm^{3+}, and Yb^{3+}, doped into the lattice. This assumption was made given that in highly irregular crystals, such as in disordered crystals, each lanthanide will find itself doped into a slightly different environment and should exhibit slightly different properties. Additionally, for these doping sites most likely no symmetry operations except the identity operation are available. Such low-symmetry sites generally lead to higher transition rates and thereby more efficient UCNPs as discussed above. [99, 100] From this observation the third research question arose, focussing on how a disordered lattice could influence the characteristic (energy transfer) required for ETU.

Overall, the research question moved away from designing a model that can cooperate all relevant aspects and model ETU in its entirety. Instead, emphasise was placed on assessing whether including disorder is a prerequisite for designing a complete model in the first place. This was deemed a relevant question since it appeared to be overlooked by earlier studies and, at the same time, seemed like an effect that could have very profound influence on a model for prediction upconversion quantum yield.

4. Results and Discussion

To gain insights into the characteristics of disordered materials relevant for ETU, two potential pathways appeared to be equally unsuitable: an exclusively experimental or a purely computational approach. An experimental approach suffers from the fact that, generally, only the actually realised state of a system can be characterised. Synthesising and characterising the same crystal in an ordered and a disordered configuration would provide insights into which of the two is the better upconverter. However, doing so did not appear to a possible option for the crystal in question, *i.e.*, β-$NaYF_4$. On the other hand, both an ordered and a disordered version of a crystal can be created computationally and their (upconverting) properties be probed. However, knowing which of the two generated crystal configurations represents the real material better could be difficult to assess from theoretical results alone. Therefore, it was decided to pursue a two-pronged approach, conducting both an experimental and a computational study of the materials. Interlinking the results of these studies provided insights so far not reported in the literature and greatly advanced the understanding of how the optical properties of lanthanides are influenced when doped into an inherently disordered lattice. Having such information at hand can help build a more complete model for predicting upconversion quantum yields of different dopant-host combinations computationally.

The results presented herein were published in two peer-reviewed manuscripts, which are part of this dissertation and attached to this dissertation (chapter 11. Manuscripts).[1, 2] For the laboratory-based part of this approach, experiments were conducted in the research facilities of Dr. Eva Hemmer at Ottawa University, Canada. The computational studies were supervised by Dr. Reinhold Fink at University of Tübingen. Significant help for working with the quantum chemical programmes CP2K and Orca were provided by Dr. Holger Euchner and Dr. Stefan Behnle, respectively, both University of Tübingen. The approach for each study and the corresponding results are summarised in the following.

4.1. Geometry Optimisation

Geometry optimisations were conducted to determine the equilibrium atomic positions for both an ordered ($LiYF_4$) and a disordered (β-$NaYF_4$) fluoride lattice. The calculations for ordered $LiYF_4$ served as a test of the computational method and the setup chosen. Furthermore, the obtained results for disordered β-$NaYF_4$ were used to assess the influence of cation disorder on local geometry, lattice symmetry, and energetic stability.

4.1.1. Lattice Structure, $LiYF_4$

The lattice structure of $LiYF_4$ is shown and described in Figure 11. The lattice is completely ordered. Ln^{3+} can be doped into the single site occupied by Y^{3+} (Wyckoff position 4b). To give the computational model more flexibility, the initial unit cell was enlarged to a supercell of size 3x3x1. A depiction of this supercell can be found in Conrad (I) *et al* (Figure S2).[1] Replacing one Y^{3+} by an Ln^{3+} in this supercell results in a doping percentage of 2.8 mol%.

4.1.2. Lattice Structure, β-$NaYF_4$

The lattice structure of β-$NaYF_4$ is discussed in Figure 10 (see above). The lattice features two disordered sites, *i.e.*, 1f and 2h, and Ln^{3+} can be doped into the lattice sites 1a and 1f,

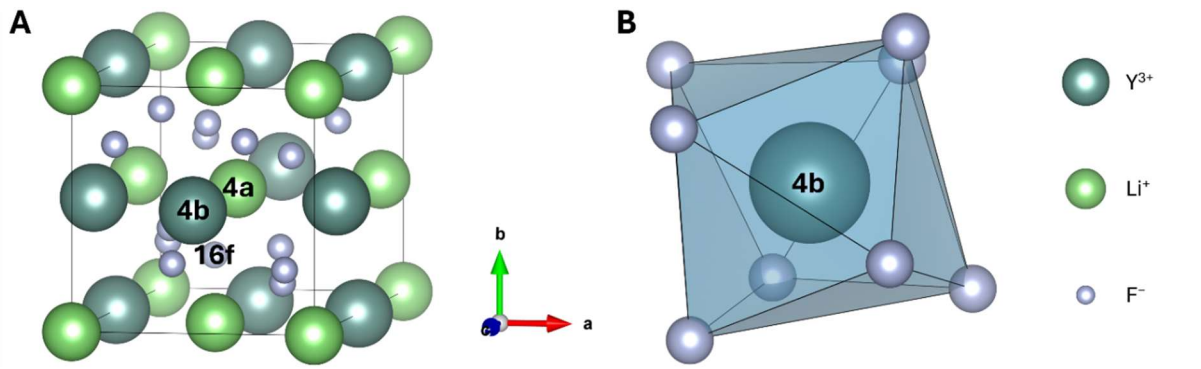

Figure 11: (A) Unit cell of $LiYF_4$, space group $I4_1/a$, with the composition $Li_4Y_4F_{16}$. Dark green spheres represent Y^{3+}, light green spheres Li^+, and small grey spheres represent F^-. $LiYF_4$ features only one potential doping site, *i.e.*, Wyckoff position 4b. The lattice features no disordered sites. Ln^{3+} doped into the lattice can occupy any of the sites previously featuring Y^{3+}. **(B)** Coordination polyhedron around Y^{3+}. Each Y^{3+} at a 4b site is surrounded by eight F^- ions, creating a distorted square antiprism. Reproduced from Ref. 1 with permission from the Royal Society of Chemistry, 2025.

replacing Y^{3+}. Each unit cell features twice as many Y^{3+} at 1a sites (1) as at 1f sites (0.5). To provide the structure with more flexibility when accounting for the disorder of the lattice, a 2x2x4 supercell was created for this crystal, Figure 12. In this supercell, both Na^{+} and Y^{3+} can be placed at the available disordered 1f sites. By alternating which ion is placed at which of the available sites, different local arrangements (configurations) are generated. In total, 16 separate supercells (configurations) of β-$NaYF_4$ were created by rearranging the distribution of Na^{+} and Y^{3+} at the 1f sites in the original supercell. These 16 configurations represent the 68 possible configurations that can be generated when placing either Na^{+} or Y^{3+} at the eight disordered 1f sites closest to the two possible doping sites, *i.e.*, 1a and 1f, in the lattice. When reducing the number of configurations from 68 to 16, the disorder at the 2h sites has to be ignored and symmetry operations be considered.

The first anionic coordination sphere of a potential 1a- and 1f-doped supercell is highlighted with black circles in Figure 12A and B, respectively. For the 1a supercell, the first anionic coordination sphere consists of six 1f and six 2h disordered sites, for the 1f supercell of two 1f and six 2h disordered sites plus six 1a sites. Specifically, the 1f

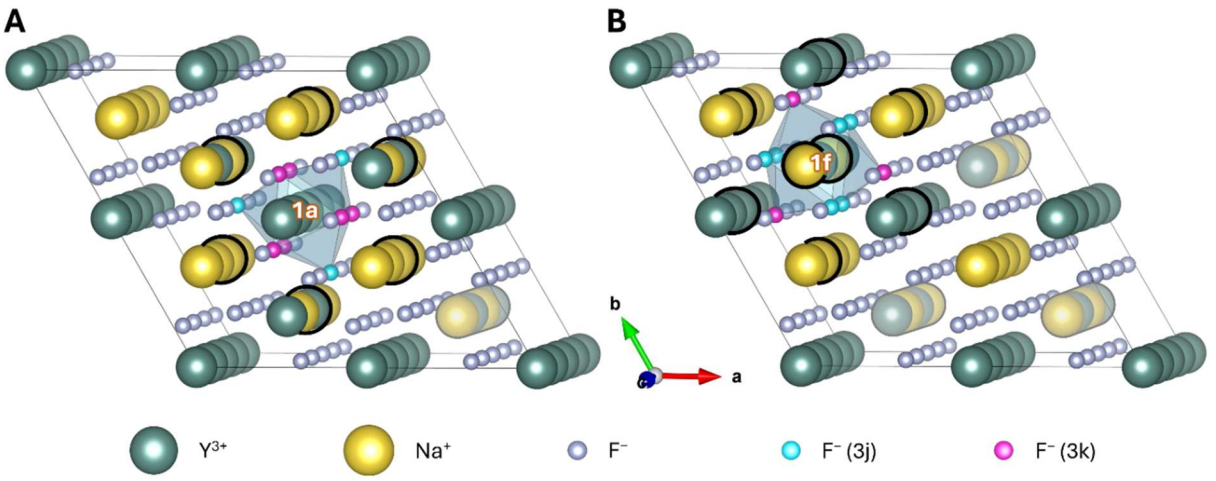

Figure 12: 2x2x4 supercell of β-$NaYF_4$ with the composition $Na_{24}Y_{24}F_{96}$ (144 atoms in total). Highlighted are a potential **(A)** 1a and **(B)** 1f doping site (white labels), and their first anionic (F^{-} ions of the blue prism that are highlighted in cyan and pink) and cationic (Na^{+} and Y^{3+} ions marked with a thick black line) coordination spheres. Na^{+} and Y^{3+} at 1f rows that are not neighbouring the central site (represented as faint) were not exchanged when creating the different configurations of the supercell. All other 1f sites were altered repeatedly. Reproduced from Ref. 1 with permission from the Royal Society of Chemistry, 2025.

supercell in Figure 12B, with its two closest disordered 1f sites (Na^+ neighbouring along the c-axis), provides 4 possible configurations (2^2), reduced to 3 relevant configurations. Instead, the 1a supercell in Figure 12A, with its six closest disordered 1f sites, provides 64 configurations (2^6), reduced to 13 relevant configurations. Together, a total of 16 configurations was obtained. Because of the occupation probabilities of Y^{3+} at the 1a and 1f sites, being $^2/_3$ and $^1/_3$, respectively, doping an Ln^{3+} into the lattice has a chance twice as high of finding the Ln^{3+} at a 1a than a 1f site. This distribution of Ln^{3+} had be considered when creating the averaging scheme for the optical properties of the doped supercells in the second part of this study. Also, when replacing a single Y^{3+} with an Ln^{3+} in these 2x2x4 supercells, a doping rate of 4.2 mol% is achieved. Additional details on the configurations of the individual supercells and further illustrations are provided in Conrad (I) *et al.*, especially in Figure 3.[1]

Finally, the influence of the 2h disordered site was assessed independently of the disorder at the 1f site by creating three more supercells with different arrangements of the Na^+ at the 2h sites. The three Na^+ arrangements were chosen based on their likelihood of occurrence in real crystals: two arrangements corresponded to frequently observed local motifs (named Na1 and Na2), while the final one represented a less common but structurally distinct arrangement (named Na3). The influence of the two different types of disordered sites, *i.e.*, 1f and 2h, was assessed separately as accounting for all possible combinations of both sites simultaneously would result in millions of configurations, even for a supercell as small as the one chosen for this study.[1]

4.1.3. Computational Details

All geometry optimisations were carried out using the CP2K programme package, which combines Gaussian type orbital and plane-wave representations.[101-104] Periodic boundary conditions within the density functional theory (DFT) ensured that the resulting structures accurately reflected the long-range periodic interactions of the crystal. The Perdew–Burke–Ernzerhof exchange–correlation functional was employed, in addition to Grimme's D3 dispersion correction for van der Waals interactions. [105, 106] Goedecker–Teter–Hutter pseudopotentials were used for Li, Na, F, and Y together with MOLOPT triple and double-zeta basis sets, optimised for condensed-matter calculations.[107, 108] Electronic self-consistency was achieved to within 10^{-6} Hartree. After optimising the undoped supercells in

the described way, the supercells were doped with the respective lanthanides (Er^{3+}, Tm^{3+}, and Yb^{3+}) and reoptimised, resulting in four times 16 optimised supercells for the 1f disordered site of β-$NaYF_4$. Additionally, six 2h disordered supercells were geometry optimised, three of these supercells were undoped and three of them were doped with Er^{3+}. Also, four optimised supercells were obtained for $LiYF_4$, one undoped and three doped with the same lanthanides as used for β-$NaYF_4$.

4.1.4. Results for $LiYF_4$

The optimised supercell of $LiYF_4$ confirmed the high degree of order experienced by this crystal. Lattice vectors, and angles between them, corresponded well to the experimental values. Bond distances for the eight F^- neighbouring each Y^{3+} could be split into two different groups, as expected for a distorted square antiprism. Deviation of the calculated lattice parameters was close to 1 % compared to experimental values reported in the literature.[109, 110] The discrepancy to the experimental values was also very similar to the deviations of other theoretical studies from the experimental values, being 1.5 – 2.5 %.[111, 112] Indeed, also the two calculated bond lengths were both close to the experimental values, with deviations of 5.9 %. Furthermore, the calculated values were also very similar to the values reported in another theoretical study, deviations of ≈ 1 %.[109, 113] Upon doping with the different Ln^{3+}, *i.e.*, Er^{3+}, Tm^{3+}, Yb^{3+}, all three structures experienced structural changes by less than 1 % compared to the undoped structures. This is most likely an effect of the small doping percentage, *i.e.*, 2.8 mol%, and the similarity of the ionic radii of the Ln^{3+} and the Y^{3+} they are replacing. Additional comparisons to values reported in the literature can be found in Conrad (I) *et al*.[1] Overall, the chosen theoretical approach and the model set up showed to be well suited for modelling inorganic crystal structures such as that of $LiYF_4$. Therefore, the employed model could be used for evaluating the effects of disorder in β-$NaYF_4$, with the baseline for an ordered structure established with the results obtained for $LiYF_4$.

4.1.5. Results for β-$NaYF_4$

For β-$NaYF_4$, 16 different supercells with different configurations were designed and optimised. Therefore, a straightforward comparison to values from the literature was not possible. As previously mentioned, other theoretical studies for this crystal often

focussed on a single configuration of the crystal's lattice structure and, thereby, obtained a single value for each lattice parameter. Naturally, experimental studies also only provide a single value (though, some uncertainty might be attached to it). In order to compare the results of this study with other values found in the literature, both experimental and computational ones, a single value had to be obtained from the 16 different supercells that were optimised. To obtain such a value, an averaging scheme was employed.

4.1.5.1. Averaging Scheme

When creating the averaging scheme, it was assumed that the 16 supercells with their different configurations (first column in Table 1) represent the 68 possible configurations in a supercell of this size (*i.e.*, 2 x 2 x 4). To account for this, each configuration had a degeneracy assigned to it (second column). The degeneracy represented the number of symmetrically equivalent ways this distribution of Na^+ and Y^{3+} could occur within the full set of the 68 possible configurations. Additionally, it was taken into consideration that the distribution of dopants at the two possible sites, *i.e.*, 1a and 1f, is 2:1 ($^2/_3$ to $^1/_3$). The

Table 1: List of generated configurations for the potential 1f (1 to 3) and 1a (4 to 16) doping sites, their degeneracy, their old and new weighting factor, and the Na^+ / Y^{3+} distribution at the 1f sites. Reproduced from Ref. 1 with permission from the Royal Society of Chemistry, 2025.

Configuration	Degeneracy	Old Weighting (%)	New Weighting (%)	Na^+ / Y^{3+} Distribution at Neighbouring 1f Sites					
Site: 1f	4	33.3		1	2				
1	1	8.3	2.4	Na^+	Na^+				
2	2	16.7	3.3	Y^{3+}	Na^+				
3	1	8.3	1.2	Y^{3+}	Y^{3+}				
Site: 1a	64	66.7		1	2	3	4	5	6
4	1	1.0	0.6	Na^+	Na^+	Na^+	Na^+	Na^+	Na^+
5	6	6.3	5.6	Na^+	Na^+	Na^+	Na^+	Na^+	Y^{3+}
6	3	3.1	2.9	Na^+	Na^+	Na^+	Na^+	Y^{3+}	Y^{3+}
7	6	6.3	9.8	Na^+	Na^+	Na^+	Y^{3+}	Y^{3+}	Na^+
8	6	6.3	10.0	Na^+	Na^+	Y^{3+}	Na^+	Y^{3+}	Na^+
9	2	2.1	3.8	Y^{3+}	Na^+	Y^{3+}	Na^+	Y^{3+}	Na^+
10	6	6.3	14.6	Y^{3+}	Na^+	Y^{3+}	Na^+	Na^+	Y^{3+}
11	12	12.5	17.0	Y^{3+}	Y^{3+}	Na^+	Y^{3+}	Na^+	Na^+
12	6	6.3	9.8	Y^{3+}	Y^{3+}	Y^{3+}	Na^+	Y^{3+}	Na^+
13	6	6.3	9.6	Y^{3+}	Y^{3+}	Na^+	Y^{3+}	Y^{3+}	Na^+
14	3	3.1	2.7	Y^{3+}	Y^{3+}	Y^{3+}	Y^{3+}	Na^+	Na^+
15	6	6.1	6.1	Y^{3+}	Y^{3+}	Y^{3+}	Y^{3+}	Y^{3+}	Na^+
16	1	1.0	0.5	Y^{3+}	Y^{3+}	Y^{3+}	Y^{3+}	Y^{3+}	Y^{3+}

respective factors for the averaging scheme, *i.e.*, 66.7 % and 33.3 %, are shown in the top row for each doping site in the third column. From the degeneracy of the supercell and the occurrence of the respective doping site, weighting factors for each of the 16 configurations were created (third column). This was achieved by dividing the degeneracy of a configuration through the total number of possible configurations for this doping sites (top row for each doping site in the second column) and multiplying it with the probability of the doping site. The resulting weighting factors are shown as percentages relative to those of all other configurations. Also, shown in the last column of Table 1 is a detailed description of the distribution of Na^+ and Y^{3+} inside the respective supercell for each configuration. When calculating averaged values for lattice parameters and bond lengths, the results of the 16 different configurations were averaged by weighing each individual value with the corresponding factor. Through this scheme, a single value was obtained.

While writing this dissertation and reevaluating the employed scheme, two possible adjustments of the approach came to mind. 1) While the distribution probability of Ln^{3+} onto the two possible doping sites is important when calculating the optical properties of a doped crystal, this distinction is not logical when examining the lattice structure, especially in the case of *undoped* β-$NaYF_4$. Indeed, instead of applying the additional $^2/_3$ and $^1/_3$ factors, all 16 configurations, irrespective of whether they originate from a 1a or 1f site, should have been pooled together when calculating their degeneracy weighting, since all of them represent the same 2 x 2 x 4 supercell. To give an example, instead of arriving at a weighting factor of 16.7 % for configuration 2, Table 1, the value should have been 2.9 % (2 degenerate configurations divided by 68 possible configurations). No additional factors need to be applied in this step. When introducing this corrected scheme, the weighting factors for configurations at 1f sites decrease significantly, whereas the ones of configurations at 1a sites increase moderately. Specifically, the weighting factor of configuration 11 would increase from 12.5 % to 17.6 %.

2) Moreover, in the employed averaging scheme the energetic separation of the different supercells was not considered when calculating the weighting factors. Even though the energetic separations were made available in the original manuscript (Table 2 below). By omitting such a Boltzmann distribution from the weighting factors, an additional error was introduced into the averaging scheme. This omission favours configurations with

local clustering of Na^+ and Y^{3+}, as their respective supercells tend to be higher in energy, Table 2. For a synthesised nanoparticle, these configurations would therefore not be found as often as implied by the weighting factors presented in Table 1.

When correcting the weighting factors for both the different degeneracies and the additional Boltzmann distribution, new weighting factors as reported in Table 1, fourth column, were obtained. Given the mostly small energetic differences between the available configurations, these weighting factors are not too different from the values based purely on the updated degeneracies. For example, instead of arriving at 2.9 % for configuration 2, 3.3 % is obtained when introducing also the second corrections. The energetic discrepancy of configuration 2 to the energetically lowest configuration (configuration 10, Table 2) is smaller than the energetic discrepancy of most other configurations. Therefore, the weighting factor of configuration 2 is slightly increased.

Table 2: Results of the structural optimisations for the 16 different configurations of β-$NaYF_4$. For undoped β-$NaYF_4$, lattice energies calculated relative to the most stable configuration (ΔE), deviations of the lattice parameters from the experimental values ($Deviation_{LP}$), and averaged bond lengths ($Y^{3+}-F^-$) are displayed. For β-$NaYF_4$ doped with 4.2 % Er^{3+}, only energy differences are shown. Reproduced from Ref. 1 with permission from the Royal Society of Chemistry, 2025.

		Undoped β-$NaYF_4$			**4.2 % Er^{3+}**
Site	Configuration	ΔE ($kJ \cdot mol^{-1}$)	$Deviation_{LP}$ (%)	$Y^{3+}-F^-$ (Å)	ΔE ($kJ \cdot mol^{-1}$)
1f	1	0.0	0.77	2.347	0.1
	2	1.9	0.83	2.342	2.4
	3	3.4	0.90	2.338	3.4
1a	4	6.5	0.78	2.372	6.5
	5	4.6	0.85	2.354	4.6
	6	4.3	0.88	2.360	3.4
	7	1.9	0.88	2.346	1.8
	8	1.8	0.92	2.345	1.8
	9	1.2	0.86	2.336	1.2
	10	0.0	0.77	2.338	0.0
	11	2.6	0.87	2.344	1.6
	12	1.9	0.92	2.333	1.9
	13	2.0	0.86	2.335	2.3
	14	4.8	0.89	2.336	4.8
	15	4.2	0.84	2.330	4.2
	16	7.9	0.76	2.326	8.3

Interestingly, the effect of these updated weighting factors on the calculated lattice characteristics is marginally. Indeed, instead of arriving at a discrepancy of 0.853 % compared to the experimental value for the lattice parameters, the updated value is 0.858 %. Additionally, the value reported below and in the corresponding manuscript was rounded to one decimal place, 0.9 %, given the limitations of the theoretical model itself.[1]

The reasons for such small changes are probably two-fold: 1) Error cancelation. The adjusted weighting factors did not favour configurations with particularly small or large deviations of the supercell compared to the experimentally observed one. When adjusting the factors, the differently weighted deviations resulted in almost the same error. 2) The deviations of all calculated supercells are very small and in a narrow percentage range, *i.e.*, between 0.76 and 0.92 %, forth column in Table 2. The effect of the adjusted weighting parameters on the final lattice parameters is, therefore, already rather small. Overall, the two shortcomings of the original weighting scheme cannot invalidate the conclusions spelled out in Conrad (I) *et al*. and in the following.[1]

4.1.5.2. Impact of Disorder, 1f

Comparison to experimental values reported in the literature revealed a deviation of the lattice parameters by 0.9 % for the values obtained via the weighted averaging, in close agreement with two other theoretical studies that reported deviations of 1.3 % and 0.3 %.[51, 59, 91] Also, the Y^{3+}-F^{-} bond length, averaged over all nine bonds of the coordination polyhedral, was calculated to be 1.2 % smaller than experimental values. This value was slightly better than the reported deviation of a previous theoretical study (5.9 %).[56, 91] Additionally, all nine bond lengths deviated from each other, pointing towards a much reduced symmetry of the coordination polyhedron. Importantly, all earlier theoretical studies did not account for the disorder of the lattice and instead assumed a single, ordered configuration of the crystal structure. Additional comparisons to values reported in the literature and other metrics can be found in Conrad (I) *et al*.[1]

Interestingly, while the Na^{+} / Y^{3+} disorder at the 1f sites pushed around the F^{-} closest to the disordered sites and affected the energetic stabilisation of the supercell overall, Table 2, the supercell as a whole did not change its shape significantly. On the other hand, the small energetic differences of the configurations from supercell to supercell implied

that it is very likely that numerous local configurations are available for the crystal structure. Largest changes in energy were found for configurations with local clustering of either Na^+ or Y^{3+}, *i.e.*, configuration 4 to 6 and 14 to 16, respectively. This finding suggest that such clustering of one cation destabilises the lattice. Indeed, the most stable configuration presented a regularly alternating distribution of Na^+ and Y^{3+}, *i.e.*, configuration 10, Table 2. This finding is in line with an earlier study.[50] Furthermore, the available doping sites varied from supercell to supercell, with the common observation being that their point groups were all reduced to C_1. This finding is different to that of a previous X-ray diffraction study, also including a Monte-Carlo simulation, which postulated that some of the doping sites should be of $C_{3v/h}$ symmetry.[50] The current study does not support this hypothesis. Instead, it is possible that the earlier study drew conclusions from the average composition of the crystal onto local arrangements. While the results presented here cannot make too many statements about long-range behaviour of the crystal structure, it has been shown unambiguously that the computational results imply a locally disordered structure for β-$NaYF_4$. The latter will be further supported by the data provided in the second manuscript that is part of this dissertation. Overall, the model designed is well capable of reproducing the structure of a disordered lattice.

4.1.5.3. Impact of Disorder, 2h

The 2h Na^+ disorder produced smaller but qualitatively similar changes compared to the 1f disorder. Through the changing lattice position of the respective Na^+, the nearest F^- were dislocated slightly within the lattice. Interestingly, energetic differences of the supercells between the differently 2h disordered configurations were much reduced compared to the 1f disorder. Indeed, the largest change, 1.4 $kJ \cdot mol^{-1}$, was observed for configuration Na3. Configuration Na3 mimicked the arrangement of configuration 1 and 16 for the 1f disordered site. These configurations were closer to a destabilisation energy of 7 $kJ \cdot mol^{-1}$. Configurations 1 and 16 either incorporated only Na^+ or only Y^{3+}, respectively, at their six closest 1f disordered sites. In configuration Na3, all Na^+ at 2h sites were shifted along the same direction, being as unlikely as having the same type of cation at all six 1f sites. The reduced energetic separation of the 2h disordered configurations indicated that this type of disorder should be even more prevalent in the lattice than chances induced through the 1f disorder. Apart from this, lattice distortions induced by the 2h disorder appeared to

be slightly smaller than those induced by the 1f disorder. Additional data regarding the 2h disorder is provided in Conrad (I) *et al*.[1]

4.1.5.4. Impact of Doping

Introduction of Ln^{3+} dopants, *i.e.*, Er^{3+}, Tm^{3+}, and Yb^{3+}, in low concentrations (< 5 mol%) into the β-$NaYF_4$ crystal produced minimal additional structural perturbations relative to those invoked by the intrinsic disorder. The dopants occupied Y^{3+}-dominated 1f site and 1a sites and the surroundings needed to adapt to the change in ionic radii and electronic configuration compared to Y^{3+}. However, the ionic radii of the ions are very similar. The lack in structural adaptation to the dopants was therefore not surprising. Lattice parameters changed by less than 1 % for each configuration compared to its undoped counterpart. Energetic differences from configuration to configuration were slightly different compared to undoped β-$NaYF_4$, Table 2. However, the trends observed earlier, that is, lower energy for more regularly alternating configurations, were fully followed by the doped configurations. This is true for both the 1f and 2h disordered configurations. The magnitude and pattern of distortion were primarily governed by the local Na^{3+}/Y^{3+} arrangement rather than by the dopant identity. Overall, low-percentage doping did not seem to induce significant additional disorder into an already inherently disordered lattice. That being said, this observation might be limited to cases were the dopant and the ion it replaces share similar ionic radii. The structural uniformity of the disorder effect across different dopants confirmed that the host lattice (disorder) dominates the local geometry. Additional data regarding the doping-induced disordered is provided in Conrad (I) *et al*.[1]

4.1.6. Conclusion

According to the computational experiments conducted and the data retrieved, β-$NaYF_4$ is intrinsically disordered at the atomic scale and its 1f and 2h disordered sites generate a network of irregular coordination polyhedra around potential Ln^{3+} doping sites. Energetic analysis showed that configurations with alternating Na^+ and Y^{3+} occupation at the 1f sites along the c-axis site are preferred but not omnipresent, since energy differences between all configurations remained small ($> 8\,kJ \cdot mol^{-1}$). Additionally, it was observed that more locally clustered Na^+ or Y^{3+} leads to more energetic destabilisation. Differences

for the 2h disordered sites were more muted. Even for the most unfavourable configuration, *i.e.*, Na3, a destabilisation of only 1.4 $kJ \cdot mol^{-1}$ compared to the most stable configuration, *i.e.*, Na1, was observed. Indeed, the cation disorder of Na^{+} at the 2h sites had much lower energetic differences associated with it compared to the cation disorder of Na^{+} and Y^{3+} at the 1f sites. Low-percentage Ln^{3+}-doping did not induce further significant disorder into the lattice. Differences of total energies of the doped supercells between the 1a and 1f sites were small, with a small preference for the 1a site (0.1 $kJ \cdot mol^{-1}$). While it is possible that some long-range order exists for the crystal, present results point towards a locally disordered arrangement of nearly all ions in the lattice.

The overall picture of (doped) β-$NaYF_4$ is that of a structurally flexible lattice with numerous configurations. Moreover, the point group of almost all available doping sites was found to be of C_1 symmetry, which should result in maximally split energy levels of Ln^{3+} doped into the lattice. Also, each doping site differed marginally from all other available sites. The result of the slightly varying surroundings should, therefore, lead to differing opto-electronic properties of the Ln^3. Also, the results obtained demonstrated that geometry optimisation using periodic DFT can capture the intrinsic complexity of a disordered lattice. The approach yielded a physically meaningful energy landscape for the disordered configurations and allowed the assignment of statistical weights based on configurational degeneracy (and possibly Boltzmann distribution). The findings provided a structural basis for understanding the optical behaviour of β-$NaYF_4$, where the diversity of local environments determines the multiplicity of crystal-field interactions experienced by dopant ions. This first study paved the way for assessing the optical properties of the Ln^{3+} in detail.

4.2. Energy Levels and Oscillator Strengths

The second study built directly upon the optimised supercells of $LiYF_4$ and β-$NaYF_4$, established in the previous work, and extends the investigation to the optical properties of lanthanide dopants embedded within these lattices. The central objective was to determine whether equally good data on crystal field energy levels and oscillator strengths of Ln^{3+} can be generated by a second computational setup, for both an ordered and a disordered structure. The study focused on three representative dopants, *i.e.*, Er^{3+}, Tm^{3+}, and Yb^{3+}, that exhibit characteristic intra-4f transitions spanning UV, Vis and NIR wavelengths. For each dopant, 14 distinct disordered configurations of β-$NaYF_4$ were considered. Furthermore, matching calculations were conducted for the ordered $LiYF_4$ structure and the same dopants. The calculations explicitly aimed at linking atomistic structural properties of the host lattices to exhibited optical properties of the dopants through a multiscale procedure, combining an embedded cluster setup, high-level wavefunction-based computational methods, and, once more, weighted averaging.

4.2.1. Embedded Cluster Calculation

The previously generated supercells with their individual configurations were used as obtained after the preceding geometry optimisation to create an embedded cluster setup, Figure 13.[114-116] In an embedded cluster setup, the properties of the central ion in a specific environment are probed. The calculation is made computationally affordable by introducing more and more approximations of the other ions present in the setup the further these ions are away from the central ion under consideration. The motivation for such a setup is that the central ion can be treated on a computational high level of accuracy, while including all relevant contributions of the environment through a slightly coarser representation of this environment.

For creating an embedded cluster, the single Ln^{3+} of a doped supercell and its closest F^- were cut from the structurally optimised supercell. These ions formed the quantum cluster of the cluster embedding (Figure 13A). In the ensuing calculations, the electrons of these ions were treated explicitly on a quantum-chemical level of accuracy. The composition of all quantum clusters was the same the same for each compound. LnF_8^{5-} in the case of $LiYF_4$, and LnF_9^{6-} for all configurations of β-$NaYF_4$. However, the exact arrangement

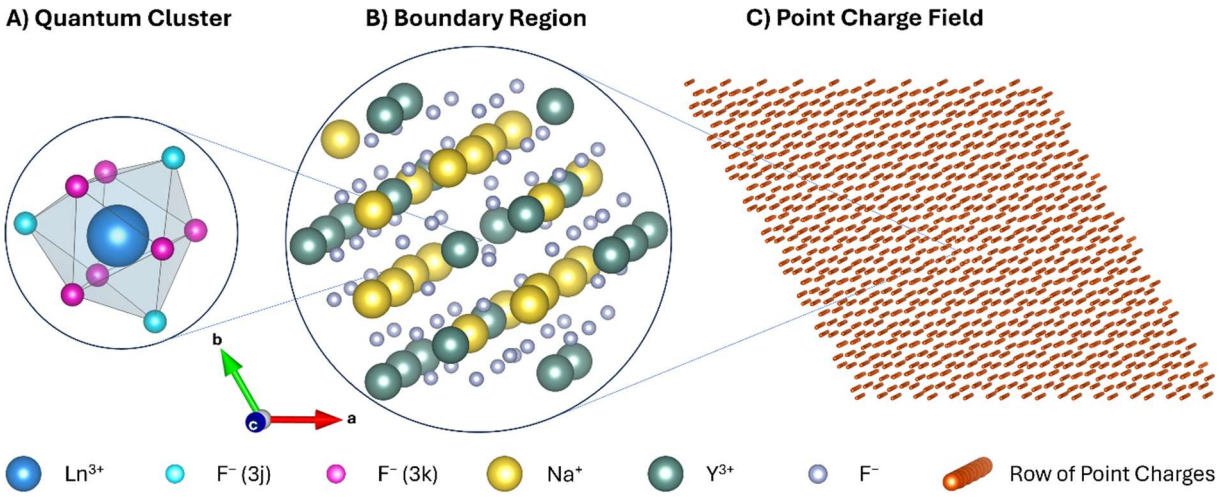

Figure 13: Ionic cluster embedding of one cluster avilable for β-$NaYF_4$:Ln^{3+}. **(A)** LnF_9^{6-} quantum cluster. **(B)** $Na_{19}Y_{22}F_{62}$ boundary region. **(C)** Field with 17,886 point charges. Reproduced with permission from Ref. 2. Copyright 2025 American Chemical Society.

of the F^- around the Ln^{3+} varied, depending on the configuration and the type of the Ln^{3+} doped into the respective supercell. Next, the two double layers of closest cations and anions were removed from the supercell and added to the embedding of the Ln^{3+} and its neighbouring F^-. These additional ions created the boundary region around the quantum cluster (Figure 13B). The boundary region confined the electrons in the quantum cluster and mimicked the local environment the electrons in the quantum cluster experience in a real crystal. In the boundary region, a point charge plus an effective core potential (ECP) is used to approximate the electrons of the respective ions (called capped point charges). This simplification is possible because in an embedded cluster calculation, the properties of the central ion, here the Ln^{3+}, are of relevance, not the properties of the structure as a whole. The boundary region of each embedded clusters typically contained around 100 ions, represented by point charges and ECPs. Finally, several thousand point charges were added around the boundary region, introducing the long-range electrostatic components of the host crystal to the calculation (Figure 13C). The exact position and magnitude of the point charges were optimised using the programme Env by LePetit and Gelle.[117]

The positions of all ions and their electronic structure were written into an Orca input file.[118-120] Three input files were created for the three Ln^{3+} doped into $LiYF_4$. Three times 14 input files were created for the different dopants and configurations of β-$NaYF_4$. Of the initial 16 configurations of β-$NaYF_4$, the two with the lowest weighting factors, *i.e.*,

configuration 4 and 16, Table 1, were not included in this calculation. Instead, the embedding was created for the 14 configurations remaining for each dopant.

4.2.2. Computational Details

The electronic structure of the lanthanide in the centre of the embedding was calculated using the CASSCF/NEVPT2/QDPT methodology with the full set of 4f orbitals in the active space. The exact computational methodology can be best described by the description provided in Conrad (II) *et al.*:[2]

"To this end, state-averaged complete active space self-consistent field (SA-CASSCF) followed by N-electron valence state second-order perturbation theory (NEVPT2) and quasi-degenerate perturbation theory (QDPT) calculations for spin-orbit coupling (SOC) were performed for the prediction of wavefunctions and corresponding energies.[121] All seven 4f-orbitals and the respective number of 4f-electrons for Er^{3+} (11), Tm^{3+} (12), and Yb^{3+} (13) were included in the active space. (...) Furthermore, the second-order scalar relativistic Douglas-Kroll-Hess (DKH) Hamiltonian was employed to account for scalar-relativistic effects.[122-124] (...) Ln^{3+} and F^- in the quantum cluster were described by the all-electron SARC2-DKH-QZVP and DKH-DEF2-TZVPP basis sets, respectively.[125-127] (...) Capped point charges in the boundary region were represented by the charge of the respective ion plus the following ECP definitions: Li SD(2,SDF),[128] F SD(2,MWB),[129] Na SD(10,SDF),[128] and Y SD(28,MWB).[130]"

For each calculation of a specific embedding, the resulting output file contained information about the energetic positioning of the corresponding crystal field energy levels and about the oscillator strengths between these energy levels.

4.2.3. Results for $LiYF_4$

Averaging was not required for the results obtained for $LiYF_4$ doped with the three different lanthanides. Each embedded cluster calculation for one lanthanide could be compared directly to the many data sets for this dopant-host system available in the literature.[131-134] This ordered structure served, once more, as a control system for validating the computational approach against which the effects of disorder in β-$NaYF_4$ could be assessed.

4.2.3.1. Crystal Field Energy Levels

The conducted calculations produced crystal field energy levels of Er^{3+}, Tm^{3+}, and Yb^{3+} doped into $LiYF_4$ with high accuracy. Selected values of Er^{3+} are shown in Table 3, values

for Tm^{3+} and Yb^{3+} can be found in the electronic supplementary information (ESI) of Conrad (II) *et al*.[2] Discrepancies between the calculated values and experimental values in the literature were generally below 100 cm^{-1} for all three Ln^{3+}. Root mean square errors (RMSE) of all crystal field energy levels for each Ln^{3+} were 64 cm^{-1} or lower.[131, 132, 134] The only exceptions to this very good accuracy were the crystal field energy levels of the $^2H_{11/2}$ multiplet of Er^{3+}, with deviations as high as 400 cm^{-1}. It appeared that the wavefunction of the multiplet did not converge as efficiently as for the other multiplets and slightly larger deviations for the crystal field energy levels were observed. A specific reason for this behaviour of the wavefunction could not be determined. The poorer performance of this multiplet and of the properties derived from it was observed for all calculations of Er^{3+}, for both $LiYF_4$ and β-$NaYF_4$ (discussed below). Still, general accuracy even of the $^2H_{11/2}$ was reasonably good. Overall, the good reproduction of the experimental values for almost all multiplets showed that the computational protocol accurately accounted for crystal-field effects in an ordered lattice on almost a quantitative level. Consequently, deviations observed for β-$NaYF_4$ could be attributed to structural disorder rather than methodological inaccuracies, except in the case of the $^2H_{11/2}$ multiplet of Er^{3+}.

4.2.3.2. Multiplet Oscillator Strengths

From the Orca calculations, also oscillator strengths between crystal field energy levels were obtained. These oscillator strengths were processed with a dedicated Python script to receive absorption oscillator strengths of multiplet-multiplet transitions for each Ln^{3+}. The multiplet oscillator strengths between the first excited states and the ground state for Er^{3+} doped into $LiYF_4$ are shown in Table 4. Displayed in the same table are the measured and fitted experimental values for the same oscillator strengths from the literature.[135, 136] Except for the transition between the ground state and the $^2H_{11/2}$ multiplet, the predicted values are in close agreement with the experimental data sets. Indeed, the computed values mostly lie in between the two data sets. Values for Tm^{3+} and Yb^{3+} can be found in Conrad (II) *et al.* No literature values were available for these two Ln^{3+}.[2] Experimentally measured or calculated *crystal field* oscillator strengths were not reported in the literature. Therefore, no comparison between individual values was possible. However, judging by the multiplet oscillator strengths, qualitative agreement between the *ab initio* values and experimental was obtained. This observation further validated the methodology

Table 3: Calculated (*ab initio* and fitted) and experimental crystal field energy levels of $LiYF_4$: Er^{3+}. Reproduced with permission from Ref. 2. Copyright 2025 American Chemical Society.

Crystal Field Energy Level[a] ($^{2S+1}L_J$)		This Work (cm^{-1})	Experiment[131, b] (cm^{-1})	Fitted[137] (cm^{-1})
$^4I_{15/2}$	1	0	0	−11
	3	41	17	8
	5	52	28	38
	7	79	57	60
	9	281	255	256
	11	324	290	298
	13	350	320	319
	15	365	355	352
$^4I_{13/2}$	1	6 537	6 540	6539
	3	6 546	6 545	6540
	5	6 597	6 585	6585
	7	6 692	6 680	6683
	9	6 705	6 704	6702
	11	6 729	6 731	6735
	13	6 762	6 745	6747
$^4I_{11/2}$	1	10 264	10 213	10215
	3	10 282	10 230	10230
	5	10 355	10 290	10284
	7	10 359	10 300	10305
	9	10 375	10 309	10312
	11	10 402	10 327	10323
$^4I_{9/2}$	1	12 461	12 364	12348
	3	12 581	12 486	12493
	5	12 626	12 540	12540
	7	12 640	12 568	12568
	9	12 716	12 663	12663
$^4F_{9/2}$	1	15 414	15 307	15306
	3	15 441	15 325	15325
	5	15 452	15 341	15343
	7	15 527	15 416	15418
	9	15 555	15 469	15471
$^4S_{3/2}$	1	18 462	18 433	18434
	3	18 492	18 492	18489
$^2H_{11/2}$	1	19 562	19 152	19170
	3	19 574	19 172	19192
	5	19 617	19 224	19233
	7	19 684	19 309	19303
	9	19 697	19 326	19313
	11	19 719	19 342	19329
$^4F_{7/2}$	1	20 624	20 571	20564
	3	20 631	20 573	20566
	5	20 710	20 662	20660
	7	20 719	20 671	20668

a: The $^{2S+1}L_J$ term symbols are derived from the state with the highest weight after the QDPT-SOC treatment. M_J values and irreducible representations for all levels are available in the work of Couto dos Santos *et al*.[131] b: The sample contained 1 mol% Er^{3+} but the obtained values should still be comparable as properties of the Ln^{3+} are fairly independent of the Ln^{3+} concentration in the low-percentage doping regime.[138]

Table 4: Calculated (*ab initio* and fitted) and experimental absorption multiplet oscillator strengths between the ground state and higher multiplets of Er^{3+} doped into $LiYF_4$. Values for the oscillator strengths were multiplied by 10^6. Reproduced with permission from Ref. 2. Copyright 2025 American Chemical Society.

$^4I_{15/2} \rightarrow$	This Work	Reference 135[a]		Reference 136[b]	
		Experiment	Fitted	Experiment	Fitted
$^4I_{13/2}$	0.96	1.54	0.95	0.72	0.70
$^4I_{11/2}$	0.28	0.42	0.41	0.16	0.31
$^4I_{9/2}$	0.01	0.15	0.17	0.06	0.04
$^4F_{9/2}$	0.51	1.23	1.35	0.61	0.62
$^4S_{3/2}$	0.28	0.34	0.37	–	–
$^2H_{11/2}$	0.14	2.36	2.68	1.29	1.26
$^4F_{7/2}$	0.88	1.01	1.42	0.47	0.93

a: The values were obtained by averaging over four samples with an Er^{3+} concentration of 4.9, 13.6, 21.4, and 41.3 mol%. No concentration effects were observed. b: The sample contained 1 mol% Er^{3+}.

4.2.4. Results for β-$NaYF_4$

The Orca output files for an embedded cluster calculation of β-$NaYF_4$ doped with one of the three Ln^{3+} looked very similar to corresponding $LiYF_4$ output files and contained the same types of information. However, the larger number of files per dopant, *i.e.*, 14, required a similar data processing as reported for the geometry optimisation.

4.2.4.1. Averaging Scheme

The averaging scheme implemented for calculating the crystal field energy levels and oscillator strengths of doped β-$NaYF_4$ is a hybrid of the two schemes, *i.e.*, old and new weighting, described in the part of this dissertation covering the geometry optimisation (chapter 4.1). The lattice of β-$NaYF_4$ has two potential doping sites for Ln^{3+}, *i.e.*, 1a and 1f, and each unit cell consists of one 1a and one 1f site. However, on average only every second 1f site is occupied by Y^{3+} and can be doped with an Ln^{3+}. Therefore, the devised

averaging scheme took into account that the probability of doping an Ln^{3+} into an 1a site is twice as high ($^2/_3$, configurations 5 to 15) as the probability of doping an Ln^{3+} into an 1f site ($^1/_3$, configurations 1 to 3). This distinction and the corresponding factors were therefore retained from the old averaging scheme of the geometry optimisation. Another factor that was kept constant between the two studies was the degeneracy of the configurations. As described earlier, each of the 14 configurations represents several of the, now reduced, 66 (4 plus 62) total configurations of the initial supercell. Therefore, each embedded cluster with its Ln^{3+} in the centre also represented the same number of configurations. These two factors were combined to provide the first part of the averaging scheme, termed statistical occurrence. Individual values for Er^{3+} are shown in Table 5, values for the other Ln^{3+} are very similar.[2]

The second part of the averaging scheme followed the arguments as laid out for the new weighting scheme used for the geometry optimisation. That is, each supercell had a varying total energy, and the distribution of these supercells in a synthesised nanoparticle should follow a Boltzmann distribution. When generating the second part of the averaging scheme, the energetic differences of the underlying supercells were retained. While in principle it would have been possible to use the energetic differences of the embedded clusters, their varying configurations prohibited this. Therefore, the calculated Boltzmann distribution, Table 5, depended on the energetic differences of the underlying supercells.

The two parts of the averaging scheme, that is, statistical occurrence and Boltzmann distribution, were multiplied with each other to arrive at a final weighting factor. This weighting factor was then expressed as a percentage relative to the factors of all other configurations, last column of Table 5. The obtained weighting factors for this second study were almost equal to the old weighting factors of the geometry optimisation (Table 1 above). However, here they accurately reflected the distribution of the Ln^{3+} into the different doping sites by applying the $^2/_3$ or $^1/_3$ factor. No subsequent adjustments were made.

4.2.4.2. Crystal Field Energy Levels

With the weighting factors at hand, single (averaged) values for crystal field energy levels of Er^{3+} doped into β-$NaYF_4$ could be calculated and compared to values reported in the literature (Table 6). The same trends as described for $LiYF_4$: Er^{3+} were observed for the current dopant-host combination. Comparison to the (limited) experimental data showed

Table 5: Calculation of weighting factors for the β-$NaYF_4$: Er^{3+} clusters. The table groups the clusters according to the site at which the Ln^{3+} is doped into, *i.e.*, the 1f site (cluster 1 to 3) and the 1a site (cluster 5 to 15). *E* in the table refers to the energy of the underlying supercells. Reproduced with permission from Ref. 2. Copyright 2025 American Chemical Society.

Cluster n, (Na^+:Y^{3+} Distribution)	Degeneracy (Deg.)	Statistical Occurrence ($^{Deg.}/_{x}\cdot{}^{y}/_{3}$)	Boltzmann Distribution $f(E_n)$ / $f(E_{10})$	Weighting Factor (%) (Statistical Occurrence · Boltzmann Distribution)
1f	($x=4$, $y=1$)			
1 (2:0)	1	0.08	0.98	12.9
2 (1:1)	2	0.17	0.61	16.0
3 (0:2)	1	0.08	0.49	6.5
1a	($x=62$, $y=2$)			
5 (5:1)	6	0.06	0.38	3.8
6 (4:2)	3	0.03	0.49	2.4
7 (4:2)	6	0.06	0.68	6.7
8 (4:2)	6	0.06	0.69	6.8
9 (3:3)	2	0.02	0.77	2.5
10 (3:3)	6	0.06	1.00	9.8
11 (3:3)	12	0.13	0.71	14.1
12 (2:4)	6	0.06	0.67	6.6
13 (2:4)	6	0.06	0.62	6.1
14 (2:4)	3	0.03	0.37	1.8
15 (1:5)	6	0.06	0.41	4.1

once more small discrepancies on average.[139, 140] As observed for $LiYF_4$: Er^{3+}, deviations for the $^2H_{11/2}$ multiplet of Er^{3+} were much more pronounced, *i.e.*, up to 500 cm^{-1}. Values for Tm^{3+} and Yb^{3+} doped into β-$NaYF_4$ are reported in Conrad (II) *et al.*[2]

Overall, the computed data reflected the measured crystal field energy levels rather well. The small deviations between the theoretical data and the experimental results for this disordered structure and the very similar deviations compared to the ordered structure validated the chosen embedding scheme, theoretical model, and averaging scheme.

4.2.4.3. Multiplet Oscillator Strengths

Different to $LiYF_4$, the oscillator strengths between crystal field energy levels from the Orca output file had to be processed twice for β-$NaYF_4$. First, the previously mentioned Python script was applied to obtain absorption oscillator strengths between multiplet-multiplet transitions for all 14 data sets for each of the three dopants. Next, per dopant all oscillator strengths for one transition were averaged using the weighting factors introduced above (Table 5). The resulting multiplet absorption oscillator strengths of Er^{3+}

Table 6: Calculated (*ab initio* and fitted) crystal field energy levels and experimental multiplets of β-$NaYF_4$ doped with Er^{3+}. Reproduced with permission from Ref. 2. Copyright 2025 American Chemical Society.

Crystal Field Energy Level ($^{2S+1}L_J$)		This Work (cm^{-1})	Experiment[139, a] (cm^{-1})	Fitted[140, b] (cm^{-1})
$^4I_{15/2}$	1	0	0	0
	3	81		2
	5	136		4
	7	194		61
	9	242		72
	11	294		79
	13	340		79
	15	411		152
$^4I_{13/2}$	1	6 586	6 636	6 519
	3	6 619		6 520
	5	6 644		6 521
	7	6 676		6 550
	9	6 702		6 553
	11	6 737		6 569
	13	6 799		6 625
$^4I_{11/2}$	1	10 312	10 226	
	3	10 334		
	5	10 353		
	7	10 370		
	9	10 400		
	11	10 439		
$^4I_{9/2}$	1	12 542	12 419	
	3	12 562		
	5	12 639		
	7	12 683		
	9	12 739		
$^4F_{9/2}$	1	15 450	15 310	15 170
	3	15 477		15 191
	5	15 505		15 220
	7	15 531		15 246
	9	15 566		15 265
$^4S_{3/2}$	1	18 507	18 529	18 440
	3	18 536		18 493
$^2H_{11/2}$	1	19 609	19 229	19 308
	3	19 644		19 314
	5	19 661		19 321
	7	19 685		19 326
	9	19 704		19 334
	11	19 723		19 343
$^4F_{7/2}$	1	20 622	20 524	
	3	20 675		
	5	20 731		
	7	20 768		

a: The sample contained 10 mol% Er^{3+} and 20 mol% Yb^{3+} and the reported wavenumbers represent the position of the multiplet at maximum intensity. b: The authors fitted the values from magnetization data, not optical spectra. Only a few multiplets were predicted.

---

between the ground state and the first excited states and an appropriate data set from the literature are shown in Table 7. Values for Tm^{3+} and Yb^{3+} doped into β-$NaYF_4$ can be found in Conrad (II) *et al*.[2]

Differences between the calculated absorption oscillator strengths (between multiplets) and measured values from the literature were larger for β-$NaYF_4$: Er^{3+} (Table 7) than for $LiYF_4$: Er^{3+} (Table 4, above). Also, the values calculated for β-$NaYF_4$: Er^{3+} did not follow the trend observed for the experimental data. This is despite the fact that the crystal field energy levels of β-$NaYF_4$: Er^{3+} were reasonably close to the experimental values. Also, the calculated multiplet absorption oscillator strengths for β-$NaYF_4$: Er^{3+} were closely resembling those of $LiYF_4$: Er^{3+} and followed the exact same trends, for both the computational and experimental data of $LiYF_4$: Er^{3+}. Furthermore, the values calculated for β-$NaYF_4$: Er^{3+} were also very similar to the experimental values of β-Na*Gd*F_4: Er^{3+}.[141] It is noteworthy that the sample used for the experimental determination of the absorption oscillator strengths of β-$NaYF_4$: Er^{3+}, β-$NaYF_4$: 2 mol% Er^{3+}, 20 mol% Yb^{3+}, was quite different in terms of composition to the sample from the computational setup, β-$NaYF_4$: 4.2 mol% Er^{3+}. The change in composition could be a possible explanation for the observed discrepancies. It will be demonstrated in the next chapter that very good agreement between the computed *crystal field* oscillator strengths and experimentally obtained emission spectra was observed. This hints towards the validity of the computational data.

4.2.5. Conclusion

Considering all available data sets and their discrepancies to experimental and fitted data, it is deduced that the computed values reproduced the experimental results with good accuracy. Largest discrepancies were observed consistently for the $^2H_{11/2}$ multiplet of Er^{3+}, results for all other multiplets of the three dopants, *i.e.*, Er^{3+}, Tm^{3+}, and Yb^{3+}, in both the ordered ($LiYF_4$) and disorder structure (β-$NaYF_4$) were significantly better. This observation proves that the validity of the computational data did not depend on the exhibited order/disorder of the host lattice. Also, these findings indicated that both the chosen

Table 7: Calculated (*ab initio* and fitted) and experimental absorption oscillator strengths between the ground state and higher multiplets of β-$NaYF_4$ doped with Er^{3+}. The oscillator strengths were multiplied by 10^6. Reproduced with permission from Ref. 2. Copyright 2025 American Chemical Society.

$^4I_{15/2}$ →	This Work	Experiment[139, a]	Fitted[139, a]
$^4I_{13/2}$	1.01	1.33	0.86
$^4I_{11/2}$	0.30	–	0.40
$^4I_{9/2}$	0.02	0.22	0.17
$^4F_{9/2}$	0.59	0.12	0.13
$^4S_{3/2}$	0.31	0.36	0.34
$^2H_{11/2}$	0.23	0.62	0.42
$^4F_{7/2}$	0.98	0.16	0.13

a: Values are from a sample containing 10 mol% Er^{3+} and 20 mol% Yb^{3+}. The Er^{3+} transition from the ground state to the $^4I_{11/2}$ multiplet could therefore not be observed.

computational setup and the employed embedding approach as well as the calculated weighting factors were of high quality.

In general, the theoretical investigation provided a coherent and quantitatively accurate description of the electronic structure (energy levels and oscillator strengths) of Er^{3+}, Tm^{3+}, and Yb^{3+} in ordered $LiYF_4$ and in disordered β-$NaYF_4$. This electronic structure serves as the basis for further investigations of the performance of Ln^{3+} in (dis)ordered materials in relation to photon upconversion.

4.3. Theoretical versus Experimental Spectra

As demonstrated in the previous chapters, little experimental measurements und theoretical calculations on a crystal field level of theory are available for β-$NaYF_4$. Instead of relying on imperfect comparisons to data sets of particles with different composition, it was, therefore, decided to synthesise and characterise custom upconverting nanoparticles (UCNP) with the same composition as created in the computational setup. To this end, a set of six batches of UCNPs with different combinations of Er^{3+}, Tm^{3+}, and Yb^{3+} in the same host material, *i.e.*, β-$NaYF_4$, was synthesised via thermal decomposition of acetate precursors (see below). The total Ln^{3+}-doping concentration for all UCNPs was chosen to be approximately equal to 4.2 mol%, matching the theoretical doping percentage of the supercells created for the first study. Three of the samples were doped with only one of each of the three Ln^{3+}, three more samples were co-doped with each two of the three Ln^{3+}. While the co-doping had the potential to alter the observed properties of the Ln^{3+}, it enabled measuring optical transitions of the Ln^{3+} that were otherwise not accessible with the setup available. In fact, the low-percentage co-doping changed the measured characteristics of the Ln^{3+} in the co-doped nanoparticles only were little, which was consistent with the expected behaviour (see discussion above). After synthesising the UCNPs, the samples were extensively characterised via X-ray diffraction (XRD), transmission electron microscopy (TEM), and optical spectroscopy. Full details regarding the results of the synthesis and characterisation of the different (co)doped samples can be found in Conrad (II) *et al.* and its ESI.[2] Results presented in the following focus on the optical properties of β-$NaYF_4$: 4.2 mol% Er^{3+} and the comparison of its properties to the spectra generated from the computational results. All relevant effects observed, and conclusions drawn, can be described via this sample only. Finally, comparing the influence of a disordered crystal field on an Ln^{3+} via computed and measured data provides a critical validation of the computational methodology.

4.3.1. Nanoparticle Synthesis and Characterisation

To obtain crystal field level of theory data of the Ln^{3+} doped into β-$NaYF_4$, upconverting nanoparticles were synthesised in a one-pot setup via, as indicated above, thermal

decomposition of the respective Y and Ln acetate precursors. The procedure is best summarised via the description provided in Conrad (II) *et al.*:[2]

"*β-$NaYF_4$ UCNPs (co-)doped with Er^{3+}, Tm^{3+}, and Yb^{3+} were synthesized following a synthesis route available in the literature.*[142] *The particles were grown from the respective Y, and Er, Tm, and Yb acetate precursors, [$Y(Ac)_3$] and [$Ln(Ac)_3$], respectively. These precursors were obtained by treating the required amounts of the analogue oxides with a one-to-one mixture of acetic acid and water overnight. The acetate precursors together with sodium oleate and ammonium fluoride as sodium and fluoride sources, respectively, and oleic acid and 1-octadecene as surfactants and solvents were then used to first create ultra-small (sub-5 nm) sodium-deficient α-phase (cubic) UCNPs. After isolating the resulting particles through repeated precipitation and washing, they were redispersed in oleic acid and octadecene and re-heated to 300 °C. Large β-phase UCNPs grew at this temperature over the course of 3 h from the gradually dissolving the α-phase particles. After the successful synthesis and isolation of the UCNPs from the reaction mixture by precipitation, the UCNPS were additionally washed with hexane and ethanol. The resulting UCNPs, ca. 800 mg per synthesis, were stored in hexane until further use. To obtain ligand-free UCNPs, the oleate ligands were removed from the surface of the nanoparticles by treatment with hydrochloric acid overnight (see ESI for details).*[143]"

The resulting nanoparticles were confirmed to be phase-pure (*i.e.*, of hexagonal phase) via XRD measurements. Images obtained via TEM allowed determining the diameter of the nanoparticles to be around 70 nm for the different batches. The oleate ligands of the nanoparticles from the employed solvents were removed after the synthesis to allow for easier precipitation of the UCNPs on a glass side for the ensuing low-temperature measurements of emission spectra. No shell was added to the particles and, therefore, a protective layer for preventing energy loss at the surface was missing. The lack of an (undoped) shell was a deliberate choice as no shell was included in the computational setup. However, it had to be ensured that many Ln^{3+} in the particles would be doped into sites that resembled doping sites of the bulk material as closely as possible (that is, as far away from the surface of the particles as possible). Having Ln^{3+} reside at these sites ensured that their optical spectra would match the computational spectra as good as possible (since no surface effects were considered in the employed models). In order to achieve this, the growing time during the synthesis was extended to 3 h for obtaining rather large particles with a smaller surface to volume ratio. After removing the surface ligands, the nanoparticles were inserted into a cryostat setup of an optical spectrometer, cooled to around 20 K, and excited with a laser at 980 or 808 nm (depending on the sample). Via

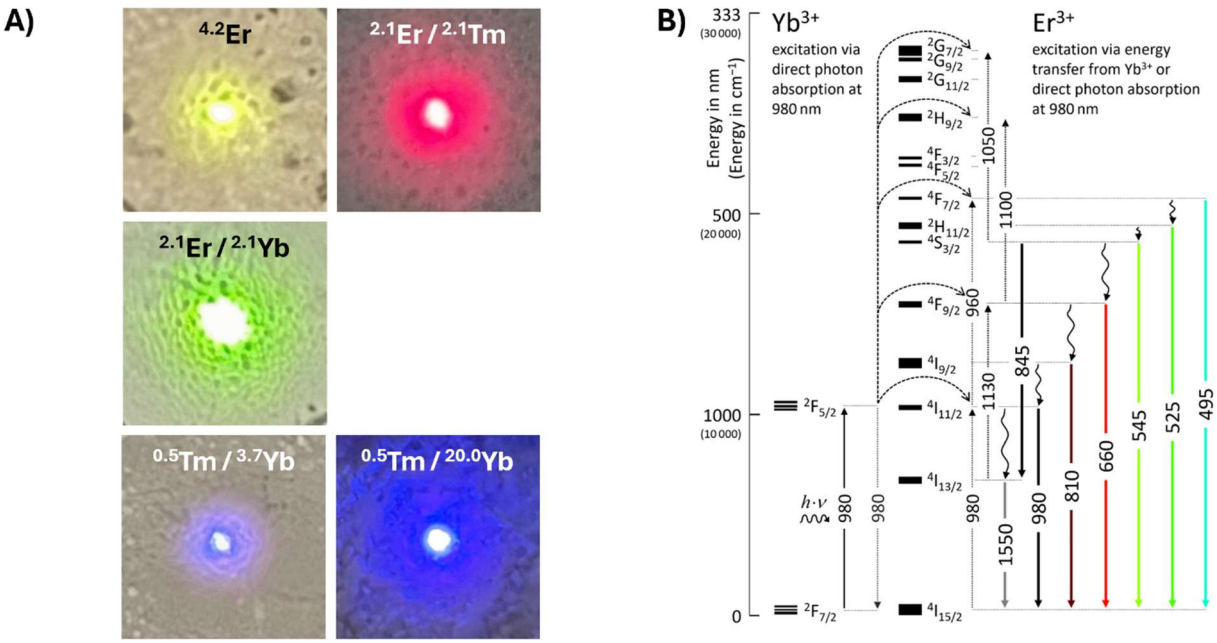

Figure 14: (A) Photographs taken with a smartphone camera of the various β-$NaYF_4$: Ln^{3+} UCNPs deposited on a glass slide (ca. 2 · 2 cm) upon excitation with a handheld 980 nm laser. The energy of the photons emitted by the laser and absorbed by the lanthanides is upconverted as shown in part B for Er^{3+}. Photons with higher energy, here in the visual region of the electromagnetic spectrum, are subsequently emitted by the sample. **(B)** Energy level diagram showing probable upconversion and downshifting pathways for Er^{3+} (together with Yb^{3+}) under 980 nm excitation. Reproduced with permission from Ref. 2. Copyright 2025 American Chemical Society.

---

employing different lasers, filters, and detectors, both upconverted and downshifted emission spectra (from 400 to 1550 nm) of the samples were recorded. Smartphone photographs of the different samples under excitation with a hand-held 980 nm laser are shown in Figure 14A.The respective upconversion and downshifting pathways for Er^{3+} (and Yb^{3+}) are presented in Figure 14B. The full set of spectra for all samples and all wavelength ranges is available in Conrad (II) *et al.* and its corresponding ESI.[2]

Agreement on a multiplet energy level basis between the experimentally synthesised and computationally designed particles was observed to be good with deviations similar to those from the earlier benchmarking against values from the literature, Figure 15. With these data sets, relative crystal field oscillator strengths (and energy level positions) could be identified for the $^4S_{3/2} \rightarrow {}^4I_{15/2}$ (multiplet to multiplet) transition of Er^{3+} (545 nm transition), which is a very important transition in the upconversion process (Figure 14B). The full set of crystal field transitions between these two multiplets is shown in

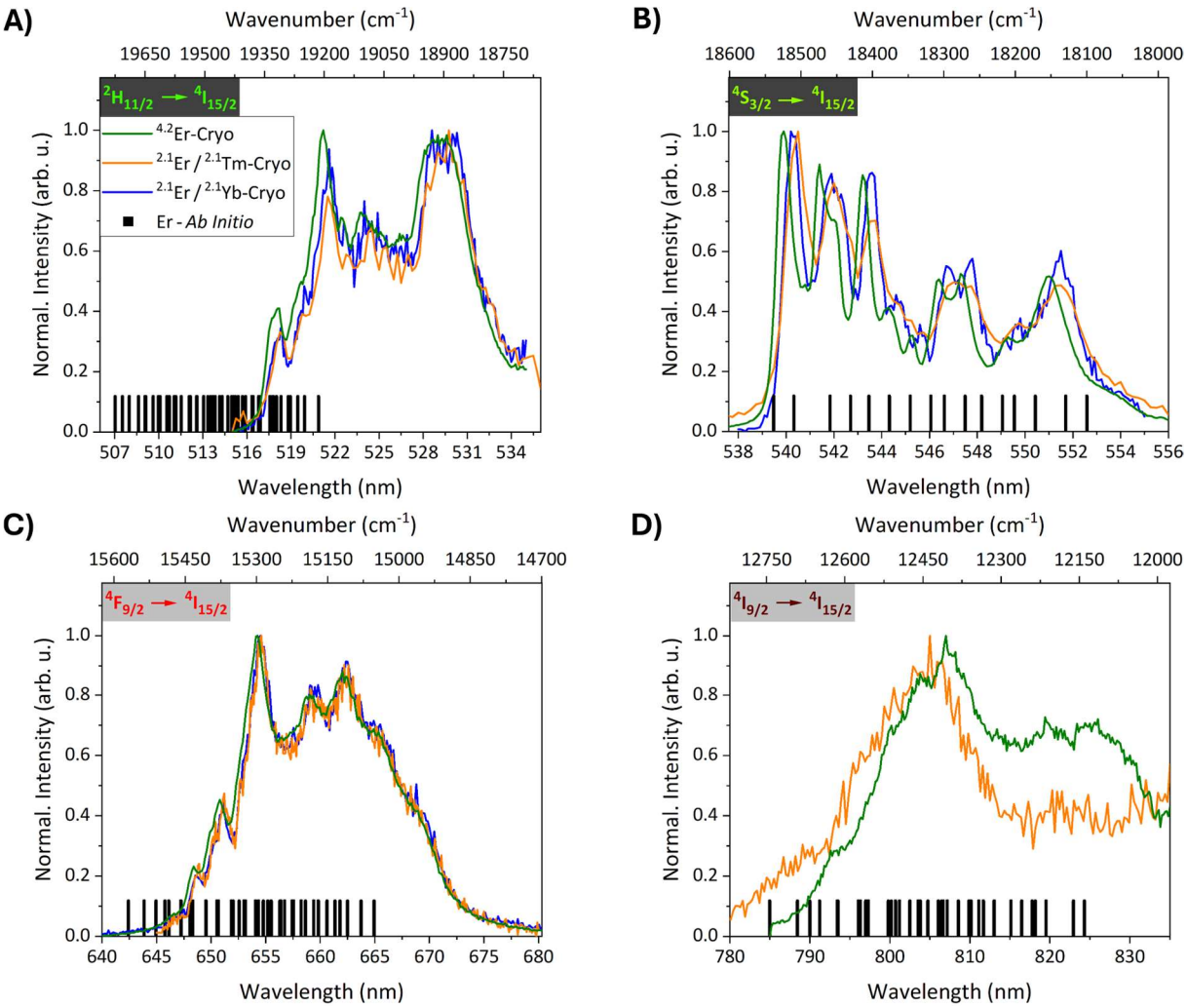

Figure 15: Low-temperature photoluminescence **(A–D)** upconversion spectra of the β-$NaYF_4$ UCNPs doped with 4.2 mol% Er^{3+}, 2.1 mol% Er^{3+} and 2.1 mol% Tm^{3+}, as well as 2.1 mol% Er^{3+} and 2.1 mol% Yb^{3+}. The legend shown in (A) applies to all spectra. Bars in black represent the positions of the averaged crystal field transitions of the respective multiplets according to the *ab initio* calculations. For B–D, the bars and the emission spectra are almost in the same wavelength region. The height of the bars was chosen arbitrarily and does not correspond to their respective oscillator strength. Reproduced with permission from Ref. 2. Copyright 2025 American Chemical Society.

Figure 16A. This transition involves two initial (from the $^4S_{3/2}$ multiplet) and eight final levels (from the $^4I_{15/2}$ multiplet). Therefore, in total sixteen different transitions were expected. The corresponding emission spectrum of the sample containing 4.2 mol% Er^{3+} is shown in Figure 16B (olive line) and discussed below.

4.3.2. Generating Emission Spectra from Computational Data

Initially, the plan was to compute emission spectra from the theoretical data by first averaging over the results of the 14 different clusters. This represents the same way how the crystal field energy levels and oscillator strengths of β-$NaYF_4$ were calculated for all tables and figures shown in the published manuscripts and in this dissertation. This scheme was also used for creating the black bars in Figure 15. In this depiction, each black bar represented a specific crystal field transition. Its position was calculated by determining the average value of the respective transition from the individual contributions of the 14 different embedded clusters. One single spectrum could be generated from these averaged transitions and their averaged oscillator strengths. However, given that 14 different cluster (with 14 different environments for the central Ln^{3+}) were determined, it seemed reasonable to assume that also the final spectrum contained individual contributions from all 14 Ln^{3+} and their individual clusters. By instead first averaging over the results for the 14 clusters, a single *mean* structure with *mean* properties would have been created (mean transition energies and mean oscillator strengths for each transition). Since configurations of the clusters do not interconvert on the on the timescale of the experiment (recording the emission spectrum), the mean structure invoked by the averaging does not exist. Therefore, averaging over the properties of the clusters and then generating a single spectrum from this data was deemed to be inappropriate.

Instead, for each of the 14 different embedded clusters first an individual spectrum was created with a Python script based on libcerf.[144] For each cluster, the 16 $^4S_{3/2}$–$^4I_{15/2}$ crystal field transitions, Figure 16A, their energetic separations (their corresponding wavelengths), and their crystal field oscillator strengths as obtained from the theoretical calculations were fed into the script. Via a Gaussian broadening factor estimated from the experimentally obtained spectra, the script then created the respective spectrum for the specific cluster. These spectra existed as tables only, where for each wavelength a normalised intensity was provided. Once all spectra for the 14 clusters were generated, the 14 different intensities per wavelength were averaged with respect to the weighting factors as displayed in Table 5. From the averaged values, a final spectrum was generated (black line in Figure 16B). Different to the earlier proposed model, the generated spectrum was, therefore, a superimposition of all 14 spectra of the separate Ln^{3+} in the different

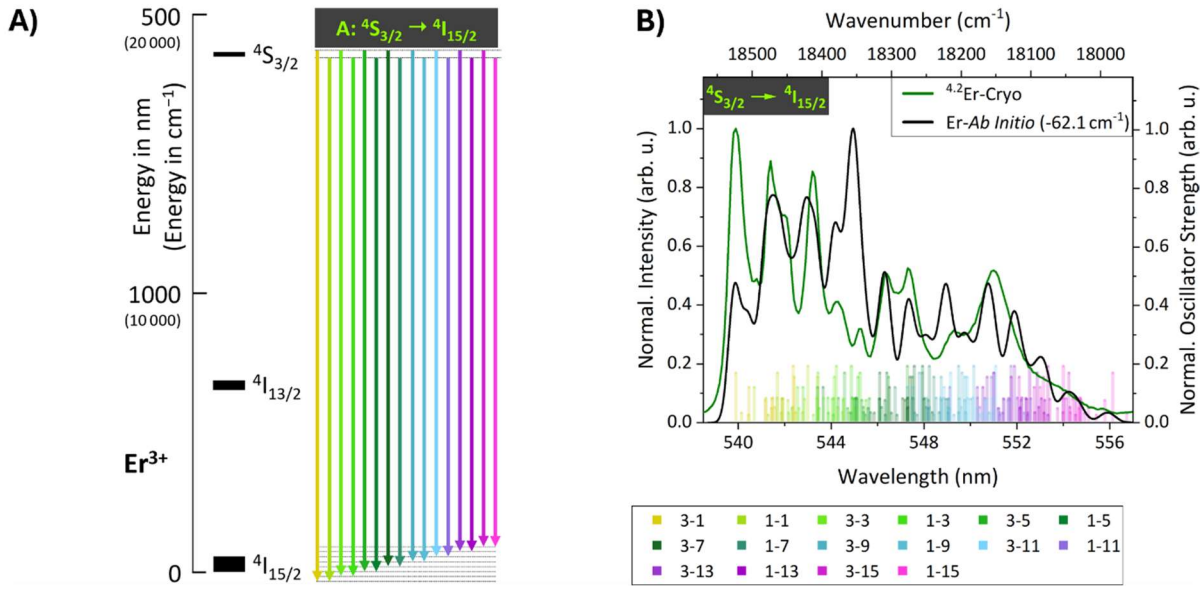

Figure 16: (A) Energy level diagram showing individual crystal field transitions for the $^4S_{3/2} \rightarrow {}^4I_{15/2}$ multiplet transition of Er^{3+}. The separations of the crystal field energy levels of the two multiplets is not true to scale. **(B):** Low-temperature photoluminescence (20 K, color code olive) and *ab initio* spectra (color code black) of Er^{3+}-doped (4.2 mol%) β-$NaYF_4$ for the 545 nm ($^4S_{3/2} \rightarrow {}^4I_{15/2}$) transition. The *ab initio* spectrum was shifted by −62 cm^{-1}. Small semitransparent bars indicate the positions of the crystal field transitions for the individual clusters. Each of the 14 clusters generated 16 individual transitions (bars). Their labeling in the legend follows *n^{th} crystal field energy level of the initial multiplet* ($^4S_{3/2}$) – *n^{th} crystal field energy level of the final multiplet* ($^4I_{15/2}$). The height of the smaller bars represents the weighting factor of the cluster they originate from (not their oscillator strength) and bars with the same height were retrieved from the same cluster. Bars with the same colour represent the same transition for the 14 different clusters. Adapted with permission from Ref. 2. Copyright 2025 American Chemical Society.

---

clusters. It accounted for the individual contributions of each Ln^{3+} and its modelled environment. Finally, to allow for better comparison of emission peaks and relative oscillator strengths, the theoretical spectrum was shifted by −62 cm^{-1}, equalling to about 0.35 %. This discrepancy was very consistent with the deviations observed when referencing the theoretical values of the crystal field energy levels to experimental data from the literature (see above).

4.3.3. Comparison of the Spectra

The spectrum that was created by superimposition of the 14 individual spectra from the different clusters was in decent agreement with the experimental spectrum of the

synthesised particles (black and olive line in Figure 16B, respectively). While no perfect overlap was created, all main features of the experimental spectrum found correspondence in the theoretical spectrum. Both the position of the peaks (crystal field energy levels) and their relative intensities (crystal field oscillator strengths) appeared to be in close relationship between these two data sets. Interestingly, it seemed that the individual peaks in the experimental spectrum were, indeed, a superimposition of contributions originating from different crystal field transitions of several clusters. Therefore, in case of a disordered host the number of observable peaks is most likely not directly related to the number of available crystal field transitions between the multiplets involved. This is different to, for example, the expected spectrum for Er^{3+} in $LiYF_4$ for the same multiplet transition. In this host material, exactly 16 peaks from the individual crystal field transitions should be observable.

Overall, despite several approximations introduced in the two computational setups used for predicting the required data sets, the generated spectrum was in close resemblance of the experimental one. This is a stark hint towards the validity of the models chosen and the approximations made. Also, the close resemblance between the two spectra indicates that for also for the experimentally synthesised nanoparticles the spectrum is generated via superimposition of several Ln^{3+} with locally differing environments. This hypothesis was further assessed by examining spectra of individual clusters and their overlap with the experimental spectrum.

4.3.3.1. Impact of Disorder, 1f and 2h

Possibly, the resemblance of the experimental and theoretical spectra could have been a coincidence. For example, there was a chance that one of the clusters with a high weighting factor already provided a good representation of the experimental spectrum, and that the contributions of the other clusters were rather insignificant. In order to probe whether this was the case and the experimentally observed spectrum could be better approximated by a spectrum of a single cluster, individual spectra of 1f disordered clusters with the highest weighting factors were plotted against the experimental spectrum and the averaged computational spectrum (Figure 17A). The resulting overview of the different spectra could not support the theory voiced above. The computational spectra of the individual clusters looked remarkably different compared to the experimental spectrum.

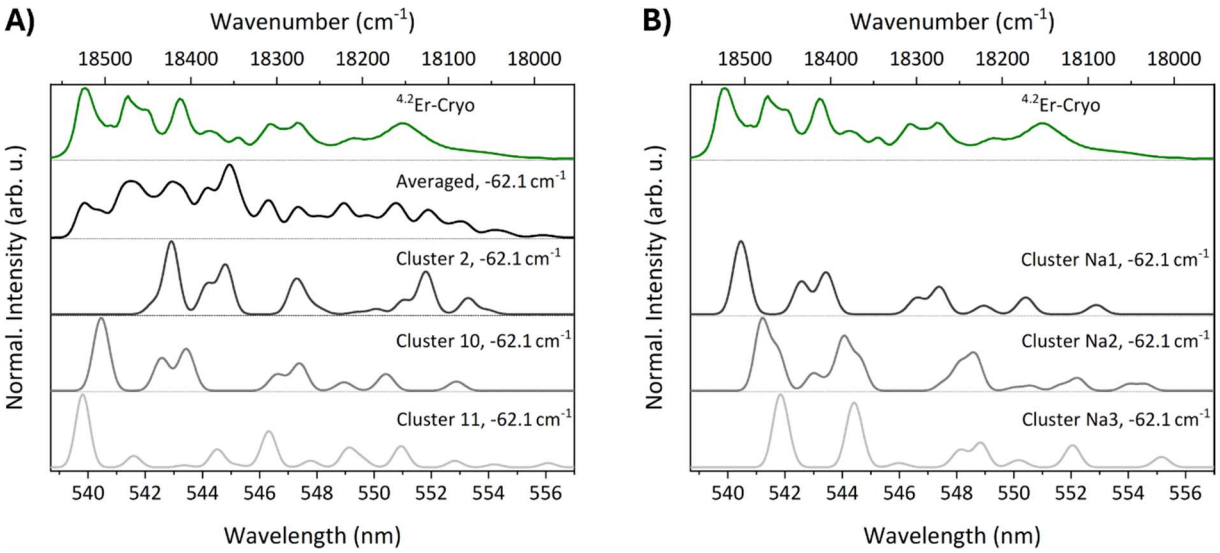

Figure 17: (A) Low-temperature photoluminescence spectrum of 4.2 mol% Er^{3+}-doped β-$NaYF_4$ for the $^4S_{3/2} \rightarrow {}^4I_{15/2}$ transition (20 K, green) together with the *ab initio* results for the averaged spectrum (black). Additionally, individual spectra of cluster 2, cluster 10, and cluster 11 (color code dark grey, grey, and light grey, respectively) are shown. These are the clusters with the heighest weighting factors, refer to Table 5 above. **(B)** Low-temperature photoluminescence spectrum of 4.2 mol% Er^{3+}-doped β-$NaYF_4$ for the $^4S_{3/2} \rightarrow {}^4I_{15/2}$ transition (20 K, green). Additionally, individual spectra of cluster Na1, cluster Na2, and cluster Na3 (color code dark grey, grey, and light grey, respectively) are shown. All *ab initio* spectra were shifted by −62 cm^{-1}. Reproduced with permission from Ref. 2. Copyright 2025 American Chemical Society.

Indeed, the individual computational spectra showed gaps where none were visible in the experimental one. Plus, the intensity distribution of the individual spectra was clearly no better match to the experimental spectra than the intensity distribution of the averaged spectrum was. To a certain extent this finding was not surprising. None of the weighting factor of the clusters exceeded 16 %, refer to Table 5 above. Therefore, the final averaged spectrum had similar contributions from many different clusters. It should also be noted that the spectrum of cluster 10, Figure 17A, is not a particularly good match to the experimental spectrum. This is despite the fact that the underlying supercell of this cluster is employed regularly when β-$NaYF_4$ is treated like an ordered material.[55-59]

Given the shape of the individual computational spectra and the experimental spectrum, the sole viable explanation appeared to be that only the superimposition of the spectra of the differently disordered clusters can generate the experimentally observed spectrum. Deduced from this conformity is the statement that the crystal lattice of

β-$NaYF_4$ is indeed highly disordered, that this disorder significantly influences the properties of Ln^{3+} doped into the lattice, and that the available theoretical models are able to truthfully represent all effects relevant with respect to this disorder.

Two more interesting observations were made from the individual spectra generated from the respective clusters. First, the area below each curve of the individual spectrum stayed almost constant. This meant that the multiplet oscillator strength between the two levels involved, $^4S_{3/2}$ and $^4I_{15/2}$, should be almost equal from cluster to cluster. Indeed, this assumption was supported by the data generated when calculating the multiplet oscillator strengths for the different transitions (Table 7). One implication that was drawn from this is that a disordered host material does not further increase the observed oscillator strengths of the dopant as long as the available doping sites are of low symmetry even before adjusting the surroundings because of the disorder experienced by the host material. The crystal field oscillator strengths might change significantly for the same transitions of different clusters, however, the strength of all crystal field transitions summed up for a multiplet transition stays constant from cluster to cluster.

Second, individual spectra were also created for the three 2h disordered clusters, Figure 17B. Even though the lattice distortions induced by the Na^+ at the 2h disordered sites were not as pronounced as the distortions induced by the disorder of Na^+ and Y^{3+} at the 1f sites, the spectra generated from the clusters with different 2h occupation shared similar characteristics with those of the 1f sites. Oscillator strengths for crystal field transitions changed from cluster to cluster and large gaps are present in the individual spectra. The spectra generated from 2h disordered clusters were not included into the averaging scheme since no systematic approach was created for accounting for this type of disorder. However, if a sufficient number of these spectra are generated, certainly thousands if not millions, and are included into the averaging scheme, the remaining discrepancies between the experimental and theoretical spectra may still not vanish but possibly be reduced even further.

4.3.4. Nano versus Bulk

One critical remark, that was voiced consistently by the referees in the review process of the two published manuscripts, was whether the results presented could be transferred

to much smaller nanoparticles. After all, the nanoparticles synthesized for this study, with a diameter of about 70 nm, could no longer be considered small. Also, the first computational model employed used periodic boundary conditions during the geometry optimisation and, thereby, generated a particle with infinite expansion. Moreover, the second computational model placed the optically active Ln^{3+} at the centre of an approximately 5 nm large particle, reducing effects the surface might have had on the Ln^{3+}. Additionally, it was shown experimentally that the emission properties of very small UCNPs (< 10 nm) were predominantly governed by Ln^{3+} residing at surface sites.[145] The Ln^{3+} in these particles had noticeably different optical properties compared to Ln^{3+} mostly residing at bulk sites in larger or shelled particles. Therefore, the underlying question was whether the calculations conducted provided meaningful insights into processes relevant to experimentalist of the respective scientific community.

One part of the answer to this question is that the calculations presented here certainly cannot provide reliable insights into the properties of Ln^{3+} at surface sites. The surroundings of an Ln^{3+} at or close to the surface are different to those of Ln^{3+} at bulk sites. Given that the here presented data suggested that the Ln^{3+} are very sensitive to their environment, a change in the (optical) properties can be expected when moving an Ln^{3+} from the bulk part of the particle closer to the surface. While the second theoretical model could easily be adjusted to reflect a surface site, finding suitable methods for the geometry optimisation would be more challenging and was therefore not considered.

However, many UCNPs that are envisioned for real-life applications take advantage of the core-shell concept. [85, 146] In this case, often a doped core is surrounded by an undoped shell of the same host material. Thereby, the shell protects the optically active Ln^{3+} and often improves the quantum yield of the respective UCNPs. Therefore, most of the Ln^{3+} in such a core-shell system reside at either bulk sites or at sites that are close to the interface between the core and the shell. Since both core and shell use the same host material, the environment of the latter sites should be closer to the environment of bulk sites than to that of surface sites. Therefore, the setup introduced above accurately represents Ln^{3+} at bulk sites and it is expected that it can provide reliable insights into larger UCNPS but also into those using a core-shell concept.

5. Conclusions

The results presented in this dissertation provide a comprehensive and cohesive picture of how crystallographic disorder determines both the local structural environment of and the optical response of Ln-doped into alkali yttrium fluorides. To this end, periodic structure calculations based on density functional theory, embedded cluster wavefunction-based calculations, and experimental measurements of in-house synthesised nanoparticles for disordered (β-$NaYF_4$) and ordered ($LiYF_4$) host lattices were combined. Calculations were conducted for both the undoped and Ln^{3+}-doped forms of these host materials. Nanoparticles synthesised for β-$NaYF_4$ had different doping combinations of Er^{3+}, Tm^{3+}, and Yb^{3+}. The current work, thereby, established a link between disorder of the host material and the resulting emission characteristics of Ln^{3+} dopants.

Initially, the atomistic structures of $LiYF_4$ and β-$NaYF_4$ were optimised with periodic DFT. The employed model was confirmed to deliver reliable results by comparing the resulting structures of $LiYF_4$ and $LiYF_4$: Ln^{3+} to other computational approaches and experimental measurements available in the literature. All comparisons of lattice parameters and bond lengths indicated that the chosen model was well suited for predicting such properties of these inorganic structures.

Next, the same calculations were conducted for undoped and doped β-$NaYF_4$. However, given the inherent disorder of its crystal lattice, β-$NaYF_4$ could not be described by a single crystal configuration. Instead, (four times) 16 different supercells were created for this crystal, considering the disorder induced by Na^+ and Y^{3+} at the 1f and by Na^+ at the 2h sites. Each 16 supercells represented the full set of 64 possible arrangements of the ions in the setup chosen (β-$NaYF_4$ undoped or doped with any of the three Ln^{3+}). Once the different supercells were optimised, the resulting lattice parameters were averaged with respect to stochastic considerations for the supercells and a Boltzmann distribution based on the energetic differences of the supercells. Initially, the Boltzmann distribution was not included into the averaging scheme and, instead, the distribution of possible Ln-dopants on the 1a and 1f doping sites was considered. While this introduced an error into the weighting scheme, it was shown that the resulting changes in lattice parameters of the final structure through the corrected weighting scheme were neglectable. Also, it should

be kept in mind that the weighting scheme used here is one possible approach of accounting for the disorder of the lattice. Other studies might arrive at other weighting factors through different assumptions, approximations, or a different weighting scheme altogether. Finally, the geometry optimisations of the different supercells and the following averaging scheme produced four structures (one for β-$NaYF_4$ and three for β-$NaYF_4$: Ln^{3+}) that compared well to experimental and computational structural data sets.

This part of the first study, for the undoped and doped versions of β-$NaYF_4$, showed that the mixed Na^+ / Y^{3+} occupancy on the 1f sites gives rise to a broad distribution of local atomic arrangements, each associated with distinct distortions and reduced symmetry around the lanthanide substitution sites. The inclusion of three representative 2h Na^+ configurations demonstrated that positional disorder on the 2h sites produces structural perturbations slightly smaller than by the 1f occupation disorder. However, both disorder types contribute, in a cumulative manner, to the range of local lanthanide environments observed. On the other hand, doping the disordered structure with any of the three Ln^{3+} did not lead to additional distortions of the surrounding ions' arrangements. These structural insights underscore that disorder in β-$NaYF_4$ is a fundamental property that dictates the microscopic environment experienced by the lattice and its dopants.

Building on these optimised structures, the second part of the research project established that treating β-$NaYF_4$: Ln^{3+} (Ln = Er, Tm, or Yb) as highly disordered, and taking into account its different local environments, results in optical properties of the Ln^{3+}-dopants that are very close to data sets reported in the literature. An embedded cluster setup was designed based on SA-CASSCF, NEVPT2, and QDPT, for capturing the different contributions to the electronic wavefunction of an Ln^{3+} dopant in the lattice. Again, the setup was tested by first calculating optical properties of $LiYF_4$: Ln^{3+}. These calculations showed very good agreement with data sets, both computational and experimental, reported in the literature. Given the order experienced by the lattice of $LiYF_4$, comparing the resulting crystal field energy levels and multiplet oscillator strengths to the reference sets available was straight forward. Also, instructions and sample files were provided for adapting the model to different (ordered) structures. Changing the host or lanthanide dopant to a different combination is deemed possible without too much effort. A powerful feature of many *ab initio* approaches.

The embedded cluster calculations for β-$NaYF_4$: Ln^{3+} reproduced the crystal field energy levels and oscillator strengths associated with each of the 14 structurally distinct configurations considered. Boltzmann-weighted ensemble averaging, incorporating the different supercell energies obtained from the earlier structural analysis, and statistical degeneracies, as used in the previous weighting scheme, were combined to arrive at final weighting factors for all 14 clusters. Once a single value was obtained, by averaging over the results of the different clusters with respect to the weighting factors, the obtained data sets were compared to those in the literature. Unfortunately, the availability of such data was much sparser for β-$NaYF_4$: Ln^{3+} than for $LiYF_4$: Ln^{3+}, especially on a crystal field level of theory. However, the comparisons that were possible showed rather good agreement of the computational data prepared for this project with experimental values of previous studies conducted.

To further validate the computational setup and the calculations conducted, β-$NaYF_4$: Ln^{3+} UCNPs with almost equal compositions as used in the theoretical setup were synthesised and optically characterised. The recorded emission spectra of the Ln^{3+} multiplet transitions were compared to the theoretical values for all three Ln^{3+} and showed very good agreement. For one transition, $^4S_{3/2} \rightarrow {}^4I_{15/2}$, it was possible to almost resolve the recorded emission spectrum in terms of its crystal field components. Therefore, this spectrum was compared with a computational spectrum based on the crystal field energy levels and oscillator strengths of the two multiplets involved, $^4S_{3/2}$ and $^4I_{15/2}$. The comparison revealed that the observed emission spectrum is very likely a superimposition of the individual spectra generated by the different Ln^{3+} in the sample and their varying local environments. Indeed, the computationally generated averaged spectrum from the individual theoretical spectra compared well to the experimental spectrum, whereas computational spectra of the individual clusters showed much poorer agreement with the experimental spectrum. This observation implies that the complex emission spectra observed for β-$NaYF_4$: Ln^{3+} nanoparticles is a consequence of the Ln being doped into the configurational disorder experienced by the host lattice. In one, structural disorder appears to be a very important mechanism that shapes the optical response of Ln^{3+}-doped β-$NaYF_4$ UCNPs.

The integrated theoretical–experimental methodology developed here demonstrated that the hexagonal phase of $NaYF_4$ cannot be meaningfully described by a single representative structural model. Instead, it must be treated like an ensemble of locally distinct configurations whose occurrence is dictated by the energetic and combinatorial landscape of the disordered lattice. Each dopant of the lattice experiences a slightly different crystal field, resulting in slightly varying crystal field energy levels and oscillator strengths for that dopant. The optical responses of all these dopants combined provide the observed emission spectra of the material in question. Computational studies, that treat β-$NaYF_4$ like an ordered material with a single configuration, cannot account for this rich variation of responses and, ultimately, predict properties for the material that, at maximum, match its real behaviour only partially. It is possible to transfer the study conducted for β-$NaYF_4$: Ln^{3+} to other disordered host materials and their respective dopants. However, if the disorder experienced by this other host structure differs from that of β-$NaYF_4$, different weighting factors need to be calculated for the new lattice. Though, in principle, the approach would still follow the guidelines as laid out in this work. Adapting certain approximations and assumptions should, therefore, not be too time-consuming.

In summary, the dissertation provides a coherent and quantitative framework by which structural disorder in β-$NaYF_4$, and related compounds, can be understood, modelled, and linked to the optical properties of lanthanide dopants. The integration of theory and experiment confirms disorder as an intrinsic and functionally decisive feature of this material. The central objective of the project was to determine how local structural variations (of the closest neighbours) influence the crystal field energy levels and oscillator strengths of trivalent lanthanide ions. This objective was fulfilled and paves they for a better (theoretical) understanding of the effects the host lattice has on the optical properties of its Ln dopants. Such a better understanding can lead to the design of devices with better efficiency or novel applications.

6. Outlook

The next logical step that should follow the here presented results is to assess how disorder influences energy transfer efficiencies as needed for energy transfer upconversion (ETU). The density of states for a disordered material, approximated by its emission profile, should be distinctively different compared to those of an ordered material. If this is the case, different energy transfer efficiencies can be expected for the two types of lattices. If the overlap between the donor and acceptor emission profiles is larger, the energy transfer between the two ions should be more efficient. When a system of two ions of the same type is transferring energy between the same energetic states, an ordered material should be superior. The available energy of the donor exactly matches the required energy of the acceptor. However, for ETU systems involving two hetero ions, *e.g.*, Er^{3+} and Yb^{3+}, the ions are of different type and in most cases the energy made available by the donor does not exactly match the energy required by the acceptor. Here, a disordered lattice that leads to a broadened emission range can be of benefit. While disorder might reduce the efficiency of transfers that perfectly match in ordered lattices, disorder might be the reason that transfers with no matching overlap in an ordered lattice are becoming possible in the first place. To test this hypothesis, all relevant emission spectra of the transitions involved in ETU for both an ordered and a disordered lattice should be generated, and their total overlap be compared. Presumably, in a system involving hetero ions, the overlap for the disordered system should be higher.

Once such a comparison has been established, and positively evaluated, the energy transfer upconversion process should be modelled as a whole. While an entirely separate approach would be required for solving the required energy transfers equations, such a complete model would allow to predict the upconversion effect in its entirety. The designed model would also allow comparing the ETU efficiency and, thereby, the quantum efficiency of different dopant-host combinations. Ultimately, this could replace the trial-and-error approach when synthesising more efficient UCNPs, replacing it with testing the material chosen in the computational model first. Only if it demonstrates the properties required, a synthesis can be attempted.

7. List of Abbreviations and Formel Symbols

$^{2S+1}L_J$	term symbol
α	cubic
β	hexagonal
CASSCF	complete active space self-consistent field
DKH	Douglas-Kroll-Hess
DFT	density functional theory
ECP	effective core potential
ESI	Electronic Supplementary Information
ETU	energy transfer upconversion
H_0	interaction between the nucleus and the electrons
H_C	Coulomb/exchange interaction between the electrons
H_{CF}	crystal field interaction
H_{SO}	spin-orbit coupling
J	total angular momentum QN
Ln	lanthanide
Ln^{3+}	trivalent lanthanide
L	total orbital QN
l	azimuthal QN
M	number of electrons in the 5d subshell
M_j	projection of J along the z-axis
N	number of electrons in the 4f subshell
n	principal QN
NEVPT2	N-electron valence state second-order perturbation theory
NIR	near infrared
$P^2(r)$	electron probability density
PSE	periodic system of the elements
QDPT	quasi-degenerate perturbation theory
QN	quantum number
r	distance from the core, atomic units
RE	rare earths
RMSE	root mean square error
S	total spin QN
SA	state-averaged
TEM	transmission electron microscopy
UCNP	upconverting nanoparticle
UV	ultraviolet
Vis	visual
XRD	X-ray diffraction

8. List of Figures

9. List of Tables

10. Bibliography

(1) Conrad, C. S.; Euchner, H.; Hemmer, E.; Fink, R. F. The True Atomistic Structure of a Disordered Crystal: A Computational Study on the Photon Upconverting Material β-$NaYF_4$ and its Er^{3+}-, Tm^{3+}-, and Yb^{3+}-Doped Derivates. *Nanoscale* **2025**, *17* (14), 8599–8613. DOI: https://doi.org/10.1039/D4NR04880F.
(2) Conrad, C. S.; Behnle, S.; Hemmer, E.; Fink, R. F. Effect of Disorder on the Emission Spectra of Er^{3+}, Tm^{3+}, and Yb^{3+}-Doped β-$NaYF_4$: Quantum Chemical and Experimental Results. *The Journal of Physical Chemistry C* **2025**, *129* (45), 20446–20464. DOI: https://doi.org/10.1021/acs.jpcc.5c06209.
(3) Cotton, S. *Lanthanide and Actinide Chemistry*; John Wiley & Sons, 2006. DOI: https://doi.org/10.1002/0470010088.ch1.
(4) Bünzli, J.-C. G.; Mcgill, I. Rare Earth Elements. In *Ullmann's Encyclopedia of Industrial Chemistry*, Ley, C. Ed.; Wiley-VCH, 2018; p 1–53.
(5) Cho, U.; Chen, J. K. Lanthanide-Based Optical Probes of Biological Systems. *Cell Chemical Biology* **2020**, *27* (8), 921–936. DOI: https://doi.org/10.1016/j.chembiol.2020.07.009.
(6) Auzel, F. Compteur Quantique par Transfert d'Energie Entre Deux Ions de Terres Rares dans un Tungstate Mixte et dans un Verre. *C.R. Acad. Sci.* **1966**, *262*, 1016–1019.
(7) Auzel, F. Compteur Quantique par Transfert Denergie de Yb^{3+} à Tm^{3+} dans un Tungstate Mixte et dans un Verre Germanate. *C.R. Acad. Sci.* **1966**, *263*, 819.
(8) Auzel, F. Upconversion and Anti-Stokes Processes with f and d Ions in Solids. *Chem. Rev.* **2004**, *104* (1), 139–174. DOI: https://doi.org/10.1021/cr020357g.
(9) Walsh, B. M. Spectroscopy and Excitation Dynamics of the Trivalent Lanthanides Tm^{3+} and Ho^{3+} in $LiYF_4$. Boston College, Chestnut Hill, 1995.
(10) Schäfer, S.; Kaufmann, S.; Rösch, E. S.; Roesky, P. W. Divalent Metallocenes of the Lanthanides – A Guideline to Properties and Reactivity. *Chem. Soc. Rev.* **2023**, *52* (12), 4006–4045. DOI: http://dx.doi.org/10.1039/D2CS00744D.
(11) Gompa, T. P.; Ramanathan, A.; Rice, N. T.; La Pierre, H. S. The Chemical and Physical Properties of Tetravalent Lanthanides: Pr, Nd, Tb, and Dy. *Dalton Trans.* **2020**, *49* (45), 15945–15987. DOI: http://dx.doi.org/10.1039/D0DT01400A.
(12) Greenwood, N. N.; Earnshaw, A. *Chemistry of the Elements*; Butterworth-Heinemann, 1997. DOI: https://doi.org/10.1016/C2009-0-30414-6.
(13) *Lanthanides - Etymology*. Wikipedia, 2025. https://en.wikipedia.org/wiki/Lanthanide#Etymology (accessed 14.10.2025).
(14) Brande, W. T. *A Manual of Chemistry*; J.W. Parker, 1841.
(15) Gray, T. *The Elements*; Black Dog & Leventhal, 2009.
(16) Krogt, P. v. d. *Elementymology & Elements Multidict*. 2010. https://elements.vanderkrogt.net/rareearths.php (accessed 09.09.2025).
(17) M. Fontani, M. C., M. V. Orna. *The Lost Elements - The Periodic Table's Shadow Side*; Oxford Academic, 2014. DOI: https://doi.org/10.1093/oso/9780199383344.001.0001.
(18) Gschneidner K. A, C. J. 1787-1987 Two hundred Years of Rare Earths. *Rare Earth Information Center News, IPRT, IS-RIC 10* **1987**.
(19) Cordier, D. J. Mineral Commodity Summaries - Rare Earths. *National Minerals Information Center* **2022**. DOI: https://pubs.usgs.gov/periodicals/mcs2022/mcs2022-rare-earths.pdf.

(20) Haynes, W. M. *CRC Handbook of Chemistry and Physics*; CRC Press, 2016. DOI: https://doi.org/10.1201/9781315380476.
(21) Dushyantha, N.; Batapola, N.; Ilankoon, I. M. S. K.; Rohitha, S.; Premasiri, R.; Abeysinghe, B.; Ratnayake, N.; Dissanayake, K. The Story of Rare Earth Elements (REEs): Occurrences, Global S

Distribution, Genesis, Geology, Mineralogy, and Global production. *Ore Geology Reviews* **2020**, *122*, 103521. DOI: https://doi.org/10.1016/j.oregeorev.2020.103521.
(22) Haxel, G. B. H., J. B.; Orris, G. J. Rare Earth Elements Critical Resources for High Technology. *National Minerals Information Center* **2006**. DOI: https://pubs.usgs.gov/fs/2002/fs087-02/fs087-02.pdf.
(23) Cotton, S. *Lanthanide and Actinide Chemistry*; John Wiley & Sons, 2024.
(24) Bradley S. Van Gosen, P. L. V., Keith R. Long, Joseph Gambogi, Robert R. Seal II. *The Rare-Earth Elements: Vital to Modern Technologies and Lifestyles*; Reston, VA, 2014. DOI: https://doi.org/10.3133/fs20143078.
(25) Cordier, D. J. Mineral Commodity Summaries - Rare Earths. *National Minerals Information Center* **2011**. DOI: https://d9-wret.s3.us-west-2.amazonaws.com/assets/palladium/production/mineral-pubs/rare-earth/mcs-2011-raree.pdf.
(26) Gambogi, J. Mineral Commodity Summaries - Rare Earths. *National Minerals Information Center* **2019**. DOI: https://d9-wret.s3-us-west-2.amazonaws.com/assets/palladium/production/atoms/files/mcs-2019-raree.pdf.
(27) Gambogi, J. Mineral Commodity Summaries - Rare Earths. *National Minerals Information Center* **2021**. DOI: https://pubs.usgs.gov/periodicals/mcs2021/mcs2021-rare-earths.pdf.
(28) Cordier, D. J. Mineral Commodity Summaries - Rare Earths. *U. S. Geological Survey - National Minerals Information Center* **2025**. DOI: https://pubs.usgs.gov/periodicals/mcs2025/mcs2025-rare-earths.pdf.
(29) Bünzli, J.-C. G.; Eliseeva, S. V. Basics of Lanthanide Photophysics. In *Lanthanide Luminescence: Photophysical, Analytical and Biological Aspects*, Hänninen, P., Härmä, H. Eds.; Springer Berlin Heidelberg, 2011; p 1–45.
(30) Zheng, W.; Huang, P.; Tu, D.; Ma, E.; Zhu, H.; Chen, X. Lanthanide-Doped Upconversion Nano-Bioprobes: Electronic Structures, Optical Properties, and Biodetection. *Chem. Soc. Rev.* **2015**, *44* (6), 1379–1415. DOI: http://dx.doi.org/10.1039/C4CS00178H.
(31) Aleem, A. R.; Liu, J.; Wang, J.; Wang, J.; Zhao, Y.; Wang, Y.; Wang, Y.; Wang, W.; Rehman, F. U. L.; Kipper, M. J.; et al. Selective Sensing of Cu2+ and Fe3+ Ions with Vis-Excitation using Fluorescent Eu3+-Induced Aggregates of Polysaccharides (EIAP) in Mammalian Cells and Aqueous Systems. *J. Hazard. Mater.* **2020**, *399*, 122991. DOI: https://doi.org/10.1016/j.jhazmat.2020.122991.
(32) Wang, Z.; He, L.; Liu, B.; Zhou, L.-P.; Cai, L.-X.; Hu, S.-J.; Li, X.-Z.; Li, Z.; Chen, T.; Li, X.; et al. Coordination-Assembled Water-Soluble Anionic Lanthanide Organic Polyhedra for Luminescent Labeling and Magnetic Resonance Imaging. *J. Am. Chem. Soc.* **2020**, *142* (38), 16409–16419. DOI: https://doi.org/10.1021/jacs.0c07514.
(33) Atal, K.; Phageria, U.; Kumari, S.; Dhayal, Y.; Bugalia, S. A Review on Designing and Synthesis of Lanthanide Based Macrocyclic Complexes and Their Potential Applications. *Inorg. Chim. Acta* **2024**, *561*, 121857. DOI: https://doi.org/10.1016/j.ica.2023.121857.

(34) Alexander, C.; Guo, Z.; Glover, P. B.; Faulkner, S.; Pikramenou, Z. Luminescent Lanthanides in Biorelated Applications: From Molecules to Nanoparticles and Diagnostic Probes to Therapeutics. *Chem. Rev.* **2025**, *125* (4), 2269–2370. DOI: https://doi.org/10.1021/acs.chemrev.4c00615.
(35) Gorai, T.; Schmitt, W.; Gunnlaugsson, T. Highlights of the Development and Application of Luminescent Lanthanide Based Coordination Polymers, MOFs and Functional Nanomaterials. *Dalton Trans.* **2021**, *50* (3), 770–784. DOI: http://dx.doi.org/10.1039/D0DT03684F.
(36) Haas, K. *Aufbau Principle*. LibreTexts Chemistry, 2025. https://chem.libretexts.org/Bookshelves/Inorganic_Chemistry/Inorganic_Chemistry_(LibreTexts)/02%3A_Atomic_Structure/2.02%3A_The_Schrodinger_equation_particle_in_a_box_and_atomic_wavefunctions/2.2.03%3A_Aufbau_Principle (accessed 15.10.2025).
(37) Walsh, B. M. Judd-Ofelt Theory: Principles and Practices. Dordrecht, 2006; Springer Netherlands: p 403–433. DOI: http://dx.doi.org/10.1007/1-4020-4789-4_21.
(38) Bünzli, J.-C. G.; Eliseeva, S. V. Intriguing Aspects of Lanthanide Luminescence. *Chem. Sci.* **2013**, *4* (5), 1939–1949. DOI: https://doi.org/10.1039/c3sC22126a.
(39) Kattoum, R. *Atomic Subshell Energies and Electron Assignments*. LibreTexts Chemistry, 2025. https://chem.libretexts.org/Courses/University_of_Arkansas_Little_Rock/Chem_1402%3A_General_Chemistry_1_(Kattoum)/Text/7%3A_The_Structure_of_Atoms_and_Periodic_Trends/7.2%3A_Atomic_Subshell_Energies_and_Electron_Assignments (accessed 15.10.2025).
(40) Freeman, A. J.; Watson, R. E. Theoretical Investigation of Some Magnetic and Spectroscopic Properties of Rare-Earth Ions. *Phys. Rev.* **1962**, *127* (6), 2058–2075. DOI: https://doi.org/10.1103/PhysRev.127.2058.
(41) Britannica. *Rare-Earth Element - Minerals and Ores*. 2013. https://www.britannica.com/science/rare-earth-element/Minerals-and-ores (accessed 2025.09.15).
(42) Ogasawara, K.; Watanabe, S.; Toyoshima, H.; Brik, M. G. Chapter 231 First-Principles Calculations of $4f^n \rightarrow 4f^{n-1}$ 5d Transition Spectra. In *Handbook on the Physics and Chemistry of Rare Earths*, Gschneidner, K. A., Bünzli, J.-C., Pecharsky, V. K. Eds.; Vol. 37; Elsevier, 2007; p 1–59.
(43) Dieke, G. H. *Spectra and Energy Levels of Rare Earth Ions in Crystals*; John Wiley & Sons, Inc., 1968.
(44) Reid, M. F. Chapter 284 - Theory of Rare-Earth Electronic Structure and Spectroscopy. In *Handbook on the Physics and Chemistry of Rare Earths*, Bünzli, J.-C. G., Pecharsky, V. K. Eds.; Vol. 50; Elsevier, 2016; p 47–64.
(45) Baur, F.; Jüstel, T. Eu^{3+} Activated Molybdates – Structure Property Relations. *Optical Materials: X* **2019**, *1*, 100015. DOI: https://doi.org/10.1016/j.omx.2019.100015.
(46) Binnemans, K. Interpretation of Europium(III) Spectra. *Coord. Chem. Rev.* **2015**, *295*, 1–45. DOI: https://doi.org/10.1016/j.ccr.2015.02.015.
(47) Görller-Walrand, C.; Binnemans, K. Rationalization of Crystal-Field Parametrization. In *Handbook on the Physics and Chemistry of Rare Earths*, Gschneidner Jr., K. A. a. E., L. Ed.; Vol. 23; Elsevier, 1996; p 121–283.
(48) Peijzel, P. S.; Meijerink, A.; Wegh, R. T.; Reid, M. F.; Burdick, G. W. A Complete $4f^n$ Energy Level Diagram for All Trivalent Lanthanide Ions. *J. Solid State Chem.* **2005**, *178* (2), 448–453. DOI: https://doi.org/10.1016/j.jssc.2004.07.046.

(49) Bahari, H.-R.; Mousavi Khaneghah, A.; Eş, I. Upconversion Nanoparticles-Modified Aptasensors for Highly Sensitive Mycotoxin Detection for Food Quality and Safety. *Compr. Rev. Food Sci. Food Saf.* **2024**, *23* (3), e13369. DOI: https://doi.org/10.1111/1541-4337.13369.
(50) Aebischer, A.; Hostettler, M.; Hauser, J.; Krämer, K.; Weber, T.; Güdel, H. U.; Bürgi, H.-B. Structural and Spectroscopic Characterization of Active Sites in a Family of Light-Emitting Sodium Lanthanide Tetrafluorides. *Angew. Chem. Int. Ed.* **2006**, *45* (17), 2802–2806. DOI: https://doi.org/10.1002/anie.200503966.
(51) Platonenko, A.; Popov, A. I. Structural and Electronic Properties of β-$NaYF_4$ and β-$NaYF_4$: Ce^{3+}. *Opt. Mater.* **2020**, *99*, 109529. DOI: https://doi.org/10.1016/j.optmat.2019.109529.
(52) Zhu, X.; Zhang, J.; Liu, J.; Zhang, Y. Recent Progress of Rare-Earth Doped Upconversion Nanoparticles: Synthesis, Optimization, and Applications. *Advanced Science* **2019**, *6* (22), 1901358. DOI: https://doi.org/10.1002/advs.201901358.
(53) Wu, Y.; Ang, M. J. Y.; Sun, M.; Huang, B.; Liu, X. Expanding the Toolbox for Lanthanide-Doped Upconversion Nanocrystals. *J. Phys. D: Appl. Phys.* **2019**, *52* (38), 383002. DOI: https://doi.org/10.1088/1361-6463/ab29c7.
(54) Bollmann, W. *Crystal Defects and Crystalline Interfaces*; Springer, 1970. DOI: https://doi.org/10.1007/978-3-642-49173-3.
(55) Yao, G.; Berry, M. T.; May, P. S.; Kilin, D. S. Optical Properties of Host Material for Phosphor Computational Modeling. *Int. J. Quantum Chem* **2012**, *112* (24), 3889–3895. DOI: https://doi.org/10.1002/qua.24292.
(56) Yao, G.; Berry, M. T.; May, P. S.; Kilin, D. DFT Calculation of Russell–Saunders Splitting for Lanthanide Ions Doped in Hexagonal (β)-$NaYF_4$ Nanocrystals. *J. Phys. Chem. C* **2013**, *117* (33), 17177–17185. DOI: https://doi.org/10.1021/jp404206e.
(57) Yao, G.; Berry, M.; May, P. S.; Wang, J.; Kilin, D. S. Relationship between Site Symmetry, Spin State, and Doping Concentration for Co(II) or Co(III) in β-$NaYF_4$. *J. Phys. Chem. C* **2016**, *120* (14), 7785–7794. DOI: https://doi.org/10.1021/acs.jpcc.5b11496.
(58) Wang, F.; Han, Y.; Lim, C. S.; Lu, Y.; Wang, J.; Xu, J.; Chen, H.; Zhang, C.; Hong, M.; Liu, X. Simultaneous Phase and Size Control of Upconversion Nanocrystals through Lanthanide Doping. *Nature* **2010**, *463* (7284), 1061–1065. DOI: https://doi.org/10.1038/nature08777.
(59) Park, K.-W.; Jang, H. S.; Cho, S.-H. Prediction of Ln^{3+}–4f Energy Levels in β-$NaYF_4$: Ln^{3+} and Understanding of Absorption Behaviors. *Mater. Chem. Phys.* **2022**, *275*, 125317. DOI: https://doi.org/10.1016/j.matchemphys.2021.125317.
(60) Simonov, A. *Order and Disorder in Crystals*. ETH Zürich, Department of Materials, 2025. https://disorder.mat.ethz.ch/research.html (accessed 19.09.2025).
(61) Wikipedia. *Googol*. 2025. https://en.wikipedia.org/wiki/Googol (accessed 17.10.2025).
(62) Momma, K.; Izumi, F. VESTA 3 for Three-Dimensional Visualization of Crystal, Volumetric and Morphology Data. *J. Appl. Crystallogr.* **2011**, *44* (6), 1272–1276.
(63) Pandey, P.; Kaushik, S. D.; Rajput, P.; Singh, M. N.; Sharma, R. K.; Giri, S. Nature of Local Disorder in β-$NaYF_4$-Based, Near-Infrared Upconverting Core Nanocrystals Due to Deliberate Incorporation of a Symmetry Perturbing Agent. *Nanoscale* **2025**, *17* (4), 2269–2280. DOI: https://doi.org/10.1039/D4NR03951C.

(64) Tu, D.; Liu, Y.; Zhu, H.; Li, R.; Liu, L.; Chen, X. Breakdown of Crystallographic Site Symmetry in Lanthanide-Doped $NaYF_4$ Crystals. *Angew. Chem. Int. Ed.* **2013**, *52* (4), 1128–1133. DOI: https://doi.org/10.1002/anie.201208218.
(65) Renero-Lecuna, C.; Martín-Rodríguez, R.; Valiente, R.; González, J.; Rodríguez, F.; Krämer, K. W.; Güdel, H. U. Origin of the High Upconversion Green Luminescence Efficiency in β-$NaYF_4$: 2 % Er^{3+}, 20 % Yb^{3+}. *Chem. Mater.* **2011**, *23* (15), 3442–3448. DOI: https://doi.org/10.1021/cm2004227.
(66) Shi, R.; Brites, C. D. S.; Carlos, L. D. Hexagonal-Phase $NaREF_4$ Upconversion Nanocrystals: The Matter of Crystal Structure. *Nanoscale* **2021**, *13* (47), 19771–19782. DOI: https://doi.org/10.1039/D1NR04209B.
(67) Blasse, G.; Grabmaier, B. C. In *Luminescent Materials*, Springer, 1994; p 123.
(68) Rudolph, P. Fundamentals and engineering of defects. *Prog. Cryst. Growth Charact. Mater.* **2016**, *62* (2), 89–110. DOI: https://doi.org/10.1016/j.pcrysgrow.2016.04.004.
(69) Shyichuk, A.; Câmara, S. S.; Weber, I. T.; Carneiro Neto, A. N.; Nunes, L. A. O.; Lis, S.; Longo, R. L.; Malta, O. L. Energy Transfer Upconversion Dynamics in YVO_4: Yb^{3+}, Er^{3+}. *J. Lumin.* **2016**, *170*, 560–570. DOI: https://doi.org/10.1016/j.jlumin.2015.07.005.
(70) Heer, S.; Lehmann, O.; Haase, M.; Güdel, H.-U. Blue, Green, and Red Upconversion Emission from Lanthanide-Doped $LuPO_4$ and $YbPO_4$ Nanocrystals in a Transparent Colloidal Solution. *Angew. Chem. Int. Ed.* **2003**, *42* (27), 3179–3182. DOI: https://doi.org/10.1002/anie.200351091.
(71) Fan, Z.; Shao, Y.; Jiang, X.; Zhou, J.; Yang, L.; Chen, H.; Liu, W. Cytotoxic effects of NIR responsive chitosan-polymersome layer coated melatonin-upconversion nanoparticles on HGC27 and AGS gastric cancer cells: Role of the ROS/PI3K/Akt/mTOR signaling pathway. *International Journal of Biological Macromolecules* **2024**, *278*, 134187. DOI: https://doi.org/10.1016/j.ijbiomac.2024.134187.
(72) Jiang, Y.; Hong, Y.; Liu, Y.-Y.; Guan, Y.; Zhou, J.; Wang, H.; Sun, L. Switching between upconversion luminescence imaging and therapy in vitro enabled by NIR excitation modulation of nanocomposites. *Journal of Materials Chemistry C* **2024**, *12* (31), 11938–11947, 10.1039/D4TC01535E. DOI: 10.1039/D4TC01535E.
(73) Xu, C.; Law, S. K.; Leung, A. W. N. Comparison of the Differences between Two-Photon Excitation, Upconversion, and Conventional Photodynamic Therapy on Cancers in In Vitro and In Vivo Studies. *Pharmaceuticals* **2024**, *17* (6), 663.
(74) Hosseinifard, M.; Jurga, N.; Brandmeier, J. C.; Farka, Z.; Hlaváček, A.; Gorris, H. H.; Grzyb, T.; Ekner-Grzyb, A. Influence of surface modification and size of lanthanide-doped upconverting nanoparticles on wheat seedlings. *Chemosphere* **2024**, *347*, 140629. DOI: https://doi.org/10.1016/j.chemosphere.2023.140629.
(75) Yu, J.; Yu, H.; Li, L.; Ni, X.; Song, K.; Wang, L. Influence of Luminescent Nanomaterials on Plant Growth and Development. *ChemNanoMat* **2021**, *7* (8), 859–872. DOI: https://doi.org/10.1002/cnma.202100138.
(76) Alotaibi, A.; Alsardi, F.; Alshwikhat, F.; Aldossary, M.; Almarwani, F. S.; Talidi, F. J.; Almenhali, S. A.; Almotawa, S. F.; Alzahrani, Y. A.; Alenzi, S.; et al. Fabrication of Erbium-Doped Upconversion Nanoparticles and Carbon Quantum Dots for Efficient Perovskite Solar Cells. *Molecules* **2024**, *29* (11), 2556.
(77) Zhang, W.; Zheng, W.; Huang, P.; Yang, D.; Shao, Z.; Chen, X. The marriage of perovskite nanocrystals with lanthanide-doped upconversion nanoparticles for advanced optoelectronic applications. *Aggregate* **2024**, *5* (5), e558. DOI: https://doi.org/10.1002/agt2.558.

(78) Wang, J.; Shangguan, P.; Lin, M.; Fu, L.; Liu, Y.; Han, L.; Chen, S.; Wang, X.; Lu, M.; Luo, Z.; et al. Dual-Site Förster Resonance Energy Transfer Route of Upconversion Nanoparticles-Based Brain-Targeted Nanotheranostic Boosts the Near-Infrared Phototherapy of Glioma. *ACS Nano* **2023**, *17* (17), 16840−16853. DOI: https://doi.org/10.1021/acsnano.3c03724.
(79) Pominova, D.; Proydakova, V.; Romanishkin, I.; Kuznetsov, S.; Linkov, K.; Tabachkova, N.; Ryabova, A. NaGdF4:Yb, Er, Tm Upconversion Nanoparticles for Bioimaging in Shortwave-Infrared Range: Study of Energy Transfer Processes and Composition Optimization. *Photonics* **2024**, *11* (1), 38.
(80) Han, S.; Deng, R.; Xie, X.; Liu, X. Enhancing Luminescence in Lanthanide-Doped Upconversion Nanoparticles. *Angewandte Chemie International Edition* **2014**, *53* (44), 11702−11715. DOI: https://doi.org/10.1002/anie.201403408.
(81) DeLoach, L. D.; Payne, S. A.; Chase, L. L.; Smith, L. K.; Kway, W. L.; Krupke, W. F. Evaluation of Absorption and Emission Properties of Yb^{3+} doped Crystals for Laser Applications. *J. Quantum Electron.* **1993**, *29* (4), 1179-1191. DOI: https://doi.org/10.1109/3.214504.
(82) Geng, S.; Li, H.; Lv, Z.; Zhai, Y.; Tian, B.; Luo, Y.; Zhou, Y.; Han, S.-T. Challenges and Opportunities of Upconversion Nanoparticles for Emerging NIR Optoelectronic Devices. *Adv. Mater.* **2025**, 2419678. DOI: https://doi.org/10.1002/adma.202419678.
(83) Malhotra, K.; Hrovat, D.; Kumar, B.; Qu, G.; Houten, J. V.; Ahmed, R.; Piunno, P. A. E.; Gunning, P. T.; Krull, U. J. Lanthanide-Doped Upconversion Nanoparticles: Exploring A Treasure Trove of NIR-Mediated Emerging Applications. *ACS Appl. Mater. Interfaces* **2023**, *15* (2), 2499−2528. DOI: https://doi.org/10.1021/acsami.2c12370.
(84) Haase, M.; Schäfer, H. Upconverting Nanoparticles. *Angew. Chem. Int. Ed.* **2011**, *50* (26), 5808−5829. DOI: https://doi.org/10.1002/anie.201005159.
(85) Li, F.; Tu, L.; Zhang, Y.; Huang, D.; Liu, X.; Zhang, X.; Du, J.; Fan, R.; Yang, C.; Krämer, K. W.; et al. Size-dependent Lanthanide Energy Transfer Amplifies Upconversion Luminescence Quantum Yields. *Nat. Photonics* **2024**, *18* (5), 440−449. DOI: https://doi.org/10.1038/s41566-024-01393-3.
(86) Homann, C.; Krukewitt, L.; Frenzel, F.; Grauel, B.; Würth, C.; Resch-Genger, U.; Haase, M. $NaYF_4$: Yb, Er / $NaYF_4$ Core / Shell Nanocrystals with High Upconversion Luminescence Quantum Yield. *Angew. Chem. Int. Ed.* **2018**, *57* (28), 8765−8769. DOI: https://doi.org/10.1002/anie.201803083.
(87) Johnson, N. J. J.; He, S.; Diao, S.; Chan, E. M.; Dai, H.; Almutairi, A. Direct Evidence for Coupled Surface and Concentration Quenching Dynamics in Lanthanide-Doped Nanocrystals. *J. Am. Chem. Soc.* **2017**, *139* (8), 3275−3282. DOI: https://doi.org/10.1021/jacs.7b00223.
(88) Würth, C.; Fischer, S.; Grauel, B.; Alivisatos, A. P.; Resch-Genger, U. Quantum Yields, Surface Quenching, and Passivation Efficiency for Ultrasmall Core/Shell Upconverting Nanoparticles. *J. Am. Chem. Soc.* **2018**, *140* (14), 4922−4928. DOI: https://doi.org/10.1021/jacs.8b01458.
(89) Fischer, S.; Bronstein, N. D.; Swabeck, J. K.; Chan, E. M.; Alivisatos, A. P. Precise Tuning of Surface Quenching for Luminescence Enhancement in Core–Shell Lanthanide-Doped Nanocrystals. *Nano letters* **2016**, *16* (11), 7241-7247. DOI: 10.1021/acs.nanolett.6b03683.

(90) Grzechnik, A.; Friese, K. Crystal Structures and Stability of $NaLnF_4$ (Ln = La, Ce, Pr, Nd, Sm and Gd) Studied with Synchrotron Single-Crystal and Powder Diffraction. *Dalton Trans.* **2012**, *41* (34), 10258–10266. DOI: https://doi.org/10.1039/C2DT30650F.
(91) Roy, D. M.; Roy, R. Controlled Massively Defective Crystalline Solutions with the Fluorite Structure. *J. Electrochem. Soc.* **1964**, *111* (4), 421. DOI: https://doi.org/10.1149/1.2426145.
(92) Burns, J. H. Crystal Structure of Hexagonal Sodium Neodymium Fluoride and Related Compounds. *Inorg. Chem.* **1965**, *4* (6), 881–886. DOI: https://doi.org/10.1021/ic50028a025.
(93) Thoma, R. E.; Insley, H.; Hebert, G. M. The Sodium Fluoride-Lanthanide Trifluoride Systems. *Inorg. Chem.* **1966**, *5* (7), 1222–1229. DOI: https://doi.org/10.1021/ic50041a032.
(94) Krämer, K. W.; Biner, D.; Frei, G.; Güdel, H. U.; Hehlen, M. P.; Lüthi, S. R. Hexagonal Sodium Yttrium Fluoride Based Green and Blue Emitting Upconversion Phosphors. *Chem. Mater.* **2004**, *16* (7), 1244–1251. DOI: https://doi.org/10.1021/cm031124o.
(95) Li, M.; Wang, X.; Cao, X.; He, Z.; Liang, C.; Ju, J.; You, F. In Situ Observation of Thermal-Driven Structural Transitions of a β-NaYF4 Single Nanoparticle Aided with Correlative Cathodoluminescence Electron Microscopy. *Nanoscale* **2024**, *16* (17), 8661–8671. DOI: http://dx.doi.org/10.1039/D4NR00442F.
(96) Calado, C. M. S.; Manali, Í. F.; Diogenis, I. M. S.; Coelho, S. F. N.; Teixeira, V. C.; de Mesquita, B. R.; Oliveira, J. L.; Sigoli, F. A.; Rezende, M. V. d. S. Defect Disorder and Optical Spectroscopy Study of Eu-Doped NaYF4 and NaYGdF4 Nanoparticles. *Opt. Mater.* **2023**, *137*, 113529. DOI: https://doi.org/10.1016/j.optmat.2023.113529.
(97) Saha, S.; Pala, R. G. S.; Sivakumar, S. Catalyzing Cubic-to-Hexagonal Phase Transition in NaYF4 via Ligand Enhanced Surface Ordering. *Crystal Growth & Design* **2018**, *18* (9), 5080–5088. DOI: https://doi.org/10.1021/acs.cgd.8b00535.
(98) Perera, S. S.; Amarasinghe, D. K.; Dissanayake, K. T.; Rabuffetti, F. A. Average and Local Crystal Structure of β-Er:Yb:NaYF4 Upconverting Nanocrystals Probed by X-ray Total Scattering. *Chem. Mater.* **2017**, *29* (15), 6289–6297. DOI: https://doi.org/10.1021/acs.chemmater.7b01495.
(99) Renata Reisfeld , C. K. J. *Lasers and Excited States of Rare Earths*; Springer-Verlag, 1977.
(100) Renata, R. Optical Properties of Lanthanides in Condensed Phase, Theory and Applications. *AIMS Materials Science* **2015**, *2* (2), 37–60. DOI: https://doi.org/10.3934/matersci.2015.2.37.
(101) Hutter, J.; Iannuzzi, M.; Schiffmann, F.; VandeVondele, J. CP2K: Atomistic Simulations of Condensed Matter Systems. *WIREs Comput. Mol. Sci.* **2014**, *4* (1), 15–25. DOI: https://doi.org/10.1002/wcms.1159.
(102) Lippert, G.; Hutter, J.; Parrinello, M. A Hybrid Gaussian and Plane Wave Density Functional Scheme. *Mol. Phys.* **1997**, *92* (3), 477–488. DOI: https://doi.org/10.1080/002689797170220.
(103) VandeVondele, J.; Krack, M.; Mohamed, F.; Parrinello, M.; Chassaing, T.; Hutter, J. Quickstep: Fast and Accurate Density Functional Calculations Using a Mixed Gaussian and Plane Waves Approach. *Comput. Phys. Commun.* **2005**, *167* (2), 103–128. DOI: https://doi.org/10.1016/j.cpc.2004.12.014.

(104) VandeVondele, J.; Hutter, J. An Efficient Orbital Transformation Method for Electronic Structure Calculations. *J. Chem. Phys.* **2003**, *118* (10), 4365–4369. DOI: https://doi.org/10.1063/1.1543154.
(105) Perdew, J. P.; Burke, K.; Ernzerhof, M. Generalized Gradient Approximation Made Simple. *Phys. Rev. Lett.* **1996**, *77* (18), 3865–3868. DOI: https://doi.org/10.1103/PhysRevLett.77.3865.
(106) Grimme, S.; Antony, J.; Ehrlich, S.; Krieg, H. A Consistent and Accurate ab Initio Parametrization of Density Functional Dispersion Correction (DFT-D) for the 94 elements H-Pu. *J. Chem. Phys.* **2010**, *132* (15), 154104. DOI: https://doi.org/10.1063/1.3382344.
(107) VandeVondele, J.; Hutter, J. Gaussian Basis Sets for Accurate Calculations on Molecular Systems in Gas and Condensed Phases. *J. Chem. Phys.* **2007**, *127* (11), 114105. DOI: https://doi.org/10.1063/1.2770708.
(108) Goedecker, S.; Teter, M.; Hutter, J. Separable Dual-Sspace Gaussian Pseudopotentials. *Phys. Rev. B: Condens. Matter* **1996**, *54* (3), 1703–1710. DOI: https://doi.org/10.1103/PhysRevB.54.1703.
(109) Thoma, R. E.; Weaver, C. F.; Friedman, H. A.; Insley, H.; Harris, L. A.; Yakel, H. A., Jr. Phase Equilibria in the System LiF—YF_3. *The Journal of Physical Chemistry* **1961**, *65* (7), 1096–1099. DOI: https://doi.org/10.1021/j100825a003.
(110) Keller, C.; Schmutz, H. Die Reaktion von Lithiumfluorid mit den Trifluoriden der Lanthaniden und Einiger Actiniden. *J. Inorg. Nucl. Chem.* **1965**, *27* (4), 900–901. DOI: https://doi.org/10.1016/0022-1902(65)80454-7.
(111) Ching, W. Y.; Xu, Y.-N.; Brickeen, B. K. Comparative Study of The Electronic Structure of Two Laser Crystals: $BeAl_2O_4$ and $LiYF_4$. *Phys. Rev. B: Condens. Matter* **2001**, *63* (11), 115101. DOI: https://doi.org/10.1103/PhysRevB.63.115101.
(112) Luong, M. V.; Empizo, M. J. F.; Gabayno, J. L. F.; Minami, Y.; Yamanoi, K.; Shimizu, T.; Sarukura, N.; Pham, M. H.; Nguyen, H. D.; Steenbergen, K. G.; et al. Direct Band Gap Tunability of the $LiYF_4$ Crystal Through High-Pressure Applications. *Comput. Mater. Sci.* **2018**, *153*, 431–437. DOI: https://doi.org/10.1016/j.commatsci.2018.07.020.
(113) Yin, J.; Zhang, Q.; Liu, T.; Guo, X.; Song, M.; Wang, X.; Zhang, H. Ab Initio Study Electronic Structures of $LiYF_4$ Crystal Containing Interstitial Oxygen Atoms. *Nuclear Instruments and Methods in Physics Research Section B:* **2009**, *267* (1), 74–78. DOI: https://doi.org/10.1016/j.nimb.2008.07.024.
(114) Staemmler, V. The Cluster Approach for the Adsorption of Small Molecules on Oxide Surfaces. In *Theoretical Aspects of Transition Metal Catalysis*, 1st ed.; Frenking, G. Ed.; Topics in Organometallic Chemistry, Vol. 12; Springer Berlin, Heidelberg, 2005; p 219–256.
(115) Aravena, D.; Atanasov, M.; Neese, F. Periodic Trends in Lanthanide Compounds through the Eyes of Multireference Ab Initio Theory. *Inorg. Chem.* **2016**, *55* (9), 4457–4469. DOI: https://doi.org/10.1021/acs.inorgchem.6b00244.
(116) Atanasov, M.; Andreici Eftimie, E.-L.; Avram, N. M.; Brik, M. G.; Neese, F. First-Principles Study of Optical Absorption Energies, Ligand Field and Spin-Hamiltonian Parameters of Cr^{3+} Ions in Emeralds. *Inorg. Chem.* **2022**, *61* (1), 178–192. DOI: https://doi.org/10.1021/acs.inorgchem.1c02650.
(117) Gellé, A.; Lepetit, M.-B. Fast Calculation of the Electrostatic Potential in Ionic Crystals by Direct Summation Method. *J. Chem. Phys.* **2008**, *128* (24), 244716. DOI: https://doi.org/10.1063/1.2931458.

(118) Neese, F. The ORCA Program System. *WIREs Comput. Mol. Sci.* **2012**, *2* (1), 73–78. DOI: https://doi.org/10.1002/wcms.81.
(119) Neese, F. The SHARK Integral Generation and Digestion System. *J. Comput. Chem.* **2023**, *44* (3), 381–396. DOI: https://doi.org/10.1002/jcc.26942.
(120) Neese, F. Software Update: The ORCA Program System—Version 6.0. *WIREs Comput. Mol. Sci.* **2025**, *15* (2), e70019. DOI: https://doi.org/10.1002/wcms.70019.
(121) Ganyushin, D.; Neese, F. First-Principles Calculations of Zero-Field Splitting Parameters. *J. Chem. Phys.* **2006**, *125* (2), 024103. DOI: https://doi.org/10.1063/1.2213976.
(122) Rösch, N.; Matveev, A.; Nasluzov, V. A.; Neyman, K. M.; Moskaleva, L.; Krüger, S. Chapter 11 - Quantum Chemistry with the Douglas-Kroll-Hess Approach to Relativistic Density Functional theory: Efficient Methods for Molecules and Materials. In *Theoretical and Computational Chemistry*, Schwerdtfeger, P. Ed.; Vol. 14; Elsevier, 2004; p 656–722.
(123) Nakajima, T.; Hirao, K. The Douglas–Kroll–Hess Approach. *Chem. Rev.* **2012**, *112* (1), 385–402. DOI: https://doi.org/10.1021/cr200040s.
(124) Reiher, M. Relativistic Douglas–Kroll–Hess Theory. *WIREs Comput. Mol. Sci.* **2012**, *2* (1), 139–149. DOI: https://doi.org/10.1002/wcms.67.
(125) Pantazis, D. A.; Neese, F. All-Electron Scalar Relativistic Basis Sets for the Lanthanides. *J. Chem. Theory Comput.* **2009**, *5* (9), 2229–2238. DOI: https://doi.org/10.1021/ct900090f.
(126) Aravena, D.; Neese, F.; Pantazis, D. A. Improved Segmented All-Electron Relativistically Contracted Basis Sets for the Lanthanides. *J. Chem. Theory Comput.* **2016**, *12* (3), 1148–1156. DOI: https://doi.org/10.1021/acs.jctc.5b01048.
(127) Weigend, F.; Ahlrichs, R. Balanced Basis Sets of Split Valence, Triple Zeta Valence and Quadruple Zeta Valence Quality for H to Rn: Design and Assessment of Accuracy. *Phys. Chem. Chem. Phys.* **2005**, *7* (18), 3297–3305. DOI: https://doi.org/10.1039/b508541a.
(128) Fuentealba, P.; Preuß, H.; Stoll, H.; Von Szentpály, L. A Proper Account of Core-Polarization with Pseudopotentials: Single Valence-Electron Alkali Compounds. *Chem. Phys. Lett.* **1982**, *89* (5), 418–422. DOI: https://doi.org/10.1016/0009-2614(82)80012-2.
(129) Bergner, A.; Michael, D.; Wolfgang, K.; Hermann, S.; and Preuß, H. Ab Initio Energy-Adjusted Pseudopotentials for Elements of Groups 13–17. *Mol. Phys.* **1993**, *80* (6), 1431–1441. DOI: https://doi.org/10.1080/00268979300103121.
(130) Andrae, D.; Häußermann, U.; Dolg, M.; Stoll, H.; Preuß, H. Energy-Adjusted ab Initio Pseudopotentials for the Second and Third Row Transition Elements. *Theor. Chim. Acta* **1990**, *77* (2), 123–141. DOI: https://doi.org/10.1007/bf01114537.
(131) Couto dos Santos, M. A.; Antic-Fidancev, E.; Gesland, J. Y.; Krupa, J. C.; Lemaître-Blaise, M.; Porcher, P. Absorption and Fluorescence of Er^{3+}-doped $LiYF_4$: Measurements and Simulation. *J. Alloys Compd.* **1998**, *275-277*, 435–441. DOI: https://doi.org/10.1016/S0925-8388(98)00363-6.
(132) Dulick, M.; Faulkner, G. E.; Cockroft, N. J.; Nguyen, D. C. Spectroscopy and Dynamics of Upconversion in Tm^{3+}: $YLiF_4$. *J. Lumin.* **1991**, *48-49*, 517–521. DOI: https://doi.org/10.1016/0022-2313(91)90183-V.
(133) Xiao, Y.; Kuang, X.; Yeung, Y.; Ju, M. Investigation of the Structure and Luminescence Mechanism of Tm^{3+}-Doped $LiYF_4$: New Theoretical Perspectives. *Inorg. Chem.* **2020**, *59* (2), 1211–1217. DOI: https://doi.org/10.1021/acs.inorgchem.9b02935.

(134) Sugiyama, A.; Katsurayama, M.; Anzai, Y.; Tsuboi, T. Spectroscopic Properties of Yb Doped YLF Grown by a Vertical Bridgman Method. *J. Alloys Compd.* **2006**, *408-412*, 780–783. DOI: https://doi.org/10.1016/j.jallcom.2005.01.094.
(135) Hubert, S.; Meichenin, D.; Zhou, B. W.; Auzel, F. Emission Properties, Oscillator Strengths and Laser Parameters of Er^{3+} in $LiYF_4$ at 2.7 μm. *J. Lumin.* **1991**, *50* (1), 7–15. DOI: https://doi.org/10.1016/0022-2313(91)90004-F.
(136) Yu, X. Y.; Chen, H. B.; Wang, S. J.; Zhou, Y. F.; Wu, A. H.; Dai, S. X. Growth and Spectral Properties of Er^{3+}: $LiYF_4$ Single Crystal. *J. Inorg. Mater.* **2011**, *26* (9), 923–928. DOI: https://doi.org/10.3724/SP.J.1077.2011.00923.
(137) Xiao, Y.; Ju, M.; Yuan, H.; Yeung, Y. Unveiling the Local Structure and Luminescence Mechanism of Er^{3+}-Doped $LiYF_4$: A Promising Near-Infrared Laser Crystal. *J. Phys. Chem. C* **2021**, *125* (32), 18015–18021. DOI: https://doi.org/10.1021/acs.jpcc.1c04845.
(138) Popova, M. N.; Chukalina, E. P.; Malkin, B. Z.; Saikin, S. K. Experimental and Theoretical Study of the Crystal-Field Levels and Hyperfine and Electron-Phonon Interactions in $LiYF_4$: Er^{3+}. *Phys. Rev. B: Condens. Matter* **2000**, *61* (11), 7421–7427. DOI: https://doi.org/10.1103/PhysRevB.61.7421.
(139) Zhang, Y.; Chen, B.; Xu, S.; Li, X.; Zhang, J.; Sun, J.; Zhang, X.; Xia, H.; Hua, R. A Universal Approach for Calculating the Judd–Ofelt Parameters of RE^{3+} in Powdered Phosphors and its Application for the β-$NaYF_4$: Er^{3+} / Yb^{3+} Phosphor Derived from Auto-Combustion-Assisted Fluoridation. *Phys. Chem. Chem. Phys.* **2018**, *20* (23), 15876–15883. DOI: https://doi.org/10.1039/C8CP02317D.
(140) García-Flores, A. F.; Matias, J. S.; Garcia, D. J.; Martínez, E. D.; Cornaglia, P. S.; Lesseux, G. G.; Ribeiro, R. A.; Urbano, R. R.; Rettori, C. Crystal-field effects in Er^{3+}- and Yb^{3+}-Doped Hexagonal $NaYF_4$ Nanoparticles. *Phys. Rev. B: Condens. Matter* **2017**, *96* (16), 165430. DOI: https://doi.org/10.1103/PhysRevB.96.165430.
(141) Villanueva-Delgado, P.; Biner, D.; Krämer, K. W. Judd–Ofelt analysis of β-$NaGdF_4$: Yb^{3+}, Tm^{3+} and β-$NaGdF_4$: Er^{3+} single crystals. *J. Lumin.* **2017**, *189*, 84–90. DOI: https://doi.org/10.1016/j.jlumin.2016.04.023.
(142) Rinkel, T.; Nordmann, J.; Raj, A. N.; Haase, M. Ostwald-Ripening and Particle Size Focussing of Sub-10 nm $NaYF_4$ Upconversion Nanocrystals. *Nanoscale* **2014**, *6* (23), 14523–14530. DOI: https://doi.org/10.1039/c4nr03833a.
(143) Liu, N.; Gobeil, N.; Evers, P.; Gessner, I.; Rodrigues, E. M.; Hemmer, E. Water Dispersible Ligand-Free Rare Earth Fluoride Nanoparticles: Water Transfer Versus $NaREF_4$-to-REF_3 Phase Transformation. *Dalton Trans.* **2020**, *49* (45), 16204–16216. DOI: https://doi.org/10.1039/d0dt01080d.
(144) S. G. Johnson, J. W. *Libcerf, Numeric Library for Complex Error Functions, version 1.5–1.19*. https://jugit.fz-juelich.de/mlz/libcerf (accessed 2025.07.01).
(145) Shi, R.; Lin, L.; Wang, Z.; Zou, Q.; Mudring, A.-V. Manipulation of Luminescence via Surface Site Occupation in Ln3+-Doped Nanocrystals. *J. Am. Chem. Soc.* **2024**, *146* (17), 11924–11931. DOI: https://doi.org/10.1021/jacs.4c00052.
(146) Ren, P.; Zheng, X.; Zhang, J.; De Camillis, S.; Jia, J.; Wang, H.; Liao, X.; Piper, J. A.; Lu, Y. Quantifying the Influence of Inert Shell Coating on Luminescence Brightness of Lanthanide Upconversion Nanoparticles. *ACS Photonics* **2022**, *9* (3), 758–764. DOI: https://doi.org/10.1021/acsphotonics.1c01695.

11. Manuscripts

1)

Conrad (I) *et al*.

ESI, Conrad (I) *et al*.

Reproduced from Ref. 1 with permission from the Royal Society of Chemistry, 2025.

2)

Conrad (II) *et al*.

ESI, Conrad (II) *et al*.

Reproduced with permission from Ref. 2. Copyright 2025 American Chemical Society.

Nanoscale

ROYAL SOCIETY OF CHEMISTRY

PAPER

View Article Online
View Journal | View Issue

Cite this: *Nanoscale*, 2025, **17**, 8599

The true atomistic structure of a disordered crystal: a computational study on the photon upconverting material β-$NaYF_4$ and its Er^{3+}-, Tm^{3+}-, and Yb^{3+}-doped derivates†

Chris Steve Conrad, [a,b] Holger Euchner, [a] Eva Hemmer *[b] and Reinhold F. Fink *[a]

Hexagonal (β-) $NaYF_4$ and $LiYF_4$ doped with trivalent lanthanide ions (Ln^{3+}, *e.g.*, Er^{3+}, Tm^{3+}, and Yb^{3+}) are well-known photon upconverting materials. This property is crucially determined by the precise location of the Ln^{3+} dopant ions and their closest neighbouring ions in the host material. However, due to the inherent disorder of the crystal structures the atomistic structure of a disordered crystal such as β-$NaYF_4$ is not unambiguously provided by X-ray diffraction techniques. Here, theoretical estimates for the true structure of the material are obtained *via* periodic density functional theory (DFT) calculations of large supercells. Our results reveal that Ln^{3+} doping of β-$NaYF_4$ occurs in a variety of low-symmetry sites, which are significantly altered by the occupational disorder of the crystal structure. Mainly, the distribution of Na^+ and Y^{3+} around a doping site significantly influences the positions of the F^- closest to the dopant. The results of this study are substantiated by applying the same method on the well-ordered host crystal $LiYF_4$ and by comparison with available experimental and theoretical data. Similar results are expected for other disordered crystalline host materials such as β-$NaGdF_4$ or cubic (α-) $NaYF_4$. The obtained structural information is a prerequisite for future accurate simulations and prediction of key parameters for the upconversion process in bulk materials and nanoparticles.

Received 20th November 2024,
Accepted 14th February 2025

DOI: 10.1039/d4nr04880f

rsc.li/nanoscale

Introduction

Photon upconversion is a process during which the energy of two or more photons of lower energy (typically in the near-infrared, NIR) is captured in a sequential manner to trigger the emission of one single photon of higher energy (in the ultraviolet, visible, or shorter-wavelength NIR regions). The process was first observed in bulk materials but later also transferred to nanomaterials.[1–3] Nanoscale upconverting materials, so-called upconverting nanoparticles (UCNPs), offer a wide range of potential applications for which the small size is a prerequisite.[4,5] Generally, these applications can be divided into two categories. For applications such as bio-imaging, sensing, and anti-counterfeiting, bright emission of upconverted light is key.[6–10] Conversely, applications such as photo-induced drug delivery, photodynamic and photothermal therapies, plant cultivation, and enhancing photovoltaics require not only bright emission but rely on high efficiency of the upconversion process as the emitted photons are used in subsequent photochemical or -thermal reactions.[11–18] For the latter, a high percentage of upconverted photons per absorbed low-energy photons, *i.e.*, high photoluminescence quantum yield, and a large amount of absorbed photons is highly desirable. While synthetic strategies have evolved over the past years, *e.g.*, dopant optimisation, host choice, core/shell architecture, in addition to computational approaches,[19–22] the relatively low quantum yield of UCNPs – maximum values of 13% have been reported to date[23] – remains one of the main challenges to bring these applications from proof of concept to real life. To advance computational models tackling these challenges, we here conduct an in-depth geometry optimisation study for different host matrices and their upconversion-inducing lanthanide dopants. It is expected that the reported results provide insights beneficial for the design of more efficient, next generation upconverting (nano)materials.

For the design of a meaningful geometry optimisation study, the accurate understanding of the upconversion process at an atomic level is helpful. The 4f–4f transitions of the trivalent lanthanide ions (Ln^{3+}) in centrosymmetric environments

[a]*Institute of Physical and Theoretical Chemistry, University of Tübingen, Tübingen (Baden-Württemberg), Germany. E-mail: Reinhold.fink@uni-tuebingen.de*
[b]*Department of Chemistry and Biomolecular Sciences, University of Ottawa, Ottawa, Ontario, Canada. E-mail: ehemmer@uottawa.ca*

† Electronic supplementary information (ESI) available. See DOI: https://doi.org/10.1039/d4nr04880f

are forbidden by Laporte's selection rule and therefore extremely weak. In non-centrosymmetric environments, this rule can be mitigated, and larger but still low transition rates are thus observed.[24,25] Moreover, the Ln^{3+} excited states have relatively long lifetimes, typically in the order of micro- or even milliseconds.[26] The transition probabilities of the lanthanides are therefore at a sweet spot that creates favourable conditions for an already excited Ln^{3+} ion to receive additional energy *via* photon absorption or energy transfer from neighbouring ions (before relaxation to the ground state can take place). The Ln^{3+} thereby reaches an even higher excited state and its radiative deexcitation to the ground state gives rise to upconverted photons.

Crystals of the type MXF_4 (M = alkali metal, X = lanthanides and yttrium) offer the required non-centrosymmetric doping sites and are therefore among the most commonly chosen host matrices for upconversion.[27–30] In addition, MXF_4 stands out due to the ease of substitution of a host ion (*e.g.*, Y^{3+}) by an emissive Ln^{3+} ion (*e.g.*, Er^{3+}, Tm^{3+}, or Yb^{3+}) given the comparable ionic radii as well as identical cation charge.[31] Furthermore, established synthetic access to nanomaterials of controlled size and (core/shell) architecture are available for these compounds.[29,32,33] Moreover, the prominence of specifically fluoride matrices is due to their comparatively high stability and the relatively low phonon energies reducing the probability for (non-radiative) quenching processes to take place.[34,35] Er^{3+} or Tm^{3+} are among the most widely studied dopants in these hosts, providing ladder-like energy levels for the upconversion process, while Yb^{3+} is commonly co-doped for its higher absorption cross section at 980 nm.[36–38]

Disordered host materials such as $NaYF_4$, which can crystallise in a cubic (α) or in a hexagonal (β) phase, have the added benefit of providing a variety of similar but not completely identical doping sites, which is advantageous for the upconversion process.[35,39,40] This study focuses on the observed structural disorder in the β-$NaYF_4$ crystal lattice, which is known to influence properties such as the exact energy level positions of dopants.[41] These on the other hand determine the energy difference to be overcome in energy transfer processes, as well as corresponding oscillator strengths and energy transfer rates.[35,40,42] The disorder of β-$NaYF_4$ and related compounds has long been established and discussed by experimentalists.[27,43–46] However, direct observation on an atomic level is difficult using methods such as X-ray diffraction alone, as this technique provides only averaged information over an ensemble of disordered sites in the crystal.[27,40,42,47]

Computational methods have been used in the past to explore the above-mentioned and other properties of β-$NaYF_4$, however, the employed models often lack consideration of lattice disorder.[48–52] If disorder has been considered, such as in the works by Platonenko *et al.* or Szefczyk *et al.*,[28,53] it was on the basis of discussing the possible unit cells of β-$NaYF_4$ and how disorder might combine the competing space group designations of β-$NaYF_4$. Huang *et al.* were the first ones to create a model of two supercells with different configurations but significantly altered the positions of Na^+ ions in the process by moving them to higher-symmetry lattice points.[54] Indeed, to the best of our knowledge, simulating more than two configurations of the created supercell for a given space group has so far not been reported for undoped β-$NaYF_4$. The knowledge gained from our study using several configurations of a large supercell has the potential to support the rational design of novel highly efficient upconverting materials, thereby aiding to solve the quest of increasing the upconversion yield and enlarging the scope of applications for these materials.

While our results confirm earlier assessments of the 1f Na^+–Y^{3+} disorder in β-$NaYF_4$ by Aebischer *et al.*,[27] more interestingly, our findings unveil the likely presence of additional configurations within the lattice at an atomistic level. Moreover, the influence of the 2h Na^+ disorder on the Ln^{3+} doping sites is reported for the first time on a purely *ab initio* computational level. Further insight is also given toward the slight disorder that is induced by low-percentage doping. The obtained results are validated by comparing the model to literature-reported experimental and theoretical data of $LiYF_4$, exhibiting a highly regular crystal structure, as well as published experimental data of disordered β-$NaYF_4$.

Structural setup

The process of determining the required size of the supercell for the calculation and the necessary number of configurations for each supercell is described in the following. Results obtained after optimising the individual structures are reported in Results and discussion.

Disordered β-$NaYF_4$

Lattice structure. In this work, the β-$NaYF_4$ structure is described in space group $P\bar{6}$, in which the Y-occuppied 1a sites are commonly placed at the edges of the lattice,[43] as reported in several other theoretical studies of this crystal.[28,48–50,52–54] This allows for a straightforward comparison of the obtained results to these studies. However, it should be noted that there also exist studies assigning space group $P6_3/m$ to β-$NaYF_4$.[51,55] In this case, Na^+ is placed at the edges of the lattice in the corresponding unit cell. A highly recommended, in-depth explanation and critical discussion of all possible space groups for β-$NaYF_4$ can be found in the review paper by Shi *et al.*[40] The unit cell of β-$NaYF_4$ in space group $P\bar{6}$ features three different cationic and two different anionic sites (Fig. 1A). The two anionic sites (Wyckoff positions 3j and 3k) are fully occupied by F^-, leaving no possibility for disorder. Among the cationic sites, one site exclusively accommodates Y^{3+} (Wyckoff position 1a). This site is nine-fold coordinated by three F^- at 3j sites and six F^- at 3k sites. These nine F^- form a tricapped trigonal prism with C_{3h} symmetry (Fig. 1B), in which the 3j F^- are located at the tips and the 3k F^- at the two caps of the prism. No disorder is possible at the 1a site. In contrast, finding Y^{3+} or Na^+ is equally likely (50% each) at the second cationic site (Wyckoff position 1f). Similar to the 1a site, this site is also coordinated by nine F^- with C_{3h} symmetry. The Wyckoff positions of the F^- that form the prism are swapped

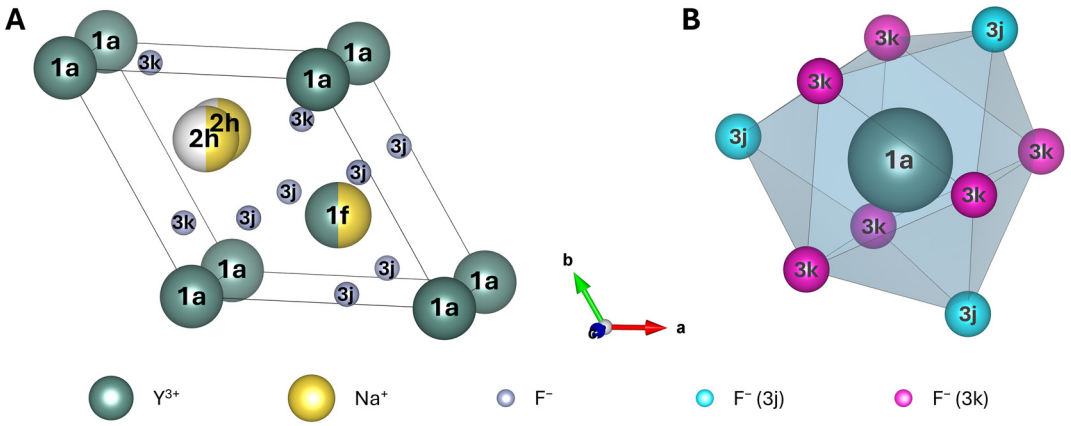

Fig. 1 (A) Unit cell of β-$NaYF_4$ with the composition $Na_{1.5}Y_{1.5}F_6$. Dark green spheres represent Y^{3+}, yellow spheres Na^+, white spheres are unoccupied sites, and small grey spheres represent F^-. Half spheres indicate a 50% occupation. (B) Both possible doping sites for Ln^{3+} (*i.e.*, 1a and 1f) are coordinated in a tricapped trigonal prismatic geometry by nine F^-. For clarity, the three 3j (caps) and the six 3k (trigonal prism) F^- are coloured in cyan and in pink, respectively. The prism for the 1f site is generated by rotating the coordination polyhedron shown in (B) by *ca.* 90° around the *c*-axis and swapping of the Wyckoff symbols for all F^-.

compared to the ones for the 1a site. When Ln^{3+} doping is considered, the Ln^{3+} ions randomly replace the Y^{3+} ions. Hence, the probability of finding an Ln^{3+} ion at a 1a site is twice as high ($^2/_3$) as the probability of finding the Ln^{3+} ion at a 1f site ($^1/_3$). Finally, the third cationic site is occupied by a single Na^+, split along the *c*-axis into two possible, equally likely sites (Wyckoff position 2h). In each unit cell only one of these two sites is occupied at a time. Both 2h positions are surrounded by six F^- with irregular octahedral symmetry.

The disorder at the 1f and the 2h site leads to more than one possible configuration for the unit cell, as will be explained further in the next subsection. Depending on the type of disorder (1f-, 2h-, or doping-originated), the positions of the F^-, forming the coordination polyhedral around the 1a and 1f sites, will be altered to a different extent. This in turn will reduce the symmetry elements available for the central site and therefore lower its point group. In most cases, even without doping, this changes the symmetry of most 1a and 1f sites from C_{3h} to C_1,[27] which significantly alters the properties of the potential Ln^{3+} dopants positioned at these 1a and 1f sites.

The available experimental evidence suggests that the occupation of the 1f site regularly alternates between Na^+ and Y^{3+} along all three spatial directions.[27] However, $NaYF_4$ and related materials are often synthesised at elevated temperatures, followed by thermal quenching, enabling energetically less favourable structural arrangements.[44,46] A regular alternation of Na^+ and Y^{3+} might therefore only be true as an averaged occupation over a large sample of unit cells. Indeed, if this regular alternation was the case, a larger unit cell with well-defined atomic positions at the 1f site could be generated. So far such a large unit cell has only been observed for β-$NaPrF_4$.[45,56] Local deviations at the 1f sites from the regularly alternating pattern on an atomic level and a less structured crystal with a higher degree of disorder therefore seem likely. Also, for the disorder at 2h sites only few theoretical studies have been conducted to date,[28,53,54] which leaves space for further investigation of the true atomistic structure of this disordered crystal.

To address these features of the β-$NaYF_4$ crystal, we developed a model that can represent disorder by creating several different configurations of the crystal structure. The required disorder was achieved by employing a large supercell, followed by alteration of the composition of the 1f and 2h sites within this supercell. Disorder at the 2h sites is straightforward to describe since the respective Na^+ occupies either one or the other Wyckoff 2h site within the unit cell. Moreover, supercells representing the disorder of the Wyckoff 1f sites also have to maintain the stochiometric composition of the crystal.

Supercell size. Depending on the inherent disorder of a unit cell, even small supercells that consist of only a few unit cells can result in an unmanageable large number of possible crystal structure configurations. For instance, any unit cell with one disordered site (like the Wyckoff 2h site), for which two possible ion occupations exist, has two possible configurations. The number of configurations in a supercell of such a crystal increases following a 2^N expression, where N is the number of unit cells in the supercell. For the 2 × 2 × 4 supercell chosen in this work, this leads to 2^{16} = 65 536 configurations formed by 16 individual unit cells for the 2h site. Additionally, for the 1f site of β-$NaYF_4$, we can distribute 8 Na^+ ions over 16 sites leading to $\binom{16}{8} = 12\,870$ configurations for this site, thus resulting in a total of more than 800 million configurations for both sites (*i.e.*, 1f and 2h). While symmetry considerations reduce these numbers, they stay much too large for computations. This is in stark contrast to $LiYF_4$, for which the completely ordered crystal is described by a single configuration, independent of the number of unit cells used.[57] Finding an appropriate supercell and a manageable

but sufficient number of configurations to describe the desired property is therefore a critical first step when creating a theoretical model for a disordered crystal.

To accurately describe the influence of the cation disorder, a 2 × 2 × 4 supercell has been chosen (Fig. 2). An in-depth discussion thereof is provided in the ESI.† In brief, a 2 × 2 × 4 supercell exhibits four rows of 1f sites along the *c*-axis. Three of these were altered when investigating disorder around the 1a site and one was altered for the investigation of the 1f site. Rows that were not neighbouring these sites are represented in faint colours in Fig. 2. These not neighbouring (faint) rows were occupied by an alternating sequence of Na^+ and Y^{3+}, which was kept fixed throughout all calculations. This simplification of the supercell induces some slight uncertainty with respect to the obtained results but the influence of these rows on the highlighted central sites should be marginal.

Occupational disorder, 1f site. For the following discussion it is assumed that the 2 × 2 × 4 supercell consisted of only six disordered 1f sites around the potential 1a and two disordered 1f sites around the potential 1f doping site (Fig. 2A and B, respectively). All other 1f sites are either coupled to one of these six/two sites, being of opposite type to prevent stoichiometric imbalances, or fixed to be either Na^+ or Y^{3+} (faint rows) and do not introduce further disorder into the 2 × 2 × 4 supercell. If the influence of the 1f disorder on (an Ln^{3+} located at) a 1a site is to be assessed (or more specifically on the F^- of the first anionic coordination sphere around the 1a site), the influence of all possible distributions of Na^+ and Y^{3+} at the six respective 1f sites of the first cationic coordination sphere is to be investigated. Stochastic considerations result in (2^6=) 64 different configurations (two possibilities for each of the six 1f sites). 13 of these 64 configurations are non-symmetry equivalent (neglecting the disorder at the 2h sites) and are to be calculated individually. A potential 1a doping site plus its first anionic and cationic coordination sphere (including six disordered 1f sites) is shown in Fig. 3A (corresponding to/extracted from configuration 10 of Table 1). The same cluster of ions is shown in Fig. 3C, this time with a different distribution of Na^+ and Y^{3+} at the 1f sites, belonging to configuration 5 of Table 1. Conversely, for the potential 1f doping site (2^2=) four different configurations can be generated, three of which are unique. Two of them are shown in Fig. 3B and D, corresponding to configuration 1 and 2, denoted in Table 1. The in total 16 different configurations (13 for the potential 1a and 3 for the potential 1f doping site) and the distributions of Na^+ and Y^{3+} onto the respective 1f sites for each of them are listed in Table 1. The same table also lists the ion at each of the six (two) 1f sites labelled in Fig. 3. We would like to emphasise at this point that the clusters of ions shown in Fig. 3 were created purely for better visualising the distribution of Na^+ and Y^{3+} at the 1f sites for the different configurations. These clusters are still embedded within their respective supercell. The remaining ions at the 1f sites in the supercell also change relative to the ions in the cluster, so that the stoichiometric ratio is retained. To recall, up to this point, no dopants have been introduced into the supercell. The close-up configurations shown in Fig. 3A and B correspond to the supercells shown in Fig. 2A (configuration 10) and Fig. 3B (configuration 1), respectively. As long as undoped, these configurations are identical and represent the configuration with the minimum energy after the optimisation process (*vide infra*).

Table 1 gives an overview of the various configurations created for the two clusters. By dividing the number of symmetry equivalent configurations (*i.e.*, degeneracy, second column) by the overall number of configurations for the individual cluster and multiplying by $^1/_3$ or $^2/_3$ for a potential 1f or 1a doping site, respectively, the weighting of this group of (symmetry equivalent) configurations is obtained (third column). The symmetry of the nine F^- around the central ion is also stated. These point groups are very crude approxi-

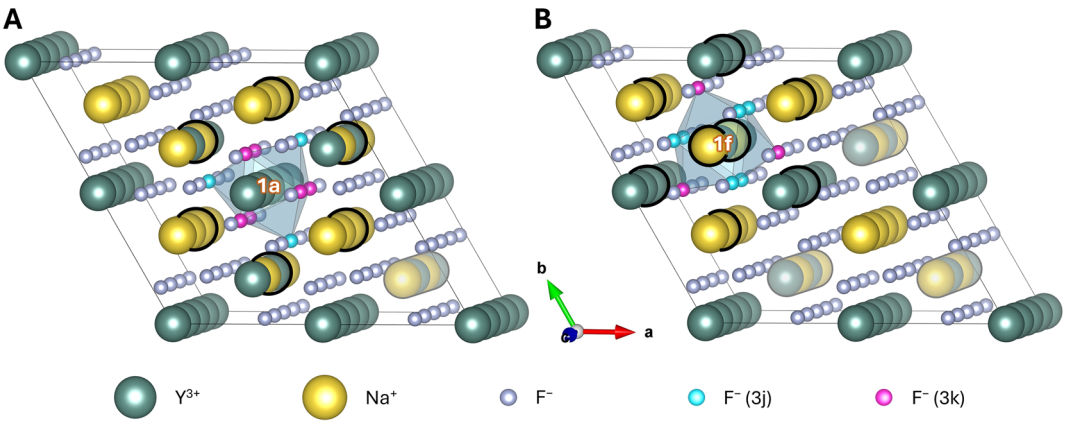

Fig. 2 2 × 2 × 4 supercell of β-$NaYF_4$ with the composition $Na_{24}Y_{24}F_{96}$. Highlighted are a potential (A) 1a and (B) 1f doping site (white labels), and their first anionic (F^- ions of the blue prism that are highlighted in cyan and pink) and cationic (Na^+ and Y^{3+} ions marked with a thick black circle) coordination spheres. Na^+ and Y^{3+} at the not neighbouring 1f rows (represented as faint) were not exchanged when creating the different configurations of the supercell. All other 1f sites were altered successively. For better visualisation, a close-up of the two potential doping sites with their nearest ions is shown in Fig. 3A and B.

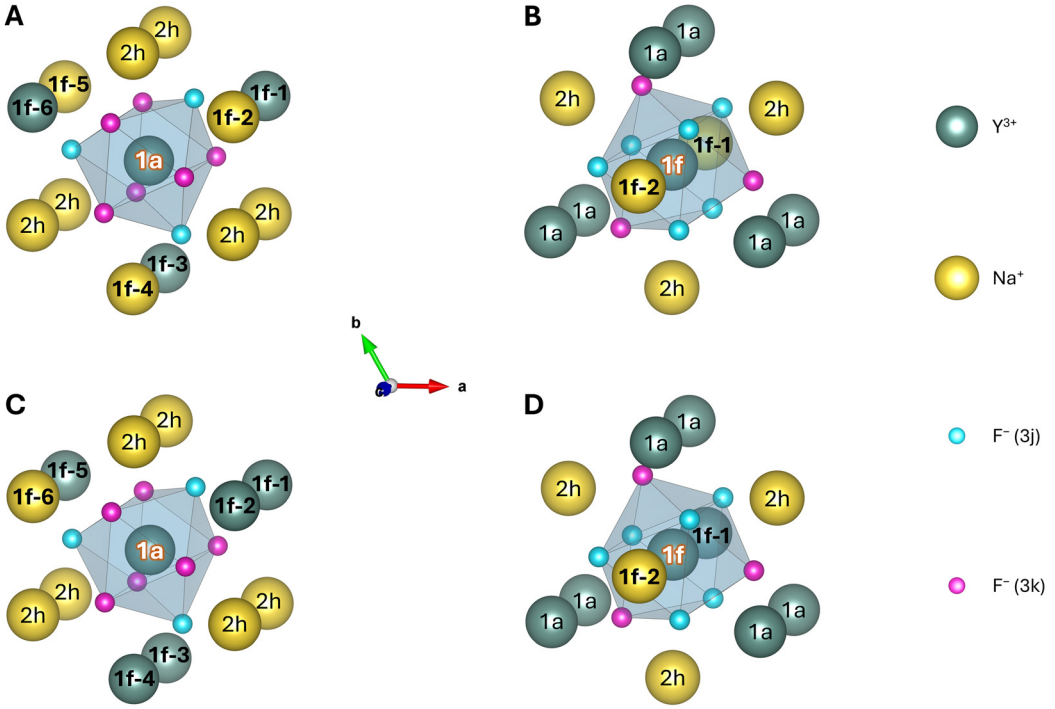

Fig. 3 Potential (A) 1a and (B) 1f doping sites and their first anionic and cationic coordination spheres for the supercells shown in Fig. 2A and B, respectively. The corresponding supercells are designated as configuration (A) 10 and (B) 1 in Table 1. Two additional configurations are shown in C and D, corresponding to configuration 15 and 2, respectively, in Table 1. Here some of the 1f sites were altered in comparison to configuration 10 and 1. For all clusters the 1a, 1f, and 2h sites are labelled by their Wyckoff symbols, the central site is labelled in white. The 1f sites for which the distribution of Na^+ and Y^{3+} were altered in this study are set in bold and numbered from (1f-) 1 to 6 (panels A and C) and 1 to 2 (panels B and D) for the potential 1a and 1f doping sites, respectively. The numbering of these sites is equivalent to the scheme used in the last column of Table 1. All clusters presented here were created for visualisation purposes only and are still embedded in their respective supercells used for the geometry optimisation.

Table 1 List of generated configurations for the potential 1f (1 to 3) and 1a (4 to 16) doping sites, their degeneracy, weighting, idealised F^- symmetry, and Na^+/Y^{3+} distribution at the 1f sites as shown in Fig. 3

Configuration	Degeneracy	Weighting (%)	F^- symmetry	Na^+/Y^{3+} distribution at neighbouring 1f sites					
Site: 1f	**4**	**33.3**		**1**	**2**				
1	1	8.3	C_{3h}	Na^+	Na^+				
2	2	16.7	C_3	Y^{3+}	Na^+				
3	1	8.3	C_{3h}	Y^{3+}	Y^{3+}				
Site: 1a	**64**	**66.7**		**1**	**2**	**3**	**4**	**5**	**6**
4	1	1.0	C_{3h}	Na^+	Na^+	Na^+	Na^+	Na^+	Na^+
5	6	6.3	C_1	Na^+	Na^+	Na^+	Na^+	Na^+	Y^{3+}
6	3	3.1	C_{3h}	Na^+	Na^+	Na^+	Na^+	Y^{3+}	Y^{3+}
7	6	6.3	C_1	Na^+	Na^+	Na^+	Y^{3+}	Y^{3+}	Na^+
8	6	6.3	C_1	Na^+	Na^+	Y^{3+}	Na^+	Y^{3+}	Na^+
9	2	2.1	C_3	Y^{3+}	Na^+	Y^{3+}	Na^+	Y^{3+}	Na^+
10	6	6.3	C_1	Y^{3+}	Na^+	Y^{3+}	Na^+	Na^+	Y^{3+}
11	12	12.5	C_1	Y^{3+}	Y^{3+}	Na^+	Y^{3+}	Na^+	Na^+
12	6	6.3	C_1	Y^{3+}	Y^{3+}	Y^{3+}	Na^+	Y^{3+}	Na^+
13	6	6.3	C_1	Y^{3+}	Y^{3+}	Na^+	Y^{3+}	Y^{3+}	Na^+
14	3	3.1	C_{3h}	Y^{3+}	Y^{3+}	Y^{3+}	Y^{3+}	Na^+	Na^+
15	6	6.1	C_1	Y^{3+}	Y^{3+}	Y^{3+}	Y^{3+}	Y^{3+}	Na^+
16	1	1.0	C_{3h}	Y^{3+}	Y^{3+}	Y^{3+}	Y^{3+}	Y^{3+}	Y^{3+}

mations that only consider shifts of the F^- along the *c*-axis, depending on the nearest neighbouring ions at the 1f sites as suggested by Aebischer *et al.*[27] Because of the differing ionic radii, Na^+ pushes the closest F^- stronger away than Y^{3+} (along the *c*-axis). This approximation is less valid when incorporating shifts along the other two axes and breaks down comple-

tely when considering changes introduced by Na^+ at the disordered 2h sites.[40] However, it is a helpful designation to understand the influence of the different distributions of Na^+ and Y^{3+} at neighbouring 1f sites onto the F^-. The last column of Table 1 states the distribution of Na^+ and Y^{3+} onto the six (two) 1f sites shown in Fig. 3.

To give an example, for configuration 5, five additional symmetry equivalent configurations exist. This can easily be deduced from the five Na^+ and one Y^{3+} that are distributed among the six 1f positions around a 1a site. The single Y^{3+} can be placed at each of the six positions, and the five remaining Na^+ are all equivalent (their placing order therefore does not matter). The total number of configurations for a 1a site is 64. Therefore, an Ln^{3+} ion doped into β-$NaYF_4$ has a probability of $6/64 \cdot {}^2/_3 = 0.0625$ or 6.3% to be located in an environment of this or an equivalent configuration. All of these considerations are purely with respect to geometric aspects. The energetic difference between individual configurations determines their actual occurrence in a real crystal and will be examined after the geometry optimisation. Finally, the positions of the F^- were considered to determine the point group of the central ion. The 1f sites 5 and 6, consisting of one Na^+ and one Y^{3+}, influence one of the F^- by moving it closer to Y^{3+}, while all other F^- stay in place. This reduces the point group around the central 1a site from C_{3h} to C_1.

The configurations listed in Table 1 were generated and energetically optimised as described in the computational details.

Occupational disorder, 2h site. So far, only the influence of the 1f sites onto the F^- has been considered. As stated above, the cations at the 2h sites, fully occupied by Na^+, also possess disorder (along the *c*-axis). However, including their influence on the positions of the F^- in the same manner as done for the 1f site was not feasible. The number of possible configurations would significantly increase as stated in the introduction. Computing such a large number of configurations constitutes a significant computational challenge.[48–51] Therefore, the 2h disorder was commonly neglected.

Nonetheless, to estimate the potential impact of the 2h disorder, three representative 2h configurations were selected and calculated. Therefore, one possible distribution was chosen for the in total 16 Na^+ at 2h sites in a 2 × 2 × 4 supercell (referred to as Na1) and used for all subsequent calculations. The occupied sites were chosen so that an equal amount of Na^+ was displaced along the +c- and −c-axis in each unit cell, reflecting the average distribution in a real crystal. After energetically minimising all configurations for the different Na^+/Y^{3+} distributions at the 1f sites, the 2h distribution was adjusted for the energetically most stable structure (configuration 10). This resulted in the creation of configurations 10-Na1, -Na2, and -Na3. Na1 is the distribution of Na^+ at the 2h site used initially (and for all other configurations of β$NaYF_4$). Na2 is another *c*-axis balanced distribution (see above). However, in comparison to Na1, in Na2 the Na^+ were shifted differently along the *c*-axis. Finally, for Na3 the eight Na^+ closest to the potential doping site were all displaced along the −*c*-axis. After creating these two additional configurations (*i.e.*, Na2 and Na3), the structures were optimised a second time. Optimization of these two configurations, Na2 and Na3, and their comparison to configuration Na1 provided evidence that the influence of the 2h disorder on the potential doping sites is less significant than the disorder at the 1f sites (*vide infra*). Therefore, no additional 2h disordered configurations were created.

Ln^{3+}-doping (Ln = Er, Tm, and Yb). To account for Ln^{3+}-doping, 48 doped configurations were created in addition to the 16 undoped configurations shown in Table 1. For this purpose, each of the optimised configurations was doped consecutively with Er^{3+}, Tm^{3+}, and Yb^{3+} at the central 1a or 1f site as highlighted in Fig. 3. Furthermore, the two additional 2h configurations were doped with Er^{3+} at the central 1a site. Subsequently, all doped structures were optimised to an energetic minimum structure. For one configuration (number 10 in Table 1) doped with Er^{3+}, the optimisation process was repeated with a larger basis set for Er^{3+} (TZV2P instead of DZVP) to estimate the influence of the latter (*vide infra*).

Overall, the 2 × 2 × 4 supercell consists of 144 ions, 24 of which being Y^{3+}. Replacing one of these Y^{3+} ions by an Ln^{3+} results in a doping concentration of 4.2 mol%. Doping concentrations, especially for activator ions such as Er^{3+} and Tm^{3+}, are usually well below these values. In fact, the most common doping concentrations for Er^{3+} and Tm^{3+} are 2 mol% and 0.5 mol%, respectively.[58,59] However, enlarging the supercell further (and thereby reducing the doping concentration) is limited by the steeply increasing computational demand and was therefore not carried out.

Ordered $LiYF_4$

Extension of the model. To demonstrate the validity of our computational protocol, $LiYF_4$ (Fig. 4) as a popular alternative host lattice for upconverting (nano)materials was modelled with the same method. Unlike β-$NaYF_4$, $LiYF_4$ crystallizes in a tetragonal crystal structure (space group $I4_1/a$) in which all lattice sites are fully occupied by a single type of ion.[57] Consequently, $LiYF_4$ constitutes an easier case than β-$NaYF_4$ with only one position for Li^+ (Wyckoff symbol 4a), one for Y^{3+} (Wyckoff symbol 4b), and one for F^- (Wykoff symbol 16f). The unit cell of $LiYF_4$ and the coordination polyhedron around the Y^{3+} sites, *i.e.*, a distorted square antiprism, are shown in Fig. 4A and B, respectively. Based on this unit cell, a 3 × 3 × 1 supercell with 216 ions was created (Fig. S2†). For this supercell, a doping rate of 2.8% is obtained upon replacement of 1 of the 36 Y^{3+} by an Ln^{3+}. Following the optimization of the undoped $LiYF_4$ structure, one of the 4b sites was doped consecutively with Er^{3+}, Tm^{3+}, and Yb^{3+}, and the three resulting structures were optimised once again.

Computational details

DFT with CP2K. All calculations were performed by applying periodic density functional theory (DFT) as implemented in

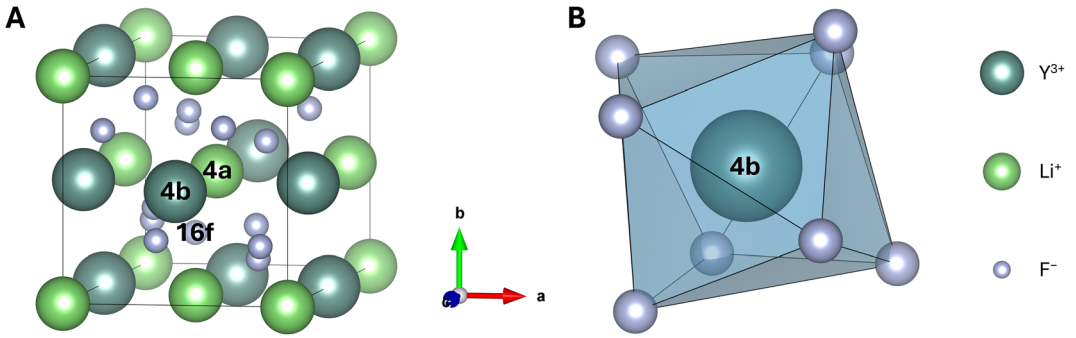

Fig. 4 (A) Unit cell of $LiYF_4$ with the composition $Li_4Y_4F_{16}$. Dark green spheres represent Y^{3+}, light green spheres Li^+, and small grey spheres represent F^-. $LiYF_4$ features only one potential doping site, *i.e.*, Wyckoff position 4b. (B) Coordination polyhedron around Y^{3+}. Each Y^{3+} at a 4b site is surrounded by eight F^- ions, creating a distorted square antiprism.

the software package CP2K, version 7.1.[60] CP2K utilises atomic Gaussian type orbitals (GTOs) in its calculations.[61–63] For Li^+, Na^+, F^-, and Y^{3+}, basis sets of split valence triple-zeta quality with double polarisation functions (TZV2P-MOLOPT-SR) were employed consistently during all calculations. The lanthanides (Er^{3+}, Tm^{3+}, and Yb^{3+}) were modelled using basis sets of double-zeta quality (DZVP-MOLOPT-SR), except for an additional study on Er^{3+} where TZV2P-MOLOPT-SR was used as well.[64] The electron-core interaction was described by using Goedecker, Teter, and Hutter (GTH) type norm-conserving pseudopotentials,[65] while exchange and correlation were expressed *via* the Perdew–Burke–Ernzerhof (PBE)[66] exchange–correlation functional. To account for dispersion, the Grimme D3 correction was applied.[67] The electron densities were expanded in plane waves, with the cutoff and relative cutoff energy corresponding to 800 Ry and 60 Ry, respectively. A 2 × 2 × 2 and a 2 × 2 × 3 Monkhorst–Pack k-point mesh was utilised to sample the reciprocal space for the β-$NaYF_4$ and $LiYF_4$ supercells, consisting of 144 and 216 atoms, respectively. The convergence criterion for the self-consistent field cycle was set to 10^{-6}. Input files for the calculation of the two different crystals are provided in the ESI.† All figures were drawn with the VESTA software package.[68]

Table 2 Comparison of (A) lattice parameters, (B) bond distances, and (C) band gaps of $LiYF_4$ obtained in this study with experimental and theoretical data taken from the available literature

$LiYF_4$	Lattice parameters (Å)			
A	$a = b$	c	Deviation (%)	Ref.
Experimental	5.26	10.94	—	57
Theoretical	5.13	10.67	2.5	70
Theoretical	5.17	10.82	1.5	71
Theoretical	5.20	10.80	1.2	This work
	Bond distances (Å)			
B	Y^{3+}–$F^-_{(1)}$	Y^{3+}–$F^-_{(2)}$	Deviation (%)	Ref.
Experimental	2.407	2.453	—	57
Theoretical	2.244	2.304	6.4	73
Theoretical	2.265	2.309	5.9	This work
C	Band gap (eV)		Deviation (%)	Ref.
Experimental	> 10.77		—	71 and 76
Theoretical	8		25.7	74
Theoretical	11.09		3.0	71
Theoretical	8.08		25.0	This work

Results and discussion

Undoped and doped (Er^{3+}, Tm^{3+}, Yb^{3+}) minimum energy structures for different configurations of β-$NaYF_4$ in a 2 × 2 × 4 supercell were calculated with the settings described above. The same was done for the single available configuration of $LiYF_4$ in a 3 × 3 × 1 supercell. The structures were evaluated in terms of relative energies, lattice parameters, and Y^{3+}–F^- bond lengths. These properties were then compared to experimental and theoretical data, if available.

Validation of the model

Ordered $LiYF_4$. $LiYF_4$ exhibits only one configuration, which renders the comparison of the obtained results with other data sets from the literature straightforward (Table 2). Therefore, $LiYF_4$ was chosen for a first evaluation of the model, prior to application of the computational setup to more complex lattices, such as β-$NaYF_4$. Deviations in this study were consistently calculated as the absolute value of the difference between the experimental value from literature and the (here) calculated theoretical values, divided by the experimental value. Also, the deviations listed in this text were calculated explicitly and not taken from the literature. The calculated lattice parameters for $LiYF_4$ deviated slightly by 1.2% from the experimental values reported by Thoma *et al.*[57] An even smaller deviation of 0.4% was obtained in comparison to work by Keller *et al.*, but little detail about crystal synthesis and characterisation was provided by the authors.[69] The values calculated in our study also compared nicely to other computational works by Ching *et al.* and Luong *et al.*, reporting unit cells, which deviated by 1.5 to 2.5% from the experimental data referenced above.[70,71]

It should be mentioned that the authors of both abovementioned computational studies stated a smaller discrepancy to experimental values. However, both referenced a $LiYF_4$ crystal structure by Garcia *et al.* that was synthesised adding 2 wt% of PrF_3.[72] Even though the influence of the dopant on the lattice structure is small (*vide infra*), comparison to an undoped sample is still preferable. For pure $LiYF_4$ and the 2 wt% of Pr^{3+} containing crystals average bond lengths for two types of Y^{3+}–F^- bonds were obtained.[57,72] Determination of the Y^{3+}–F^- bond lengths for the crystal structure optimised in our study unveiled discrepancies to the experimental values of 5.8% and 0.7%, respectively. Yin *et al.* calculated the same bond lengths for pure $LiYF_4$, and deviations were at a similar range (6.4% and 0.2%, respectively).[73] With respect to the calculated band gap, our results very closely matched computed values that used a functional of the same type (generalized gradient approximation, GGA).[74,75] However, both our and their computational studies deviated from the experimental value by about 25%.[71,76] In fact, calculations describing exchange and correlation by GGA type functionals are known to underestimate the band gap of semiconductors and insulators.[77] Hence, our calculated values were within the expected margin of error. Better results can be achieved with more sophisticated methods, if required.[71] Our results further demonstrated that doping the structure with Er^{3+}, Tm^{3+}, or Yb^{3+} only marginally changes the lattice structure (on average less than 1% for all three dopants). This is most likely due to the small doping concentration and the similarity of the ionic radii. This will be discussed in more detail for β-$NaYF_4$. Thus, all values assessed suggest that our approach is well suited for predicting structural parameters of inorganic crystals beyond $LiYF_4$.

Disordered β-$NaYF_4$. In the case of β-$NaYF_4$, the predicted values for the 16 individual configurations were averaged with respect to their weighting (Table 1). Table 3 provides a summary of the obtained data, including data taken from the literature. Compared to macroscopic crystals synthesised and characterised by Roy *et al.*, slightly larger lattice parameters *a* and *b* and a slightly smaller parameter *c* were predicted by the designed model.[45] As the disorder affects the symmetry of the crystal, *a* and *b* were found to be no longer equal in length. However, it should be noted that the difference between these values was less than 0.01%, and the angle γ was only 0.1% larger than the experimental value of 120°. Overall, the size of the unit cell changed by only 0.9%. These findings are in very good agreement with other theoretical calculations, such as the ones by Platonenko *et al.* or Park *et al.*, who predicted very similar values.[28,52] Moreover, the bond length between Y^{3+} and F^- averaged over all nine bonds yielded a 1.2% shorter bond length compared to experimental results,[45] being in good agreement with the literature. For instance, a different computational model by Yao *et al.* predicted a 5.9% shorter bond length.[49] With respect to band gap calculations, as seen for $LiYF_4$, the calculated band gap was also underestimated for β-$NaYF_4$, namely by 8.9% compared to the experimental value.[78] Again, this value is in line with previously reported computational results (10.4%) that used the same type of functional.[48] Similar to $LiYF_4$, doping the structure with Er^{3+}, Tm^{3+}, and Yb^{3+} generated only minor overall changes, as detailed in the following section (Impact of disorder for β-$NaYF_4$).

Table 3 Comparison of (A) lattice parameters, (B) bond distances, and (C) band gaps of β-$NaYF_4$ obtained in this study with experimental and theoretical data taken from the available literature

β-$NaYF_4$	Lattice parameters (Å)			
A	$a = b$	c	Deviation (%)	Ref.
Experimental	6.00	3.58	—	45
Theoretical	6.07	3.53	1.3	52
Theoretical	6.01	3.60	0.3	28
Theoretical	$6.04 \neq b$	3.54	0.9	This work
	Bond distance (Å)			
B	Y^{3+}–F^-		Deviation (%)	Ref.
Experimental	2.371		—	45
Theoretical	2.230		5.9	49
Theoretical	2.342		1.2	This work
C	Band gap (eV)		Deviation (%)	Ref.
Experimental	= 8		—	78
Theoretical	= 7.17		10.4	48
Theoretical	= 7.83		2.1	52
Theoretical	= 7.29		8.9	This work

Thus, we have demonstrated the suitability of our protocol to predict lattice parameters and average bond lengths for two lattices with different crystallographic properties, *i.e.*, $LiYF_4$ and β-$NaYF_4$, with reasonable accuracy. The chosen approach of averaging over 16 different configurations for β-$NaYF_4$ indeed provided results that are close to reported experimental values. More importantly though, now that individual configurations have been created and optimised, they can be compared to each other, and possible trends may be deduced.

Impact of disorder for β-$NaYF_4$

Occupational disorder, 1f site. Aebischer *et al.* considered the cation disorder for β-$NaLaF_4$ and related compounds such as β-$NaYF_4$.[27] Based on patterns obtained *via* diffuse X-ray scattering and Monto Carlo simulations, they concluded that the 1f site preferentially produces rows of regularly alternating Na^+ and La^{3+} along the *c*-axis. Furthermore, it was theorised that the positions of Na^+ and La^{3+} within these rows are interchanged for two neighbouring 1f rows. For each 1f row, six such neighbouring rows exist (a set of four neighbouring 1f rows is shown in Fig. 4). The results of our computational model further validate this claim; the configuration that consists of alternating rows resulted in the lowest lattice energy (*i.e.*, configuration 10). For reference, ΔE in Table 4 and Table S1† represents the difference between the energy of the respective configuration and the overall energetically lowest configuration (of the respective undoped or doped structure). It becomes clear that configuration 10 (and 1, which is identi-

Table 4 Results of the structural optimisations for the 16 different configurations of undoped β-$NaYF_4$. Lattice energies relative to the most stable configuration (ΔE), deviations of the lattice parameters from the experimental values ($Dev._{LP}$), and averaged bond lengths (Y^{3+}–F^-) are displayed. For β-$NaYF_4$ doped with 4.2% Er^{3+} only the energy differences are showcased (additional data for β-$NaYF_4$ doped with Er^{3+}, Tm^{3+}, and Yb^{3+} are provided in Table S1†)

		Undoped β-$NaYF_4$			4.2% Er^{3+}
Site	Config.	ΔE (kJ mol^{-1})	$Dev._{LP}$ (%)	Y^{3+}–F^- (Å)	ΔE (kJ mol^{-1})
1f	1	0.0	0.77	2.347	0.1
	2	1.9	0.83	2.342	2.4
	3	3.4	0.90	2.338	3.4
1a	4	6.5	0.78	2.372	6.5
	5	4.6	0.85	2.354	4.6
	6	4.3	0.88	2.360	3.4
	7	1.9	0.88	2.346	1.8
	8	1.8	0.92	2.345	1.8
	9	1.2	0.86	2.336	1.2
	10	0.0	0.77	2.338	0.0
	11	2.6	0.87	2.344	1.6
	12	1.9	0.92	2.333	1.9
	13	2.0	0.86	2.335	2.3
	14	4.8	0.89	2.336	4.8
	15	4.2	0.84	2.330	4.2
	16	7.9	0.76	2.326	8.3

cal to 10 as long as being undoped, Fig. 3) has the lowest lattice energy of all assessed configurations (ΔE = 0 as it exhibits the minimum energy). All other configurations are higher in energy. It is also noteworthy that the energies of all examined configurations follow the pattern of lower energy for regularly alternating distributions (configurations 7 to 13) to higher energies for configurations with more locally clustered Na^+ and Y^{3+} (configurations 4 to 6 and 14 to 16, respectively).

Another important parameter to assess is the deviation of the lattice parameters (Dev_{LP}, Table 4). This parameter describes the deviation of the calculated lattice parameters from the experimental values and was obtained by averaging over the relative deviations of the individual cell vectors. Again, configuration 10 featured one of the smallest deviations. The highly regular alternation of Na^+ and Y^{3+} for this configuration is probably the main reason for the low lattice energy and small lattice parameter deviation observed. However, the difference in lattice energy for the remaining 14 configurations is at most 7.9 kJ mol^{-1}, even for the two configurations with the most locally clustered distributions of Na^+ and Y^{3+} (configuration 4 and 16 with six Na^+ and six Y^{3+}, respectively).

Indeed, nanoparticles of this crystal type are typically synthesised at temperatures of up to 300 °C. At this temperature, the Boltzmann population of the energetically most unfavourable configuration (configuration 16) amounts to 0.19 (Table 5) as compared to the most stable configuration (configuration 10). Under the assumption of elevated synthesis temperatures and rapidly cooled crystallites, all configurations are therefore likely to be present (locally) in such a crystal. Adding to this, the sample used for characterisation by Aebischer *et al.* was

Table 5 Occupation probability and percentage of C_1 symmetry according to Boltzmann distribution for a potential 1a doping site (configurations 4 to 16). In the first part of the table (all columns except the last one) the occupation probability, $f(E_n)/f(E_{10})$, for each configuration relative to the energetically lowest configuration (*i.e.*, configuration 10) is calculated at three different temperatures (*i.e.*, 20, 300, and 590 °C), where k_B is the Boltzmann and N_A the Avogadro constant. The weighting of each configuration according to the statistical distribution as presented in Table 1 is given in the bottom row of the table. In the last column of this table, the percentage of configurations with C_1 symmetry relative to all configurations is calculated, taking into account the Boltzmann distribution at the three different temperatures (*i.e.*, T = 20, 300, and 590 °C) and only the statistical weighting ($T = \infty$; from top to bottom)

n (=configuration) symmetry		4 C_{3h}	5 C_1	6 C_{3h}	7 C_1	8 C_1	9 C_{3v}	10 C_1	11 C_1	12 C_1	13 C_1	14 C_{3h}	15 C_1	16 C_{3h}	Total C_1 (%)
$\Delta E = E_n - E_{10}$ (kJ mol^{-1})		6.509	4.588	4.331	1.901	1.791	1.180	0	2.586	1.911	2.002	4.801	4.158	7.948	
$\frac{f(E_n)}{f(E_{10})} = e^{-\frac{\Delta E}{k_B \cdot N_A \cdot T}}$	T = 20 °C	0.07	0.15	0.17	0.46	0.48	0.62	1.00	0.35	0.46	0.44	0.14	0.18	0.04	91.1
	T = 300 °C	0.26	0.38	0.40	0.67	0.69	0.78	1.00	0.58	0.67	0.66	0.37	0.42	0.19	88.7
	T = 590 °C	0.40	0.53	0.55	0.77	0.78	0.85	1.00	0.70	0.77	0.76	0.51	0.56	0.33	87.5
Weighting (%)		1.0	6.3	3.1	6.3	6.3	2.1	6.3	12.5	6.3	6.3	3.1	6.3	1.0	84.4

prepared at even higher temperatures, *i.e.*, 590 °C.[27,46] At such high temperature, the expected relative population of configuration 16 is as high as 0.33. On the other hand, once a reaction mixture has cooled down, especially if quenched, a positional change of Na^+ and Y^{3+} to produce energetically favourable alternating rows after the formation of a disordered crystal is unlikely as ion swapping is associated with a significant energy barrier.[44,46,79] Considering Boltzmann distribution and the statistical weighting (Table 5), it can also be deduced that for temperatures above 170 °C configuration 11 is the most likely to be found in a crystal. This is because the statistical weighting of configuration 11 is twice as high as that of configuration 10, and its occupation probability raises above 0.5 at this temperature compared to configuration 10. Furthermore, it must be emphasized that, in principle, configurational entropy has to be considered for the disordered configurations as well, thus, making their occurrence even more likely.

The original report by Aebischer *et al.* also mentions symmetry considerations supporting that configuration 10 might be the most likely one.[27] Nonetheless, this configuration is definitely not the only one to be found in such a crystal. The authors conducted Monte Carlo simulations from which they deduced that in 93–95% of the modelled cells the surrounding of a 1a site was reduced to C_1 symmetry because of the disorder at the 1f site and its influence on the F^- surrounding the 1a site. However, if all 1f rows strictly followed the previously proposed alternation along the *c*-axis, every single 1a site must be of C_1 symmetry (=100%). This is because each 1a cluster will have two 1f rows with opposite Na^+/Y^{3+} allocation in their first cationic coordination sphere. Each of them will therefore push one F^- of the 1a site into different (opposite) directions, resulting in C_1 symmetry.

The discrepancy between 93–95% and 100% C_1 symmetry can be partially explained through the data made available by this study. When looking at the distribution of the different symmetries through the weighted average of the configurations for a potential 1a doping site (Table 1, configuration 4 to 16), 84.4% of these configurations will be of C_1 symmetry (*i.e.*, 54 of the in total 64 configurations; last column of Table 5). If furthermore varying occupational probabilities between these different configurations (induced by their relative energetic differences) *via* Boltzmann distribution are considered, almost 89% of the potential doping sites (depending on the temperature) should be of C_1 symmetry. While this does not provide direct evidence for the actual symmetry distribution around the 1a sites, it strongly suggests that there is deviation from the energetically favoured strictly alternating 1f rows.

Also, it should be noted that all symmetry considerations are invalidated once the disorder at the 2h sites is considered. Except for specific and rather rare configurations of the six 2h Na^+ around a 1a site, these Na^+ remove any remaining symmetry elements by pushing the closest F^- in different directions, resulting in C_1 symmetry for most if not all 1a (and also 1f) sites. Based on all of the above aspects of symmetry and energetic consideration, we therefore concluded that the F^- around the 1a sites were considerably more disordered than suggested by Aebischer *et al.*, and that probably almost all 1a and 1f sites were of C_1 symmetry.

Aebischer *et al.* additionally mentioned a displacement of the three 3j F^- along the *c*-axis in between two neighbouring 1f sites depending on the distribution of Na^+ and La^{3+} at these sites.[27] It was stated that an F^- between a pair of Na^+ and La^{3+} at adjacent 1f sites will be displaced by 0.07 Å towards La^{3+} because of the larger ionic radius of Na^+. Thereby, the bond between F^- and La^{3+} is shortened as evidenced in the datasets generated in our study. In configuration 1, the central 1f Y^{3+} has two Na^+ at the two neighbouring 1f sites (Fig. 2B, and Table 1). Such an arrangement is quite different from configuration 3, in which the two neighbouring 1f sites are both occupied by Y^{3+}. While the average bond length for all nine F^- presented in Table 4 suggests that configuration 3 has shorter bonds (contrary to the Monte Carlo model of Aebischer *et al.*),[27] a detailed analysis revealed that the bonds between Y^{3+} and the six 3j F^- in configuration 1 were indeed shortened on average by 0.03 Å compared to configuration 3 (one bond is even reduced by 0.08 Å). The apparent elongation in the averaged result can be explained by the three 3k F^- that show a significant increase in bond length by 0.04, 0.09, and 0.14 Å. The discrepancies (*i.e.*, shorting by 0.03 Å compared to 0.07 Å) between these *ab initio* results and the Monto Carlo model can either be rooted in the model itself, the different ions being used (although the ionic radius of Y^{3+} is smaller than that of La^{3+}, and therefore, a larger and not smaller displacement of the six 3j F^- for Y^{3+} seems therefore plausible), or possibly in the different occupation of Na^+ at the 2h sites. While Aebischer *et al.*[27] did not report on the 2h sites, our results provide evidence that these sites have significant influence on the bond lengths (see next section).

Similar to the potential 1f doping site, the general trend observed for the Y^{3+}–F^- bond lengths at the 1a sites can be summarised as following: the more of the neighbouring 1f sites were occupied by Na^+, the more distorted prisms as well as overall longer average bond lengths (Table 4) were observed. In summary, the distribution of Na^+ and Y^{3+} at the 1f sites has a significant influence on the position of both the 3j and 3k F^- and thereby has a profound impact on the coordination sphere of Ln^{3+} ions at both the 1a and 1f sites.

Occupational disorder, 2h site. Encompassing all structural variations that were generated by the Na^+ configurations at the disordered 2h sites in a 2 × 2 × 4 supercell is neither practical nor particularly informative. Instead, 3 different 2h-disordered structures of configuration 10 were created and optimised to gain a first insight into this type of disorder. The results of this approach are presented in Table 6A. Note that by introducing the 2h disorder, the six-fold degeneracy of configuration 10 (as shown in the second column of Table 1) is lifted, increasing the number of 2h disordered configurations from 6 to 384 (64 × 6; though, some of these are symmetry equivalent). To limit the computational demand and since preliminary results indicated that the 2h disorder had less influence on the crystal structure than the 1f disorder, only these three configurations were investigated.

Table 6 Comparison of lattice energies relative to configuration 10 (ΔE), deviations of the lattice parameters (Dev.$_{LP}$), and bond lengths (Y^{3+}–F^-) for different Na^+ distributions (NaX) at the 2h sites of configuration 10 for undoped (A) and Er^{3+}-doped (B) β-$NaYF_4$

NaX	ΔE (kJ mol^{-1})	Dev.$_{LP}$ (%)	Y^3–F^- (Å)
A	**β-$NaYF_4$**		
Na1	0.0	0.77	2.338
Na2	0.1	0.79	2.334
Na3	1.4	0.81	2.332
B	**β-$NaYF_4$: 4.2% Er^{3+}**		
Na1	0.0	0.76	2.338
Na2	0.8	0.82	2.334
Na3	1.7	0.93	2.330

Changing the disorder at the 2h sites randomly but c-axis balanced (Na1 to Na2) resulted in rather insignificant changes in the lattice energy of 0.1 kJ mol^{-1}. Even aligning all Na^+ closest to the central ion towards one direction (Na3) increased the lattice energy by only 1.4 kJ mol^{-1}. These values are smaller than most energy difference observed when changing the occupation of Na^+ and Y^{3+} at the 1f-disordered sites (third column of Table 3). Deviations of the lattice parameters and average bond lengths were more pronounced, although still small when considering the significant changes observed from the 1f disorder. A noteworthy change induced by the 2h disorder is the observed reduction of individual Y^{3+}–F^- bond lengths of up to 0.05 Å when a 2h Na^+ is very close to or aligning with the central 1f site along the *c*-axis (compared to a structure where it is placed much further away). The corresponding 3k F^- in between the 2h Na^+ and the 1f site is thereby pushed closer to the 1f site by the 2h Na^+. Overall, the influence of the Na^+ at the 2h sites onto the F^- very much resembles that of Na^+ and Y^{3+} at the 1f sites. In both cases, the closest F^- is pushed away from its ideal position. Therefore, disorder at 2h sites might not have as much of an impact on the overall crystal structure but great local influence on the positions of specific F^-. With small energetic differences between individual distributions of Na^+ at 2h sites, a high prevalence of different arrangements can be expected. At the same time, the presumably significantly lower energy barrier for the rearrangement of 2h Na^+ (no ion swapping is required in this case) is probably also connected to a higher degree of variation for this disordered site.[40,53]

Ln^{3+}-doping induced disorder (Ln = Er, Tm, and Yb). The above discussion of the individual configurations of undoped β-$NaYF_4$ also applies largely to the doped versions of these configurations. As for the undoped lattice, configuration 10 was the energetically most stable one, irrespective of the Ln^{3+} dopant (Table S1†). It must be kept in mind though, that upon doping, configuration 10 is no longer identical to configuration 1 due to the exchange of one Y^{3+} by an Ln^{3+} at two differing positions in the supercell. The data obtained for configuration 1 and 10 (Table S1†) suggest that doping at the 1a site was minimally more favourable than at the 1f site ($\Delta E \approx$ 0.1 kJ mol^{-1}) for all three dopants. This is at odds with what Park *et al.* found in their study, reporting a stabilisation of approximately 1, 2, and 4 kJ mol^{-1} for Er^{3+}, Tm^{3+}, and Yb^{3+}, respectively, for doping at the 1f site (no exact values were given, and they were instead estimated from a figure provided in the publication).[52] Although the authors used a different methodology, model, and doping concentration, there is no apparent explanation for this discrepancy. Experimental measurements point to an equal occupation of the two sites (*i.e.*, 1a and 1f), inferring a rather small energetic difference, which supports our results.[27] Homologous to the undoped configurations, the doped versions were found to prefer configurations where Na^+ and Y^{3+} alternate regularly and no local clusters of either ion (configurations 7 to 13) are formed. Lattice energies and bond lengths for the doped configurations also mimicked their undoped counterparts as shown for configuration 10 in Table S1† and Table 7, respectively. Especially the reduction of bond lengths due to the lanthanide contraction was not as pronounced for two of the three investigated Ln^{3+} as observed in an earlier study.[49] A reduction of about 2.6% was observed for Yb^{3+}, compared to an expected value of 3.3%. Though, for Er^{3+} and Tm^{3+} almost no change was observed. A possible reason for this might be the almost identical ionic sizes of Er^{3+} and Tm^{3+}, compared to Y^{3+}, and the low doping percentage. Furthermore, when doping Er^{3+} into the three configurations with different 2h disorder (Table 6B), differences were overall minor. Changes from configuration to configuration were small and mostly followed the ones described for the undoped crystal.

Considering these results, for structures with a low doping concentration, the intrinsic disorder induced by the lattice itself seems to be far more influential than the disorder induced by the dopant ion. These findings contradict the statements of an earlier experimental study, which assumed severe structural changes induced by doping and how these changes explain why $P6_3/m$ is the more appropriate space group for β-$NaYF_4$.[42] While we do not argue whether $P6_3/m$ or $P\bar{6}$ is the more accurate designation, we would like to emphasise that the results obtained from the present study do not support the previously made hypothesis. Instead of arguing that doping will distort the lattice and thereby create different local environments for the dopant, it seems more appropriate that different dopant sites are created through the occupational

Table 7 Comparison of lattice energies relative to configuration 10 (ΔE), deviations of the lattice parameters (Dev.$_{LP}$), and bond lengths (Y^{3+}–F^-) of configuration 10 for β-$NaYF_4$ doped with Er^{3+} (DZVP and TZV2P), Tm^{3+}, or Yb^{3+}

Ln^{3+}	ΔE (kJ mol^{-1})	Dev.$_{LP}$ (%)	Y^{3+}–F^- (Å)
	β-$NaYF_4$: 4.2% Ln^{3+}		
—	—	0.77	2.338
Er^{3+}	0.00	0.76	2.338
Er^{3+}_{TZV2P}	−0.12	0.76	2.338
Tm^{3+}	—	0.76	2.338
Yb^{3+}	—	0.77	2.333

disorder of the lattice, and at these sites, ions can be doped into. This should be true for both space groups discussed for β-$NaYF_4$ but also α-$NaYF_4$ and related compounds. The earlier report even provides evidence for this explanation as it demonstrated that the local surrounding of the dopants does not change when increasing the dopant concentration from 0.5 to 20 mol%.

Lastly, one additional calculation for Er^{3+}-doped β-$NaYF_4$ in configuration 10 was conducted in which the basis set for Er^{3+} was expanded (TZV2P). This calculation was repeated with all other parameters kept constant. In principle, increasing the size of the basis set is expected to improve the reliability of the obtained results (on the expense of an increased computational demand). Compared to the results obtained with the smaller DZVP basis set, increasing the basis set reduced the energy of the supercell by 0.12 kJ mol^{-1}, and influenced the lattice parameters as well as the average positions of the nine F^- by about 0.1% (Table 7). Note that different to all other tables the reference value for ΔE in this table was not the lowest value displayed (*i.e.*, the TZV2P value) but the one from the DZVP calculation for better comparison with the energetic differences for the other Er^{3+}-doped configurations (*i.e.*, Table 4, Table S1† and Table 6). Hence, there was no indication that the overall trends observed will significantly change when recalculating all doped structures with this larger basis set on Ln^{3+}.

From infinite and defect-free computational crystal structures to nanoscale materials: potentials and limitations

While results obtained from computational studies undoubtedly provide valuable insights, their direct applicability to the properties of experimentally obtained (nano)materials may remain uncertain as a computational model always comes with inherent simplifications and assumptions not necessarily transferable to real life. This indeed holds also true for the here presented study. Hence, in light of this, the following considerations, including potential and limitations of the presented model, shall be kept in mind.

It is important to acknowledge that the synthesis of nanoparticles (but also bulk materials) inevitably induces a plethora of defects within the lattice and at the material's surface. In case of upconverting nanoparticles, these defects can influence the structural properties of the host material as well as the optical properties of the dopants.[80] Such deviations from the perfectly ordered, infinitely repeating unit cell that forms the basis of the computational approach become especially relevant for nanoparticles with their small volume-to-surface ratio. With a large share of unit cells close to the surface, lattice defects, dangling bonds, and the nanoparticle's environment become more and more relevant as particle size decreases. This constitutes a limitation of the model designed for this (and other) computational study as such surface effects cannot be easily assessed.

Most studies in the literature focus on the upconverting ions doped into inorganic host crystals. Conversely, the focus of this study explicitly lays on the lattice structure of the examined crystals and its disorder. Other groups computationally predicted the properties of dopant ions in crystals such as α- and β-$NaYF_4$.[28,49,52,81–84] Indeed, some of these studies appreciate differently induced disorder, yet, typically at a more shallow level. In most of these computational approaches, surface effects and transferability to the nanoscale remain unaddressed – an open question to be tackled in future works by the community.

A key challenge when setting up appropriate computational models is that defects are not necessarily distributed homogeneously across a nanoparticle but tend to accumulate near the surface.[85] On the other hand, the larger a nanoparticle the larger its portion that is sufficiently far away from the surface so that close-to-bulk properties may be assumed.[86] We would therefore argue that – except for the smallest nanoparticles – the chosen configurations become representative for most parts of a nanoparticle.

With these aspects in mind, the presented calculations are foreseen to act as stepping stone towards more realistic modelling at the nanoscale. While our model may still be closer to the bulk material than to a nanoparticle, it is arguably closer to the latter than the computational models previously designed. This is due to the fact that it incorporates disorder on a level much closer to experimentally obtained materials. Nevertheless, it is important to acknowledge that future work will have to consider effects of surface, disorder, and defects on the structure in general and dopant properties in particular at the nanoscale.

Conclusions

In this study, the atomistic structure of two model systems for photon upconverting crystals were investigated with density functional theory, namely the ordered crystal structure of $LiYF_4$ and the disordered structure of β-$NaYF_4$. Undoped as well as Er^{3+}-, Tm^{3+}-, or Yb^{3+}-doped crystals were created in the developed model, and the relative stability of different disordered atomistic arrangements was investigated. Results obtained from these systems were compared to already existing data when available to validate the model. Furthermore, new data were generated to answer questions about the effect of occupational disorder and disorder induced *via* doping into the crystal structure.

The results of this study can be best evaluated by dividing them into four categories. First, it was demonstrated that the chosen methodology (DFT with periodic boundary conditions) and programme (CP2K) are well suited for predicting atomistic properties of an ordered inorganic crystal structure, such as $LiYF_4$. We then verified the suitability of this model to predict crystal structures and to examine local variations for a disordered crystal, namely β-$NaYF_4$. Second, a rational for creating such a model was provided. It was found that a sufficiently large supercell of the crystal must be created, and a significant although not too extensive number of configurations must be assessed. These configurations must be chosen wisely so that

each represents one possible and ideally highly likely distribution of ions in the disordered lattice. Third, in the case of β-$NaYF_4$, three potential sources of variations within the crystal were examined: disordered 1f sites, disordered 2h sites, and disorder induced through doping with Er^{3+}, Tm^{3+}, or Yb^{3+}. Of these three possible sources of disorder, disordered 1f and 2h sites were identified as those that most significantly influence the positions of the F^- ions around potential doping sites. While changes at 1f sites seemed to be more relevant than those at 2h sites, both were found to be much more important than changes introduced by low-concentration doping. In general, low-percentage doping does not appear to be a significant source of distortion for these crystal structures. Forth and finally, assumptions of earlier studies focusing on the 1f disorder (alternating rows of Na^+ and Y^{3+}) were mostly confirmed but more importantly also refined. After all, the X-ray structural information of β-$NaYF_4$ is in line with the results of our protocol (once averaged over the different configurations) and the crystal structure should be considered as being significantly disordered.

In summary, this study showed the high likelihood that the β-$NaXF_4$ (X = lanthanides plus yttrium) crystal family is best described as consisting of a variety of unit cells, all with differing configurations of the ionic positions. The knowledge gained about the local variations of ions around potential doping sites can act as stepping stone for future studies to more accurately predict properties such as energy levels and energy gaps of individual Ln^{3+} or oscillator strengths and energy transfer rates between pairs of dopants in these crystals. Ultimately, this may lead to the design of next-generation upconverting nanoparticles overcoming current limitations such as low quantum yield.

Author contributions

Chris Steve Conrad: investigation, formal analysis, writing – original draft, conceptualization (general project, approach, model setup), funding acquisition; Holger Euchner: investigation, conceptualisation (theoretical approach), writing – review and editing; Eva Hemmer: conceptualisation (underlying goal and compound selection), writing – review and editing, supervision; Reinhold F. Fink: conceptualisation (approach, model setup), writing – review and editing, supervision, funding, resources.

Data availability

The optimised crystal structures of $LiYF_4$ and of configuration 10 of undoped β-$NaYF_4$ are provided in the ESI.† All other are available from the authors upon request or at **https://doi.org/10.6084/m9.figshare.27846741.v1**.

Conflicts of interest

There are no conflicts to declare.

Acknowledgements

CSC is grateful for a scholarship by Friedrich-Ebert-Stiftung and support from MITACS. CSC and RFF acknowledge support by the state of Baden-Württemberg through bwHPC and the German Research Foundation (DFG) through grant no INST 40/575-1 FUGG (JUSTUS 2 cluster). EH acknowledges the Natural Sciences and Engineering Research Council of Canada (NSERC RGPIN-2023-03985). Images shown in the ToC figure were partially made in BioRender (**https://www.biorender.com**).

References

1 F. Auzel, *C. R. Acad. Sci.*, 1966, **262**, 1016.
2 F. Auzel, *C. R. Acad. Sci.*, 1966, **263**, 819.
3 F. Auzel, *Chem. Rev.*, 2004, **104**, 139–174.
4 S. Heer, O. Lehmann, M. Haase and H.-U. Güdel, *Angew. Chem., Int. Ed.*, 2003, **42**, 3179–3182.
5 M. Haase and H. Schäfer, *Angew. Chem., Int. Ed.*, 2011, **50**, 5808–5829.
6 S. Qiao, R. Pu, X. Guo, Y. Ni, C. Wu, B. Wang, Y. Du, J. Huang, K. Zheng, W. Wei and Q. Zhan, *ACS Appl. Nano Mater.*, 2024, **7**, 12795–12805.
7 R. S. Ajee, P. S. Roy, S. Dey and S. Sundaresan, *J. Nanopart. Res.*, 2024, **26**, 50.
8 S. Varghese, A. S. Madanan, M. K. Abraham, A. I. Shkhair, G. Indongo, G. Rajeevan, B. K. Arathy and S. George, *Microchem. J.*, 2024, **206**, 111539.
9 M. Liu, J. Liang and F. Vetrone, *Acc. Chem. Res.*, 2024, **57**, 2653–2664.
10 J. Y. Jung, J. Y. Park and H. K. Yang, *Adv. Opt. Mater.*, 2024, **12**, 2401210.
11 Z. Fan, Y. Shao, X. Jiang, J. Zhou, L. Yang, H. Chen and W. Liu, *Int. J. Biol. Macromol.*, 2024, **278**, 134187.
12 Y. Yang, K. Q. Long, Y. X. Chu, H. P. Lu, W. P. Wang and C. Y. Zhan, *Adv. Funct. Mater.*, 2024, **34**, 2402975.
13 Y. Jiang, Y. Hong, Y.-Y. Liu, Y. Guan, J. Zhou, H. Wang and L. Sun, *J. Mater. Chem. C*, 2024, **12**, 11938–11947.
14 C. Xu, S. K. Law and A. W. N. Leung, *Pharmaceuticals*, 2024, **17**, 663.
15 M. Hosseinifard, N. Jurga, J. C. Brandmeier, Z. Farka, A. Hlaváček, H. H. Gorris, T. Grzyb and A. Ekner-Grzyb, *Chemosphere*, 2024, **347**, 140629.
16 J. Yu, H. Yu, L. Li, X. Ni, K. Song and L. Wang, *ChemNanoMat*, 2021, **7**, 859–872.
17 A. Alotaibi, F. Alsardi, F. Alshwikhat, M. Aldossary, F. S. Almarwani, F. J. Talidi, S. A. Almenhali, S. F. Almotawa, Y. A. Alzahrani, S. Alenzi, A. Alanazi and M. Alkahtani, *Molecules*, 2024, **29**, 2556.
18 W. Zhang, W. Zheng, P. Huang, D. Yang, Z. Shao and X. Chen, *Aggregate*, 2024, **5**, e558.
19 N. Dubey and S. Chandra, *J. Rare Earths*, 2022, **40**, 1343–1359.
20 A. A. Ansari, M. A. M. Khan, B. P. Singh and A. K. Parchur, *J. Mater. Sci.: Mater. Electron.*, 2023, **34**, 1625.

21 S. Mohanty and A. M. Kaczmarek, *Chem. Soc. Rev.*, 2022, **51**, 6893–6908.
22 X. Xia, E. Sivonxay, B. A. Helms, S. M. Blau and E. M. Chan, *Nano Lett.*, 2023, **23**, 11129–11136.
23 F. Li, L. Tu, Y. Zhang, D. Huang, X. Liu, X. Zhang, J. Du, R. Fan, C. Yang, K. W. Krämer, J. Marques-Hueso and G. Chen, *Nat. Photonics*, 2024, **18**, 440–449.
24 C. K. J. Renata Reisfeld, *Lasers and Excited States of Rare Earths*, Springer-Verlag, Berlin Heidelberg New York, 1977.
25 R. Renata, *AIMS Mater. Sci.*, 2015, **2**, 37–60.
26 W. T. Carnall, in *Handbook on the Physics and Chemistry of Rare Earths*, ed. K. A. Gschneidner and L. Eyring, North-Holland Publishing Company, Amsterdam, 1979, vol. 3, ch. 24, p. 171–208.
27 A. Aebischer, M. Hostettler, J. Hauser, K. Krämer, T. Weber, H. U. Güdel and H.-B. Bürgi, *Angew. Chem., Int. Ed.*, 2006, **45**, 2802–2806.
28 A. Platonenko and A. I. Popov, *Opt. Mater.*, 2020, **99**, 109529.
29 X. Zhu, J. Zhang, J. Liu and Y. Zhang, *Adv. Sci.*, 2019, **6**, 1901358.
30 Y. Wu, M. J. Y. Ang, M. Sun, B. Huang and X. Liu, *J. Phys. D: Appl. Phys.*, 2019, **52**, 383002.
31 R. Shannon, *Acta Crystallogr., Sect. A*, 1976, **32**, 751–767.
32 I. Halimi, E. M. Rodrigues, S. L. Maurizio, H.-Q. T. Sun, M. Grewal, E. M. Boase, N. Liu, R. Marin and E. Hemmer, *J. Mater. Chem. C*, 2019, **7**, 15364–15374.
33 C. Homann, N. Liu, H. Barbosa and E. Hemmer, in *Handbook on the Physics and Chemistry of Rare Earths*, ed. J.-C. G. Bünzli and S. M. Kauzlarich, Elsevier, 2024, vol. 65, pp. 137–212.
34 J. F. Suyver, J. Grimm, M. K. van Veen, D. Biner, K. W. Krämer and H. U. Güdel, *J. Lumin.*, 2006, **117**, 1–12.
35 C. Renero-Lecuna, R. Martín-Rodríguez, R. Valiente, J. González, F. Rodríguez, K. W. Krämer and H. U. Güdel, *Chem. Mater.*, 2011, **23**, 3442–3448.
36 D. Pominova, V. Proydakova, I. Romanishkin, S. Kuznetsov, K. Linkov, N. Tabachkova and A. Ryabova, *Photonics*, 2024, **11**, 38.
37 S. Han, R. Deng, X. Xie and X. Liu, *Angew. Chem., Int. Ed.*, 2014, **53**, 11702–11715.
38 L. D. DeLoach, S. A. Payne, L. L. Chase, L. K. Smith, W. L. Kway and W. F. Krupke, *IEEE J. Quantum Electron.*, 1993, **29**, 1179–1191.
39 G. Blasse and B. C. Grabmaier, *Luminescent Materials*, Springer, Berlin, 1994, pp. 123.
40 R. Shi, C. D. S. Brites and L. D. Carlos, *Nanoscale*, 2021, **13**, 19771–19782.
41 P. Pandey, S. D. Kaushik, P. Rajput, M. N. Singh, R. K. Sharma and S. Giri, *Nanoscale*, 2025, **17**, 2269–2280.
42 D. Tu, Y. Liu, H. Zhu, R. Li, L. Liu and X. Chen, *Angew. Chem., Int. Ed.*, 2013, **52**, 1128–1133.
43 J. H. Burns, *Inorg. Chem.*, 1965, **4**, 881–886.
44 R. E. Thoma, H. Insley and G. M. Hebert, *Inorg. Chem.*, 1966, **5**, 1222–1229.
45 D. M. Roy and R. Roy, *J. Electrochem. Soc.*, 1964, **111**, 421.
46 K. W. Krämer, D. Biner, G. Frei, H. U. Güdel, M. P. Hehlen and S. R. Lüthi, *Chem. Mater.*, 2004, **16**, 1244–1251.
47 A. A. Bunaciu, E. G. Udriștioiu and H. Y. Aboul-Enein, *Crit. Rev. Anal. Chem.*, 2015, **45**, 289–299.
48 G. Yao, M. T. Berry, P. S. May and D. S. Kilin, *Int. J. Quantum Chem.*, 2012, **112**, 3889–3895.
49 G. Yao, M. T. Berry, P. S. May and D. Kilin, *J. Phys. Chem. C*, 2013, **117**, 17177–17185.
50 G. Yao, M. Berry, P. S. May, J. Wang and D. S. Kilin, *J. Phys. Chem. C*, 2016, **120**, 7785–7794.
51 F. Wang, Y. Han, C. S. Lim, Y. Lu, J. Wang, J. Xu, H. Chen, C. Zhang, M. Hong and X. Liu, *Nature*, 2010, **463**, 1061–1065.
52 K.-W. Park, H. S. Jang and S.-H. Cho, *Mater. Chem. Phys.*, 2022, **275**, 125317.
53 B. Szefczyk, R. Roszak and S. Roszak, *RSC Adv.*, 2014, **4**, 22526–22535.
54 B. Huang, H. Dong, K.-L. Wong, L.-D. Sun and C.-H. Yan, *J. Phys. Chem. C*, 2016, **120**, 18858–18870.
55 B. P. Sobolev, D. A. Mineev and V. Pashutin, *Dokl. Akad. Nauk SSSR*, 1963, **150**, 791–794.
56 A. Grzechnik and K. Friese, *Dalton Trans.*, 2012, **41**, 10258–10266.
57 R. E. Thoma, C. F. Weaver, H. A. Friedman, H. Insley, L. A. Harris and H. A. Yakel Jr, *J. Phys. Chem.*, 1961, **65**, 1096–1099.
58 V. T. Vera, D. Mendez-Gonzalez, D. J. Ramos-Ramos, A. Igalla, M. Laurenti, R. Contreras-Caceres, E. Lopez-Cabarcos, E. Díaz, J. Rubio-Retama, S. Melle and O. G. Calderón, *J. Mater. Chem. C*, 2021, **9**, 8902–8911.
59 R. Joshi, R. S. Perala, S. B. Shelar, A. Ballal, B. P. Singh and R. S. Ningthoujam, *ACS Appl. Mater. Interfaces*, 2021, **13**, 3481–3490.
60 J. Hutter, M. Iannuzzi, F. Schiffmann and J. VandeVondele, *Wiley Interdiscip. Rev.:Comput. Mol. Sci.*, 2014, **4**, 15–25.
61 G. Lippert, J. Hutter and M. Parrinello, *Mol. Phys.*, 1997, **92**, 477–488.
62 J. VandeVondele, M. Krack, F. Mohamed, M. Parrinello, T. Chassaing and J. Hutter, *Comput. Phys. Commun.*, 2005, **167**, 103–128.
63 J. Vande Vondele and J. Hutter, *J. Chem. Phys.*, 2003, **118**, 4365–4369.
64 J. VandeVondele and J. Hutter, *J. Chem. Phys.*, 2007, **127**, 114105.
65 S. Goedecker, M. Teter and J. Hutter, *Phys. Rev. B:Condens. Matter Mater. Phys.*, 1996, **54**, 1703–1710.
66 J. P. Perdew, K. Burke and M. Ernzerhof, *Phys. Rev. Lett.*, 1996, **77**, 3865–3868.
67 S. Grimme, J. Antony, S. Ehrlich and H. Krieg, *J. Chem. Phys.*, 2010, **132**, 154104.
68 K. Momma and F. Izumi, *J. Appl. Crystallogr.*, 2011, **44**, 1272–1276.
69 C. Keller and H. Schmutz, *J. Inorg. Nucl. Chem.*, 1965, **27**, 900–901.
70 W. Y. Ching, Y.-N. Xu and B. K. Brickeen, *Phys. Rev. B: Condens. Matter Mater. Phys.*, 2001, **63**, 115101.

71 M. V. Luong, M. J. F. Empizo, J. L. F. Gabayno, Y. Minami, K. Yamanoi, T. Shimizu, N. Sarukura, M. H. Pham, H. D. Nguyen, K. G. Steenbergen, P. Schwerdtfeger and M. Cadatal-Raduban, *Comput. Mater. Sci.*, 2018, **153**, 431–437.
72 E. Garcia and R. R. Ryan, *Acta Crystallogr., Sect. C:Cryst. Struct. Commun.*, 1993, **49**, 2053–2054.
73 J. Yin, Q. Zhang, T. Liu, X. Guo, M. Song, X. Wang and H. Zhang, *Nucl. Instrum. Methods Phys. Res., Sect. B*, 2009, **267**, 74–78.
74 S. Li, R. Ahuja and B. Johansson, *J. Phys.: Condens. Matter*, 2004, **16**, 983.
75 J. P. Perdew, *Phys. Rev. B:Condens. Matter Mater. Phys.*, 1986, **33**, 8822–8824.
76 R. Moncorgé, in *Ultraviolet Spectroscopy and UV Lasers*, ed. M. A. D. P. Misra, Marcel Dekker Inc., New York, Basel, 2005, pp. 337–370.
77 Á. Morales-García, R. Valero and F. Illas, *J. Phys. Chem. C*, 2017, **121**, 18862–18866.
78 K. Chong, T. Hirai, T. Kawai, S. Hashimoto and N. Ohno, *J. Lumin.*, 2007, **122–123**, 149–151.
79 H. Sato and R. Kikuchi, *J. Chem. Phys.*, 1971, **55**, 677–702.
80 P. Rudolph, *Prog. Cryst. Growth Charact. Mater.*, 2016, **62**, 89–110.
81 Y. Han, D. J. Vogel, T. M. Inerbaev, P. S. May, M. T. Berry and D. S. Kilin, *Mol. Phys.*, 2018, **116**, 697–707.
82 C. M. S. Calado, Í.F Manali, I. M. S. Diogenis, S. F. N. Coelho, V. C. Teixeira, B. R. de Mesquita, J. L. Oliveira, F. A. Sigoli and M. V. D. S. Rezende, *Opt. Mater.*, 2023, **137**, 113529.
83 X. Qin and X. Liu, *Nanoscale*, 2021, **13**, 19561–19567.
84 X. Qin, L. Shen, L. Liang, S. Han, Z. Yi and X. Liu, *J. Phys. Chem. C*, 2019, **123**, 11151–11161.
85 G. Tessitore, G. A. Mandl, M. G. Brik, W. Park and J. A. Capobianco, *Nanoscale*, 2019, **11**, 12015–12029.
86 M. Quintanilla, E. Hemmer, J. Marques-Hueso, S. Rohani, G. Lucchini, M. Wang, R. R. Zamani, V. Roddatis, A. Speghini, B. S. Richards and F. Vetrone, *Nanoscale*, 2022, **14**, 1492–1504.

Electronic Supplementary Information (ESI)

The true atomistic structure of a disordered crystal: A computational study on the photon upconverting material β-$NaYF_4$ and its Er^{3+}-, Tm^{3+}-, and Yb^{3+}-doped derivates

Chris Steve Conrad,[a,b] Holger Euchner,[a] Eva Hemmer,[b,*] Reinhold F. Fink[a,*]

[a] Institute of Physical and Theoretical Chemistry, University of Tübingen, Tübingen (Baden-Württemberg), Germany.

[b] Department of Chemistry and Biomolecular Sciences, University of Ottawa, Ottawa (Ontario), Canada.

* Corresponding Authors E-mail:

Reinhold.fink@uni-tuebingen.de

ehemmer@uottawa.ca

Table of Contents

1 β-$NaYF_4$ 2x2x2 Supercell

To accurately represent the influence of the cation disorder on the F^- sites (and thereby on the potential cationic doping sites), initially, a 2x2x2 supercell of β-$NaYF_4$ was created. The structures shown in Figure S1 represent such a supercell with one possible Na^+/Y^{3+} distribution at the 1f sites.

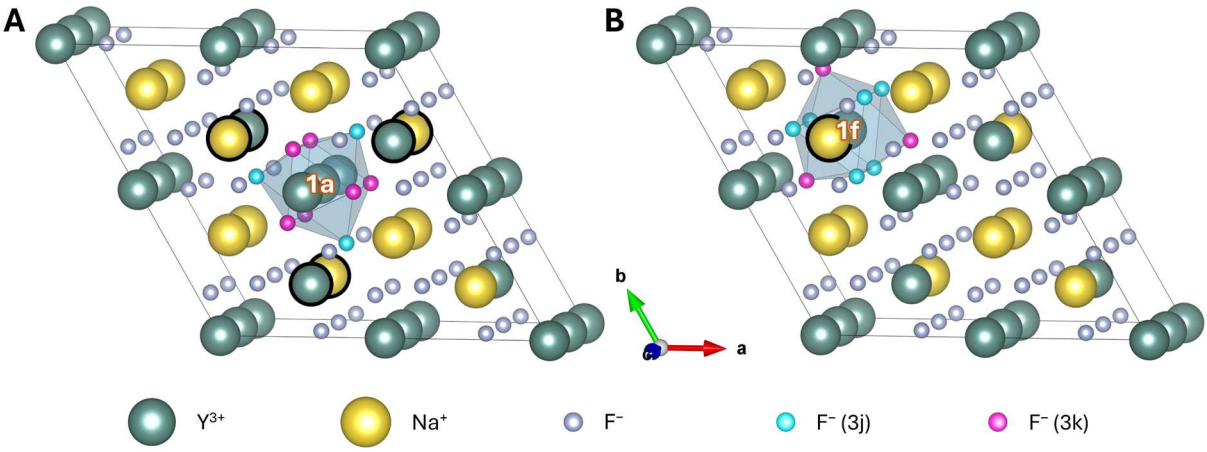

Figure S1. 2x2x2 supercell of β-$NaYF_4$ with the composition $Na_{12}Y_{12}F_{48}$. Highlighted are a potential (A) 1a and (B) 1f doping site (white labels), and their first anionic (F^- ions of the blue prism that are highlighted in cyan and pink) as well as cationic (Na^+ and Y^{3+} ions marked with a thick black line) coordination spheres.

This distribution is very similar to the one reported to be the most probable based on experimentally derived X-ray diffraction patterns. However, in this work, we aim to address structural disorder, which means that all possible surroundings of each Y^{3+} ion (potential Ln^{3+} doping site) should be represented by configurations. The 2x2x2 supercell is not large enough to represent all possible (and required) Na^+/Y^{3+} distributions at the 1f sites. Specifically, for the 1f doping site (Figure S1B), the positions of the six 3j F^- are heavily influenced by the two neighbouring 1f cations along the c-axis. For the 2x2x2 supercell shown, this means that, due to the periodic boundary conditions, the Y^{3+} at the 1f site has two Na^+ as neighbouring ions along the c-axis. When creating a second configuration of this supercell by exchanging Na^+ for Y^{3+} at this neighbouring 1f site, both neighbouring ions will correspond to Y^{3+}. To instead account for such configurations in which one neighbouring cation is Na^+ and the other is Y^{3+}, at least a 2x2x4 supercell is required (Figure 2B).

As for the 1f site, similar considerations made for the 1a site (Figure S1A) required a 2x2x4 supercell (Figure 2A). The reason for this is that three of the nine F^- around the 1a site are located at 3j sites (Figure 1B). Each of these three sites is considerably influenced by the distribution of Na^+ and Y^{3+} within a set of two closest 1f sites (large black circles in Figure S1A). In a 2x2x2 supercell eight such 1f sites exist, and the composition of the crystal remains stoichiometrically correct only if exactly four of these are occupied by Na^+ and the other four by Y^{3+}. If instead six or five of the closest 1f sites are to be of the same type, additional 1f positions must be created to counterbalance the above average occurrence of either Na^+ or Y^{3+}. In a 2x2x4 supercell, a total of 16 1f sites are available. By manipulating the12 1f sites closest to the central site, all required configurations could be created without changing the stoichiometric ratio of the crystal.

2 $LiYF_4$ 3x3x1 Supercell

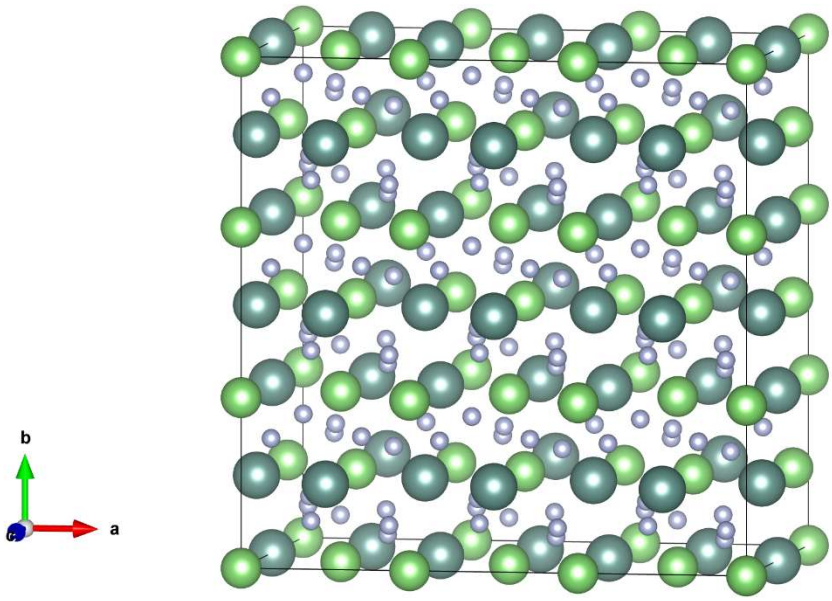

Figure S2. 3x3x1 supercell of $LiYF_4$ with the composition $Li_{36}Y_{36}F_{144}$. Dark green spheres represent Y^{3+}, light green spheres Li^+, and small grey spheres F^-.

3 Additional Structural Parameters for β-$NaYF_4$ doped with Er^{3+}, Tm^{3+}, and Yb^{3+}

Table S1. Results of the structural optimisations for three times 16 different configurations of doped β-$NaYF_4$. For the configurations doped with 4.2 % Er^{3+}, Tm^{3+}, or Yb^{3+} lattice energies relative to the most stable configuration of the respective column (ΔE) and deviations of the lattice parameters from the experimental values ($Dev._{LP}$) are being displayed.

		4.2 % Er^{3+}		**4.2 % Tm^{3+}**		**4.2 % Yb^{3+}**	
Site	Config.	ΔE ($kJ \cdot mol^{-1}$)	$Dev._{LP}$ (%)	ΔE ($kJ \cdot mol^{-1}$)	$Dev._{LP}$ (%)	ΔE ($kJ \cdot mol^{-1}$)	$Dev._{LP}$ (%)
1f	1	0.1	0.77	0.2	0.77	0.1	0.76
	2	2.4	0.83	2.2	0.83	1.9	0.83
	3	3.4	0.90	3.4	0.90	3.3	0.91
1a	4	6.5	0.78	6.6	0.78	6.5	0.78
	5	4.6	0.85	4.9	0.86	4.6	0.86
	6	3.4	0.88	4.1	0.91	3.9	0.88
	7	1.8	0.89	2.2	0.89	1.9	0.90
	8	1.8	0.92	2.0	0.92	1.8	0.93
	9	1.2	0.86	1.3	0.86	1.2	0.85
	10	0.0	0.76	0.0	0.76	0.0	0.77
	11	1.6	0.86	2.9	0.87	2.5	0.88
	12	1.9	0.92	2.2	0.92	1.7	0.93
	13	2.3	0.86	1.9	0.86	1.9	0.88
	14	4.8	0.88	4.7	0.89	4.7	0.91
	15	4.2	0.84	4.5	0.85	4.0	0.85
	16	8.3	0.76	7.4	0.76	7.7	0.79

4 $LiYF_4$ Input File

```
&GLOBAL
 RUN_TYPE  CELL_OPT
 PROJECT_NAME LiYF4-Blank
 PRINT_LEVEL LOW
&END GLOBAL
&MOTION
 &GEO_OPT
  OPTIMIZER  LBFGS
  MAX_ITER  500
  STEP_START_VAL  1
 &END GEO_OPT
 &CELL_OPT
  TYPE  DIRECT_CELL_OPT
  OPTIMIZER  LBFGS
  MAX_ITER  500
  STEP_START_VAL  1
 &END CELL_OPT
 &PRINT
  &TRAJECTORY  SILENT
   COMMON_ITERATION_LEVELS  300
   FILENAME TRAJECTORY
  &END TRAJECTORY
 &END PRINT
&END MOTION
&FORCE_EVAL
 METHOD  QS
 STRESS_TENSOR  ANALYTICAL
 &DFT
  BASIS_SET_FILE_NAME ./basissets
  POTENTIAL_FILE_NAME ./potentials
  &SCF
   MAX_SCF  500
   EPS_SCF    9.9999999999999995E-07
   SCF_GUESS  ATOMIC
   ADDED_MOS  150
   &DIAGONALIZATION  T
   &END DIAGONALIZATION
   &SMEAR  T
    METHOD  FERMI_DIRAC
   &END SMEAR
   &MIXING  T
    METHOD  DIRECT_P_MIXING
   &END MIXING
  &END SCF
  &MGRID
   CUTOFF    8.0000000000000000E+02
   REL_CUTOFF    6.0000000000000000E+01
  &END MGRID
  &XC
   DENSITY_CUTOFF    1.0000000000000000E-10
   GRADIENT_CUTOFF    1.0000000000000000E-10
   TAU_CUTOFF    1.0000000000000000E-10
   &XC_FUNCTIONAL  NO_SHORTCUT
    &PBE  T
    &END PBE
   &END XC_FUNCTIONAL
   &VDW_POTENTIAL
    POTENTIAL_TYPE  PAIR_POTENTIAL
    &PAIR_POTENTIAL
     R_CUTOFF    5.0200000000000003E+01
```

```
      TYPE  DFTD3
      PARAMETER_FILE_NAME dftd3.dat
      REFERENCE_FUNCTIONAL PBE
     &END PAIR_POTENTIAL
    &END VDW_POTENTIAL
   &END XC
   &KPOINTS
    SCHEME MONKHORST-PACK 2 2 3
   &END KPOINTS
   &PRINT
    &MO on
     EIGENVALUES
     &EACH
      QS_SCF 0
     &END EACH
    &END MO
   &END PRINT
  &END DFT
  &SUBSYS
   &CELL
    A  1.5644593877023894E+001  0.0000000000000000E+000  0.0000000000000000E+000
    B  3.0751337049354889E-008  1.5644593901750460E+001  0.0000000000000000E+000
    C  1.8303734203235855E-008 -1.6648299085864796E-008  1.0796010118000813E+001
    PERIODIC  XYZ
    MULTIPLE_UNIT_CELL  1 1 1
   &END CELL
   &COORD
!coordinates from crystal structure
   &END COORD
   &KIND Li
    BASIS_SET ORB TZV2P-MOLOPT-SR-GTH
    ELEMENT Li
    POTENTIAL GTH-PBE
   &END KIND
   &KIND Y
    BASIS_SET ORB TZV2P-MOLOPT-SR-GTH
    ELEMENT Y
    POTENTIAL GTH-PBE
   &END KIND
   &KIND F
    BASIS_SET ORB TZV2P-MOLOPT-GTH
    ELEMENT F
    POTENTIAL GTH-PBE
   &END KIND
   &TOPOLOGY
    NUMBER_OF_ATOMS  216
    MULTIPLE_UNIT_CELL  1 1 1
   &END TOPOLOGY
   &PRINT
    &ATOMIC_COORDINATES  SILENT
     FILENAME SUBSYS_ATOMIC_COORDINATES
    &END ATOMIC_COORDINATES
    &SYMMETRY  SILENT
     FILENAME SUBSYS_SYMMETRY
    &END SYMMETRY
   &END PRINT
  &END SUBSYS
 &END FORCE_EVAL
```

5 β-$NaYF_4$ Input File

```
&GLOBAL
  PRINT_LEVEL  MEDIUM
  PROJECT_NAME NaYF4_10-Blank
  RUN_TYPE  CELL_OPT
 &END GLOBAL
 &MOTION
  &GEO_OPT
   OPTIMIZER  LBFGS
   MAX_ITER  500
   STEP_START_VAL  1
  &END GEO_OPT
  &CELL_OPT
   OPTIMIZER  LBFGS
   MAX_ITER  500
   STEP_START_VAL  38
   TYPE  DIRECT_CELL_OPT
  &END CELL_OPT
  &PRINT
   &TRAJECTORY  SILENT
    COMMON_ITERATION_LEVELS  300
    FILENAME TRAJECTORY
   &END TRAJECTORY
  &END PRINT
 &END MOTION
 &FORCE_EVAL
  METHOD  QS
  STRESS_TENSOR  ANALYTICAL
  &DFT
   BASIS_SET_FILE_NAME ./basissets
   POTENTIAL_FILE_NAME ./potentials
   &SCF
    MAX_SCF  500
    EPS_SCF    9.9999999999999995E-07
    SCF_GUESS  ATOMIC
    ADDED_MOS  150
    &DIAGONALIZATION  T
    &END DIAGONALIZATION
    &SMEAR  T
     METHOD  FERMI_DIRAC
    &END SMEAR
    &MIXING  T
     METHOD  PULAY_MIXING
     ALPHA    5.0000000000000000E-01
     NBUFFER  15
    &END MIXING
   &END SCF
   &MGRID
    CUTOFF    8.0000000000000000E+02
    REL_CUTOFF    6.0000000000000000E+01
   &END MGRID
   &XC
    DENSITY_CUTOFF    1.0000000000000000E-10
    GRADIENT_CUTOFF    1.0000000000000000E-10
    TAU_CUTOFF    1.0000000000000000E-10
    &XC_FUNCTIONAL  NO_SHORTCUT
     &PBE  T
     &END PBE
    &END XC_FUNCTIONAL
    &VDW_POTENTIAL
     POTENTIAL_TYPE  PAIR_POTENTIAL
```

```
      &PAIR_POTENTIAL
       R_CUTOFF    5.0200000000000003E+01
       TYPE  DFTD3
       PARAMETER_FILE_NAME dftd3.dat
       REFERENCE_FUNCTIONAL PBE
      &END PAIR_POTENTIAL
     &END VDW_POTENTIAL
    &END XC
    &KPOINTS
     SCHEME MONKHORST-PACK 2 2 2
    &END KPOINTS
    &PRINT
     &MO  ON
      EIGENVALUES  T
      &EACH
       QS_SCF  0
      &END EACH
     &END MO
    &END PRINT
   &END DFT
   &SUBSYS
    &CELL
     A    1.2056455649536725E+01    0.0000000000000000E+00    0.0000000000000000E+00
     B   -5.9969696235235199E+00    1.0473148683213021E+01    0.0000000000000000E+00
     C    1.2854716280689413E-03   -2.5761615563509414E-03    1.4150780327536356E+01
     PERIODIC  XYZ
     MULTIPLE_UNIT_CELL  1 1 1
    &END CELL
    &COORD
!coordinates from crystal structure
    &END COORD
    &KIND Y
     BASIS_SET ORB TZV2P-MOLOPT-SR-GTH
     ELEMENT Y
     POTENTIAL GTH-PBE
     &POTENTIAL
 4 6 1
  0.4750000000000000E+00 2  0.1216776904000000E+02 -0.2328551030000000E+01
 3
  0.2467407000000000E+00 2  0.2345027195000000E+02 -0.8325357479999999E+01
  0.1074799029000000E+02
  0.2965639700000000E+00 2  0.5978634010000000E+01 -0.5852349640000000E+01
  0.6924593480000000E+01
  0.4504556900000000E+00 2  0.1187490480000000E+01 -0.1318673310000000E+01
  0.1495234990000000E+01
      # Potential name:  GTH-PBE  for symbol:  Y
      # Potential read from the potential filename: ./potentials
     &END POTENTIAL
    &END KIND
    &KIND Na
     BASIS_SET ORB TZV2Pd-MOLOPT-SR-GTH
     ELEMENT Na
     POTENTIAL GTH-PBE
     &POTENTIAL
 3 6
  0.2365232200000000E+00 2  0.2951049900000000E+00 -0.9138848800000000E+00
 2
  0.1435604600000000E+00 1  0.3460149228000000E+02
  0.1299322400000000E+00 1 -0.1427746168000000E+02
      # Potential name:  GTH-PBE  for symbol:  NA
      # Potential read from the potential filename: ./potentials
     &END POTENTIAL
```

```
   &END KIND
   &KIND F
    BASIS_SET ORB TZV2P-MOLOPT-GTH
    ELEMENT F
    POTENTIAL GTH-PBE
    &POTENTIAL
2 5
 0.2149295900000000E+00 2 -0.2157302836000000E+02  0.3199776150000000E+01
2
 0.1946840200000000E+00 1  0.2374354045000000E+02
 0.1861560800000000E+00 0
     # Potential name:  GTH-PBE  for symbol:  F
     # Potential read from the potential filename: ./potentials
    &END POTENTIAL
   &END KIND
   &TOPOLOGY
    NUMBER_OF_ATOMS  144
    MULTIPLE_UNIT_CELL  1 1 1
   &END TOPOLOGY
   &PRINT
    &ATOMIC_COORDINATES  SILENT
     FILENAME SUBSYS_ATOMIC_COORDINATES
    &END ATOMIC_COORDINATES
    &SYMMETRY  SILENT
     FILENAME SUBSYS_SYMMETRY
    &END SYMMETRY
   &END PRINT
  &END SUBSYS
&END FORCE_EVAL
```

6 $LiYF_4$ Optimised Structure

A 1.5590789280516516E+001 0.0000000000000000E+000 0.0000000000000000E+000
B -2.8432707705266898E-007 1.5590790987587299E+001 0.0000000000000000E+000
C 1.9155742583311419E-007 5.3049961588265117E-006 1.0796216065757379E+001

Y -4.1607352347972938E-006 1.1809756185841686E-005 5.3980910013375230E+000
Y 6.3667099915062943E-006 2.5984518899919644E+000 8.0971728531118323E+000
Y -1.2870083174417532E-005 5.1969261318730480E+000 5.3981230435123582E+000
Y 3.3282662687771921E-006 1.2992340091253741E+001 8.0971420700317740E+000
Y 1.7203327690416883E-005 1.0393851432141476E+001 5.3981331851305754E+000
Y 8.2264748823394782E-006 7.7953993056505828E+000 8.0971777075019133E+000
Y 2.5984811898045725E+000 2.5984773314046961E+000 1.6860044854635764E-005
Y 2.5984586480688932E+000 -1.2616745458689936E-005 2.6990331188062133E+000
Y 2.5984565435460789E+000 1.2992302138747354E+001 -6.8092148192635361E-006
Y 2.5984676510297811E+000 5.1969293921933835E+000 2.6990767365099830E+000
Y 2.5984655910729297E+000 7.7953818396838104E+000 1.0704473184765118E-005
Y 2.5984596667056965E+000 1.0393834314900527E+001 2.6990645563345574E+000
Y 5.1969223992334843E+000 8.7130522751939742E-006 5.3980915595330581E+000
Y 5.1969169339098267E+000 2.5984621677382553E+000 8.0971496884276899E+000
Y 5.1969482990175262E+000 5.1969394838367382E+000 5.3981102751122911E+000
Y 5.1969141616502501E+000 7.7954183240999475E+000 8.0971643962889281E+000
Y 5.1969320421950318E+000 1.2992337104925022E+001 8.0971401776973941E+000
Y 5.1969136080116298E+000 1.0393865954492828E+001 5.3981075139741304E+000
Y 7.7953809817596742E+000 1.2992325440424736E+001 1.1832391487551440E-005
Y 7.7954039134670898E+000 1.0393858532644071E+001 2.6990762559331989E+000
Y 7.7953754581786505E+000 4.6611133380840367E-006 2.6990349545563990E+000
Y 7.7953838199479257E+000 2.5984593921461698E+000 -1.3086188074244632E-005
Y 7.7953909660250966E+000 5.1969233704342352E+000 2.6990352468104972E+000
Y 7.7954149146569494E+000 7.7953856833174120E+000 -3.4534865780270547E-005
Y 1.0393829375663675E+001 2.5984732074344272E+000 8.0971547340419310E+000
Y 1.0393855576393110E+001 3.6557993507484617E-005 5.3981043398980955E+000
Y 1.0393870871444145E+001 1.2992338526226417E+001 8.0971729419064662E+000
Y 1.0393888592922343E+001 1.0393878338818357E+001 5.3981237093876784E+000
Y 1.0393853549813382E+001 5.1969240812783202E+000 5.3980962552668048E+000
Y 1.0393841545708394E+001 7.7953878163511359E+000 8.0971548495417274E+000
Y 1.2992313252664474E+001 -1.1664437386132348E-005 2.6990409086256069E+000
Y 1.2992310830541740E+001 2.5984779356181544E+000 -7.5019567628088851E-006
Y 1.2992335624611306E+001 5.1969309446580310E+000 2.6990656709648033E+000
Y 1.2992318349478776E+001 1.0393851774420511E+001 2.6990402773975184E+000
Y 1.2992340991306696E+001 1.2992322742253871E+001 -4.6589501555216913E-006
Y 1.2992313584283236E+001 7.7953832804741774E+000 -1.0201246915748443E-006
Li 6.9854658545623726E-006 3.6655449708764760E-006 -2.2619505397620094E-006
Li -1.9622576826813114E-007 2.5984685228623832E+000 2.6990511176820964E+000
Li -1.6085820713768719E-006 5.1969301073285914E+000 1.9021932788836594E-006
Li 5.5652163252846686E-006 1.2992324077172185E+001 2.6990554170195735E+000
Li -4.0322366718664773E-006 1.0393861447392641E+001 3.1246368151995270E-006
Li -4.9933715286457953E-006 7.7953907681496721E+000 2.6990497923779206E+000
Li 2.5984636235584246E+000 2.5984712760491719E+000 5.3981057602064864E+000
Li 2.5984602098299447E+000 6.7663744068666475E-006 8.0971629251575141E+000
Li 2.5984557318768915E+000 1.2992328457088389E+001 5.3980975210627866E+000
Li 2.5984639938151073E+000 5.1969352005952594E+000 8.0971582107677946E+000
Li 2.5984626515882145E+000 7.7953865474362436E+000 5.3981056154032414E+000
Li 2.5984630641065878E+000 1.0393868541538382E+001 8.0971635212317121E+000
Li 5.1969269817883497E+000 -4.9052950774385548E-006 -6.9192994813142087E-006
Li 5.1969280554078274E+000 2.5984688745180224E+000 2.6990551667483591E+000
Li 5.1969327505201957E+000 5.1969317201585188E+000 -9.1576560709166545E-006
Li 5.1969345920405647E+000 7.7953930644248217E+000 2.6990516375974893E+000
Li 5.1969239398883005E+000 1.2992324653845118E+001 2.6990496643048183E+000
Li 5.1969237986725725E+000 1.0393867960536465E+001 -4.4740895540839021E-006
Li 7.7953871096619531E+000 -2.2110503917875776E-006 8.0971555407072238E+000
Li 7.7953908744191338E+000 2.5984662858515279E+000 5.3981112198752097E+000

Li 7.7953909550361793E+000 5.1969361984899267E+000 8.0971691613320047E+000
Li 7.7954010899221853E+000 7.7954003706426462E+000 5.3980989202358609E+000
Li 7.7953920373013776E+000 1.0393868751746105E+001 8.0971550112393427E+000
Li 7.7953919187999237E+000 1.2992329768386705E+001 5.3981062921299321E+000
Li 1.0393862734702180E+001 2.5984665753352805E+000 2.6990454901021637E+000
Li 1.0393856781115764E+001 -2.6744615386754152E-006 -3.0199084949118625E-006
Li 1.0393855236201565E+001 1.2992323204339231E+001 2.6990478655680521E+000
Li 1.0393858364625643E+001 1.0393861562105958E+001 -6.9707061175807123E-006
Li 1.0393856164691362E+001 5.1969310433710874E+000 -1.6663856856115725E-006
Li 1.0393851727856978E+001 7.7953953516145695E+000 2.6990530707985068E+000
Li 1.2992327950156648E+001 2.5984603209230976E+000 5.3981077883937720E+000
Li 1.2992323417000264E+001 7.7089940509272686E-006 8.0971593115704152E+000
Li 1.2992321694898825E+001 5.1969320714425127E+000 8.0971592560795003E+000
Li 1.2992320542999481E+001 1.0393863000518607E+001 8.0971686660207549E+000
Li 1.2992325848942759E+001 1.2992333539789655E+001 5.3981063949654313E+000
Li 1.2992318383137603E+001 7.7953970105328185E+000 5.3981148609287635E+000
F 8.6714626503252068E-001 1.4145466746408667E+001 9.8995876562277800E+000
F 8.6714934351583639E-001 1.1531421564677728E+000 3.5956770670375486E+000
F 8.6715027778094012E-001 8.9485376366317944E+000 9.8995930089506672E+000
F 8.6715034523207224E-001 1.1546996004761951E+001 3.5956812943748329E+000
F 8.6715076362885923E-001 3.7516079582267015E+000 9.8995929765128032E+000
F 8.6714869653908444E-001 6.3500695571753552E+000 3.5956809954871050E+000
F 1.1531382368313590E+000 1.7313208782292868E+000 6.2947319896955998E+000
F 1.1531368037439831E+000 1.4723646761785778E+001 7.2005323315403507E+000
F 1.1531393295560568E+000 1.2125179670953392E+001 6.2947323126395895E+000
F 1.1531402198761038E+000 9.5267163389628156E+000 7.2005371387886106E+000
F 1.1531372897497005E+000 6.9282499185051698E+000 6.2947344574010131E+000
F 1.1531368884843798E+000 4.3297854009970749E+000 7.2005356606464455E+000
F 1.4453288778038293E+000 8.6715241347430994E-001 8.9662635469468277E-001
F 1.4453286020945291E+000 3.4656170296416882E+000 1.8024324853167402E+000
F 1.4453273572890963E+000 6.0640775881969224E+000 8.9662968006694443E-001
F 1.4453237039574289E+000 8.6625395120700581E+000 1.8024293650635446E+000
F 1.4453245157990220E+000 1.1261003069737557E+001 8.9662883429558171E-001
F 1.4453248604251208E+000 1.3859474199296884E+001 1.8024262361574102E+000
F 1.7313157667949699E+000 4.0437948487200019E+000 4.5014834484771482E+000
F 1.7313180485568149E+000 1.4453350390328219E+000 8.9937912393469261E+000
F 1.7313179133315644E+000 9.2407192626638412E+000 4.5014855921699768E+000
F 1.7313176865752793E+000 6.6422622307970771E+000 8.9937900917154447E+000
F 1.7313160125006393E+000 1.4437656350547581E+001 4.5014804055390716E+000
F 1.7313145165679735E+000 1.1839189064013544E+001 8.9937827800216414E+000
F 3.4656134963116667E+000 1.4145466125024681E+001 8.9937845860586716E+000
F 3.4656108639340979E+000 1.1531420065453706E+000 4.5014786703248237E+000
F 3.4656085869869480E+000 8.9485403772873440E+000 8.9937895748975620E+000
F 3.4656106551587511E+000 1.1546998578553929E+001 4.5014836445373234E+000
F 3.4656141071165569E+000 3.7516083085679348E+000 8.9937889150048633E+000
F 3.4656146920689768E+000 6.3500709564295210E+000 4.5014825207746085E+000
F 4.0437912844904336E+000 8.6715052630096157E-001 7.2005328187977149E+000
F 4.0437921837254347E+000 3.4656180895960582E+000 6.2947307389758222E+000
F 4.0437927323303517E+000 6.0640840467975448E+000 7.2005351326764391E+000
F 4.0437859295156713E+000 8.6625467114807844E+000 6.2947325171116262E+000
F 4.0437880828361310E+000 1.1261009634958929E+001 7.2005348891947207E+000
F 4.0437894241031058E+000 1.3859477911002934E+001 6.2947282316287305E+000
F 3.7516059920334848E+000 1.7313192288747117E+000 1.8024311600995055E+000
F 3.7515998858977189E+000 1.4723640560427970E+001 8.9662408208849298E-001
F 3.7515965686484454E+000 1.2125170901303472E+001 1.8024310389324911E+000
F 3.7516002042219236E+000 9.5267091571925278E+000 8.9662698908914806E-001
F 3.7516025139423661E+000 6.9282469683642978E+000 1.8024318188446711E+000
F 3.7516068180246265E+000 4.3297874844461015E+000 8.9663032199174608E-001
F 4.3297824257572666E+000 4.0437931143487704E+000 3.5956799585922088E+000
F 4.3297825773766565E+000 1.4453339131408434E+000 9.8995909904385240E+000
F 4.3297818829614982E+000 9.2407191440286720E+000 3.5956824697423531E+000
F 4.3297797698031504E+000 6.6422633419557657E+000 9.8995916782536302E+000

F 4.3297804953140648E+000 1.4437655459607795E+001 3.5956783640543932E+000
F 4.3297814351389450E+000 1.1839192280620315E+001 9.8995848277621867E+000
F 6.0640774014438525E+000 1.4145468079644814E+001 9.8995874110209261E+000
F 6.0640764877519420E+000 1.1531429783323670E+000 3.5956776664477852E+000
F 6.0640768515391699E+000 8.9485390320561038E+000 9.8995893506891495E+000
F 6.0640760490491443E+000 1.1546999494342494E+001 3.5956830012410399E+000
F 6.0640761747068508E+000 3.7516078608734005E+000 9.8995885607817513E+000
F 6.0640779314716990E+000 6.3500695512908738E+000 3.5956779998505115E+000
F 6.6422542353459910E+000 8.6714896533934793E-001 8.9662453705084055E-001
F 6.6422537948326204E+000 3.4656126861600356E+000 1.8024267695132743E+000
F 6.6422556239267339E+000 6.0640789615249098E+000 8.9662444412741527E-001
F 6.6422574656662006E+000 8.6625442531211618E+000 1.8024276621136319E+000
F 6.6422561765224382E+000 1.1261009007149717E+001 8.9662763206958096E-001
F 6.6422550773618712E+000 1.3859475598222657E+001 1.8024300980365584E+000
F 6.3500668501775070E+000 1.7313195443586329E+000 6.2947315669656732E+000
F 6.3500654287420071E+000 1.4723648142384972E+001 7.2005305957187913E+000
F 6.3500655140770297E+000 1.2125177329863071E+001 6.2947303534220183E+000
F 6.3500640886225490E+000 9.5267171217836761E+000 7.2005352547280852E+000
F 6.3500664950288490E+000 6.9285245362541160E+000 6.2947339297017786E+000
F 6.3500680414554918E+000 4.3297842142279395E+000 7.2005355564157369E+000
F 6.9282472908630144E+000 4.0437932874235782E+000 4.5014803116187725E+000
F 6.9282449909869896E+000 1.4453318748006589E+000 8.9937854822129299E+000
F 6.9282416325513640E+000 9.2407259709738039E+000 4.5014847042893749E+000
F 6.9282428385197248E+000 6.6422649223018846E+000 8.9937863921049956E+000
F 6.9282439214003286E+000 1.4437657413117554E+001 4.5014814500442162E+000
F 6.9282439956869988E+000 1.1839193229173533E+001 8.9937856922701265E+000
F 8.6625433571666264E+000 1.4145469056290416E+001 8.9937887925423485E+000
F 8.6625418017602716E+000 1.1531410731483989E+000 4.5014811658884701E+000
F 8.6625430133955170E+000 8.9485384459431145E+000 8.9937867627107124E+000
F 8.6625447297416294E+000 1.1547001074958811E+001 4.5014837445688416E+000
F 8.6625422244945032E+000 3.7516085265709420E+000 8.9937877555906596E+000
F 8.6625417019366679E+000 6.3500681291949199E+000 4.5014790936880607E+000
F 9.2407209385489359E+000 8.6715278882097757E-001 7.2005368450187879E+000
F 9.2407200321731047E+000 3.4656153262546403E+000 6.2947334882874530E+000
F 9.2407205854051799E+000 6.0640802844143975E+000 7.2005351793590942E+000
F 9.2407233977249295E+000 8.6625483056545178E+000 6.2947335312665453E+000
F 9.2407243516736699E+000 1.1261014502151740E+001 7.2005371525987751E+000
F 9.2407231469357800E+000 1.3859478905525359E+001 6.2947342967191959E+000
F 8.9485303808489185E+000 1.7313183923660798E+000 1.8024257771978627E+000
F 8.9485319549526068E+000 1.4723643483890243E+001 8.9662639430995272E-001
F 8.9485320965219604E+000 1.2125178517745043E+001 1.8024292757693394E+000
F 8.9485330019244422E+000 9.5267125293137145E+000 8.9662523543198391E-001
F 8.9485315859989640E+000 6.9282467000105195E+000 1.8024265510012947E+000
F 8.9485309043710632E+000 4.3297810423020415E+000 8.9662307435966981E-001
F 9.5267101745398914E+000 4.0437928512267227E+000 3.5956773784046439E+000
F 9.5267102984351446E+000 1.4453330086227874E+000 9.8995901199932259E+000
F 9.5267131373668299E+000 9.2407249961367448E+000 3.5956813866984074E+000
F 9.5267124920534467E+000 6.6422602969352980E+000 9.8995898897123276E+000
F 9.5267100824033815E+000 1.4437656485121444E+001 3.5956784901832579E+000
F 9.5267108765571393E+000 1.1839193670439025E+001 9.8995916315481853E+000
F 1.1261011245102472E+001 1.4145468697097174E+001 9.8995925608286690E+000
F 1.1261008660926882E+001 1.1531398900272150E+000 3.5956781450547934E+000
F 1.1261007010311868E+001 8.9485367970622267E+000 9.8995891778824880E+000
F 1.1261008482901490E+001 1.1547001180042509E+001 3.5956789250102621E+000
F 1.1261005789856426E+001 3.7516091752278564E+000 9.8995894493789400E+000
F 1.1261009054034419E+001 6.3500687303454013E+000 3.5956792156466069E+000
F 1.1546998184640650E+001 1.7313216152899029E+000 6.2947346191050002E+000
F 1.1546999032618034E+001 1.4723648624619575E+001 7.2005362195035199E+000
F 1.1547000886197965E+001 1.2125183333497507E+001 6.2947357948303972E+000
F 1.1546998434463548E+001 9.5267144282061036E+000 7.2005382798207753E+000
F 1.1546995334585908E+001 6.9282475254817646E+000 6.2947330510934991E+000
F 1.1546996134249035E+001 4.3297846172589169E+000 7.2005358559238211E+000

F 1.1839184713632656E+001 8.6714854520671858E-001 8.9662409845143276E-001
F 1.1839188171999945E+001 3.4656164459868180E+000 1.8024299618219155E+000
F 1.1839186287261846E+001 6.0640771814423342E+000 8.9662733238686687E-001
F 1.1839184891349856E+001 8.6625426284388816E+000 1.8024269439971807E+000
F 1.1839187036321169E+001 1.1261010284623570E+001 8.9662388992581743E-001
F 1.1839185796181368E+001 1.3859472082369342E+001 1.8024249744417873E+000
F 1.2125177755769595E+001 4.0437928288665850E+000 4.5014832714206721E+000
F 1.2125174654321127E+001 1.4453323280105383E+000 8.9937873066977527E+000
F 1.2125177137231582E+001 9.2407244335169736E+000 4.5014817759010697E+000
F 1.2125175003958157E+001 6.6422604647562142E+000 8.9937871583210960E+000
F 1.2125175873340865E+001 1.4437655520571150E+001 4.5014817009371404E+000
F 1.2125178424349816E+001 1.1839191495470981E+001 8.9937886896068395E+000
F 1.3859473327196888E+001 1.4145468244236735E+001 8.9937858055244178E+000
F 1.3859470608358947E+001 1.1531402242855100E+000 4.5014793971657898E+000
F 1.3859472693270433E+001 8.9485371033397918E+000 8.9937887532341314E+000
F 1.3859473173351523E+001 1.1546999038719767E+001 4.5014825977021706E+000
F 1.3859472089842804E+001 3.7516087488844563E+000 8.9937874109601363E+000
F 1.3859473261764975E+001 6.3500710796188562E+000 4.5014844680383277E+000
F 1.4145460237238620E+001 1.7313161829663606E+000 1.8024284241098563E+000
F 1.4145463512899651E+001 1.4723642587034584E+001 8.9662425452932093E-001
F 1.4145463124974867E+001 1.2125178373843953E+001 1.8024279831136765E+000
F 1.4145461008170722E+001 9.5267102837574882E+000 8.9662381259859025E-001
F 1.4145462612019076E+001 6.9282473594218414E+000 1.8024285591844160E+000
F 1.4145462494534110E+001 4.3297831033043241E+000 8.9662802498349781E-001
F 1.4437651323419271E+001 8.6715177368943053E-001 7.2005345966522203E+000
F 1.4437649378262540E+001 3.4656156511401282E+000 6.2947336585169991E+000
F 1.4437651141722355E+001 6.0640826058762052E+000 7.2005380249802409E+000
F 1.4437652537355588E+001 8.6625462612241027E+000 6.2947356488209429E+000
F 1.4437651283069114E+001 1.1261012182087908E+001 7.2005362909039148E+000
F 1.4437651888948750E+001 1.3859479200838329E+001 6.2947315594595095E+000
F 1.4723643376182999E+001 4.0437928627941089E+000 3.5956828253236202E+000
F 1.4723639049736787E+001 1.4453326212248228E+000 9.8995908956473961E+000
F 1.4723639853736614E+001 1.4437654360377497E+001 3.5956774305496464E+000
F 1.4723643835858594E+001 1.1839191511252061E+001 9.8995877964168386E+000
F 1.4723641012283322E+001 6.6422619085445014E+000 9.8995911546209676E+000
F 1.4723642348853417E+001 9.2407238109665073E+000 3.5956799322709356E+000

7 β-$NaYF_4$ Optimised Structure (configuration 10)

A 1.2056437308948636E+01 0.0000000000000000E+00 0.0000000000000000E+00
B -5.9969677559366437E+00 1.0473134435223811E+01 0.0000000000000000E+00
C 1.1946225120407898E-03 -2.5457702667339905E-03 1.4150749505173852E+01

Na -3.0991034750626576E+00 8.7255508673403668E+00 2.0362000133700908E+00
Na -2.8216057271276478E+00 8.7268137878219161E+00 5.4728920595659591E+00
Na -3.1522734330892455E+00 8.7232878030521732E+00 8.6764918782534366E+00
Na -2.9285322605466177E+00 8.7249974384335811E+00 1.1942622203951792E+01
Y -2.9636936093284114E+00 5.2737508804849842E+00 -2.4579568525484536E-03
Y -3.0021139092004887E+00 5.2474826649645694E+00 3.5377792126626564E+00
Y -3.0286074422615141E+00 5.2212655313906673E+00 7.0667148650680245E+00
Y -3.0044646450413381E+00 5.2409880576806129E+00 1.0618075665042904E+01
Y 2.7676928998108814E-02 7.0066694411543997E+00 1.7640511039751179E+00
Na 2.2147865792835730E-02 6.9803603897049786E+00 5.1860830241629579E+00
Y 1.9741214221277478E-03 7.0172065465228144E+00 8.8240875052389320E+00
Na -3.2916672343578278E-02 6.9799061670760381E+00 1.2403130601026891E+01
Y 4.1205529246391759E-02 -2.1627011646898815E-03 -3.3544400549856395E-03
Y 2.0021275337053887E-03 1.2717468343624479E-02 3.5303877122026548E+00
Y 6.8745263331278852E-03 2.2196781203409947E-02 7.0766922334643576E+00
Y -2.3405740878333713E-02 7.4088766400859157E-03 1.0607344632347841E+01
Na 1.2317124267511297E-01 3.4907353013595430E+00 1.8049385008340177E+00
Na -1.0111875385510047E-01 3.4888393350823494E+00 5.3003259474844588E+00
Na 6.9445567898141367E-02 3.4907005129505229E+00 8.9666699206485294E+00
Na -9.9935885285807338E-02 3.4868752230290334E+00 1.2346494685128219E+01
Na 2.9924971335532660E+00 1.6975224982966202E+00 1.7477473058894772E+00
Y 3.0093141933466478E+00 1.7677064282492734E+00 5.3086239214342568E+00
Na 3.0201694673349042E+00 1.7442448555261099E+00 8.8511148060178435E+00
Y 3.0261466494097360E+00 1.7726088496497989E+00 1.2369775241364819E+01
Y 3.0170825822127703E+00 5.2461831089635433E+00 8.7884586607661803E-03
Y 3.0449033105368568E+00 5.2537867386949779E+00 3.5325703355186664E+00
Y 3.0280992601363423E+00 5.2239495359150734E+00 7.0832023231617347E+00
Y 3.0149281985262282E+00 5.2779897597776140E+00 1.0610204476540366E+01
Na 3.2049408242013220E+00 8.7280972484962280E+00 1.5736173393530233E+00
Na 2.9822900336753055E+00 8.7255274759991259E+00 5.2400259512628020E+00
Na 3.1538909212806230E+00 8.7259950538880364E+00 8.6199115530486647E+00
Na 2.9286929911394970E+00 8.7239904854204617E+00 1.2401969872322317E+01
Na 6.0493169376766538E+00 6.9808644807952769E+00 1.7477820392905958E+00
Y 6.0591996598359934E+00 7.0002283221529318E+00 5.3081425634270989E+00
Na 6.0487901079647655E+00 6.9794148718743347E+00 8.7942629378553079E+00
Y 6.0333280485473475E+00 6.9998433027422040E+00 1.2390943173290411E+01
Y 5.9862965973400275E+00 -2.6385011880447097E-04 -1.3243300082842109E-02
Y 6.0405677048038973E+00 9.6568469874954189E-03 3.5337705743128351E+00
Y 6.0593144228762137E+00 3.8356994520040329E-02 7.0620110520894501E+00
Y 6.0459081549306255E+00 -8.6235953132078273E-03 1.0616667585876977E+01
Na 5.9262976451905702E+00 3.4895630066648229E+00 1.4585304062565059E+00
Na 6.0977055972006706E+00 3.4898964208545711E+00 4.8953856389385866E+00
Na 5.9264307890623691E+00 3.4887262564410939E+00 9.2552243407602077E+00
Na 6.2051527056818934E+00 3.4893259640267926E+00 1.2576284638990971E+01
Y 9.0386759186532970E+00 1.7719891811044683E+00 1.7505968090580668E+00
Na 9.0471988056332329E+00 1.7442940455908142E+00 5.1861508547724284E+00
Y 9.0401647369475349E+00 1.7562278524129837E+00 8.8215454137717888E+00
Na 9.0483813158526996E+00 1.7422561488209980E+00 1.2402963816296724E+01
F -3.6996154088102351E+00 6.5423271330404891E+00 1.7512305857247310E+00
F -3.7341993558442637E+00 6.5117986585842731E+00 8.8557750195367806E+00
F -3.6456337806220658E+00 6.6545072942872316E+00 5.2945413465026991E+00
F -3.6471594244791388E+00 6.6507419165776938E+00 1.2399984155122056E+01
F -6.4162368670822800E-01 1.4104641198215093E+00 1.7493709463400291E+00
F -6.5529904129718164E-01 1.4123069299928366E+00 8.8461988207992981E+00
F -7.2502088816499843E-01 1.2861937010179649E+00 5.2978316408890365E+00
F -7.1831073927331279E-01 1.2898921741385974E+00 1.2399116761763890E+01

F -1.4435674214181957E+00 5.1478959465662628E+00 1.8037991474273196E+00
F -1.4652801214513425E+00 5.1868754155384531E+00 8.8481246168557881E+00
F -1.5191040996638239E+00 5.1865829839440849E+00 5.2977717077429913E+00
F -1.4939425134928279E+00 5.1875227612645904E+00 1.2351391442314068E+01
F -4.4877614261915619E+00 1.0418458869996577E+01 1.7955628443427969E+00
F -4.5067857837070440E+00 1.0432082593669776E+01 8.8549950621054698E+00
F -4.4517085746233915E+00 1.0412102608813866E+01 5.2987352573563165E+00
F -4.4442238003774435E+00 1.0384572551272134E+01 1.2348206944148341E+01
F -1.5910384236647890E+00 7.1138616294230017E+00 1.6738082230576737E-01
F -1.7054853478996204E+00 7.1768108485051583E+00 7.2212900725916596E+00
F -1.6534484494954984E+00 7.1737608956181802E+00 3.3791461507506990E+00
F -1.7003139275637507E+00 7.1773225213808951E+00 1.0476012533264903E+01
F 1.3708588638109780E+00 1.9014278077617766E+00 -1.6837956839842735E-01
F 1.3302660462716003E+00 1.9062603602512564E+00 6.9274105933562904E+00
F 1.3421624528764475E+00 1.9336283040212701E+00 3.6719339388952079E+00
F 1.3349477886089585E+00 1.9362233672681577E+00 1.0771674280726648E+01
F 3.7149554626577341E+00 2.9785520828753242E-01 -1.7885193349785156E-01
F 3.7307613755173104E+00 1.9841302904127475E-01 6.8759282175736258E+00
F 3.7307310769552764E+00 2.0552201013258792E-01 3.7259418043785377E+00
F 3.7157384732662044E+00 2.4109531568083378E-01 1.0772308854388074E+01
F 7.2116689010414936E-01 5.4407356600880217E+00 1.8226073346915619E-01
F 7.1500706360651411E-01 5.4867024909524025E+00 7.2288598188425324E+00
F 7.2115213902095632E-01 5.4800234739495650E+00 3.3718889941291876E+00
F 7.0887035306424429E-01 5.4765509263338874E+00 1.0425166199579582E+01
F 2.2976212538868004E+00 3.9682985476626937E+00 1.7930310036762565E+00
F 2.2525184582529043E+00 3.9827318023832814E+00 8.8546496728076871E+00
F 2.1277243781145785E+00 3.9725630809857488E+00 5.2971303898013247E+00
F 2.1356577346332708E+00 3.9685655949738656E+00 1.2398966269558679E+01
F -8.6983047700233351E-01 9.2066091047970673E+00 1.7525976710093352E+00
F -8.7202052638438965E-01 9.2062578949845282E+00 8.8476025494932742E+00
F -6.8559749920943935E-01 9.2128029446714681E+00 5.2993207987050743E+00
F -7.5612552602526584E-01 9.2118983646271744E+00 1.2396730170880376E+01
F 1.0070379654992516E+00 8.3795687720008978E+00 1.7255514362977167E-01
F 1.0003750661289981E+00 8.3825530525581673E+00 7.2272715021884784E+00
F 1.0006076310773844E+00 8.3788377875417126E+00 3.3700756489939163E+00
F 9.6370884171211513E-01 8.3459938977241706E+00 1.0475967805641483E+01
F 4.0500891467783120E+00 3.1521042137403925E+00 -1.7493675366197861E-01
F 3.9198099568099893E+00 3.1011624758210838E+00 6.9255410593765623E+00
F 4.0041931882408734E+00 3.1361515712075709E+00 3.7235688675386203E+00
F 4.0000887639191802E+00 3.1534704663801487E+00 1.0774191396871027E+01
F 2.3817452812901569E+00 6.6567638302192389E+00 1.7544659288545998E+00
F 2.3674660130494254E+00 6.6708280632893295E+00 8.8479191801361914E+00
F 2.3337618075620141E+00 6.5393898862047823E+00 5.2995280735520494E+00
F 2.2857120836234648E+00 6.5389839030449419E+00 1.2401804920684045E+01
F 5.2937612421033409E+00 1.3041427453119414E+00 1.7564569133843000E+00
F 5.3336478098838125E+00 1.3033579153755408E+00 8.8519410299453032E+00
F 5.3873216645207265E+00 1.4177763267799166E+00 5.3002227867023057E+00
F 5.3813446663855631E+00 1.4265865261149759E+00 1.2347093500883837E+01
F 1.5698046780210519E+00 1.0422444412081461E+01 1.7472170989681377E+00
F 1.5895917671699351E+00 1.0375613287876844E+01 8.8532168332461101E+00
F 1.5546458559295084E+00 1.0423695774665839E+01 5.2932080747435046E+00
F 1.5135928596577322E+00 1.0418588579471976E+01 1.2402266747507877E+01
F 4.5275011800404519E+00 5.1835913741550321E+00 1.7507339995495759E+00
F 4.5126359099028353E+00 5.1855941426593599E+00 8.8522965028941343E+00
F 4.5880838893614131E+00 5.1565352259792556E+00 5.3057419726556958E+00
F 4.5640905448108766E+00 5.1817815981520878E+00 1.2400661922279541E+01
F 4.3657166202436137E+00 7.1752273494540919E+00 -1.2176601637749769E-01
F 4.3763659896367075E+00 7.1717504639781993E+00 6.9289343758135846E+00
F 4.4014953633451697E+00 7.1395201310277647E+00 3.6707015249814647E+00
F 4.3729960518962159E+00 7.1660566929655092E+00 1.0774602171194998E+01
F 7.3334768896687539E+00 1.9516367464199027E+00 1.2024438497023203E-01
F 7.4311534042043572E+00 1.8661620114942663E+00 7.2190727917252770E+00

F	7.3700908573120634E+00	1.9363038432004465E+00	3.3761475972474595E+00
F	7.3981611454287917E+00	1.8982406990077132E+00	1.0480773974211512E+01
F	9.7432074115863969E+00	2.3734192100095650E-01	1.7546057494284542E-01
F	9.7665025143652464E+00	1.9689488267415270E-01	7.2290516874559074E+00
F	9.7461562683690897E+00	2.3939615581518128E-01	3.3580664354504379E+00
F	9.7455155154789619E+00	2.3994521070208016E-01	1.0426173452229072E+01
F	6.7469320812438349E+00	5.4827433989947263E+00	3.6756108681244020E+00
F	6.7390791369626033E+00	5.4243415332274347E+00	1.0828712161006459E+01
F	6.7400450163356664E+00	5.4322523489956511E+00	-1.7541612916177868E-01
F	6.7599141646544307E+00	5.5333227073133884E+00	6.9182662360789058E+00
F	5.3337534913915015E+00	9.2138308881398849E+00	1.7536282788980915E+00
F	5.3260625632758556E+00	9.2078316352149514E+00	8.8472351275027403E+00
F	5.1882039557641066E+00	9.1840890679114349E+00	5.3029035964200242E+00
F	5.1591831691148569E+00	9.2064649027910832E+00	1.2397939387211515E+01
F	8.2723099070860915E+00	3.9769184928956998E+00	5.2959296507600362E+00
F	8.3390906704527001E+00	3.9710857784224429E+00	1.2400413684163414E+01
F	8.1589347256693028E+00	3.9724038423101597E+00	1.7498793822057461E+00
F	8.1414516145474067E+00	3.9402335962540582E+00	8.8510649104376480E+00
F	7.0407030816488030E+00	8.3781269986191891E+00	3.7190304314305132E+00
F	7.0103890683851668E+00	8.3433472084050262E+00	1.0773348524659545E+01
F	6.9986920168420044E+00	8.3447744413683882E+00	-1.7415865674029460E-01
F	7.0803973323468776E+00	8.3901051943809630E+00	6.9262491728249982E+00
F	1.0003910366208904E+01	3.1088628806286205E+00	3.3754918706323171E+00
F	1.0037057590204213E+01	3.1432825676067369E+00	1.0425639004683530E+01
F	1.0030885008289502E+01	3.1457084455115703E+00	1.7393274440645973E-01
F	1.0027468752057370E+01	3.1426772653612911E+00	7.2263667944613657E+00

THE JOURNAL OF PHYSICAL CHEMISTRY C
A JOURNAL OF THE AMERICAN CHEMICAL SOCIETY

pubs.acs.org/JPCC
Article

Effect of Disorder on the Emission Spectra of Er^{3+}, Tm^{3+}, and Yb^{3+}-Doped β-$NaYF_4$: Quantum Chemical and Experimental Results

Chris Steve Conrad, Stefan Behnle, Eva Hemmer,* and Reinhold F. Fink*

Cite This: J. Phys. Chem. C 2025, 129, 20446−20464

Read Online

ACCESS | Metrics & More | Article Recommendations | Supporting Information

ABSTRACT: Exact optical characteristics of the trivalent lanthanide ions (Ln^{3+}) are crucially determined by their nearest neighbors and in turn govern the quantum efficiency of Ln^{3+}-doped upconverting nanoparticles (UCNPs). Their often extremely low quantum efficiency can be increased considerably by doping Ln^{3+} into disordered host lattices. In these lattices, each Ln^{3+} experiences a slightly different low-symmetry environment, which leads to small variations in its (optical) properties. To this end, we predict crystal field energy levels and oscillator strengths of Er^{3+}, Tm^{3+}, and Yb^{3+} doped into disordered hexagonal (β-)$NaYF_4$ and ordered $LiYF_4$. In addition, theoretical photoluminescence spectra for β-$NaYF_4$:Er^{3+} were determined. The results were obtained using a wave function-based ab initio computational approach and an embedded cluster model. The disorder of β-$NaYF_4$:Ln^{3+} was accounted for through weighted averaging, in which stochastic considerations and Boltzmann distributions for several local configurations were included. Comparison to experimental and semiempirical data showed particularly good agreement for both the ordered and disordered material. The disordered lattice significantly shifted the crystal field energy levels and changed the oscillator strengths of the respective Ln^{3+} transitions. Importantly, the computed photoluminescence spectra showed the best agreement with experimental spectra when including the predicted results of all disordered configurations individually. This reveals that the observed energetic splitting and transition rates of the excited Ln^{3+} dopants can only be accurately described if the disorder of the β-$NaYF_4$ crystal is properly considered. The proposed quantum chemical protocol paves the way for the future simulation of photon upconversion processes in UCNPs.

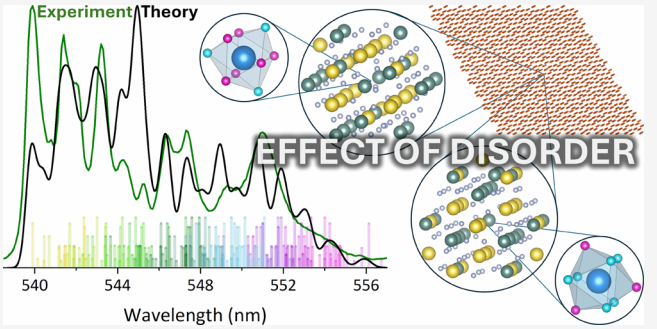

INTRODUCTION

In recent years, growing attention has been dedicated to photon upconversion and how employing upconverting nanoparticles (UCNPs) might help tackling current societal challenges such as treating cancer, detecting potential heart failure, in vivo temperature measurements and manipulations, ensuring food safety, or monitoring aquatic organisms.[1−7] In fact, the underlying fundamentals of the upconversion process have been well-studied in more than 50 years since the phenomenon has been first described.[8,9] Most upconverting systems operate by the energy transfer upconversion (ETU) mechanism, which can be split into four separate steps: (1) A photon is absorbed by an ion, and the ion uses the photon's energy for reaching an exited state. (2) The energy is nonradiatively transferred to a second ion. As a result, the second ion is excited while the first ion relaxes back to the ground state. (3) Another photon is absorbed by the first or another ion, and the energy is again transferred to the second ion. Since the second ion is already in an exited state, it uses the transferred energy to reach an even higher exited state. (4) If the second ion relaxes back to the ground state radiatively, a photon with more energy than each of the initially absorbed photons is emitted, finalizing the upconversion process.[10]

Efficient upconverters are several of the trivalent lanthanide ions (Ln^{3+}) doped into inorganic host crystals, e.g., cubic- (α) and hexagonal- (β) phase $NaYF_4$ and $NaGdF_4$ or $LiYF_4$ doped with Er^{3+} or Tm^{3+} and Yb^{3+} as a codopant.[11−13] The 4f−4f transitions of the Ln^{3+} in these matrices combine long lifetimes of the excited states with still meaningful transition rates between these states.[14,15] Both properties are needed for an efficient upconversion process. The transition rates between the energy levels can be quantified by the respective oscillator strengths. Because of Laporte's rule, these oscillator strengths are near to zero for lanthanides in a centrosymmetric environment. However, once the Ln^{3+} are subjected to a noncentrosymmetric surrounding by a host crystal, the previously degenerate states (multiplets) split into crystal field energy levels called Stark levels. Due to the reduced

Received: September 4, 2025
Revised: October 15, 2025
Accepted: October 16, 2025
Published: October 30, 2025

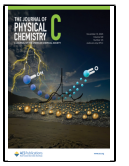

https://doi.org/10.1021/acs.jpcc.5c06209
J. Phys. Chem. C 2025, 129, 20446−20464

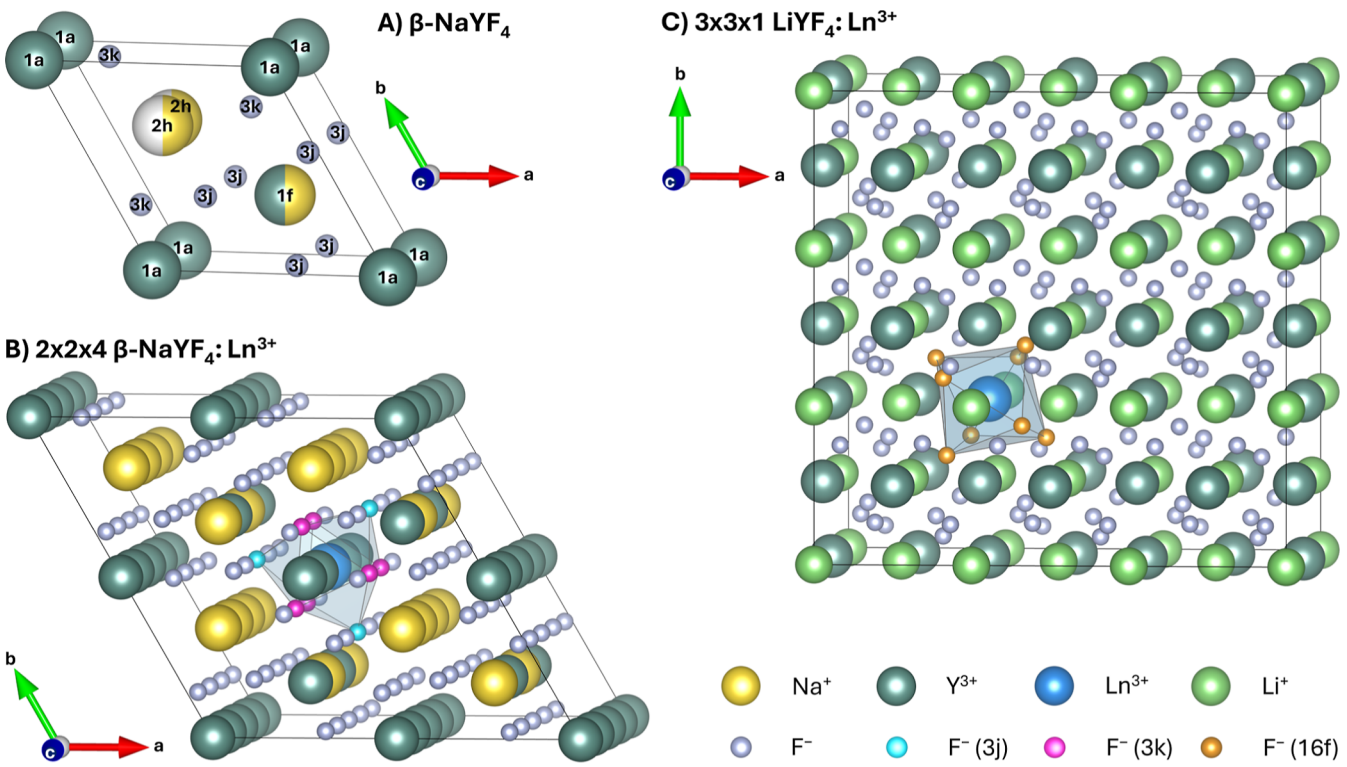

Figure 1. Unit cell and Ln^{3+}-doped supercells of β-$NaYF_4$ and $LiYF_4$. (A) Unit cell of β-$NaYF_4$ (space group $P\bar{6}$) with the composition $Na_{1.5}Y_{1.5}F_6$ and labeling of the Wyckoff sites. Yellow spheres represent Na^+, dark green spheres Y^{3+}, small gray spheres F^-, white spheres are unoccupied sites, and half spheres indicate a 50% occupation. (B) $2 \times 2 \times 4$ supercell of β-$NaYF_4$:Ln^{3+} with the composition $Na_{24}Y_{23}Ln_1F_{96}$. In addition to the color code used in (A), blue spheres represent Ln^{3+}, and small cyan and pink spheres stand for the nine F^- at the two different Wyckoff positions closest to the Ln^{3+} doping site. For better visualization, a polyhedron (tricapped trigonal prism) was drawn around the Ln^{3+} doping site, connecting the F^- at the edges of the polyhedron. The Ln^{3+} ion is doped into one of two possible sites (Wyckoff position 1a, alternatively 1f). (C) $3 \times 3 \times 1$ supercell of $LiYF_4$:Ln^{3+} with the composition $Li_{36}Y_{35}Ln_1F_{144}$. In addition to the color code used in (A), light green spheres represent Li^+, and small orange spheres stand for the eight F^- closest to the Ln^{3+} doping site. The included polyhedron (distorted square antiprism) connects the F^- neighboring the central Ln^{3+} doping site. The space group of the unit cell used to construct the supercell is $I4_1/a$ (tetragonal).

symmetry, larger transition rates can be observed between these states. Still, the quantum yield remains low for UCNPs, with values typically being in the range of less than 1%,[16,17] slowing UCNPs on their way to real-life applicability, although progress has been made.[18−20]

To overcome this challenge, a variety of strategies has been developed over the years to boost the upconversion quantum yield of nanoparticles.[20−23] Notably, record emissions—recently up to 13%—were commonly observed for dopant−host systems with a disordered host lattice.[18,24−27] Possible sources of disorder within a crystal lattice are sites that are occupied only partially or by different ions. The higher quantum yield in disordered crystals has been associated with the Ln^{3+} ions being doped into low-symmetry sites, which results in higher transition intensities. In turn, this results in a more efficient upconversion process assuming all other parameters are kept the same. Moreover, in a disordered host, the Ln^{3+} are doped into sites that all differ marginally, but importantly not negligibly, from each other.[28,29] Therefore, each Ln^{3+} has energy levels with slightly different positions, and the transitions between these energy levels have different oscillator strengths. These nuanced changes can potentially be beneficial in the energy transfer processes as needed for ETU and thereby also aid in increasing the quantum yield of UCNPs.

In an ETU process that involves two different types of ions, e.g., Er^{3+} and Yb^{3+} or Tm^{3+} and Yb^{3+}, the energy levels of the donor and acceptor ions usually do not align perfectly causing an energy mismatch.[30] This energy mismatch and the oscillator strengths of the involved transitions crucially determine the efficiency of the energy transfer process.[31] To elaborate on this further, in any dopant−host system, the donor (i.e., Yb^{3+}) has a certain number of acceptor ions (i.e., Er^{3+} or Tm^{3+}) in its immediate surrounding. In an ordered host crystal, all these acceptors (and donors) have the same properties. In our previous work, we implied that in the disordered β-$NaYF_4$ crystal, ions will be doped into a variety of low-symmetry sites, all of which have slightly different environments.[29] Therefore, all of the dopants should exhibit slightly varying properties. If any combination of a donor and an acceptor results in a smaller energy mismatch coupled with higher oscillator strengths, the efficiency of the energy transfer process and thereby the quantum yield of the system should increase compared to that of an ordered system.

Shyichuk et al. previously modeled ETU and the corresponding upconversion processes for Er^{3+} and Yb^{3+} within an ordered host crystal (YVO_4), using a semiempirical approach.[31] Conversely, to the best of our knowledge, disordered hosts have not been addressed to date. A comparative study where similar ordered and disordered host materials are modelled on the same footing could provide evidence that disordered host crystals are especially beneficial for ETU processes. Moreover, such modeling has the potential to foster the discovery of even better host materials or

https://doi.org/10.1021/acs.jpcc.5c06209
J. Phys. Chem. C 2025, 129, 20446−20464

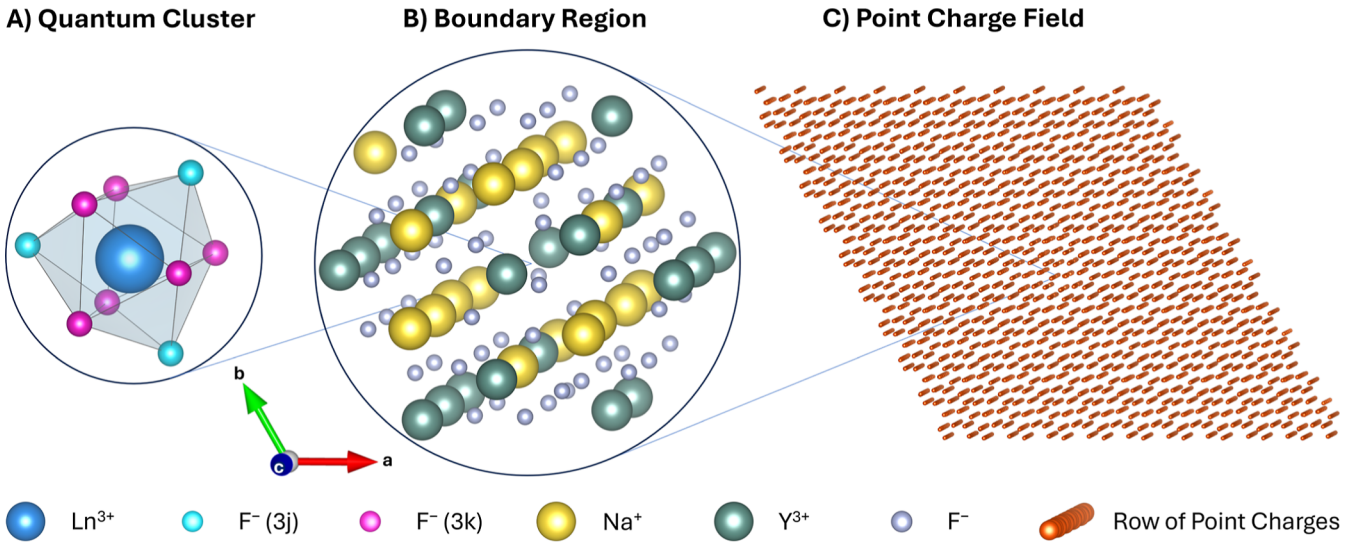

Figure 2. Ionic cluster embedding for one cluster of β-$NaYF_4$:Ln^{3+}. (A) LnF_9 quantum cluster. (B) $Na_{19}Y_{22}F_{62}$ boundary region. (C) Field with 17,886 point charges.

dopant−host combinations. However, because of the enormous number of configurations observed in disordered crystals, the semiempirical approach of Shyichuk et al. is not suitable for this endeavor. Consequently, a different computational approach must be followed, where ab initio strategies stand out as a suitable alternative. More precisely, we propose here an ab initio computational model to probe properties like crystal field energy levels and oscillator strengths of three different Ln^{3+} (i.e., Er^{3+}, Tm^{3+}, and Yb^{3+}) for both an ordered ($LiYF_4$) and a disordered (β-$NaYF_4$) host crystal.

In the following, first, the structural properties of the ordered and disordered host materials and its dopants will be summarized based on our previous investigation.[29] The sources of disorder in β-$NaYF_4$ will also be highlighted, followed by the setup of the ab initio calculations for both the ordered and the disordered systems. Having a suitable model on hand, the energy levels and oscillator strengths of the Ln^{3+} under consideration could be determined. Importantly, the modeled data, i.e., energy levels, oscillator strengths, and photoluminescence spectra, showed good agreement with data taken from the literature as well as experimentally obtained emission spectra from UCNPs synthesized in-house.[32−40] Our calculations also provide evidence that a single configuration of atomic positions is insufficient to predict the optical properties of a disordered structure. Instead, at least a representative ensemble of possible configurations must be included to obtain meaningful insights into such materials. These insights have the potential to contribute to the discovery of novel dopant−host combinations for UCNPs, with highly efficient ETU and increased quantum yield, possibly fostering their real-life application.

THEORETICAL SETUP

β-$NaYF_4$ Disordered Crystal Structure. The unit cell of β-$NaYF_4$ is shown in Figure 1A. Assuming the $P\bar{6}$ space group for its lattice, it contains two disordered sites.[41] One site, at Wyckoff position 1f, is occupied by either Na^+ or Y^{3+}, with equal probabilities for both ions. The other disordered site consists of two connected sites, both at Wyckoff position 2h. In each unit cell, exactly one of the two 2h sites is occupied by Na^+, with equal probability. The β-$NaYF_4$ crystal structure is therefore highly irregular even without accounting for additional defects such as vacancies, dopants, or interstitial atoms.[42,43] Consequently, from a computational perspective, the accurate description of this structure is challenging but has been addressed before.[44−47] In our previously reported approach,[29] we proposed the creation of a $2 \times 2 \times 4$ supercell of β-$NaYF_4$ and alteration of the distribution of Na^+ and Y^{3+} at the two disordered sites around the two potential Ln^{3+} doping sites (at the Wyckoff positions 1f and 1a). Hereby, the overall composition of the supercell was kept constant, while 16 supercells with different configurations were created to represent the disordered crystal. These 16 configurations were subsequently doped with either Er^{3+}, Tm^{3+}, or Yb^{3+} and then structurally optimized employing a density functional theory (DFT) with periodic boundary conditions ansatz. One of these doped supercells is shown in Figure 1B. More details on the computational ansatz can be found in the original publication.[29] The different arrangements of Na^+ and Y^{3+} in each supercell induced slight rearrangements of all other ions in the immediate surroundings, including the anions (F^-) next to the Ln^{3+} doping sites. Therefore, each supercell exhibited slightly varying structural properties after the optimization, and nuanced changes were observed in the environments of the available doping sites.[29] From these supercells, cluster embeddings were generated to probe the electronic properties of the dopants.

Cluster Embedding. *β-$NaYF_4$:Ln^{3+}.* Initially, 16 individual supercells for each of the three Ln^{3+} considered herein (i.e., Er^{3+}, Tm^{3+}, and Yb^{3+}, 48 in total) were available for further investigation. Of the 16 supercells for each Ln^{3+}, the 14 with the lowest energy were considered for the current work, excluding two supercells for each Ln^{3+}. Thereby, the total number of structures considered for β-$NaYF_4$:Ln^{3+} was reduced to 42. The unfavorable structural arrangements for the two omitted configurations resulted in significantly increased energies of the supercells, making them unlikely to be found in real crystals. Details on the exact arrangements of the Na^+ and Y^{3+} around the respective doping sites can be found in our previous work.[29]

An ionic cluster embedding scheme based on these supercells was created following the procedure reviewed by

https://doi.org/10.1021/acs.jpcc.5c06209
J. Phys. Chem. C 2025, 129, 20446−20464

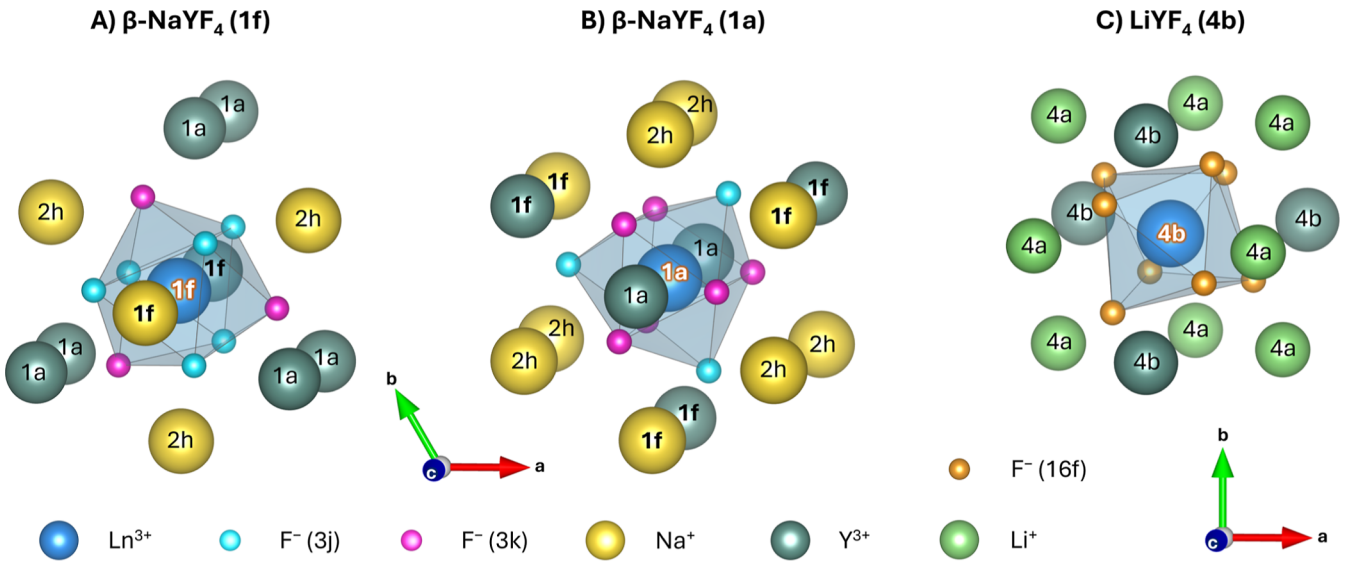

Figure 3. Examples for quantum clusters and first layer of the boundary regions for β-$NaYF_4$:Ln^{3+} (A,B) and $LiYF_4$:Ln^{3+} (C). (A) Two disordered 1f sites (set in bold) are part of the first anionic coordination sphere, and one of the two sites is occupied by Y^{3+}. (B) Six 1f sites are included, and three of these are occupied by Y^{3+}. Variations of the clusters are possible not only by changing the ratio of Na^+ to Y^{3+} at the 1f sites but also by arranging them differently at the available sites. Through the varied distribution of Na^+ and Y^{3+} at the disordered sites and the slightly differing radii of these ions, the F^- in the quantum cluster are located at marginally different positions, thereby changing the electronic properties of the central Ln^{3+}. Na^+ ions at the 2h sites are also subject to disorder, having a similar influence. (C) No disordered sites are present in the crystal structure of $LiYF_4$:Ln^{3+}; exactly one anionic coordination sphere exists.

Staemmler,[48] including the adjustments introduced by Aravena et al. and Atanasov et al.[49,50] For each supercell, an embedded cluster model was designed as described in the following. The embedding scheme for one of the clusters is depicted in Figure 2. This cluster is derived from supercell 10 of our previous work and is used most often when β-$NaYF_4$ is treated as an ordered crystal.[29,51−53] The numbering for the different supercells is explained in detail below. For this particular structure, Na^+ and Y^{3+} at the 1f sites form regularly alternating columns (Figure 1B). For further illustrations of the supercells with different Na^+-Y^{3+} arrangements, the interested reader is referred to our previous publication and its Supporting Information.[29]

Quantum Cluster. For creating each cluster, the central Ln^{3+} ion and its closest neighbors (nine F^- for β-$NaYF_4$) were cut from the supercell (Figure 1B). These ions formed the quantum cluster, Figure 2A, in which all interactions between all electrons of all ions were calculated explicitly at a quantum-mechanical level (see the section Computational Details). Although the composition of the quantum cluster is the same for all 42 clusters of β-$NaYF_4$ (one Ln^{3+} plus nine F^-), the positions of the F^- ions within each cluster vary slightly. This is predominantly due to the changing distribution of Na^+ and Y^{3+} being directly adjacent.

Boundary Region. The ions in the supercell adjacent to the Ln^{3+} and F^- of the core quantum cluster are included into the setup by adding them to the boundary region (Figure 2B). More precisely, the boundary region forms an intermediate layer between the quantum cluster and the point charge field (Figure 2C). Ions in the boundary region are approximated by a point charge plus an effective core potential (ECP). The term we prefer to use for these is therefore capped point charges.[54] The reason for equipping point charges closest to the quantum clusters with ECPs is to accurately mimic the Pauli repulsion between the electrons of the F^- in the quantum cluster and the core electrons of the surrounding ions. This addition prevents unphysical "leaking" of electrons into the boundary region. Also, by representing an ion not only by its charge but also by a potential that mimics the electronic structure of the original ion at least to a certain degree, the electrons in the quantum cluster are surrounded by an environment that better reflects the conditions in a real crystal. This allows for minimizing the size of the quantum cluster, which drastically reduces computational effort, while only marginally influencing the obtained results.[49,54]

The size of the boundary region for all clusters was chosen such that approximately 23 Y^{3+} were included as capped point charges. The exact number depended on the distance of each ion to the central Ln^{3+} and the structural configuration. 23 Y^{3+} plus 1 Ln^{3+} was also the same distribution as found in the supercells from which the embedding was created.[29] The ratio of one Ln^{3+} in the center to the number of Y^{3+} in the boundary region corresponded to a doping concentration of 4−5 mol % for the quantum cluster and boundary region. Overall, the boundary region typically consisted of 110 capped point charges arranged in about two double layers around the quantum cluster. Figure 3A depicts the quantum cluster and the first layer of the boundary region for the cluster with the highest weighting factor (explained below). In Figure 3B, the same information is provided for the cluster commonly used for β-$NaYF_4$:Ln^{3+} in other works.

Point Charge Field. The third part of the embedding consisted of pure ionic point charges, their positions being iteratively added as additional layers around the boundary region (Figure 2C). These point charges were incorporated to model the electrostatic potential (long-range Coulomb effects) of the host crystal. Typically, up to 18,000 charges were added for β-$NaYF_4$:Ln^{3+}. The size of the created clusters corresponded to nanoparticles of approximately 5 nm in diameter. The charges of the point charges were slightly adjusted to reproduce the correct electrostatic potential of the crystal at the embedding site.[55]

https://doi.org/10.1021/acs.jpcc.5c06209
J. Phys. Chem. C 2025, 129, 20446−20464

With these three layers discussed above, the surroundings of the Ln^{3+} dopant were set up to model the real environment experienced by the central ion as accurately as possible. However, this setup also assumed that the particle is defect-free and a single Ln^{3+} is doped almost exactly into the cluster's center.

$LiYF_4$:Ln^{3+}. A similar procedure for creating the ionic embedding was applied for $LiYF_4$:Ln^{3+}. It differed from that of β-$NaYF_4$:Ln^{3+} in the number of F^- in the quantum cluster (eight for $LiYF_4$:Ln^{3+}) and through the associated structural changes. Additionally, the boundary region consisted of Li^+, Y^{3+}, and F^-, and the point charge field had up to 27,000 charges. Also, since the unit cell of $LiYF_4$ is completely ordered, a single configuration sufficed to describe its lattice. Therefore, only three cluster embeddings were created for this crystal, one for each of the Ln^{3+} under consideration, i.e., Er^{3+}, Tm^{3+}, and Yb^{3+}. The supercell for $LiYF_4$:Ln^{3+} is shown in Figure 1C.

Two additional calculations were conducted for $LiYF_4$ doped with either Er^{3+} or Yb^{3+}. Herein, the first layer of the boundary region (Li_8Y_4, Figure 3C) was added to the quantum cluster to test the size convergence of our model. The resulting energy levels shifted on average by less than 0.1%, while the computational demand increased significantly by more than 1 order of magnitude. No further structures with the increased size of the quantum cluster were therefore considered. The output files containing the respective data sets for these and for all other calculations mentioned in this study are provided via a research data repository (RDR), to which a link is provided in the section Associated Content.

Computational Details. The previously optimized geometries were converted from the CP2K output into CIF files with a Python script and the VESTA crystal visualization program by Momma and Izumi.[56] The VESTA software package was also used for drawing all of the shown crystal structures and cluster embeddings. The thereby obtained CIF files were utilized for the creation of the ionic cluster embedding (i.e., quantum cluster, boundary region, and point charge field) using the program Env by LePetit and Gelle.[55] Two input files for Env (one for β-$NaYF_4$:Ln^{3+} and one for $LiYF_4$:Ln^{3+}) are provided in the Supporting Information (section Env Input Files). All other input files are available at the RDR.

Information about the positions of the ions in the embedding scheme was written into an input file for the ORCA 6.0.1 program package, which was used to model the spectroscopic properties of the prepared clusters.[57−59] To this end, state-averaged complete active space self-consistent field (SA-CASSCF) followed by N-electron valence state second-order perturbation theory (NEVPT2) and quasi-degenerate perturbation theory (QDPT) calculations for spin−orbit coupling (SOC) were performed for the prediction of wave functions and corresponding energies.[60] All seven 4f-orbitals and the respective number of 4f-electrons for Er^{3+} (11), Tm^{3+} (12), and Yb^{3+} (13) were included in the active space. All states (multiplets) with all possible multiplicities were included in the state averaging. While SA-CASSCF provides a qualitative description of this multiplet structure and accounts for the static electron correlation, NEVPT2 captures a majority of the dynamical electron correlation that has not yet been accounted for through the mean-field treatment at the CASSCF level.[61−67] Furthermore, the second-order scalar-relativistic Douglas−Kroll−Hess (DKH) Hamiltonian was employed to account for scalar-relativistic effects.[68−70] Finally, SOC of the f-electrons was included via QDPT.[71] Accurate treatment of SOC is absolutely crucial for the current investigation due to the semicore nature of the 4f-electrons and their high angular momentum.

Ln^{3+} and F^- in the quantum cluster were described by the all-electron SARC2-DKH-QZVP and DKH-DEF2-TZVPP basis sets, respectively.[72−74] Calculations were accelerated by using the Resolution of Identity (RI) for the Coulomb integrals in conjunction with autogenerated fitting basis sets (AutoAux) and the chain-of-spheres approximation (COSX) for the exchange integrals with default grids.[75−77] Capped point charges in the boundary region were represented by the charge of the respective ion plus the following ECP definitions: Li SD(2,SDF),[78] F SD(2,MWB),[79] Na SD(10,SDF),[78] and Y SD(28,MWB).[80]

To simplify the setup of the active space, the newly developed atomic valence active space (AVAS) functionality of Orca was used. In case this failed, first, a CASSCF calculation for the Ln^{3+} with one iteration was performed. Afterward, the desired 4f-orbitals were rotated into the active space. Subsequently, a full CASSCF calculation was performed, delivering the required results. In a second step, the preoptimized Ln^{3+} was combined with the remaining parts of the cluster via the Orca mergefrag feature, followed by the full calculation as described above. The mergefrag functionality reliably ensured that the 4f-orbitals stay within the active space but required user involvement (different to AVAS). The resulting output files, also containing the Orca inputs, including the respective geometries, are available at the RDR. Input files for cluster 10 (relying on AVAS) and cluster 12 (making use of mergefrag) are available in the Supporting Information.

The ab initio emission spectra were generated from energy and intensity data by a custom program based on libcerf version 1.5−1.19.[81] The stick spectra in the energy domain (cm^{-1}) were convoluted with pure Gaussian functions with a full width at half-maximum of 20 cm^{-1}. The simulated spectra were sampled with a resolution of 1 cm^{-1} in the energy domain, normalized to the largest signal, and subsequently transformed into the wavelength domain for comparison to the experimental photoluminescence spectra. The final simulated spectra were obtained as a weighted average over 14 individual spectra of the different clusters. The broadening parameter was estimated as the average from the two most intense lines of the experimental spectrum at 539.9 and 840.0 nm of β-$NaYF_4$:Er^{3+}. The raw data for the individual spectra are provided in the RDR.

METHODOLOGY

Chemicals. Yttrium oxide (Y_2O_3, 99.999%), erbium oxide (Er_2O_3, 99.99%), and thulium oxide (Tm_2O_3, 99.99%) were purchased from Alfa Aesar (Ward Hill, MA, U.S). Ytterbium oxide (Yb_2O_3, 99.998%), acetic acid (CH_3COOH, > 99.7%), sodium oleate ($CH_3(CH_2)_{16}COONa$, > 82%), ammonium fluoride (NH_4F, > 98%), oleic acid ($CH_3(CH_2)_7CH{=}CH(CH_2)_7COOH$, 90%), and 1-octadecene ($CH_2{=}CH\text{-}(CH_2)_{15}CH_3$, 90%) were purchased from Sigma-Aldrich (Oakville, ON, Canada). Hexane (analytical grade), hydrochloric acid (HCl, 36.5%), and acetone (analytical grade) were purchased from Fischer Scientific (Waltham, MA, USA). Ethanol (99%) was purchased from Commercial Alcohols Inc. (Toronto, ON, Canada). All chemicals were used as received.

https://doi.org/10.1021/acs.jpcc.5c06209
J. Phys. Chem. C 2025, 129, 20446−20464

Synthesis. The synthesis of UCNPs is briefly described in the following. Detailed information about all steps and quantities used is available in the Supporting Information (Synthesis of β-$NaYF_4$:Ln^{3+}UCNPs and Table S3). β-$NaYF_4$ UCNPs (co)doped with Er^{3+}, Tm^{3+}, and Yb^{3+} were synthesized following a synthesis route available in the literature.[82] The particles were grown from the respective Y as well as Er, Tm, and Yb acetate precursors [$Y(Ac)_3$] and [$Ln(Ac)_3$]. These precursors were obtained by treating the required amounts of the analogue oxides with a one-to-one mixture of acetic acid and water overnight. The acetate precursors together with sodium oleate and ammonium fluoride as sodium and fluoride sources, respectively, and oleic acid and 1-octadecene as surfactants and solvents were then used to first create ultrasmall (sub-5 nm) sodium-deficient α-phase UCNPs. After isolating the resulting particles through repeated precipitation and washing, they were redispersed in oleic acid and octadecene and reheated to 300 °C. Large β-phase UCNPs grew at this temperature over the course of 3 h from the gradually dissolving α-phase particles. After the successful synthesis and isolation of the UCNPs from the reaction mixture by precipitation, the UCNPs were additionally washed with hexane and ethanol. The resulting UCNPs, ca. 800 mg per synthesis, were stored in hexane until further use. To obtain ligand-free UCNPs, the oleate ligands were removed from the surface of the nanoparticles by treatment with hydrochloric acid overnight (see Supporting Information for details).[83]

Characterization. For the determination of the crystalline phase and phase purity via powder X-ray diffraction (XRD), a freshly stirred UCNP dispersion in hexane was dropped onto a glass slide and left to dry. Afterward, the nanoparticles were analyzed with a Bruker D8 Endeavor (Cu Kα, λ = 1.5401 Å) with the following settings: operating voltage and current of 44 kV and 40 mA with a step size of 0.02°, scanning speed of 1°·min^{-1}, and scan range of 20−60° 2Θ. Transmission electron microscopy (TEM) was used to determine the morphology and size of the UCNPs, employing an FEI Tecnai Spirit microscope (operating at 120 kV). Therefore, a diluted sample of the UCNPs in hexane was drop-cast onto a Formvar and carbon coated film on top of a 300-mesh copper TEM grid. The resulting TEM images were analyzed with FIJI/ImageJ (U.S. National Institutes of Health, Bethesda, MA, USA). The obtained mean sizes and associated standard deviations were plotted with OriginPro 2021 (OriginLab Corporation, Northampton, MA, USA). Photoluminescence spectroscopy was performed on ligand-free UCNPs. Therefore, the nanoparticles were precipitated by adding an equal amount of acetone to the aqueous UCNP dispersion, followed by centrifuging the mixture for 5 min at a RCF of 8346*g*. After the supernatant was discarded, the resulting pellet was spread out onto a piece of aluminum foil (2 × 2 cm), covered by an appropriately sized glass slide, and then set to completely dry overnight. The as-prepared samples were mounted into the sample holder of a QuantaMaster 8075−21 spectrofluorometer from HORIBA Scientific (Burlington, ON, Canada) combined with a close-cycle helium cryostat CS202*E-DMX-1AL from Advanced Research Systems (Macungie, PA, USA), controlled by a LakeShore (Westerville, OH, USA) 335 temperature controller. Measurements were started once the samples were cooled to 20 K or lower. The spectrometer itself was equipped with double grating emission monochromators, a red-extended photomultiplier detector R13456 PMT (250 to 1010 nm), and a liquid nitrogen cooled InGaAs detector (800 to 1599 nm). The Er^{3+}, Tm^{3+}, and Yb^{3+}-doped nanoparticles were excited using a 980 or 808 nm laser diode in continuous-wave mode with a maximum power density of 9.6 and 8.1 W·cm^{-2}, respectively. The low-temperature emission spectra showing single multiplet transitions were obtained by averaging over three individual emission spectra with an integration time of 1 s per step each. Slit widths for the emission side were 0.5 nm or smaller, and step sizes were likewise 0.5 nm or smaller. All data obtained from the measurements were plotted using OriginPro.

RESULTS AND DISCUSSION

Ordered $LiYF_4$:Ln^{3+}. *Energy Levels.* All clusters of $LiYF_4$:Ln^{3+} were evaluated in terms of the energy levels of the central Ln^{3+} provided by the ab initio calculations. The resulting energy levels of Er^{3+} up to 20,700 cm^{-1} (≈485 nm, $^4F_{7/2}$) are reported in Table 1. Energy levels for Tm^{3+} (up to 28,000 cm^{-1}, ≈355 nm, $^1D_2$) and Yb^{3+} are shown in Tables S1 and S2, respectively. Moreover, the full set of calculated energy levels, including all multiplets, for Er^{3+} and Tm^{3+} is provided in the RDR. The energy levels can be compiled in a separate file with the Python script *Calc_EnLev-OscStr.py*, also available there.

Compared to experimental values reported in the literature,[34,36−38] all energy levels for the three different Ln^{3+} showed a reasonable match. The root-mean-square error (RMSE) for Er^{3+} was determined to be 155 cm^{-1}, which was significantly larger than that for Tm^{3+} (64 cm^{-1}) and Yb^{3+} (47 cm^{-1}). The RMSE for Er^{3+} can be reduced to 60 cm^{-1} when the $^2H_{11/2}$ multiplet is removed from the RMSE calculation. The energy of the $^2H_{11/2}$ multiplet is overestimated by about 400 cm^{-1}. This should possibly be corrected for simulations of Er(-Yb) upconversion systems as the transitions from the $^2H_{11/2}$, $^4S_{3/2}$, and $^4F_{9/2}$ multiplets to the ground state are the three most important ones.[11,12] Nevertheless, the relative excitation energies of the NEVPT2 approach are of good quality. The varying quality of the multiplet energies, especially the $^2H_{11/2}$ multiplet, is probably due to different capture of dynamic correlation, state interactions, relativistic effects, and failures of the perturbation theory in general. Also, a shift of 2% (overestimation of 400 cm^{-1} at around 19,250 cm^{-1}) for the $^2H_{11/2}$ multiplet is still quite good for this level of theory.[84,85] Discrepancies for the other multiplets are less than 0.5%.

For Tm^{3+}, a greater deviation between computational and experimental energy levels was observed with increasing distance to the ground state (Table S1). Interestingly, the RMSE of Tm^{3+} (64 cm^{-1}) was remarkably close to the RMSE of Er^{3+} when the $^2H_{11/2}$ multiplet was excluded (60 cm^{-1}). Indeed, the RMSE for Yb^{3+} was also quite similar (47 cm^{-1}, Table S2). A deviation of 60 cm^{-1} corresponds to approximately 6 nm at a wavelength of 1000 nm (10,000 cm^{-1}) and 1.5 nm at a wavelength of 500 nm (20,000 cm^{-1}), since the nanometer scale is inversely proportional to the wavenumber scale. Such an observation points toward the general accuracy of the setup, while also indicating a larger error of about 400 cm^{-1} for the $^2H_{11/2}$ multiplet. In any case, the observed deviation should be kept in mind when employing calculated values where no reference data is available. For the $^2H_{11/2}$ multiplet, similar errors were also observed when comparing computational and experimental data for β-$NaYF_4$:Er^{3+} (see below). Overall, the RMSE of Yb^{3+}

https://doi.org/10.1021/acs.jpcc.5c06209
J. Phys. Chem. C 2025, 129, 20446−20464

Table 1. Calculated (Ab Initio and Fitted) and Experimental Crystal Field Energy Levels of $LiYF_4:Er^{3+}$

crystal field energy level[a] ($^{2S+1}L_J$)		this work (cm^{-1})	experiment[b34] (cm^{-1})	fitted[35] (cm^{-1})
$^4I_{15/2}$	1	0	0	−11
	3	41	17	8
	5	52	28	38
	7	79	57	60
	9	281	255	256
	11	324	290	298
	13	350	320	319
	15	365	355	352
$^4I_{13/2}$	1	6537	6540	6539
	3	6546	6545	6540
	5	6597	6585	6585
	7	6692	6680	6683
	9	6705	6704	6702
	11	6729	6731	6735
	13	6762	6745	6747
$^4I_{11/2}$	1	10264	10213	10215
	3	10282	10230	10230
	5	10355	10290	10284
	7	10359	10300	10305
	9	10375	10309	10312
	11	10402	10327	10323
$^4I_{9/2}$	1	12461	12364	12348
	3	12581	12486	12493
	5	12626	12540	12540
	7	12640	12568	12568
	9	12716	12663	12663
$^4F_{9/2}$	1	15414	15307	15306
	3	15441	15325	15325
	5	15452	15341	15343
	7	15527	15416	15418
	9	15555	15469	15471
$^4S_{3/2}$	1	18462	18433	18434
	3	18492	18492	18489
$^2H_{11/2}$	1	19562	19152	19170
	3	19574	19172	19192
	5	19617	19224	19233
	7	19684	19309	19303
	9	19697	19326	19313
	11	19719	19342	19329
$^4F_{7/2}$	1	20624	20571	20564
	3	20631	20573	20566
	5	20710	20662	20660
	7	20719	20671	20668
RMSE		155 (60)[c]		9

[a]The $^{2S+1}L_J$ labels are derived from the state with the highest weight after the QDPT-SOC treatment. M_J values and irreducible representations for all levels are available in the work of Couto dos Santos et al.[34] [b]The sample contained 1 mol % Er^{3+}, but the obtained values should still be comparable as properties of the Ln^{3+} are fairly independent of the Ln^{3+} concentration in the low-percentage doping regime.[86] [c]The value in brackets refers to the RMSE of only the quartet states ($S = 4$).

was the lowest among the three Ln^{3+} (47 cm^{-1}, Table S2). However, since only two multiplets with rather small energetic separation are present and the number of energy levels used for calculating this error was rather low, the RMSE value might not be as significant as those for Er^{3+} and Tm^{3+}.

Xiao et al. employed an adapted fitting procedure for the same dopant−host system to improve earlier predictions obtained with crystal field theory and generated energy levels with an RMSE of 9 cm^{-1} for Er^{3+} and Tm^{3+}.[34,35,37] Hence, their fit of energy levels was clearly superior to that of our ab initio results. However, obtaining the same precision is challenging when no fitting data are available. In this case, parameters must be taken from other structures or be obtained by a computational approach. An ab initio ansatz is possible for almost all systems where information about the crystal structure is available. It is also superior in the sense of adaptation. Once an input file has been designed, it can easily be adjusted for different structures (as demonstrated for β-$NaYF_4:Ln^{3+}$). Additionally, while we provided data for three different Ln^{3+} doped into $LiYF_4$, the corresponding input files can easily be tuned to predict properties for the other Ln^{3+} ions. To the best of our knowledge, no other wave function-based approaches have been reported to date that predicted crystal field energy levels for $LiYF_4$ doped with Er^{3+}, Tm^{3+}, or Yb^{3+}.

Finally, for $LiYF_4$, all Ln^{3+} are doped into sites with tetragonal S_4 point group symmetry.[34] For ions with an even number of electrons (i.e., Tm^{3+}), this results in some degenerate energy levels beyond the regular Kramer's degeneracy observed for ions with an odd number of electrons (i.e., Er^{3+} and Yb^{3+}).[87] This effect was correctly reproduced by our calculations, as seen, for example, for the $^3F_4$ multiplet (Table S1). The states 2 and 3 as well as 8 and 9 of that multiplet shared the same energy. Therefore, the number of observable energy levels was reduced from seven to five as predicted by crystal field theory. The same effect was apparent in the reference data. That being said, the precise energetic order of the degenerate levels did not exactly follow our values, e.g., for the $^3H_5$ multiplet.

Oscillator Strengths. In addition to the energy levels, the oscillator strengths between all crystal field energy levels were calculated. Table 2 lists (absorption) oscillator strengths obtained in this study in comparison to values from the literature for $LiYF_4$ doped with (A) Er^{3+}, (B) Tm^{3+}, and (C) Yb^{3+}.[39,40] The multiplet oscillator strengths calculated in this work were obtained by first averaging the oscillator strengths to a given excited state over the ground state multiplet components (crystal field energy levels). All components were assumed to be equally populated. These averaged oscillator strengths were then added across the excited state multiplet components. All oscillator strengths involving higher multiplets can be generated with the Python script *Calc_EnLev-OscStr.py* and the output file of the respective Ln^{3+} (both available in the RDR). Results for the individual crystal field oscillator strengths are also available there.

Two data sets for $LiYF_4:Er^{3+}$ were available in the literature (Table 2A) for benchmarking the values calculated by the ab initio model.[39,40] Interestingly, these two data sets differed by up to a factor of 3 for individual multiplet oscillator strengths. However, they followed the same trend in terms of the relative strength among the multiplets. Our calculated values mostly fell between the two sets of values reported in the literature. Their relative strengths also followed the trend observed previously. An exception was the $^2H_{11/2}$ multiplet, the oscillator strength of which was off by an order of magnitude. Thus, in general, the wave function for the $^2H_{11/2}$ multiplet appeared to converge poorly. Consequently, all derived properties suffered from the same shortcoming. The values fitted from the

https://doi.org/10.1021/acs.jpcc.5c06209
J. Phys. Chem. C 2025, 129, 20446−20464

Table 2. Calculated (Ab Initio and Fitted) and Experimental Absorption Multiplet Oscillator Strengths between the Ground State and Higher Multiplets of (A) Er^{3+}, (B) Tm^{3+}, and (C) Yb^{3+} Doped into $LiYF_4$[a]

(A) Er^{3+}					
$^4I_{15/2}$ →	this work	ref 39[b]		ref 40[c]	
		experiment	fitted	experiment	fitted
$^4I_{13/2}$	0.96	1.54	0.95	0.72	0.70
$^4I_{11/2}$	0.28	0.42	0.41	0.16	0.31
$^4I_{9/2}$	0.01	0.15	0.17	0.06	0.04
$^4F_{9/2}$	0.51	1.23	1.35	0.61	0.62
$^4S_{3/2}$	0.28	0.34	0.37		
$^2H_{11/2}$	0.14	2.36	2.68	1.29	1.26
$^4F_{7/2}$	0.88	1.01	1.42	0.47	0.93
(B) Tm^{3+}					
$^3H_6$ →				this work	
$^3F_4$				0.11	
$^3H_5$				0.64	
$^3H_4$				0.52	
$^3F_3$				0.82	
$^3F_2$				0.26	
$^1G_4$				0.02	
$^1D_2$				0.20	
(C) Yb^{3+}					
$^2F_{7/2}$ →				this work	
$^2F_{5/2}$				0.98	

[a]The oscillator strengths were multiplied by 1×10^6. [b]These values were obtained by averaging over four samples with an Er^{3+} concentration of 4.9 mol %, 13.6 mol %, 21.4 mol %, and 41.3 mol %, and no concentration effects were observed. [c]The sample contained 1 mol % Er^{3+}.

experimental data seem therefore a better choice for the oscillator strength of the ground to $^2H_{11/2}$ multiplet excitation.

Experimental oscillator strengths for $LiYF_4$ doped with either Tm^{3+} or Yb^{3+} are not available in the literature. However, oscillator strengths for $LiYF_4$:Er^{3+} provided reliable data for multiplets with correctly predicted energy levels (Tables 1 and 2). Moreover, energy levels for Tm^{3+} and Yb^{3+} (Tables S1 and S2, respectively) were in good agreement with the measured values. Therefore, the values listed in Table 2B,C are expected to accurately predict the oscillator strengths or, at least, the trends between the different multiplets.

Finally, oscillator strengths were also calculated for $LiYF_4$ doped with Er^{3+} as well as Yb^{3+} using the setup with the larger quantum cluster (see above). Values differed by at most 5% and on average by 3% compared to the setups with the smaller quantum cluster. Hence, a larger quantum cluster is not expected to drastically correct the energy levels or oscillator strengths. The respective data are provided in the RDR.

Overall, the general trend for the ab initio results of $LiYF_4$:Ln^{3+} was found to be quite positive. Crystal field energy levels and oscillator strengths were reproduced with good accuracy. This paves the way for examining the equivalent properties for a disordered crystal.

Disordered β-$NaYF_4$:Ln^{3+}. *Averaging Scheme.* Given its ordered structure with only one possible configuration per supercell, the analysis of data obtained for $LiYF_4$:Ln^{3+} was straightforward. Conversely, the disordered character of β-$NaYF_4$:Ln^{3+} required the development of a method that involves averaging over the results obtained for the different clusters. This was addressed by introducing a weighting factor to each cluster that reflects the probability of finding the specific ion arrangement of that cluster in the material (Table 3). This weighting factor is comprised of two parts: the statistical occurrence (degeneracy of the configuration) and the occupation probability (from the relative energy) of the cluster. A general overview that describes the steps required for obtaining the weighting factors is provided hereafter. The exact numbers for the calculation and the resulting factors can be found in the file *Energy-Levels_NaYF4-b_Ln* in the RDR.

Table 3. Calculation of Weighting Factors for the β-$NaYF_4$:Er^{3+} Clusters[a]

cluster n, (Na^+:Y^{3+} distribution)	degeneracy (deg.)	statistical occurrence (deg./64·x/3)	$\Delta E = E_n - E_{10}$ (kJ·mol^{-1})	Boltzmann distribution[b] $f(E_n)/f(E_{10})$	weighting factor (%)[c] (statistical occurrence Boltzmann distribution)
Wyckoff site: 1f		(x = 1)			
1 (2:0)	1	0.08	0.10	0.98	12.9
2 (1:1)	2	0.17	2.36	0.61	16.0
3 (0:2)	1	0.08	3.38	0.49	6.5
Wyckoff site: 1a		(x = 2)			
5 (5:1)	6	0.06	4.57	0.38	3.8
6 (4:2)	3	0.03	3.37	0.49	2.4
7 (4:2)	6	0.06	1.82	0.68	6.7
8 (4:2)	6	0.06	1.79	0.69	6.8
9 (3:3)	2	0.02	1.23	0.77	2.5
10 (3:3)	6	0.06	0.00	1.00	9.8
11 (3:3)	12	0.13	1.60	0.71	14.1
12 (2:4)	6	0.06	1.92	0.67	6.6
13 (2:4)	6	0.06	2.29	0.62	6.1
14 (2:4)	3	0.03	4.79	0.37	1.8
15 (1:5)	6	0.06	4.21	0.41	4.1

[a]The table groups the clusters according to the site at which they are centered, i.e., the 1f site (clusters 1 to 3) and the 1a site (clusters 5 to 15). E in the table refers to the energy of the underlying supercell as calculated in our previous work.[29] The energies (E) were obtained from supercells optimized by means of DFT with periodic boundary conditions.[29] [b]T_{syn} = 300 °C, the temperature at which the nanoparticles for this study were prepared. [c]Similar values were obtained for Tm^{3+} and Yb^{3+}. Detailed information for all three Ln^{3+} is available in the file *Energy-Levels_NaYF4-b_Ln* in the RDR.

https://doi.org/10.1021/acs.jpcc.5c06209
J. Phys. Chem. C 2025, 129, 20446−20464

Table 4. Calculated (Ab Initio) Crystal Field Energy Levels and Experimental Multiplets as well as Fitted Crystal Field Energy Levels (as Available in the Literature) of β-$NaYF_4$ Doped with (A) Er^{3+}, (B) Tm^{3+}, and (C) Yb^{3+}

(A) Er^{3+}

crystal field energy level ($^{2S+1}L_J$)		this work (cm^{-1})	experiment[32a] (cm^{-1})	fitted[33b] (cm^{-1})
$^4I_{15/2}$	1	0	0	0
	3	81		2
	5	136		4
	7	194		61
	9	242		72
	11	294		79
	13	340		79
	15	411		152
$^4I_{13/2}$	1	6586	6636	6519
	3	6619		6520
	5	6644		6521
	7	6676		6550
	9	6702		6553
	11	6737		6569
	13	6799		6625
$^4I_{11/2}$	1	10312	10226	
	3	10334		
	5	10353		
	7	10370		
	9	10400		
	11	10439		
$^4I_{9/2}$	1	12542	12419	
	3	12562		
	5	12639		
	7	12683		
	9	12739		
$^4F_{9/2}$	1	15450	15310	15170
	3	15477		15191
	5	15505		15220
	7	15531		15246
	9	15566		15265
$^4S_{3/2}$	1	18507	18529	18440
	3	18536		18493
$^2H_{11/2}$	1	19609	19229	19308
	3	19644		19314
	5	19661		19321
	7	19685		19326
	9	19704		19334
	11	19723		19343
$^4F_{7/2}$	1	20622	20524	
	3	20675		
	5	20731		
	7	20768		

(B) Tm^{3+}

crystal field energy level ($^{2S+1}L_J$)		this work (cm^{-1})	crystal field energy level ($^{2S+1}L_J$)		this work (cm^{-1})
$^3H_6$	1	0	$^3H_4$	1	12546
	2	9		2	12566
	3	54		3	12588
	4	80		4	12613
	5	122		5	12642
	6	149		6	12673
	7	187		7	12721
	8	223		8	12766
	9	246		9	12776
	10	296			
	11	314	$^3F_3$	1	14279
	12	405		2	14317
	13	417		3	14341
				4	14361
$^3F_4$	1	5634		5	14380
	2	5661		6	14398
	3	5689		7	14420
	4	5717			
	5	5730	$^3F_2$	1	14936
	6	5750		2	14951
	7	5761		3	15018
	8	5782		4	15061
	9	5823		5	15084
$^3H_5$	1	8207	$^1G_4$	1	21188
	2	8218		2	21222
	3	8267		3	21250
	4	8288		4	21300
	5	8317		5	21323
	6	8348		6	21351
	7	8377		7	21384
	8	8428		8	21446
	9	8440		9	21502
	10	8528			
	11	8539	$^1D_2$	1	27961
				2	27971
				3	28056
				4	28115
				5	28137

(C) Yb^{3+}

crystal field energy level ($^{2S+1}L_J$)		this work (cm^{-1})	crystal field energy level ($^{2S+1}L_J$)		this work (cm^{-1})
$^2F_{7/2}$	1	0	$^2F_{5/2}$	1	10126
	3	120		3	10265
	5	244		5	10466
	7	416			

[a]The sample contained 10 mol % Er^{3+} and 20 mol % Y^{3+} and values represent the position of the multiplet at maximum intensity. [b]The authors fitted the values from magnetization data, not optical spectra. Only a few multiplets were predicted.

The statistical occurrence reflects the fact that not all clusters are equally likely from stochastic considerations. When calculating its value, it was assumed that all disordered sites are independent of each other, and only the total composition of the respective cluster must stay constant. For example, there are six different possibilities of arranging five Na^+ and one Y^{3+} at the six disordered 1f sites around an Ln^{3+} doped into a 1a site (first and second column of Table 3). This arrangement was denoted as a 5:1 distribution. A 1:5 distribution involves one Na^+ and five Y^{3+}. Indeed, it does not matter at which exact position the single ion is placed. Hence, all six arrangements were combined into one 6-fold degenerate cluster (cluster 5 for

https://doi.org/10.1021/acs.jpcc.5c06209
J. Phys. Chem. C 2025, 129, 20446−20464

a 5:1 distribution and cluster 15 for the 1:5 distribution). Having said this, for a 4:2 (and 2:4) distribution, already 15 different arrangements exist. Also, for these and the other remaining distributions, two additional aspects must be considered. First, the location of the two Y^{3+} matters for the surroundings of the central ion, being either located in the same column along the *c*-axis or in two separate ones. Second, if these Y^{3+} ions are not in the same column, they can share the same c-coordinate or not. To account for these two aspects, the 15 arrangements were subdivided into three different clusters. These clusters were labeled 6, 7, and 8 for the 4:2 distribution, as well as 12, 13, and 14 for the 2:4 distribution, respectively (Table 3). Further, a degeneracy was assigned to each cluster. This scheme was once more repeated for a 3:3 distribution, resulting in three different clusters (9, 10, and 11) with their respective degeneracies. Finally, for the cluster centered at a 1f site, only two 1f disordered sites are part of the first anionic coordination sphere (Figure 3A). The distribution of Na^+ and Y^{3+} at these sites was dissected into three cases, i.e., a 2:0, 0:2, and 1:1 distribution (clusters 1, 2, and 3, respectively), with the latter being doubly degenerate.

Once the number of degenerate configurations for each cluster was established, it was divided by the overall number of configurations for this site, i.e., by 4 for a 1f-doped site and 64 for the 1a-doped site. Subsequently, this number was multiplied by a factor of 1/3 and 2/3 for the 1f and 1a site, respectively, representing the relative doping probability of an Ln^{3+} at this site. This is because in the β-$NaYF_4$ crystal, there are half as many 1f sites occupied by Y^{3+} as there are 1a sites occupied by Y^{3+} (Figure 1A). A Ln^{3+} can only be doped into sites occupied by Y^{3+}. Ultimately, this resulted in the statistical occurrence for each cluster, being the first factor to be used in the averaging scheme (Table 3, third column). It must be pointed out that the disorder at the 2h sites was not considered for this scheme, even though energetic differences for supercells with different 2h disorder are less pronounced than for the ones with 1f disorder.[29] It has previously been shown that for a 2 × 2 × 4 supercell, several hundreds of millions of configurations are possible when accounting for both disordered sites at the same time.[29] Instead, additional calculations were conducted to specifically investigate the influence of the disorder at the 2h sites (see below).

The second factor included in the averaging scheme was the occupation probability for each cluster. This factor is derived from the Boltzmann distribution since the supercells, from which the respective clusters were created, exhibited varying total energies. These energetic differences (Table 3, fourth column) led to different probabilities of forming the underlying supercell and, thus, the respective cluster. The Boltzmann distribution was calculated as

$$\frac{f(E_n)}{f(E_{10})} = \exp(-\Delta E_n \cdot (k_B \cdot N_A \cdot T_{syn})^{-1}) \quad (1)$$

with $f(E_n)/f(E_{10})$ being the occupation probability of the *n*th cluster relative to that of cluster 10, k_B the Boltzmann constant, N_A the Avogadro constant, and T_{syn} the synthesis temperature. Here, T_{syn} refers to the temperature at which the particles were synthesized. T_{syn} determines the energy available in the system and, therefore, the ability of the system to overcome energetic differences between the available clusters. Temperatures used in later calculations instead refer to the condition under which the particles were optically characterized. Additionally, during the synthesis of UCNPs, entropic and kinetic effects play critical roles, which were not accounted for here. However, the energetic difference by itself will be an influential parameter, which was accounted for. The calculated occupation probabilities obtained from these energetic differences make up the second part of the weighting scheme (Table 3, fifth column).

Ultimately, for each cluster, the statistical occurrence and occupation probability were multiplied and then expressed as a percentage relative to all of the weighting factors. The last column of Table 3 represents this value. Preliminary results for clusters 4 and 16 (representing a 6:0 and 0:6 distribution, respectively) indicated very low weighting factors. Therefore, these clusters were omitted from the calculations.

Given the few different clusters of the 1f site, cluster 2 (Figure 3A) had the highest weighting factor. Interestingly, the second in line is cluster 11. This is surprising as cluster 10 represents the go-to configuration when treating β-$NaYF_4$(:Ln^{3+}) as an ordered crystal consisting of a single configuration and as the configuration with the lowest energy. If this single cluster was an appropriate representative of the structure overall, its weighting factor is expected to be much higher. These results indicate that designing a crystal structure of β-$NaYF_4$ for theoretical calculations solely based on the supercell of cluster 10 might not yield results that are representative of the whole crystal. Rather, averaging over multiple clusters using weighting factors, as proposed in this work, is required to provide a more complete picture.

Energy Levels. Once the weighting factors were established, the weighted average of all clusters with respect to the weighting factors was calculated for the crystal field energy levels and oscillator strengths (see below). The resulting energy levels for β-$NaYF_4$ doped with (A) Er^{3+}, (B) Tm^{3+}, and (C) Yb^{3+} are presented in Table 4. Energy levels up to 20,800 cm^{-1} (≈485 nm, $^4F_{7/2}$) and 28,000 cm^{-1} (≈355 nm, $^1D_2$) are displayed for Er^{3+} and Tm^{3+}, respectively. The energy levels for the individual clusters are provided in the RDR (*Energy-Levels_NaYF4-b_Ln*). The full set of calculated energy levels (for all multiplets and all clusters) is available in the respective output files in the RDR and can be extracted using the Python script also deposited there.

Comparison of our data obtained for the crystal field energy levels of Er^{3+} with the positions of the maximum emission intensity of the corresponding multiplet as reported by Zhang et al. unveiled a satisfactory match (Table 4A),[32] though the different chemical composition of the sample by Zhang et al., i.e., β-$NaYF_4$ codoped with 10 mol % Er^{3+} and 20 mol % Yb^{3+}, should be noted. Moreover, the maximum intensity was not necessarily found at the barycenter of the multiplet. Therefore, this comparison should be treated as a first indication of the reliability of the ab initio results and not as proof of their qualitative accuracy. Similar to $LiYF_4$:Er^{3+}, prediction of the position of the $^2H_{11/2}$ multiplet resulted again in significantly higher energies than those obtained experimentally. Unfortunately, to the best of our knowledge, no other data on experimental crystal field levels for any of the three lanthanide ions are available in the literature. Also, Er^{3+} is the only lanthanide for which theoretical data for at least some crystal field energy levels was reported.[33] That being said, good agreement with this data set was observed (Table 4A).

To allow for better comparison of ab initio and experimental data, several UCNPs (co)doped with Er^{3+}, Tm^{3+}, and Yb^{3+} in various concentrations were synthesized following a procedure

https://doi.org/10.1021/acs.jpcc.5c06209
J. Phys. Chem. C 2025, 129, 20446−20464

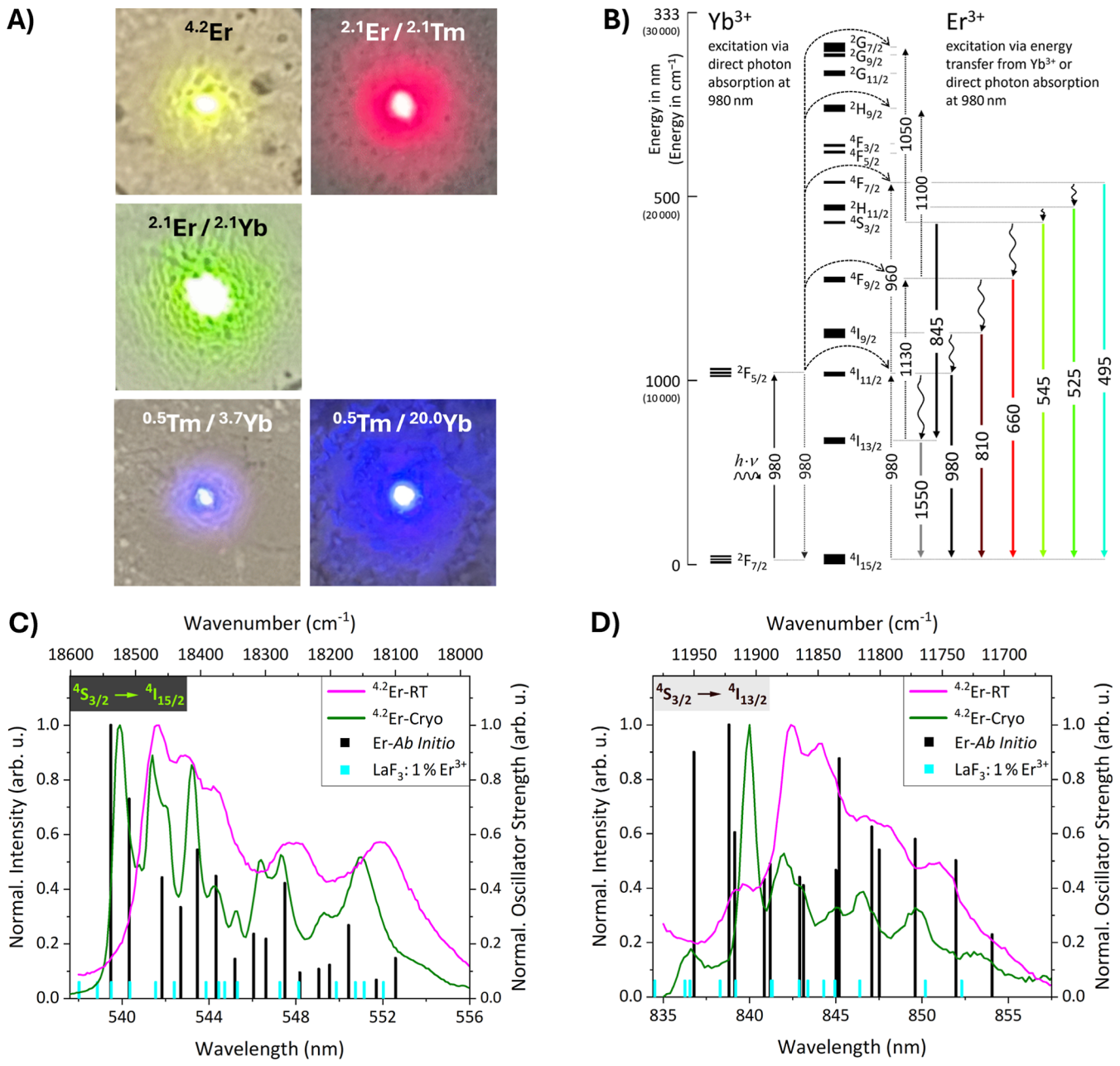

Figure 4. (A) Photographs taken with a smartphone camera of various β-$NaYF_4$:Ln^{3+} UCNPs deposited on a glass slide (ca. 2 × 2 cm) upon excitation with a hand-held 980 nm laser. (B) Energy level diagram showing probable upconversion and downshifting pathways for Er^{3+} together with Yb^{3+} under 980 nm excitation. (C,D) Photoluminescence spectra recorded at room temperature (color code magenta) as well as 20 K (color code olive) of β-$NaYF_4$ UCNPs doped with 4.2 mol % Er^{3+} showing the (C) $^4S_{3/2} \rightarrow {}^4I_{15/2}$ and (D) $^4S_{3/2} \rightarrow {}^4I_{13/2}$ transition, respectively. Excitation wavelength (λ_{ex}) = 980 nm; power density = 9.6 W·cm^{-2}. Vertical bars in black represent the averaged positions of the crystal field transitions of the respective multiplets according to ab initio calculations. The heights of the bars are equal to the averaged oscillator strengths for the respective crystal field transitions. Vertical bars in cyan represent the positions of crystal field transitions obtained from experimental literature data for LaF_3:1 mol % Er^{3+}.[30] The heights of these bars were chosen arbitrarily.

reported by Rinkel et al. (see Experimental Details and Supporting Information).[82] The single-doped samples (i.e., samples $^{4.2}$Er and $^{4.2}$Tm) almost exactly matched the simulated particles in the embedding model in terms of dopant concentration. The codoped samples (i.e., samples $^{2.1}$Er/$^{2.1}$Yb, $^{2.1}$Er/$^{2.1}$Tm, $^{0.5}$Tm/$^{3.7}$Yb, and $^{0.5}$Tm/^{20}Yb) were synthesized as they allowed for more flexible excitation wavelength choice and thus the observation of additional transitions, otherwise not possible due to overlap between excitation and emission wavelength, for example, the $^4I_{11/2}$–$^4I_{15/2}$ transition of Er^{3+} at 980 nm, the $^2F_{5/2}$–$^2F_{7/2}$ transition of Yb^{3+} at 980 nm, and the $^3H_4$–$^4H_6$ transition of Tm^{3+} at 820 nm.

An overview of all synthesized samples, including their chemical compositions and sizes, is given in Table S3. X-ray powder diffraction (XRD) analysis confirmed that all UCNPs crystallized in the hexagonal (β) phase of $NaYF_4$ (Figure S1). Transmission electron microscopy (TEM) images showed monodisperse nanoparticles with sizes ranging from 57 to 109 nm and narrow size distribution (Figures S2 and S3). The

https://doi.org/10.1021/acs.jpcc.5c06209
J. Phys. Chem. C 2025, 129, 20446−20464

nanoparticles exhibited a characteristic morphology of hexagonal platelets. Photographs taken with a smartphone camera of five of the six samples under excitation with a hand-held 980 nm laser are shown in Figure 4A, showing the characteristic green, red, and blue upconversion emission of Er^{3+} and Tm^{3+}-doped UCNPs. The purely Tm^{3+}-doped UCNPs did not show any visible emission, neither under 980 nor 808 nm excitations with the hand-held laser diodes. This was to be expected, given the lack of Yb^{3+} as a codopant acting as a sensitizer. Moreover, it has been shown that for high Tm^{3+} dopant concentration (such as our 4.2 mol %), cross-relaxation processes often result in the loss of emission intensity.[88,89]

Low-temperature and room temperature photoluminescence spectra of the synthesized UCNPs, exhibiting the characteristic upconversion and downshifting emission bands of Er^{3+}, Tm^{3+}, and Yb^{3+} under 980 or 808 nm excitation, are provided in Figures S4−S6. An overview of the samples and color codes for the spectra recorded at the different temperatures is provided in Table S4. The origins of the mentioned transitions are shown in detail in the energy level and energy transfer diagram for Er^{3+}−Yb^{3+} codoped systems in Figure 4B. Partial energy level diagrams for Tm^{3+} and Yb^{3+} are shown in Figures S7 and S8.

The following discussion of experimental spectra in comparison with theoretical data will focus on the photoluminescence spectra of β-$NaYF_4$ UCNPs (co)doped with Er^{3+}. The reason for this is that Er^{3+}, with its uneven number of electrons and due to a lack of a magnetic field, features multiplets that split into a small number of crystal field energy levels. This is especially true for the $^4S_{3/2}$ multiplet (two Stark sublevels), which at the same time is also one of the main emitting states of Er^{3+}-doped UCNPs. This reduced the number of observable crystal field transitions. Additionally, the relatively high emission intensity made it possible to resolve individual transitions in the recorded signal. On the other hand, most multiplets of Tm^{3+} split into many more crystal field energy levels, and thus, many more transitions form the observed signal. Resolving the multiplet into individual crystal field transitions was therefore not achievable.

Intensity-normalized low-temperature spectra of Er^{3+}-doped samples ascribed to the respective Er^{3+} f−f transitions are depicted in Figure S9. The analogous spectra for samples (co)doped with Tm^{3+} and Yb^{3+} are provided in Figures S10 and S11, respectively. The exact upconversion and population dynamics and shapes of the spectra are not relevant for the comparison with the theoretical data as discussed in the following. Indeed, as expected, changes with respect to spectral shape and position between the differently doped samples were minor. The observed similarities conveniently allow for a transfer of knowledge gained from these samples to other UCNPs with similar doping concentrations—particularly to those that are most commonly considered in the field, i.e., 2 mol % for Er^{3+}, 20 mol % for Yb^{3+}, and 0.5 mol % for Tm^{3+}.[11,12]

None of the recorded photoluminescence spectra provided clearly separated crystal field transitions. This is because all crystal field transitions of the involved multiplets for a specific transition overlap (especially for multiplets with large J values). Additionally, the disordered lattice results in a variety of transitions from individual Ln^{3+}. Both effects combined result in the observed spectra. Indeed, to still prove that the theoretical results are a good fit, the computed transition positions were added as black bars to each spectrum in Figures S9 and S10 as well as Figure S11 for Er^{3+} and Tm^{3+} as well as Yb^{3+}, respectively. It is important to note that these transition positions represent the weighted average over all clusters instead of individual clusters. For most transitions, the experimental emission range and theoretical positions showed good agreement for all three Ln^{3+}. For the $^2H_{11/2}$−$^4I_{15/2}$ transition of Er^{3+}, Figure S5A, however, the predicted transition positions shifted toward higher wavenumbers by about 350 cm^{-1}. This is in line with the observation that the $^2H_{11/2}$ multiplet is predicted at energies that are too high. The difference between the emission range of the experimental photoluminescence spectra and the calculated transition wavenumbers for all other multiplets and those of Tm^{3+} and Yb^{3+} was in the order of 60 cm^{-1} (1.5 nm at 500 nm, 6 nm at 1000 nm). The discrepancy between the data sets is, therefore, similar to the discrepancy reported above for $LiYF_4$:Ln^{3+}.

While it was not possible to resolve all individual crystal field transitions for any transition, for two transitions of Er^{3+}, the number of crystal field energy levels involved was low enough to almost identify the expected number of crystal field transitions (peaks). Especially in the case of spectra recorded from β-$NaYF_4$ UCNPs doped with 4.2 mol % Er^{3+} at low temperature (olive line in Figure 4C,D), the expected 16 peaks of the $^4S_{3/2} \rightarrow {}^4I_{15/2}$ transition and 14 peaks of the $^4S_{3/2} \rightarrow {}^4I_{13/2}$ transition could mostly be identified upon close inspection. Added to Figure 4C,D are the average positions of the respective crystal field transitions as black bars, together with their averaged oscillator strengths as the height of the bars according to the ab initio calculations. Their positions and heights mostly overlap with the positions of the experimentally observed peaks. This constitutes a first indication of the validity of the proposed disordered model.

Room temperature photoluminescence spectra for the $^4S_{3/2} \rightarrow {}^4I_{15/2}$ and $^4S_{3/2} \rightarrow {}^4I_{13/2}$ transition are depicted in Figure 4C,D, respectively. Both room temperature spectra are shifted by several nanometers to longer wavelengths compared to the respective low-temperature spectra. The significant peak shift of Er^{3+} upon cooling has been reported previously and was ascribed to the contraction of the crystal lattice at low temperature.[90,91] This explanation fits nicely to the observation that the low-temperature peaks were of better match with the ab initio results, since the DFT crystal structure optimizations, on which these ab initio calculations were based on, did not incorporate temperature-induced effects.[29]

Overall, the computationally predicted and averaged crystal field transitions were in very good agreement with the experimental results. Furthermore, the transitions calculated at an ab initio level of theory also matched the low-temperature spectra in Figure 4C,D better than do the experimental transitions measured for Er^{3+} doped into a different host material (LaF_3).[30] This underlines the predictive power of the computational model presented in this work. Moreover, the averaged relative oscillator strengths matched the experimental values well, which are discussed further below.

Influence of the 1f-Disorder. So far, only averaged transition positions and averaged oscillator strengths from the ab initio calculations were compared to the respective spectra. Averaging of the results for the different clusters produces clean data sets that can easily be displayed and compared to other data sets. However, the "mean structure" that is invoked by the averaging does in fact not exist as the

https://doi.org/10.1021/acs.jpcc.5c06209
J. Phys. Chem. C 2025, 129, 20446−20464

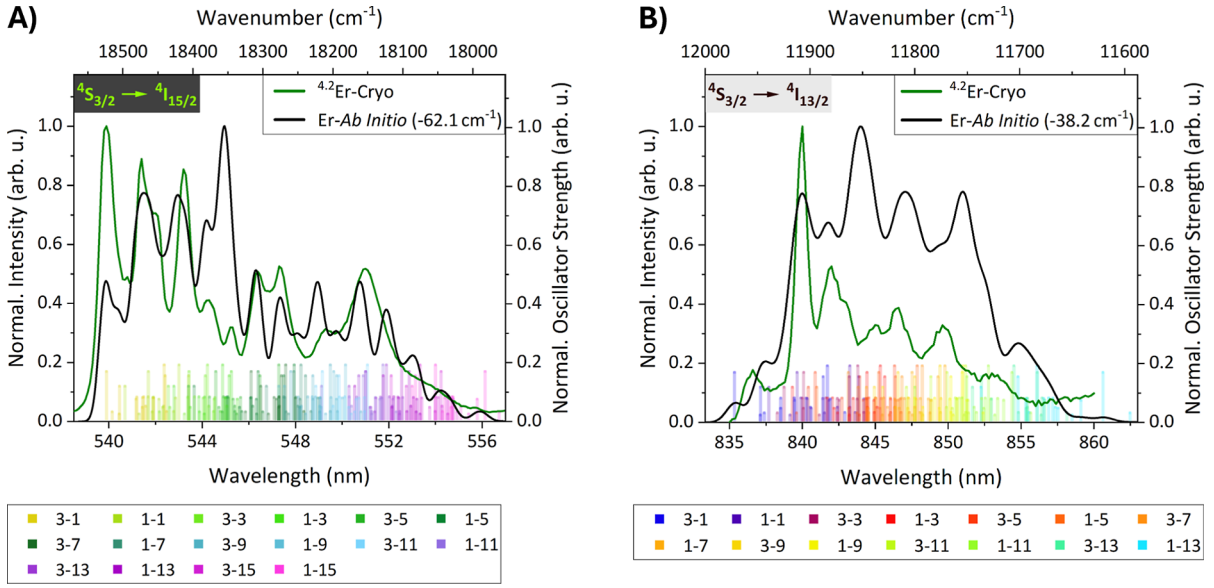

Figure 5. Low-temperature photoluminescence (20 K, color code olive) and ab initio spectra (color code black) of Er^{3+}-doped β-$NaYF_4$ for the (A) 545 nm ($^4S_{3/2} \rightarrow {}^4I_{15/2}$) and (B) 845 nm ($^4S_{3/2} \rightarrow {}^4I_{13/2}$) transition. The ab initio spectra in (A,B) were shifted by -62 cm^{-1} and -38 cm^{-1}, respectively. Small semitransparent bars indicate the positions of the crystal field transitions for individual clusters. Each of the 14 clusters generates (A) 16 and (B) 14 individual transitions. Their labeling in the legend follows the scheme n_1-n_2" where n_1 indicates the crystal field energy level of the initial multiplet ($^4S_{3/2}$) and n_2 that of the final multiplet ($^4I_{15/2}$). The height of the smaller bars represents the weighting factor of the cluster they originate from (not their oscillator strength), and bars with the same height were retrieved from the same cluster.

individual clusters do not interconvert on the time scale of the experiment. For truly meaningful comparisons with the experimental data, the contribution of each cluster needs to be accounted for individually, while retaining the weighting factors for the respective clusters. Such an approach can be insightful, for example, when predicting an emission spectrum for a disordered structure.

To this end, the low-temperature photoluminescence spectra shown in Figure 4C,D were combined with the predicted results for the transition positions from each cluster individually (Figure S12A,B, respectively). Herein, the short semitransparent bars represent the individual transition positions. A color code was applied so that each bar can be retraced to its respective crystal field transition (Figure S13). To also give a sense of the oscillator strengths of the individual transitions, the large bars from Figure 4 were retained (recolored large opaque bars in Figure S12).

The height of a large bar therefore represents the oscillator strength of all small bars of the same color. The heights of the small bars instead represent their weighting factors.

In Figure S12A,B, the influence of the 1f-disordered sites on the positions of the crystal field transitions is clearly visible. The transitions are spread considerably along the whole emission range of the experimental spectra for the respective multiplet transitions. Indeed, they reproduce the experimental emission range rather accurately. The experimental spectra should therefore also be the result of an overlap of all the individual contributions. This could also explain the inability to resolve the peaks of the experimental spectra further. To test this hypothesis, individual crystal field oscillator strengths were assigned to the individual crystal field transitions and, together with the transition positions, used for simulating the respective emission spectra.

Crystal Field Oscillator Strengths. With the information about the individual clusters available, both their energy levels, and the oscillator strengths between them, it was possible to reproduce the experimental spectra to a very satisfying degree. For each cluster, a spectrum was created by convoluting the crystal field transitions and oscillator strengths with pure Gaussian functions. Next, a single spectrum was received by averaging the individual spectra. Finally, the ab initio spectra were shifted and the theoretical spectra shown in Figure 5A,B (black line) were obtained. When generating the ab initio spectra, it was assumed that the two crystal field levels of the $^4S_{3/2}$ multiplet had equal population (= 1). Note that it is not straightforward to select a specific temperature for a sample that, on one hand, is cooled to 20 K using a cryostat setup and, on the other hand, exhibits excitation laser-induced heating (excitation power density: 10 $W \cdot cm^{-2}$). To account for such temperature effects, future investigations need to probe whether a different temperature and, therefore, Boltzmann population might be more appropriate. The spectral shift was introduced so that the relative separation of the crystal field transitions and the overlap between the experimental and ab initio spectra could be observed better. The ab initio spectra in Figure 5A,B were shifted based on the first dominant transition of each set of spectra. Details on the values for the different clusters can be found in the files *Spectrum_NaYF4-b_Er-545nm* and *Spectrum_NaYF4-b_Er-845nm* in the RDR.

The theoretical spectra showed promising agreement with the experimental ones after slightly shifting them to lower wavenumbers. These shifts correspond to less than 0.4% of the band's average wavelengths and are motivated by the discrepancy between experimental and calculated results discussed above. Shifting the spectrum allows observation of the remarkable overlap between the computed and measured spectra on a relative scale. All transition energies were shifted by a constant value; therefore, the shape of the calculated spectrum stayed the same. As mentioned above, a shift of less than 1% for the assessed system is still quite good for this level of theory.[84,85]

https://doi.org/10.1021/acs.jpcc.5c06209
J. Phys. Chem. C 2025, 129, 20446−20464

The crystal field oscillator strengths are similarly predicted qualitatively correct, although slight misalignments still exist for some of the peaks. It is important to note that the crystal field oscillator strengths (but also the crystal field energy levels) seem to be highly susceptible to the ion arrangement in the disordered lattice. Their specific values for the oscillator strengths varied significantly from cluster to cluster, by more than 1 order of magnitude. Detailed information is available in the file *Oscillator-Strengths_NaYF4-b_Ln* in the RDR. To visualize this sensitivity to the environment, the low-temperature emission spectrum of the $^4S_{3/2} \rightarrow {}^4I_{15/2}$ transition for β-$NaYF_4$:Er^{3+} and its ab initio counterpart of the averaged results are combined with ab initio spectra for individual clusters (Figure S14A). In particular, the spectra of clusters 2 and 11, with the two highest weighting factors, and cluster 10, commonly used in other works, are displayed in this figure. The individual spectra predicted transitions at energies that are too high or low, left gaps where none are in the experimental emission spectrum, and misrepresented the respective oscillator strengths. Thus, results from the individual clusters did not provide theoretical spectra with similar agreement to the experimental data, and only the averaged result provided a good fit.

Overall, the crystal field energy levels and oscillator strength from the ab initio results showed a crucial dependency on the actual positions of the F^- around the Ln^{3+}. Including disorder into a computational model was therefore identified as a prerequisite for obtaining realistic predictions of the photoluminescence spectra. These findings lend great credibility to the computational model but also the setup including disorder.

Multiplet Oscillator Strengths. Because of the way the experimental photoluminescence spectra were recorded, relative intensities of different multiplets cannot be directly compared to the computed oscillator strengths. The population of the initial state (the excited multiplet) in an upconversion emission spectrum is unknown and is unlikely to be equal among the different excited multiplets involved. Indeed, oscillator strengths are therefore often determined from absorption spectra, where transitions originate from the ground state (multiplet).[32] Therefore, the calculated multiplet (absorption) oscillator strengths for Er^{3+} were compared to those of a data set available in the literature. Table 5 lists multiplet absorption oscillator strengths of β-$NaYF_4$ doped with (A) Er^{3+}, (B) Tm^{3+}, and (C) Yb^{3+} calculated in this work and taken from the literature for comparison.[32] The multiplet oscillator strengths were calculated as described for $LiYF_4$. Additional values for the transitions not involving the ground state multiplet can be found in the file *Oscillator-Strengths_NaYF4-b_Ln* in the RDR. All remaining oscillator strengths (involving higher multiplets) can be generated with the Python script *Calc_EnLev-OscStr.py* and the output file of the respective Ln^{3+} (both available in the RDR). Oscillator strengths of all crystal field transitions for all clusters are also available there.

Agreement between the calculated values for β-$NaYF_4$:Er^{3+} and the experimental data of Zhang et al. for the same dopant−host system is not as good as for $LiYF_4$ and its respective reference data (Table 5A).[32] The trends for β-$NaYF_4$:Er^{3+} by the ab initio model and the actual values of the experimental data did not show a good match, although the magnitudes of the values were similar. Remarkably, however, the computed results for β-$NaYF_4$:Er^{3+} very closely matched those calculated for $LiYF_4$:Er^{3+} (Table 2A), both in trend and actual value. This is down to the fact that the oscillator strength for the $^2H_{11/2}$ multiplet is severely underestimated in both data sets. Additionally, crystal field spectra calculated from our ab initio data for β-$NaYF_4$:Er^{3+} showed very good agreement for the two multiplets examined (Figure 5A,B, as well as the discussion above). Furthermore, oscillator strengths reported by Villanueva-Delgado et al. for β-$NaGdF_4$:Er^{3+} reproduced the trends observed for the multiplet oscillator strengths of $LiYF_4$:Er^{3+} and β-$NaYF_4$:Er^{3+} predicted through the ab initio calculations.[92] The same observations were made for the multiplet oscillator strength of Yb^{3+} (Table 5C). The computed values for β-$NaYF_4$ and $LiYF_4$ were similar and of the same order of magnitude as the experimental results for β-$NaGdF_4$. The experimental value reported by Zhang et al. for β-$NaYF_4$:Yb^{3+}, however, is more than 1 order of magnitude higher.[32] Reasons for the relatively large disagreement between the ab initio and experimental multiplet oscillator strengths of β-$NaYF_4$(:Er^{3+}, Tm^{3+}, and Yb^{3+}) are not clear and require further investigation.

Finally, the multiplet oscillator strengths varied only very slightly from cluster to cluster. This observation is remarkable as it is opposed to the trends observed for the crystal field oscillator strengths, which differed significantly from cluster to cluster. Also, the lack of variation in multiplet oscillator strength suggests that disordered materials do not induce further emission based on stronger oscillator strengths if the available doping sites are already of lowest symmetry (see the file *Oscillator-Strengths_NaYF4-b_Ln* in the RDR for individual values). Therefore, if one is interested in only predicted multiplet oscillator strengths, it might be sufficient to run a single calculation even for a disordered structure, although it is

Table 5. Calculated (Ab Initio and Fitted) and Experimental Absorption Oscillator Strengths between the Ground State and Higher Multiplets of β-$NaYF_4$ Doped with (A) Er^{3+}, (B) Tm^{3+}, and (C) Yb^{3+}[a]

(A) Er^{3+}			
$^4I_{15/2} \rightarrow$	this work	experiment[32b]	fitted[32b]
$^4I_{13/2}$	1.01	1.33	0.86
$^4I_{11/2}$	0.30		0.40
$^4I_{9/2}$	0.02	0.22	0.17
$^4F_{9/2}$	0.59	0.12	0.13
$^4S_{3/2}$	0.31	0.36	0.34
$^2H_{11/2}$	0.23	0.62	0.42
$^4F_{7/2}$	0.98	0.16	0.13
(B) Tm^{3+}			
$^3H_6 \rightarrow$		this work	
$^3F_4$		0.14	
$^3H_5$		0.66	
$^3H_4$		0.55	
$^3F_3$		0.87	
$^3F_2$		0.28	
$^1G_4$		0.03	
$^1D_2$		0.24	
(C) Yb^{3+}			
$^2F_{7/2} \rightarrow$	this work	experiment[32a]	
$^2F_{5/2}$	1.60	30.72	

[a]The oscillator strengths were multiplied by 10^6. [b]Values are from a sample containing 10 mol % Er^{3+} and 20 mol % Yb^{3+}. The transition from the ground state of Er^{3+} to the $^4I_{11/2}$ multiplet could therefore not be observed.

https://doi.org/10.1021/acs.jpcc.5c06209
J. Phys. Chem. C 2025, 129, 20446−20464

still recommended to pick a configuration of that structure with a high weighting factor. In general, the chosen ab initio approach is well-suited for predicting multiplet oscillator strengths for the materials under consideration.

Influence of the 2h Disorder. So far, only the influence of the disorder at the 1f sites onto the optical properties of the Ln^{3+} was examined. However, it was shown previously that also the second disordered site, 2h, has considerable influence on the structure of the host crystal.[29] Changes at these sites are, in fact, at least as probable as at the 1f sites. This is due to the resulting clusters being generally less unfavorable in terms of total energy compared to the energetic differences of the 1f clusters discussed so far.[29] It was therefore expected that a similar influence on the optical properties of the Ln^{3+} could be observed.

To obtain first insights into the significance of the 2h disorder, three more embeddings from clusters with the same 1f configuration but different 2h configurations were created and subsequently submitted to the ab initio calculation. While any selection of three configurations out of millions of possible ones only provides an estimate, these configurations were chosen to represent the relevance of all 2h configurations available. More specifically, the first two clusters, i.e., Na1 and Na2, exhibit a balanced distribution of the six Na^+ at the available 2h sites, where three Na^+ are shifted along the +*c*-axis and three along the −*c*-axis by equal amounts. Na1 and Na2 differ in exactly which Na^+ shifts in either direction. Such a distribution is like placing each three Na^+ and Yb^{3+} at the six 1f disordered sites around a central Ln^{3+}. Of the 64 possible configurations (2^6), 20 configurations should follow such a distribution according to stochastic considerations (Table 3). This makes Na1 and Na2 good representatives of very likely Na^+ arrangements at the 2h sites. The third configuration, Na3, represents a more extreme case, where all six Na^+ ions shift along the +*c*-axis. This is similar to having either six Na^+ or six Yb^{3+} at the six 1f disordered sites (2 of 64 possible configurations). The motivation for this arrangement was to test whether such an imbalanced distribution would result in a severe change in the properties of central Ln^{3+}. The individual results of the three clusters are shown in the RDR, files *Energy-Levels_NaYF4-b_Ln*, *Oscillator-Strengths_NaYF4-b_Ln*, and *Spectrum_NaYF4-b_Er-545nm* under the keywords Na1, Na2, and Na3.

Our previous work showed that the disorder at the 2h sites induced similar local distortions of the F^- closest to the Ln^{3+} doping site as the 1f disordered sites.[29] The data reported here confirmed that these changes have a related effect on the crystal field energy levels and oscillator strengths of the Ln^{3+} as well. The ab initio photoluminescence spectra of the individual Na-disordered clusters (Figure S14B) exposed the same features as reported for the Na^+−Y^{3+} disordered clusters (Figure S14A): transitions were predicted at too high or low energies, gaps were left between transitions, and oscillator strengths were only roughly representing the experimentally observed trends. Interestingly, even for the highly distorted Na^+ distribution at the 2h sites, i.e., configuration Na3, only changes already present for Na1 and Na2 were observed, meaning that this imbalanced distribution did not invoke any additional changes.

Photoluminescence spectra generated from a model including both the 2h and 1f disorder could possibly show even better agreement with experimental emission spectra. However, accounting for all possible distributions of Na^+ at the 2h site results in millions of configurations.[29] To tackle this challenge, a large degree of automatic input generation and data analysis are likely required. Additionally, structural optimization probably must be performed using an iteratively trained machine-learning model instead of a periodic boundary condition DFT calculation for every disordered configuration. Such an approach is beyond the scope of this work but might be attractive for researchers focusing on emerging technologies.

Nano versus Bulk. In a recent investigation, Shi et al. demonstrated that photoluminescence properties of highly (>5 mol %) Ln^{3+}-doped ultrasmall nanoparticles are predominantly determined by Ln^{3+} that are located at the surface.[93] This seems to contrast our finding that the emission spectra of UCNPs can be accurately modeled by a bulk model of the nanoparticle material. Yet, the difference in size between the UCNPs studied by Shi et al. and by us should be kept in mind (5 versus 70 nm), having a significant influence on the number of surface versus bulk sites. Indeed, the authors reported a significant change in luminescence behavior when a passivating shell was added to their nanoparticles.[93] This change was attributed to the Ln^{3+}, which previously were situated at the surface, now being in an environment that more closely resembles the bulk part of the particle. Although no shell was added to our nanoparticles, their relatively large size reduces surface effects and, hence, the influence of surface Ln^{3+} on the overall properties. Importantly, UCNPs envisioned for real-life application typically include a passivating (undoped) shell that, among others, increases their luminescence intensity.[18,94] The work by Shi et al. suggests that such nanoparticles have their Ln^{3+} reside at bulk sites. Our computational results are in line with that, providing very good agreement between experimental and computed spectra using relatively large UCNPs and bulk conditions, respectively. Therefore, we expect that our bulk-based computational strategy will be well-suited to predicting luminescence properties of diverse UCNPs, especially those that exhibit a core/shell architecture.

CONCLUSION

Crystal field energy levels (and thereby transition energies) and corresponding crystal field oscillator strengths were predicted for three Ln^{3+}, i.e., Er^{3+}, Tm^{3+}, and Yb^{3+}, doped into an ordered ($LiYF_4$) and a disordered (β-$NaYF_4$) host lattice. This was achieved by using previously geometry optimized supercells of these structures for creating a variety of embedded clusters with Ln^{3+} in the center of the clusters. The three parts of the embedding (quantum cluster, boundary region, and point charge field) were treated with different quantum-chemical precision by the Orca program.

Results obtained for $LiYF_4$:Ln^{3+} and β-$NaYF_4$:Ln^{3+} were compared to experimental and semiempirical reference data from the literature. Almost all calculated crystal field energy levels showed good agreement when compared with data in the literature, with RMSEs of 67 cm^{-1} or lower. Calculated multiplet oscillator strengths for $LiYF_4$:Ln^{3+} were also in close agreement to experimental values, except for the $^2H_{11/2}$ multiplet of Er^{3+}. For β-$NaYF_4$:Ln^{3+}, the calculated multiplet oscillator strengths did vary more significantly from a literature value, although our ab initio values followed the same trends as those found in other structures. Most interestingly, a comparison of the ab initio crystal field energy levels and oscillator strengths with experimental values specifically obtained for this study showed particularly good agreement.

https://doi.org/10.1021/acs.jpcc.5c06209
J. Phys. Chem. C 2025, 129, 20446−20464

This was achieved by generating experimental and computational photoluminescence spectra of the same dopant−host combination.

All of this was possible by employing a high-level wave function-based ab initio computational model and, more importantly, by accounting for the disorder of the β-$NaYF_4$ host crystal. The disorder exhibited by its lattice was captured by creating several local configurations (clusters) of the crystal structure. Indeed, it was shown that for a disordered structure, if treated as such, the employed computational model can reliably predict the optical properties of Ln^{3+} doped into the crystal. It became apparent that for maximum accuracy of the crystal field energy levels, it is important to account for the results obtained from all the clusters available individually. This includes assigning appropriate weighting factors that represent the probability of occurrence of the specific cluster in a real nanoparticle. It was further demonstrated that the disorder experienced by the host lattice has a considerable influence on the properties of a Ln^{3+}-doped crystal. Using only one single configuration of a disordered structure will most likely not result in meaningful results. Accounting for the disorder of β-$NaYF_4$, and other disordered structures, should therefore be a top priority for any computational model if an exact understanding of the material is required.

Knowledge of the (crystal field) energy levels and oscillators strengths is crucially important when trying to understand what governs the efficiency of an, for example, upconverting material. Being able to theoretically predict these properties has therefore the potential to foster the design of new, more efficient upconverting dopant−host systems. As such, this study should serve as a significant steppingstone on the path of accurately modeling properties of Ln^{3+} doped into disordered materials or other optically active or magnetic materials showing signs of disorder. Finally, further research is necessary to show to what extent energy transfer, a key requirement for ETU in upconverting particles, is influenced by this type of disorder.

■ ASSOCIATED CONTENT

Data Availability Statement

The following additional material is available in an RDR at 10.6084/m9.figshare.29391644: Env input files for all clusters; Orca output files for all clusters; energy levels for all β-$NaYF_4$ clusters; oscillator strengths between multiplets for β-$NaYF_4$; Python script for extracting additional energy levels and oscillator strengths from the output files; and ab initio spectra for the 545 and 845 nm transition for all clusters.

Supporting Information

The Supporting Information is available free of charge at https://pubs.acs.org/doi/10.1021/acs.jpcc.5c06209.

> Energy levels for $LiYF_4$ doped with Tm^{3+} and Yb^{3+}; additional experimental details; X-ray diffractograms, TEM images, size distributions, and photoluminescence spectroscopy data for all synthesized UCNPs; Env input files for $LiYF_4$:Er^{3+} and cluster 10 of β-$NaYF_4$:Er^{3+}; and Orca input files for cluster 10 and cluster 12 of β-$NaYF_4$:Er^{3+} (PDF)

■ AUTHOR INFORMATION

Corresponding Authors

Eva Hemmer − *Department of Chemistry and Biomolecular Sciences, University of Ottawa, Ottawa, Ontario K1N 6N5, Canada;* orcid.org/0000-0002-9222-1219; Email: ehemmer@uottawa.ca

Reinhold F. Fink − *Institute of Physical and Theoretical Chemistry, University of Tübingen, Tübingen, Baden-Württemberg 72076, Germany;* orcid.org/0000-0002-8288-924X; Email: Reinhold.fink@uni-tuebingen.de

Authors

Chris Steve Conrad − *Institute of Physical and Theoretical Chemistry, University of Tübingen, Tübingen, Baden-Württemberg 72076, Germany; Department of Chemistry and Biomolecular Sciences, University of Ottawa, Ottawa, Ontario K1N 6N5, Canada;* orcid.org/0009-0007-7401-0120

Stefan Behnle − *Institute of Physical and Theoretical Chemistry, University of Tübingen, Tübingen, Baden-Württemberg 72076, Germany;* Present Address: IT Center (ZDV), University of Tübingen, Tübingen (Baden-Württemberg), 72074, Germany; orcid.org/0000-0003-3797-7272

Complete contact information is available at: https://pubs.acs.org/10.1021/acs.jpcc.5c06209

Author Contributions

C.S.C.: investigation (theoretical and experimental), formal analysis, writing—original draft, conceptualization (general project, approach, and model setup), and funding acquisition; S.B.: investigation, conceptualization (theoretical approach), and writing—review and editing; E.H.: conceptualization (underlying goal and compound selection and experimental setup), writing—review and editing, supervision, funding, and resources; R.F.F.: conceptualization (approach and model setup), writing—review and editing, supervision, funding, and resources.

Notes

The authors declare no competing financial interest.

■ ACKNOWLEDGMENTS

C.S.C. is grateful for a scholarship by Friedrich-Ebert-Stiftung and support from MITACS. C.S.C. and R.F.F. acknowledge support by the state of Baden-Württemberg through bwHPC and the German Research Foundation (DFG) through grant no. INST 40/575-1FUGG (JUSTUS 2 cluster). C.S.C. and E.H. acknowledge the Natural Sciences and Engineering Research Council of Canada (NSERC RGPIN-2023-03985) and Canada Foundation for Innovation Fund. Furthermore, C.S.C. would like to thank N. Avram for the introduction to Env, H. Euchner for support in converting structures from CP2K output files, and C. Homann, E. Tunang, and S. Funk for assistance with nanoparticle synthesis. Additionally, C.S.C. appreciates the advice given and the troubleshooting provided by F. Neese, the ORCA development team, and several members of the Orca forum (https://orcaforum.kofo.mpg.de).

■ ABBREVIATIONS

AutoAux, autogenerated fitting basis sets; AVAS, atomic valence active space; CASSCF, complete active space self-consistent field; COSX, chain-of-spheres approximation; DFT, density functional theory; ECP, effective core potential; ETU, energy transfer upconversion; Ln^{3+}, trivalent lanthanide ion; NEVPT2, N-electron valence state second-order perturbation theory; QDPT, quasi-degenerate perturbation theory; RDR,

research data repository; RI, resolution of identity; RMSE, root-mean-square error; RT, room temperature; SA, state-averaged; SOC, spin−orbit coupling; SS, state-specific; TEM, transmission electron microscopy; UCNP, upconverting nanoparticle; XRD, X-ray powder diffraction

REFERENCES

(1) Chen, X.; Zhang, X.; Liu, Y.; Chen, Y.; Zhao, Y. Upconversion Nanoparticle-Anchored Metal-Organic Framework Nanostructures for Remote-Controlled Cancer Optogenetic Therapy. *J. Am. Chem. Soc.* **2024**, *146* (50), 34475−34490.

(2) Jia, M.; Sun, Y.; Jiang, W.; Wang, Q.; Huang, X.; Wang, G.; Wu, H.; Wei, P.; Yi, T. Near-Infrared Light-Triggered In Situ Construction of 3D "Fishing Net" Polymer Networks Using Upconversion Nanoparticles for Tumor Therapy. *ACS Nano* **2025**, *19* (25), 23379−23392.

(3) Varghese, S.; Madanan, A. S.; Abraham, M. K.; Shkhair, A. I.; Indongo, G.; Rajeevan, G.; Arathy, B. K.; George, S. Photon Upconversion Immunoprobe Based on Resonance Energy Transfer for Brain Natriuretic Peptide - A Prognostic Biomarker for Heart Failure. *Microchem. J.* **2024**, *206*, 111539.

(4) Maestro, L. M.; Antón, M. A.; Cabrera-Granado, E.; Weigand, R.; Hernandez-Rueda, J. Intrinsic Optical Response of Levitating Upconverting Single Particles. *ACS Photonics* **2025**, *12* (4), 1783−1792.

(5) Toodeshki, E. H.; Frencken, A. L.; van Veggel, F. C. J. M.; Gordon, R. Thermometric Analysis of Nanoaperture-Trapped Erbium-Containing Nanocrystals. *ACS Photonics* **2024**, *11* (4), 1390−1395.

(6) Bahari, H.-R.; Mousavi Khaneghah, A.; Eş, I. Upconversion Nanoparticles-Modified Aptasensors for Highly Sensitive Mycotoxin Detection for Food Quality and Safety. *Compr. Rev. Food Sci. Food Saf.* **2024**, *23* (3), No. e13369.

(7) Popov, A.; Timofeyev, M.; Bykov, A.; Meglinski, I. Luminescent Upconversion Nanoparticles Evaluating Temperature-Induced Stress Experienced by Aquatic Organisms Owing to Environmental Variations. *iScience* **2022**, *25* (7), 104568.

(8) Auzel, F. Compteur Quantique par Transfert d'Energie Entre Deux Ions de Terres Rares dans un Tungstate Mixte et dans un Verre. *C.R. Acad. Sci.* **1966**, *262*, 1016−1019.

(9) Auzel, F. Compteur Quantique par Transfert Denergie de Yb^{3+} à Tm^{3+} dans un Tungstate Mixte et dans un Verre Germanate. *C.R. Acad. Sci.* **1966**, *263*, 819.

(10) Auzel, F. Upconversion and Anti-Stokes Processes with f and d Ions in Solids. *Chem. Rev.* **2004**, *104* (1), 139−174.

(11) Geng, S.; Li, H.; Lv, Z.; Zhai, Y.; Tian, B.; Luo, Y.; Zhou, Y.; Han, S.-T. Challenges and Opportunities of Upconversion Nanoparticles for Emerging NIR Optoelectronic Devices. *Adv. Mater.* **2025**, 2419678.

(12) Malhotra, K.; Hrovat, D.; Kumar, B.; Qu, G.; Houten, J. V.; Ahmed, R.; Piunno, P. A. E.; Gunning, P. T.; Krull, U. J. Lanthanide-Doped Upconversion Nanoparticles: Exploring A Treasure Trove of NIR-Mediated Emerging Applications. *ACS Appl. Mater. Interfaces* **2023**, *15* (2), 2499−2528.

(13) Haase, M.; Schäfer, H. Upconverting Nanoparticles. *Angew. Chem., Int. Ed.* **2011**, *50* (26), 5808−5829.

(14) Carnall, W. T. The Absorption and Fluorescence Spectra of Rare Earth Ions in Solution. In *Handbook on the Physics and Chemistry of Rare Earths*, Gschneidner, K. A.; Eyring, L., Eds.; Vol. 3; North-Holland Publishing Company, 1979, pp 171−208.

(15) Wu, Y.; Ang, M. J. Y.; Sun, M.; Huang, B.; Liu, X. Expanding the Toolbox for Lanthanide-Doped Upconversion Nanocrystals. *J. Phys. D: Appl. Phys.* **2019**, *52* (38), 383002.

(16) Matias, J. S.; Komolibus, K.; Kiang, W. K.; Konugolu-Venkata-Sekar, S.; Andersson-Engels, S. Beam-Profile Compensation for Quantum Yield Characterisation of Yb-Tm Codoped Upconverting Nanoparticles Emitting at 474 nm, 650 and 804 nm. *Nanoscale* **2024**, *16* (7), 3641−3649.

(17) Quintanilla, M.; Hemmer, E.; Marques-Hueso, J.; Rohani, S.; Lucchini, G.; Wang, M.; Zamani, R. R.; Roddatis, V.; Speghini, A.; Richards, B. S.; et al. Cubic Versus Hexagonal - Phase, Size and Morphology Effects on the Photoluminescence Quantum Yield of NaGdF4:Er3+/Yb3+ Upconverting Nanoparticles. *Nanoscale* **2022**, *14* (4), 1492−1504.

(18) Li, F.; Tu, L.; Zhang, Y.; Huang, D.; Liu, X.; Zhang, X.; Du, J.; Fan, R.; Yang, C.; Krämer, K. W.; et al. Size-Dependent Lanthanide Energy Transfer Amplifies Upconversion Luminescence Quantum Yields. *Nat. Photonics* **2024**, *18* (5), 440−449.

(19) Chen, B.; Wang, F. Emerging Frontiers of Upconversion Nanoparticles. *Trends Chem.* **2020**, *2* (5), 427−439.

(20) Dubey, N.; Chandra, S. Upconversion Nanoparticles: Recent Strategies and Mechanism Based Applications. *J. Rare Earths* **2022**, *40* (9), 1343−1359.

(21) Ansari, A. A.; Khan, M. A. M.; Singh, B. P.; Parchur, A. K. Upconversion Nanoparticles: Influence of the Host Lattices on Crystallographic and Luminescent Properties. *J. Mater. Sci.: Mater. Electron.* **2023**, *34* (22), 1625.

(22) Mohanty, S.; Kaczmarek, A. M. Unravelling the Benefits of Transition-Metal-Co-Doping in Lanthanide Upconversion Nanoparticles. *Chem. Soc. Rev.* **2022**, *51* (16), 6893−6908.

(23) Xia, X.; Sivonxay, E.; Helms, B. A.; Blau, S. M.; Chan, E. M. Accelerating the Design of Multishell Upconverting Nanoparticles through Bayesian Optimization. *Nano Lett.* **2023**, *23* (23), 11129−11136.

(24) Homann, C.; Krukewitt, L.; Frenzel, F.; Grauel, B.; Würth, C.; Resch-Genger, U.; Haase, M. $NaYF_4$: Yb, Er/$NaYF_4$ Core/Shell Nanocrystals with High Upconversion Luminescence Quantum Yield. *Angew. Chem., Int. Ed.* **2018**, *57* (28), 8765−8769.

(25) Johnson, N. J. J.; He, S.; Diao, S.; Chan, E. M.; Dai, H.; Almutairi, A. Direct Evidence for Coupled Surface and Concentration Quenching Dynamics in Lanthanide-Doped Nanocrystals. *J. Am. Chem. Soc.* **2017**, *139* (8), 3275−3282.

(26) Würth, C.; Fischer, S.; Grauel, B.; Alivisatos, A. P.; Resch-Genger, U. Quantum Yields, Surface Quenching, and Passivation Efficiency for Ultrasmall Core/Shell Upconverting Nanoparticles. *J. Am. Chem. Soc.* **2018**, *140* (14), 4922−4928.

(27) Fischer, S.; Bronstein, N. D.; Swabeck, J. K.; Chan, E. M.; Alivisatos, A. P. Precise Tuning of Surface Quenching for Luminescence Enhancement in Core-Shell Lanthanide-Doped Nanocrystals. *Nano Lett.* **2016**, *16* (11), 7241−7247.

(28) Wisser, M. D.; Chea, M.; Lin, Y.; Wu, D. M.; Mao, W. L.; Salleo, A.; Dionne, J. A. Strain-Induced Modification of Optical Selection Rules in Lanthanide-Based Upconverting Nanoparticles. *Nano Lett.* **2015**, *15* (3), 1891−1897.

(29) Conrad, C. S.; Euchner, H.; Hemmer, E.; Fink, R. F. The True Atomistic Structure of a Disordered Crystal: A Computational Study on the Photon Upconverting Material β-$NaYF_4$ and its Er^{3+}-, Tm^{3+}-, and Yb^{3+}-Doped Derivates. *Nanoscale* **2025**, *17* (14), 8599−8613.

(30) Dieke, G. H. *Spectra and Energy Levels of Rare Earth Ions in Crystals*; John Wiley & Sons, Inc., 1968.

(31) Shyichuk, A.; Câmara, S. S.; Weber, I. T.; Carneiro Neto, A. N.; Nunes, L. A. O.; Lis, S.; Longo, R. L.; Malta, O. L. Energy Transfer Upconversion Dynamics in YVO_4: Yb^{3+}, Er^{3+}. *J. Lumin.* **2016**, *170*, 560−570.

(32) Zhang, Y.; Chen, B.; Xu, S.; Li, X.; Zhang, J.; Sun, J.; Zhang, X.; Xia, H.; Hua, R. A Universal Approach for Calculating the Judd-Ofelt Parameters of RE^{3+} in Powdered Phosphors and its Application for the β-$NaYF_4$: Er^{3+}/Yb^{3+} Phosphor Derived from Auto-Combustion-Assisted Fluoridation. *Phys. Chem. Chem. Phys.* **2018**, *20* (23), 15876−15883.

(33) García-Flores, A. F.; Matias, J. S.; Garcia, D. J.; Martínez, E. D.; Cornaglia, P. S.; Lesseux, G. G.; Ribeiro, R. A.; Urbano, R. R.; Rettori, C. Crystal-field effects in Er^{3+}- and Yb^{3+}-Doped Hexagonal $NaYF_4$ Nanoparticles. *Phys. Rev. B: Condens. Matter* **2017**, *96* (16), 165430.

(34) Couto dos Santos, M. A.; Antic-Fidancev, E.; Gesland, J. Y.; Krupa, J. C.; Lemaıtre-Blaise, M.; Porcher, P. Absorption and

https://doi.org/10.1021/acs.jpcc.5c06209
J. Phys. Chem. C 2025, 129, 20446−20464

Fluorescence of Er^{3+}-doped $LiYF_4$: Measurements and Simulation. *J. Alloys Compd.* **1998**, *275*−*277*, 435−441.
(35) Xiao, Y.; Ju, M.; Yuan, H.; Yeung, Y. Unveiling the Local Structure and Luminescence Mechanism of Er^{3+}-Doped $LiYF_4$: A Promising Near-Infrared Laser Crystal. *J. Phys. Chem. C* **2021**, *125* (32), 18015−18021.
(36) Dulick, M.; Faulkner, G. E.; Cockroft, N. J.; Nguyen, D. C. Spectroscopy and Dynamics of Upconversion in Tm^{3+}: $YLiF_4$. *J. Lumin.* **1991**, *48*−*49*, 517−521.
(37) Xiao, Y.; Kuang, X.; Yeung, Y.; Ju, M. Investigation of the Structure and Luminescence Mechanism of Tm^{3+}-Doped $LiYF_4$: New Theoretical Perspectives. *Inorg. Chem.* **2020**, *59* (2), 1211−1217.
(38) Sugiyama, A.; Katsurayama, M.; Anzai, Y.; Tsuboi, T. Spectroscopic Properties of Yb Doped YLF Grown by a Vertical Bridgman Method. *J. Alloys Compd.* **2006**, *408*−*412*, 780−783.
(39) Hubert, S.; Meichenin, D.; Zhou, B. W.; Auzel, F. Emission Properties, Oscillator Strengths and Laser Parameters of Er^{3+} in $LiYF_4$ at 2.7 μm. *J. Lumin.* **1991**, *50* (1), 7−15.
(40) Yu, X. Y.; Chen, H. B.; Wang, S. J.; Zhou, Y. F.; Wu, A. H.; Dai, S. X. Growth and Spectral Properties of Er^{3+}: $LiYF_4$ Single Crystal. *J. Inorg. Mater.* **2011**, *26* (9), 923−928.
(41) Burns, J. H. Crystal Structure of Hexagonal Sodium Neodymium Fluoride and Related Compounds. *Inorg. Chem.* **1965**, *4* (6), 881−886.
(42) Roy, D. M.; Roy, R. Controlled Massively Defective Crystalline Solutions with the Fluorite Structure. *J. Electrochem. Soc.* **1964**, *111* (4), 421.
(43) Shi, R.; Brites, C. D. S.; Carlos, L. D. Hexagonal-Phase $NaREF_4$ Upconversion Nanocrystals: The Matter of Crystal Structure. *Nanoscale* **2021**, *13* (47), 19771−19782.
(44) Platonenko, A.; Popov, A. I. Structural and Electronic Properties of β-$NaYF_4$ and β-$NaYF_4$: Ce^{3+}. *Opt. Mater.* **2020**, *99*, 109529.
(45) Szefczyk, B.; Roszak, R.; Roszak, S. Structure of the Hexagonal $NaYF_4$ Phase from First-Principles Molecular Dynamics. *RSC Adv.* **2014**, *4* (43), 22526−22535.
(46) Huang, B.; Dong, H.; Wong, K.-L.; Sun, L.-D.; Yan, C.-H. Fundamental View of Electronic Structures of β-$NaYF_4$, β-$NaGdF_4$, and β-$NaLuF_4$. *J. Phys. Chem. C* **2016**, *120* (33), 18858−18870.
(47) Chen, G.; Shao, W.; Valiev, R. R.; Ohulchanskyy, T. Y.; He, G. S.; Ågren, H.; Prasad, P. N. Efficient Broadband Upconversion of Near-Infrared Light in Dye-Sensitized Core/Shell Nanocrystals. *Adv. Opt. Mater.* **2016**, *4* (11), 1760−1766.
(48) Staemmler, V. The Cluster Approach for the Adsorption of Small Molecules on Oxide Surfaces. In *Theoretical Aspects of Transition Metal Catalysis*, 1st ed.; Frenking, G., Ed.; *Topics in Organometallic Chemistry*, Vol. *12*; Springer Berlin, Heidelberg, 2005, pp 219−256.
(49) Aravena, D.; Atanasov, M.; Neese, F. Periodic Trends in Lanthanide Compounds through the Eyes of Multireference Ab Initio Theory. *Inorg. Chem.* **2016**, *55* (9), 4457−4469.
(50) Atanasov, M.; Andreici Eftimie, E.-L.; Avram, N. M.; Brik, M. G.; Neese, F. First-Principles Study of Optical Absorption Energies, Ligand Field and Spin-Hamiltonian Parameters of Cr^{3+} Ions in Emeralds. *Inorg. Chem.* **2022**, *61* (1), 178−192.
(51) Yao, G.; Berry, M.; May, P. S.; Wang, J.; Kilin, D. S. Relationship between Site Symmetry, Spin State, and Doping Concentration for Co(II) or Co(III) in β-$NaYF_4$. *J. Phys. Chem. C* **2016**, *120* (14), 7785−7794.
(52) Wang, F.; Han, Y.; Lim, C. S.; Lu, Y.; Wang, J.; Xu, J.; Chen, H.; Zhang, C.; Hong, M.; Liu, X. Simultaneous Phase and Size Control of Upconversion Nanocrystals through Lanthanide Doping. *Nature* **2010**, *463* (7284), 1061−1065.
(53) Park, K.-W.; Jang, H. S.; Cho, S.-H. Prediction of Ln^{3+}-4f Energy Levels in β-$NaYF_4$: Ln^{3+} and Understanding of Absorption Behaviors. *Mater. Chem. Phys.* **2022**, *275*, 125317.
(54) Dittmer, A.; Stoychev, G. L.; Maganas, D.; Auer, A. A.; Neese, F. Computation of NMR Shielding Constants for Solids Using an Embedded Cluster Approach with DFT, Double-Hybrid, DFT, and MP2. *J. Chem. Theory Comput.* **2020**, *16* (11), 6950−6967.
(55) Gellé, A.; Lepetit, M.-B. Fast Calculation of the Electrostatic Potential in Ionic Crystals by Direct Summation Method. *J. Chem. Phys.* **2008**, *128* (24), 244716.
(56) Momma, K.; Izumi, F. VESTA 3 for Three-Dimensional Visualization of Crystal, Volumetric and Morphology Data. *J. Appl. Crystallogr.* **2011**, *44* (6), 1272−1276.
(57) Neese, F. The ORCA Program System. *Wiley Interdiscip. Rev.: Comput. Mol. Sci.* **2012**, *2* (1), 73−78.
(58) Neese, F. The SHARK Integral Generation and Digestion System. *J. Comput. Chem.* **2023**, *44* (3), 381−396.
(59) Neese, F. Software Update: The ORCA Program System—Version 6.0. *Wiley Interdiscip. Rev.: Comput. Mol. Sci.* **2025**, *15* (2), No. e70019.
(60) Ganyushin, D.; Neese, F. First-Principles Calculations of Zero-Field Splitting Parameters. *J. Chem. Phys.* **2006**, *125* (2), 024103.
(61) Kollmar, C.; Sivalingam, K.; Helmich-Paris, B.; Angeli, C.; Neese, F. A Perturbation-Based Super-CI Approach for the Orbital Optimization of a CASSCF Wave Function. *J. Comput. Chem.* **2019**, *40* (14), 1463−1470.
(62) Angeli, C.; Bories, B.; Cavallini, A.; Cimiraglia, R. Third-Order Multireference Perturbation Theory: The N-Electron Valence State Perturbation-Theory Approach. *J. Chem. Phys.* **2006**, *124* (5), 054108.
(63) Angeli, C.; Cimiraglia, R.; Evangelisti, S.; Leininger, T.; Malrieu, J.-P. Introduction of N-Electron Valence States for Multireference Perturbation Theory. *J. Chem. Phys.* **2001**, *114* (23), 10252−10264.
(64) Angeli, C.; Cimiraglia, R.; Malrieu, J.-P. N-Electron Valence State Perturbation Theory: A Fast Implementation of the Strongly Contracted Variant. *Chem. Phys. Lett.* **2001**, *350* (3), 297−305.
(65) Kollmar, C.; Sivalingam, K.; Guo, Y.; Neese, F. An Efficient Implementation of the NEVPT2 and CASPT2 Methods Avoiding Higher-Order Density Matrices. *J. Chem. Phys.* **2021**, *155* (23), 234104.
(66) Guo, Y.; Sivalingam, K.; Neese, F. Approximations of Density Matrices in N-Electron Valence State Second-Order Perturbation Theory (NEVPT2). I. Revisiting the NEVPT2 Construction. *J. Chem. Phys.* **2021**, *154* (21), 214111.
(67) Ugandi, M.; Roemelt, M. A Recursive Formulation of One-Electron Coupling Coefficients for Spin-Adapted Configuration Interaction Calculations Featuring Many Unpaired Electrons. *Int. J. Quantum Chem.* **2023**, *123* (5), No. e27045.
(68) Rösch, N.; Matveev, A.; Nasluzov, V. A.; Neyman, K. M.; Moskaleva, L.; Krüger, S. Chapter 11 - Quantum Chemistry with the Douglas-Kroll-Hess Approach to Relativistic Density Functional theory: Efficient Methods for Molecules and Materials. In *Theoretical and Computational Chemistry*, Schwerdtfeger, P., Ed.; Vol. *14*; Elsevier, 2004, pp 656−722.
(69) Nakajima, T.; Hirao, K. The Douglas-Kroll-Hess Approach. *Chem. Rev.* **2012**, *112* (1), 385−402.
(70) Reiher, M. Relativistic Douglas-Kroll-Hess Theory. *Wiley Interdiscip. Rev.: Comput. Mol. Sci.* **2012**, *2* (1), 139−149.
(71) Lang, L.; Neese, F. Spin-Dependent Properties in the Framework of the Dynamic Correlation Dressed Complete Active Space Method. *J. Chem. Phys.* **2019**, *150* (10), 104104.
(72) Pantazis, D. A.; Neese, F. All-Electron Scalar Relativistic Basis Sets for the Lanthanides. *J. Chem. Theory Comput.* **2009**, *5* (9), 2229−2238.
(73) Aravena, D.; Neese, F.; Pantazis, D. A. Improved Segmented All-Electron Relativistically Contracted Basis Sets for the Lanthanides. *J. Chem. Theory Comput.* **2016**, *12* (3), 1148−1156.
(74) Weigend, F.; Ahlrichs, R. Balanced Basis Sets of Split Valence, Triple Zeta Valence and Quadruple Zeta Valence Quality for H to Rn: Design and Assessment of Accuracy. *Phys. Chem. Chem. Phys.* **2005**, *7* (18), 3297−3305.
(75) Eichkorn, K.; Treutler, O.; Öhm, H.; Häser, M.; Ahlrichs, R. Auxiliary Basis Sets to Approximate Coulomb Potentials. *Chem. Phys. Lett.* **1995**, *240* (4), 283−290.

https://doi.org/10.1021/acs.jpcc.5c06209
J. Phys. Chem. C 2025, 129, 20446−20464

(76) Helmich-Paris, B.; de Souza, B.; Neese, F.; Izsák, R. An Improved Chain of Spheres for Exchange Algorithm. *J. Chem. Phys.* **2021**, *155* (10), 104109.
(77) Stoychev, G. L.; Auer, A. A.; Neese, F. Automatic Generation of Auxiliary Basis Sets. *J. Chem. Theory Comput.* **2017**, *13* (2), 554−562.
(78) Fuentealba, P.; Preuß, H.; Stoll, H.; Von Szentpály, L. A Proper Account of Core-Polarization with Pseudopotentials: Single Valence-Electron Alkali Compounds. *Chem. Phys. Lett.* **1982**, *89* (5), 418−422.
(79) Bergner, A.; Michael, D.; Wolfgang, K.; Hermann, S.; Preuß, H. Ab Initio Energy-Adjusted Pseudopotentials for Elements of Groups 13−17. *Mol. Phys.* **1993**, *80* (6), 1431−1441.
(80) Andrae, D.; Häußermann, U.; Dolg, M.; Stoll, H.; Preuß, H. Energy-Adjusted ab Initio Pseudopotentials for the Second and Third Row Transition Elements. *Theor. Chim. Acta* **1990**, *77* (2), 123−141.
(81) Johnson, S. G.; Libcerf, J. W. Numeric Library for Complex Error Functions, version 1.5−1.19. https://jugit.fz-juelich.de/mlz/libcerf (accessed 01 July 2025).
(82) Rinkel, T.; Nordmann, J.; Raj, A. N.; Haase, M. Ostwald-Ripening and Particle Size Focussing of Sub-10 nm $NaYF_4$ Upconversion Nanocrystals. *Nanoscale* **2014**, *6* (23), 14523−14530.
(83) Liu, N.; Gobeil, N.; Evers, P.; Gessner, I.; Rodrigues, E. M.; Hemmer, E. Water Dispersible Ligand-Free Rare Earth Fluoride Nanoparticles: Water Transfer Versus $NaREF_4$-to-REF_3 Phase Transformation. *Dalton Trans.* **2020**, *49* (45), 16204−16216.
(84) Kotyk, C. M.; Weber, J. E.; Hyre, A. S.; McNeely, J.; Monteiro, J. H. S. K.; Domin, M.; Balaich, G. J.; Rheingold, A. L.; de Bettencourt-Dias, A.; Doerrer, L. H. Luminescence of Lanthanide Complexes with Perfluorinated Alkoxide Ligands. *Inorg. Chem.* **2020**, *59* (14), 9807−9823.
(85) Aziza, S.; Iimura, S.; Jin, C.; Fink, K.; Hayun, S.; Livneh, T. Order-Disorder Transitions in Cerium Hydrides, Manifested in Temperature-Dependent Raman Scattering Spectroscopy. *J. Phys. Chem. C* **2025**, *129* (37), 16826−16843.
(86) Popova, M. N.; Chukalina, E. P.; Malkin, B. Z.; Saikin, S. K. Experimental and Theoretical Study of the Crystal-Field Levels and Hyperfine and Electron-Phonon Interactions in $LiYF_4$: Er^{3+}. *Phys. Rev. B: Condens. Matter* **2000**, *61* (11), 7421−7427.
(87) Bünzli, J.-C. G.; Eliseeva, S. V. Intriguing Aspects of Lanthanide Luminescence. *Chem. Sci.* **2013**, *4* (5), 1939−1949.
(88) Misiak, M.; Prorok, K.; Cichy, B.; Bednarkiewicz, A.; Stręk, W. Thulium Concentration Quenching in the Up-Converting α-Tm^{3+}/Yb^{3+} $NaYF_4$ Colloidal Nanocrystals. *Opt. Mater.* **2013**, *35* (5), 1124−1128.
(89) Huang, D.; Li, F.; Ågren, H.; Chen, G. Inhibiting Concentration Quenching in Yb^{3+}-Tm^{3+} Upconversion Nanoparticles by Suppressing Back Energy Transfer. *Nat. Commun.* **2025**, *16* (1), 4218.
(90) Wu, K.; Cui, J.; Kong, X.; Wang, Y. Temperature Dependent Upconversion Luminescence of Yb/Er Codoped $NaYF_4$ nanocrystals. *J. Appl. Phys.* **2011**, *110* (5), 053510.
(91) Silver, J.; Martinez-Rubio, M. I.; Ireland, T. G.; Withnall, R. Yttrium Oxide Upconverting Phosphors. Part 2: Temperature Dependent Upconversion Luminescence Properties of Erbium in Yttrium Oxide. *J. Phys. Chem. B* **2001**, *105* (30), 7200−7204.
(92) Villanueva-Delgado, P.; Biner, D.; Krämer, K. W. Judd-Ofelt analysis of β-$NaGdF_4$: Yb^{3+}, Tm^{3+} and β-$NaGdF_4$: Er^{3+} single crystals. *J. Lumin.* **2017**, *189*, 84−90.
(93) Shi, R.; Lin, L.; Wang, Z.; Zou, Q.; Mudring, A.-V. Manipulation of Luminescence via Surface Site Occupation in Ln3+-Doped Nanocrystals. *J. Am. Chem. Soc.* **2024**, *146* (17), 11924−11931.
(94) Ren, P.; Zheng, X.; Zhang, J.; De Camillis, S.; Jia, J.; Wang, H.; Liao, X.; Piper, J. A.; Lu, Y. Quantifying the Influence of Inert Shell Coating on Luminescence Brightness of Lanthanide Upconversion Nanoparticles. *ACS Photonics* **2022**, *9* (3), 758−764.

https://doi.org/10.1021/acs.jpcc.5c06209
J. Phys. Chem. C 2025, 129, 20446−20464

Electronic Supplementary Information (ESI)

Effect of Disorder on the Emission Spectra of Er^{3+}, Tm^{3+}, and Yb^{3+} Doped β-$NaYF_4$: Quantum Chemical and Experimental Results

Chris Steve Conrad,[a,b] Stefan Behnle,[a,†] Eva Hemmer,[b,*] Reinhold F. Fink[a,*]

a Institute of Physical and Theoretical Chemistry, University of Tübingen, Tübingen (Baden-Württemberg), 72076, Germany.

b Department of Chemistry and Biomolecular Sciences, University of Ottawa, Ottawa (Ontario), K1N 6N5, Canada.

† Present Address: IT Center (ZDV), University of Tübingen, Tübingen (Baden-Württemberg), 72074, Germany.

* Corresponding Authors E-mail:

Reinhold.fink@uni-tuebingen.de

ehemmer@uottawa.ca

Table of Contents

1 Crystal Field Energy Levels

Table S1: Calculated (*ab initio* and fitted) and experimental crystal field energy levels of $LiYF_4:Tm^{3+}$. Root mean square errors (RMSE) for the *ab initio* results and fitted values compared to the experimental results are reported in the last row.

Crystal Field Energy Level[a] ($^{2S+1}L_J$)		This Work (cm^{-1})	Experiment[1, b] (cm^{-1})	Fitted[2] (cm^{-1})
$^3H_6$	1	0	0	−7
	2	43	27	24
	3	43		
	4	90	56	56
	5	298	270	270
	6	339	305	298
	7	344	319	333
	8	363	334	347
	9	363		
	10	378	372	387
	11	379		
	12	385	407	391
	13	409	419	417
$^3F_4$	1	5 611	5 599	5 600
	2	5 743	5 756	5 753
	3	5 743		
	4	5 774	5 757	5 768
	5	5 795	5 820	5 816
	6	5 896	5 942	5 943
	7	5 903	5 968	5 964
	8	5 914	5 972	5 969
	9	5 914		
$^3H_5$	1	8 269	8 284	8 276
	2	8 287	8 300	8 294
	3	8 292	8 319	8 317
	4	8 292		
	5	8 497	8 501	8 497
	6	8 504	8 519	8 526
	7	8 504		
	8	8 514		8 539
	9	8 514		8 542
	10	8 514		
	11	8 536	8 535	8 550
$^3H_4$	1	12 601	12 599	12 595
	2	12 632	12 624	12 621
	3	12 632		
	4	12 638	12 643	12 635
	5	12 763	12 745	12 745
	6	12 770	12 804	12 804
	7	12 831	12 835	12 838
	8	12 831		
	9	12 870	12 891	12 914
$^3F_3$	1	14 392	14 520	14 517
	2	14 392		
	3	14 416	14 549	14 544
	4	14 468	14 594	14 591
	5	14 472		14 592
	6	14 472		
	7	14 478	14597	14 607
$^3F_2$	1	15 018	15 094	15 101
	2	15 097	15 203	15 202
	3	15 097		
	4	15 100		15 231
	5	15 157	15 275	15 270
$^1G_4$	1	21 076	20 973	20 988
	2	21 264	21 186	21 191
	3	21 264		
	4	21 345	21 272	21 269
	5	21 418	21 300	21 315
	6	21 532		21 475
	7	21 560	21 554	21 536
	8	21 578	21 562	21 547
	9	21 578		
$^1D_2$	1	28 047	27 961	27 955
	2	28 104	27 991	28 003
	3	28 136	28 053	28 055
	4	28 136		
	5	28 197	28 075	28 067
RMSE		64		9

a: Irreducible representations for all levels are available in the work of Dulick *et al.*[1] b: The concentration of Tm^{3+} in the sample was either 1.5 mol%, 5 mol%, or 7 mol% or the results are an average of all of these samples.

Table S2: Calculated (*ab initio* and fitted) and experimental crystal field energy levels of $LiYF_4:Yb^{3+}$. RMSEs for the *ab initio* results and fitted values compared to the experimental results are reported in the last row.

Crystal Field Energy Level ($^{2S+1}L_J$)		This Work (cm^{-1})	Experiment[3, a] (cm^{-1})	Fitted[3] (cm^{-1})
$^2F_{7/2}$	1	0	0	0
	3	271	237	236
	5	357	375	398
	7	462	477	449
$^2F_{5/2}$	1	10 196	10 288	10 288
	3	10 354	10 420	10 409
	5	10 538	10 570	10 566
RMSE		47		14

a: The concentration of Yb^{3+} in the sample was not clearly specified but presumably is 5 mol%.

2 Synthesis and Structural Characterization of Ln^{3+}-doped β-$NaYF_4$ UCNPs

2.1 Additional Experimental Details

Oleate-capped β-$NaYF_4$ UCNPs (co-)doped with Er^{3+}, Tm^{3+}, and Yb^{3+} were synthesized following a synthesis originally published by Rinkel *et al.*[4] In each synthesis, 5 mmol β-$NaYF_4$:Ln^{3+} UCNPs were synthesized by first creating the respective acetate precursors ([$Y(Ac)_3$] and [$Ln(Ac)_3$], Ln = Er^{3+}, Tm^{3+}, and Yb^{3+}). Therefore, the required amounts of the respective oxides (Table S3) were added to 30 mL of a 1 : 2 mixture of water to acetic acid in a 250-mL three-necked round-bottom flask. The slurry was refluxed under rigorous stirring for several hours at 135°C until it became clear. Afterwards, the solvent was evaporated by drying the precursors over night at 65 °C and slow stirring, yielding a fine white powder.

The resulting powder was subsequently combined with 7.5 mmol sodium oleate (1.5:1 Na^+-to-Ln^{3+} ion ratio), 50 mL octadecene, and 50 mL oleic acid. The mixture was degassed while stirring under vacuum at 110°C using a heating mantle until a transparent solution formed and no more bubbles emerged. In the next step, the flask was flushed with nitrogen, followed by quickly adding 22.5 mmol ammonium fluoride to the flask (4.5:1 F^--to-Ln^{3+} ion ratio). Thereafter, vacuum was quickly (2 s) applied to the flask, and the flask immediately flushed with nitrogen, for a total of three times. Afterwards, the temperature was increased to 200 °C and the yellow solution was stirred under reflux for 1 h. The employed heating mantle was subsequently removed from the flask for faster cooling, and the flask was allowed to cool to room temperature. This procedure resulted in the formation of ultra-small (sub-5 nm) sodium-deficient sacrificial α-phase $NaYF_4$:Ln^{3+} UCNPs. The UCNPs were isolated by first washing the reaction mixture with two and a half times the volume of ethanol and centrifugation at 9000 RPM for 5 min. The resulting white pellet was then washed with a 1:3 hexane-to-ethanol mixture and centrifuged using the same conditions.

In the second step of the synthesis, all of the sacrificial α-phase $NaYF_4$:Ln^{3+} UCNPs were redispersed in each 10 mL octadecene and oleic acid in a 100-mL three-necked round-bottom flask and degassed at 110°C as described above. Afterwards, the temperature was increased to 300 °C, dissolving the α-phase UCNPs while simultaneously creating the β-phase UCNPs over the course of 3 h under constant stirring. The employed heating mantle was subsequently removed from the flask for faster cooling, and the flask was allowed to cool to room temperature. This procedure resulted in the formation of large (> 60 nm) β-$NaYF_4$ UCNPs. The UCNPs were isolated and washed as described above. After purification, ca. 800 mg of the white-yellow oleate-capped β-$NaYF_4$:Ln^{3+} UCNPs were stored in 5 mL of hexane.

Table S3: Overview for the compositions and dopant concentrations of the six β-$NaYF_4$: Ln^{3+} UCNPs synthesized for this study. Additionally, the molar amounts and masses used to prepare the respective [$Y(Ac)_3$] and [$Ln(Ac)_3$] precursors (Ln = Er^{3+}, Tm^{3+}, and Yb^{3+}) are included in the table.

	Host, β-$NaYF_4$, Y^{3+}		Dopant			Co-Dopant		
Sample Code	Concentration [mol%]	Y_2O_3 [mmol]; [mg]	Ln^{3+}	Concentration [mol%]	Ln_2O_3 [mmol]; [mg]	Ln^{3+}	Concentration [mol%]	Ln_2O_3 [mmol]; [mg]
$^{4.2}$Er	95.8	2.40; 541.7	Er^{3+}	4.2	0.10; 40.0			
$^{2.1}$Er / $^{2.1}$Tm	95.8	2.49; 563.2	Er^{3+}	2.1	0.05; 20.8	Tm^{3+}	2.1	0.06; 21.1
$^{2.1}$Er / $^{2.1}$Yb	95.8	2.40; 542.7	Er^{3+}	2.1	0.05; 20.0	Yb^{3+}	2.1	0.05; 20.8
$^{4.2}$Tm	95.8	2.39; 540.6	Tm^{3+}	4.2	0.10; 40.2			
$^{0.5}$Tm / $^{3.7}$Yb	95.8	2.39; 540.5	Tm^{3+}	0.5	0.01; 4.8	Yb^{3+}	3.7	0.09; 36.8
$^{0.5}$Tm / $^{20.0}$Yb	79.6	2.02; 456.8	Tm^{3+}	0.5	0.01; 4.9	Yb^{3+}	20.0	0.51; 199.9

2.2 Preparation of Ligand-Free UCNPs for Photoluminescence Characterization

400 mg of the oleate-capped β-$NaYF_4$: Ln^{3+} UCNPs dispersed in 2.5 mL hexane were added to a mixture of 9.5 mL hexane and 24 mL of an aqueous solution of hydrochloric acid (pH = 1.5) in a 150 mL Erlenmeyer flask. The mixture was stirred at room temperature overnight. Subsequently, the bi-phasic system was separated using a separation funnel. The organic phase was discarded. 72 mL of acetone were added to the aqueous phase (three times the initial volume) and well shaken, following centrifugation at 9000 RPM for 5 min. Afterwards, the white ligand-free β-$NaYF_4$: Ln^{3+} UCNPs were stored in 5 mL of water until further characterizations.[5]

2.3 Structural Characterization

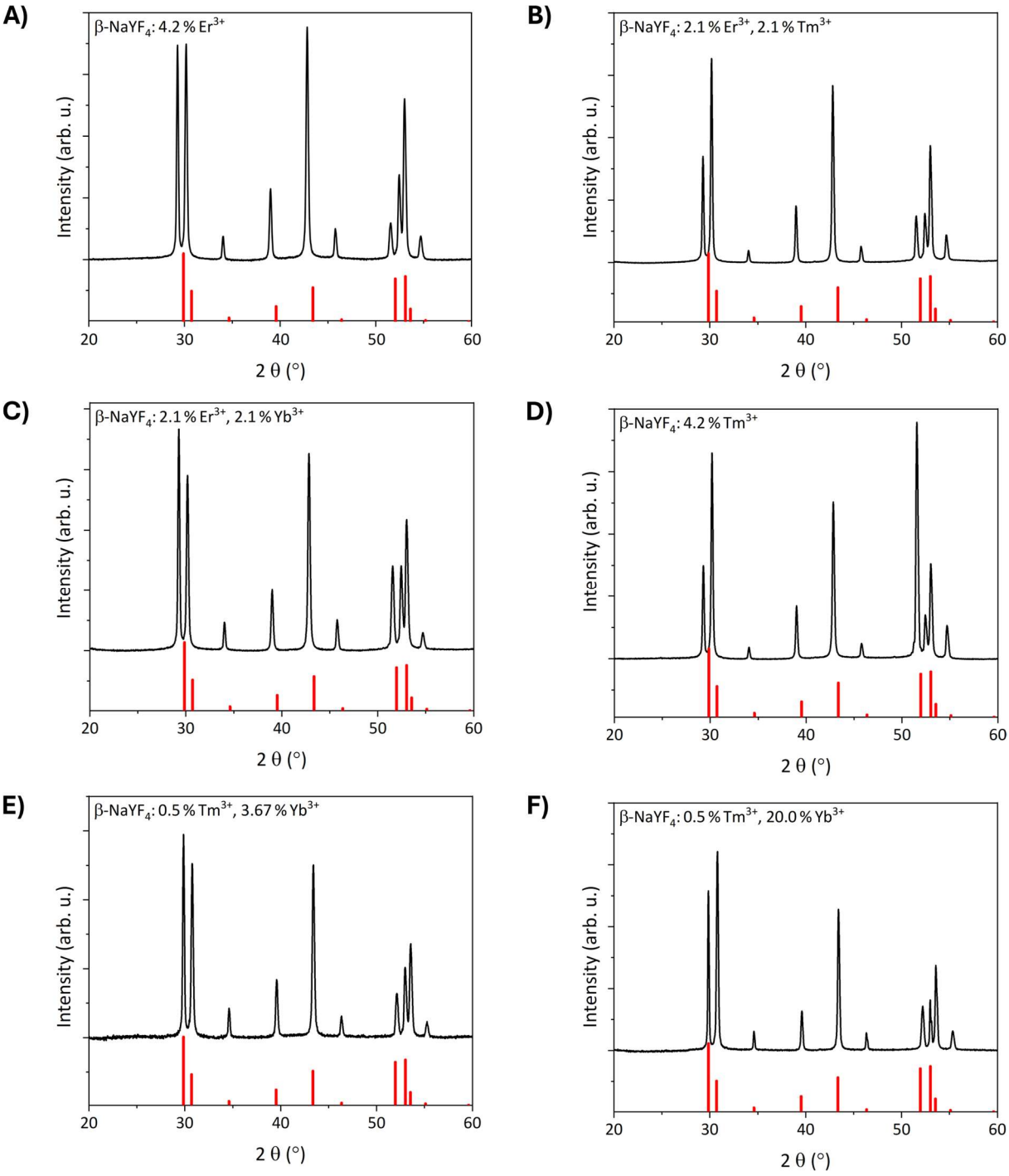

Figure S1: XRD patterns of **(A)** β-$NaYF_4$: 4.2 % Er^{3+}, **(B)** β-$NaYF_4$: 2.1 % Er^{3+}, 2.1 % Tm^{3+}, **(C)** β-$NaYF_4$: 2.1 % Er^{3+}, 2.1 % Yb^{3+}, **(D)** β-$NaYF_4$: 4.2 % Tm^{3+}, **(E)** β-$NaYF_4$: 0.5 % Tm^{3+}, 3.7 % Yb^{3+}, and **(F)** β-$NaYF_4$: 0.5 % Tm^{3+}, 20.0 % Yb^{3+} UCNPs. Reference: β-$NaYF_4$, PDF card [70413].

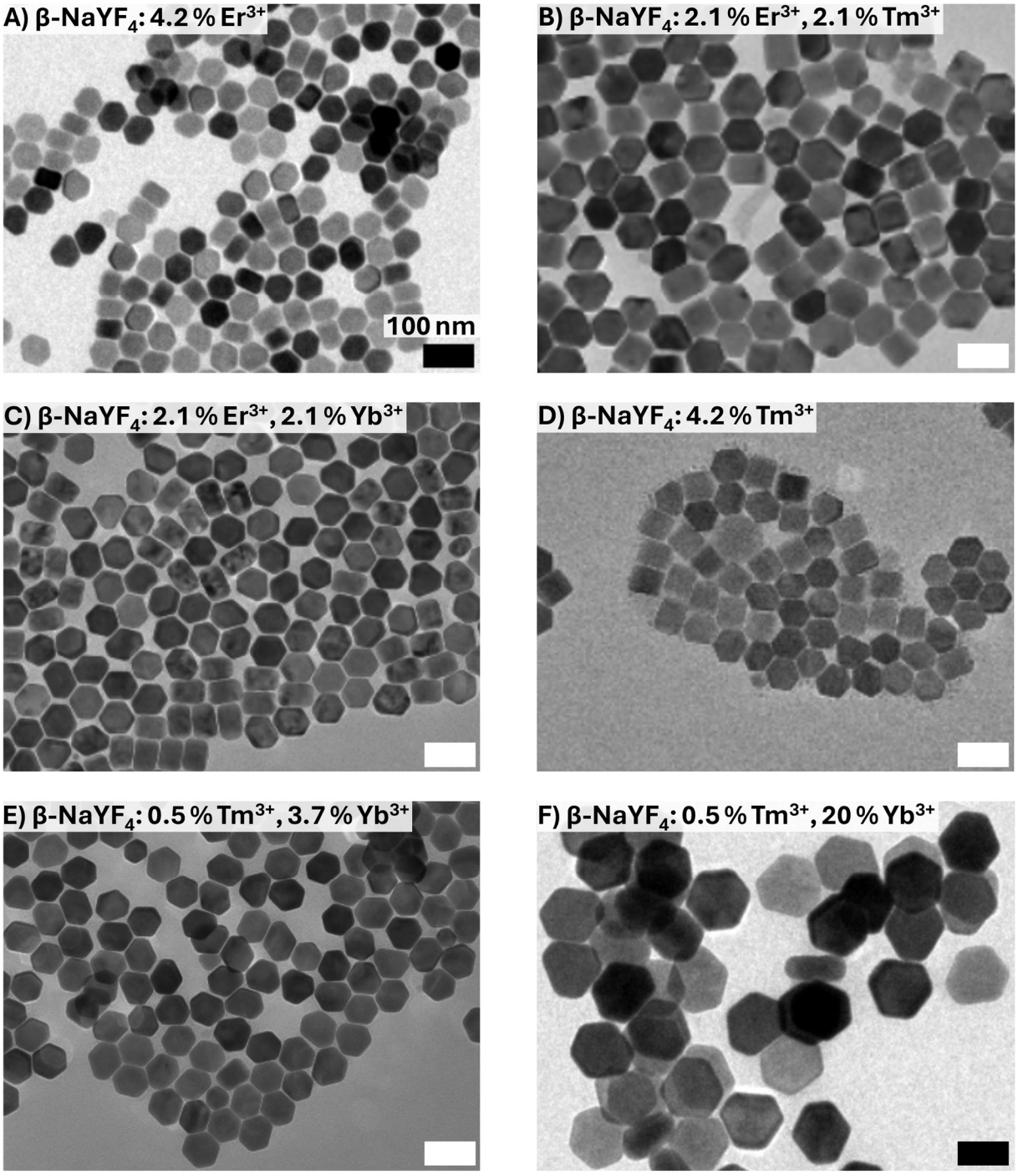

Figure S2: TEM images of **(A)** β-$NaYF_4$: 4.2 % Er^{3+}, **(B)** β-$NaYF_4$: 2.1 % Er^{3+}, 2.1 % Tm^{3+}, **(C)** β-$NaYF_4$: 2.1 % Er^{3+}, 2.1 % Yb^{3+}, **(D)** β-$NaYF_4$: 4.2 % Tm^{3+}, **(E)** β-$NaYF_4$: 0.5 % Tm^{3+}, 3.7 % Yb^{3+}, and **(F)** β-$NaYF_4$: 0.5 % Tm^{3+}, 20.0 % Yb^{3+} UCNPs. The scale bar in (A) applies to all images.

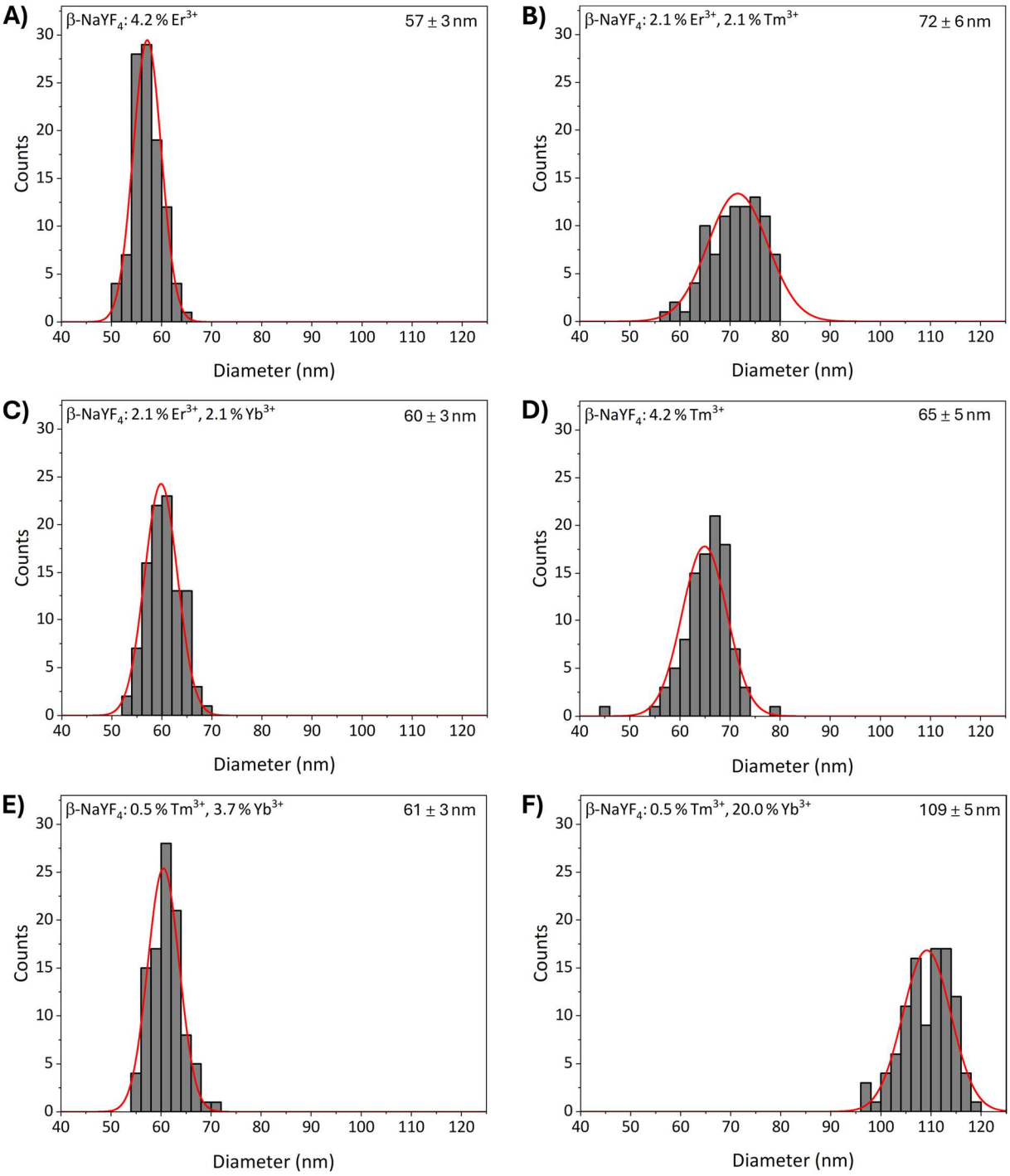

Figure S3: Size distributions of **(A)** β-$NaYF_4$: 4.2 % Er^{3+}, **(B)** β-$NaYF_4$: 2.1 % Er^{3+}, 2.1 % Tm^{3+}, **(C)** β-$NaYF_4$: 2.1 % Er^{3+}, 2.1 % Yb^{3+}, **(D)** β-$NaYF_4$: 4.2 % Tm^{3+}, **(E)** β-$NaYF_4$: 0.5 % Tm^{3+}, 3.7 % Yb^{3+}, and **(F)** β-$NaYF_4$: 0.5 % Tm^{3+}, 20.0 % Yb^{3+}. The diameters of the UCNPs were added to each size distribution in the top right corner.

3 Optical Characterization of the Synthesized UCNPs

Upconversion and Downshifting Emission Spectra, Energy Level Diagrams, Theoretical Spectra

Table S4: Overview of all samples, including color codes, composition, and particle size for the different UCNPs synthesized. Additionally, the temperature, at which the respective photoluminescence spectra were recorded is provided. The applied color code differentiates between the temperatures, *i.e.*, room temperature (RT) and 20 K, at which the photoluminescence spectrum of the respective samples were recorded. It is used consistently in both the manuscript and ESI for all spectra shown.

Sample and Color Code	Composition	Size (nm)	Temperature
$^{4.2}$Er-RT (**magenta**)	β-$NaYF_4$: 4.2 mol% Er^{3+}	57 ± 3	RT
$^{4.2}$Er-Cryo (**olive**)	β-$NaYF_4$: 4.2 mol% Er^{3+}	57 ± 3	20 K
$^{2.1}$Er / $^{2.1}$Tm-Cryo (**orange**)	β-$NaYF_4$: 2.1 % mol% Er, 2.1 mol% Tm^{3+}	72 ± 6	20 K
$^{2.1}$Er / $^{2.1}$Yb-Cryo (**blue**)	β-$NaYF_4$: 2.1 % mol% Er, 2.1 mol% Yb^{3+}	60 ± 3	20 K
$^{4.2}$Tm-RT (**green**)	β-$NaYF_4$: 4.2 mol% Tm^{3+}	65 ± 5	RT
$^{4.2}$Tm-Cryo (**wine**)	β-$NaYF_4$: 4.2 mol% Tm^{3+}	65 ± 5	20 K
$^{0.5}$Tm / $^{3.7}$Yb-Cryo (**brown**)	β-$NaYF_4$: 0.5 % mol% Er, 3.7 mol% Yb^{3+}	61 ± 3	20 K
$^{0.5}$Tm / $^{20.0}$Yb-Cryo (**red**)	β-$NaYF_4$: 0.5 % mol% Er, 20.0 mol% Yb^{3+}	109 ± 5	20 K

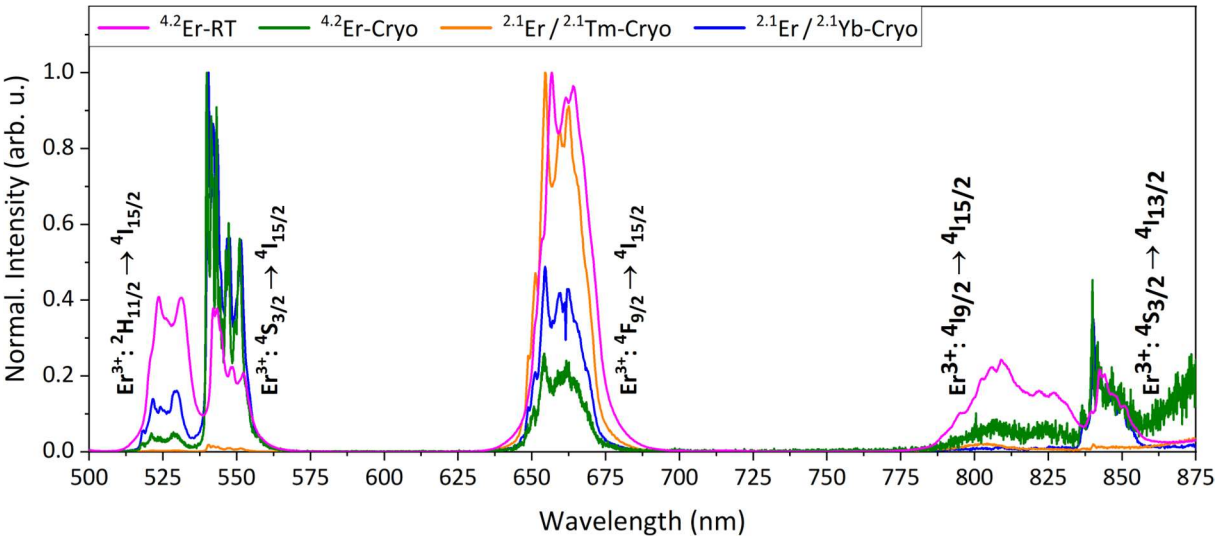

Figure S4: Solid-state upconversion emission spectra of the β-$NaYF_4$ UCNPs doped with 4.2 mol% Er^{3+} recorded at room temperature (color code magenta) and 20 K (color code olive), 2.1 mol% Er^{3+} and 2.1 mol% Tm^{3+} recorded at 20 K (color code orange), as well as 2.1 mol% Er^{3+} and 2.1 mol% Yb^{3+} recorded at 20 K (color code blue). Excitation wavelength (λ_{ex}) = 980 nm; power density = 9.6 W · cm^{-2}.

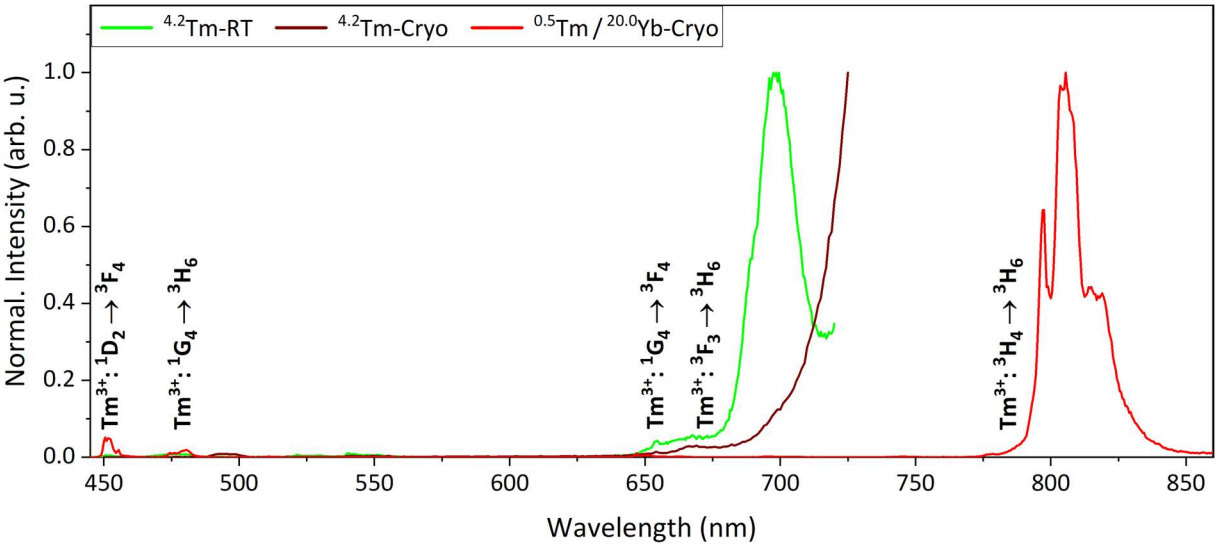

Figure S5: Solid-state upconversion emission spectra of the β-$NaYF_4$ UCNPs doped with 4.2 mol% Tm^{3+} recorded at room temperature (color code green) and 20 K (color code wine), as well as 0.5 mol% Tm^{3+} and 20.0 mol% Tm^{3+} recorded at 20 K (color code red). 4.2 mol% Tm^{3+}: λ_{ex} = 808 nm; power density = 8.1 W · cm^{-2}. 0.5 mol% Tm^{3+} and 20.0 mol% Tm^{3+}: λ_{ex} = 980 nm; power density = 9.6 W · cm^{-2}.

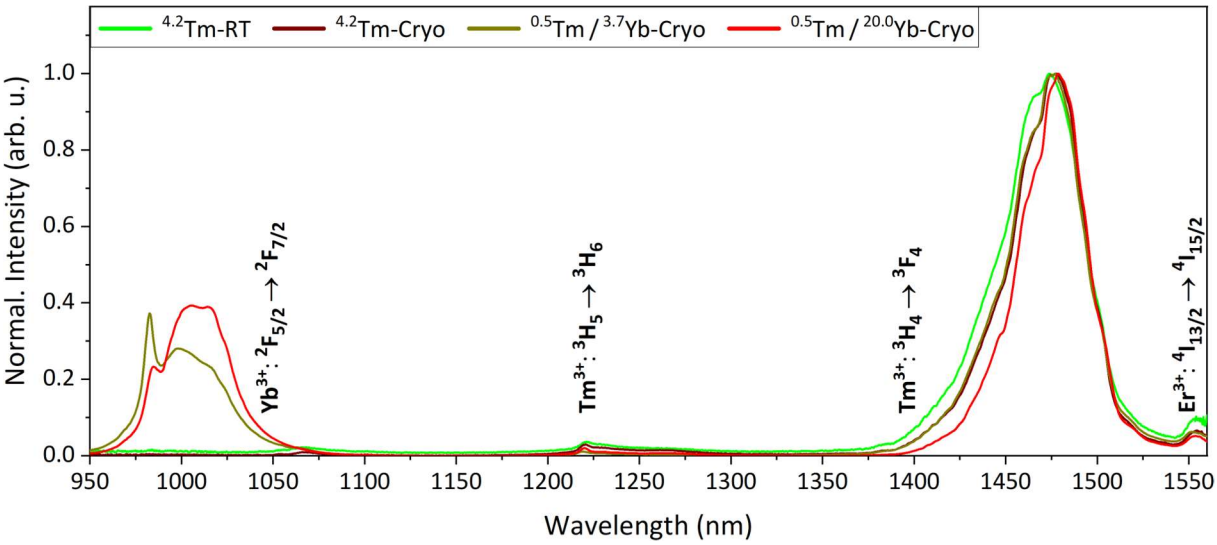

Figure S6: Solid-state downshifting spectra of the β-$NaYF_4$ UCNPs doped with 4.2 mol% Tm^{3+} recorded at room temperature (color code green) and 20 K (color code wine), 0.5 mol% Tm^{3+} and 3.7 mol% Tm^{3+} recorded at 20 K (color code brown), as well as 0.5 mol% Tm^{3+} and 20.0 mol% Tm^{3+} recorded at 20 K (color code red). All samples show contamination with Er^{3+}, which was either already present in the respective oxides or was introduced during the synthesis of the particles. Given the small changes between the differently doped samples, the influence of the Er^{3+} contamination on the positions of the energy levels and oscillator strengths of the corresponding transitions can be considered neglectable. λ_{ex} = 808 nm; power density = 8.1 W · cm^{-2}.

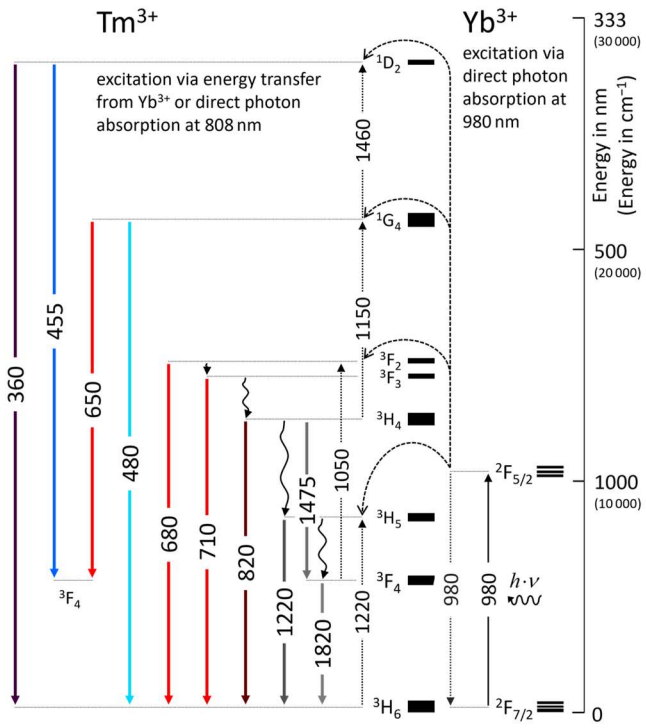

Figure S7: Energy level diagram showing probable upconversion and downshifting pathways for Tm^{3+} together with Yb^{3+} under 980 nm excitation. The photoluminescence spectra of several of the highlighted transitions are presented in Figure S10.

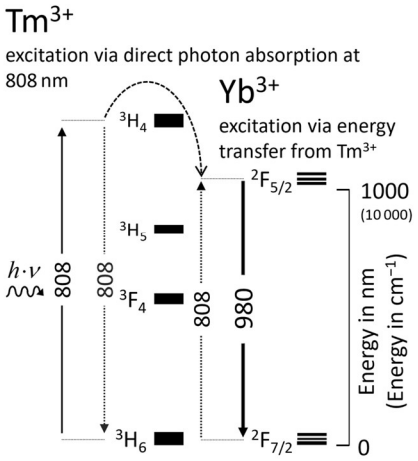

Figure S8: Energy level diagram showing the energy transfer pathways from Tm^{3+} to Yb^{3+} for the photoluminescence spectrum shown in Figure S11.

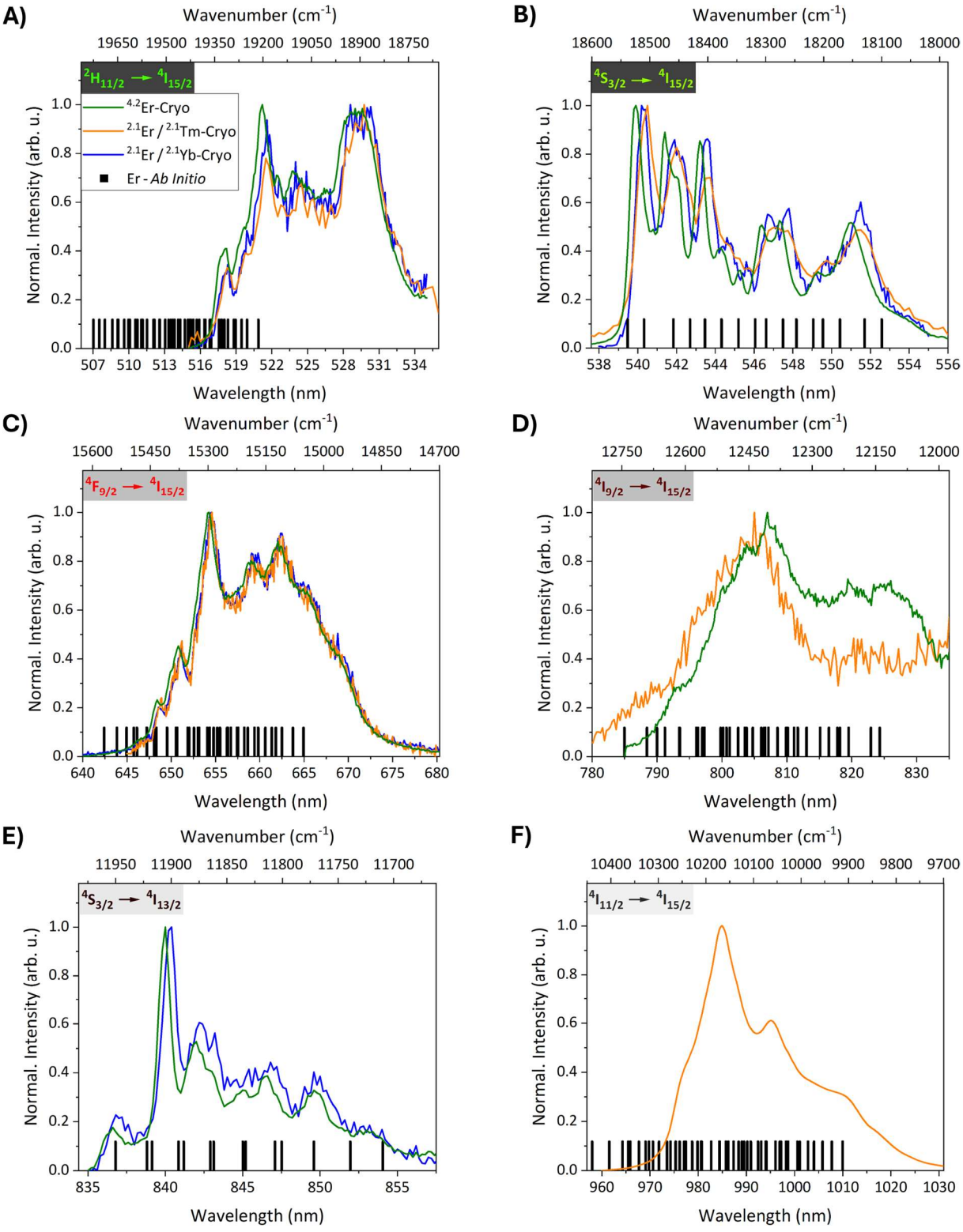

Figure S9: Low-temperature photoluminescence **(A–E)** upconversion and **(F)** downshifting spectra of the β-$NaYF_4$ UCNPs doped with 4.2 mol% Er^{3+}, 2.1 mol% Er^{3+} and 2.1 mol% Tm^{3+}, as well as 2.1 mol% Er^{3+} and 2.1 mol% Yb^{3+} for selected transitions. The legend shown in (A) applies to all spectra. (A–E): λ_{ex} = 980 nm; power density = 9.6 W · cm^{-2}. (F): λ_{ex} = 808 nm; power density = 8.1 W · cm^{-2}. Bars in black represent the averaged positions of the crystal field transitions of the respective multiplets according to the *ab initio* calculations. The height of the bars was chosen arbitrarily.

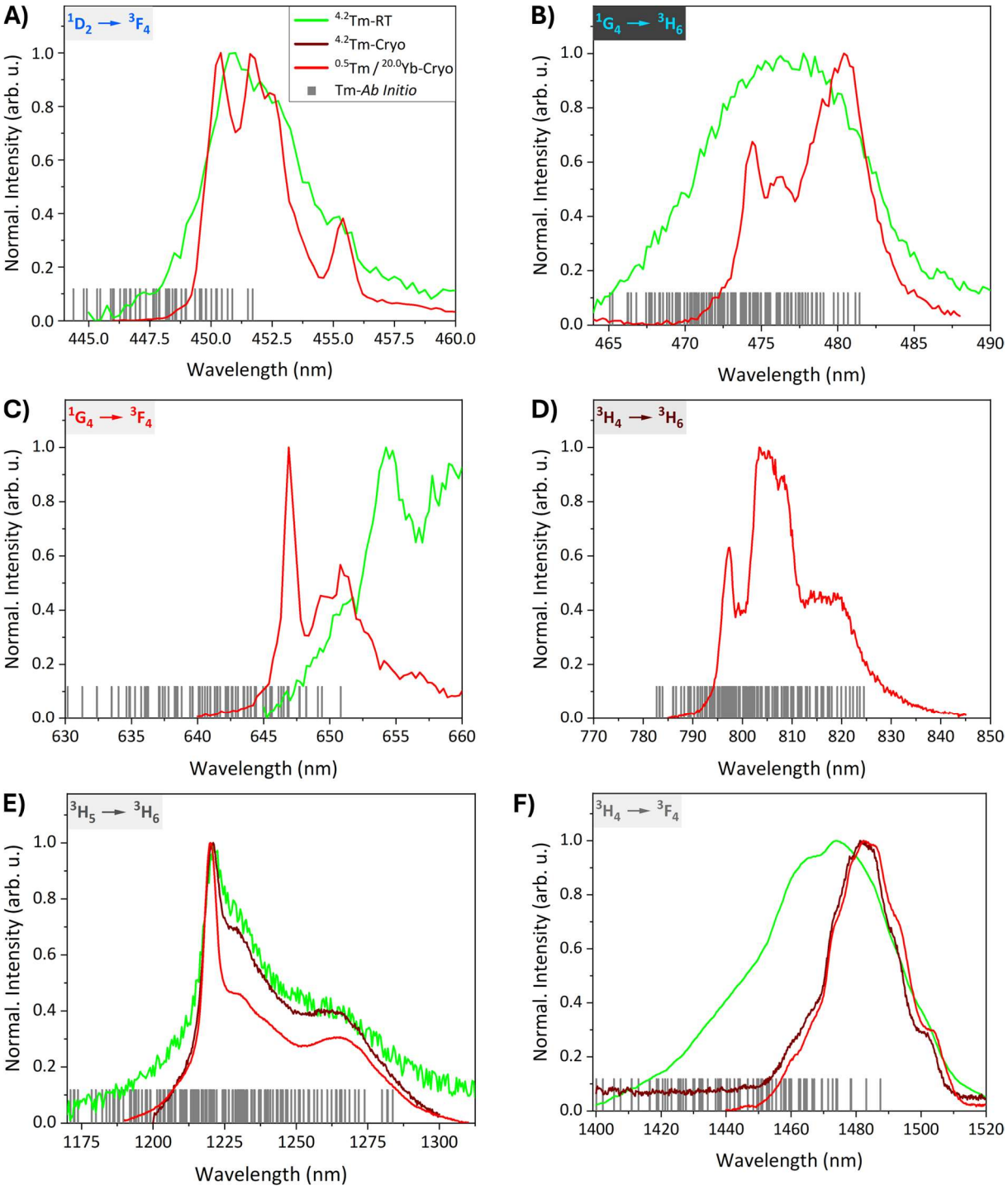

Figure S10: Photoluminescence **(A–D)** upconversion and **(E** and **F**) downshifting spectra of the β-$NaYF_4$ UCNPs doped with 4.2 mol% Tm^{3+} recorded at room temperature and 20 K, as well as 0.5 mol% Tm^{3+} and 20.0 mol% Yb^{3+} recorded at 20 K for specific transitions. The legend shown in (A) applies to the whole figure. 4.2 mol% Tm^{3+}: λ_{ex} = 808 nm; power density = 8.1 W · cm^{-2}. 0.5 mol% Tm^{3+} and 20.0 mol% Tm^{3+}: λ_{ex} = 980 nm; power density = 9.6 W · cm^{-2}. Bars in grey represent the averaged positions of the crystal field transitions of the respective multiplets according to the *ab initio* calculations. The height of the bars was chosen arbitrarily.

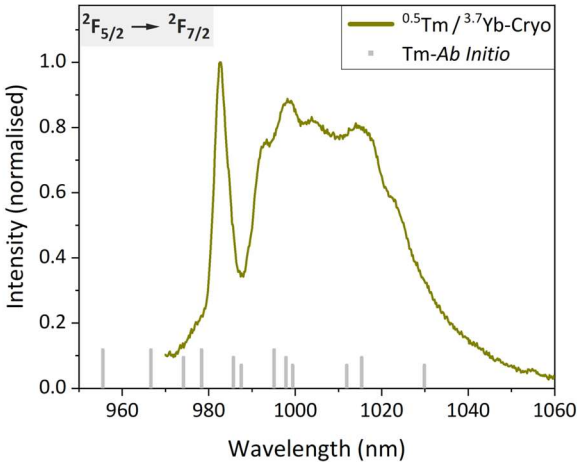

Figure S11: Low-temperature photoluminescence (downshifting) spectrum of β-$NaYF_4$ UCNPs doped with 0.5 mol% Tm^{3+} and 3.7 mol% Yb^{3+} for the 980 nm transitions of Yb^{3+}. λ_{ex} = 808 nm; power density = 8.1 W · cm^{-2}. Bars in light grey represent the averaged positions of the crystal field transitions of the respective multiplets according to the *ab initio* calculations. The different heights of the bars indicate whether a transition originates from the energetically highest (tallest bars), intermediate (medium bars), or lowest (shortest bars) level of the $^2F_{5/2}$ multiplet (they do not represent oscillator strengths).

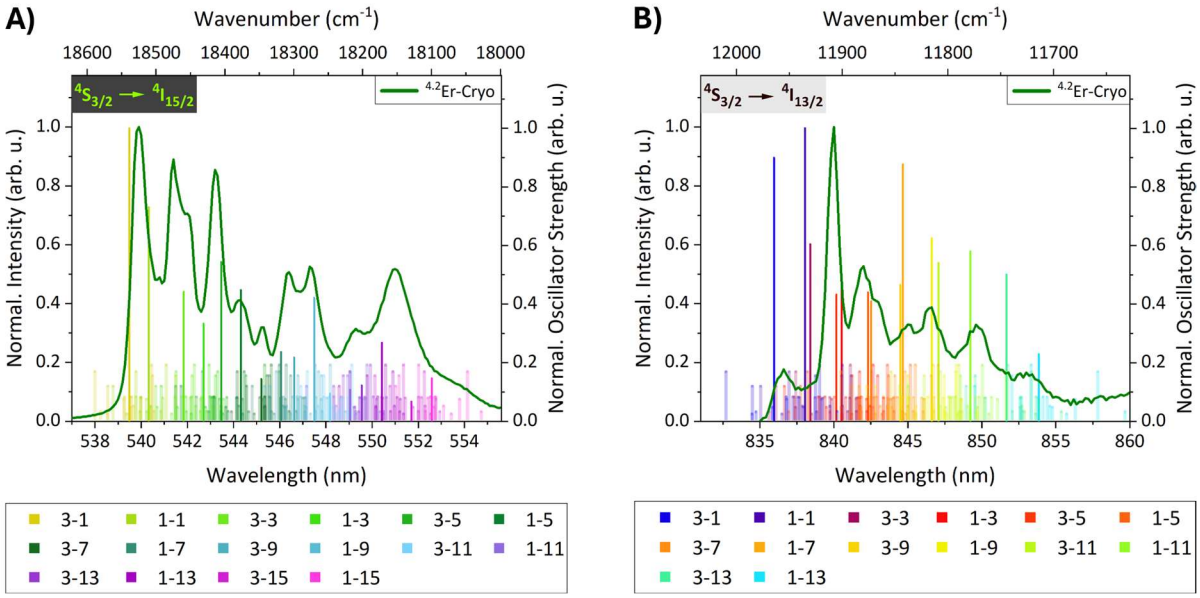

Figure S12: Normalized low-temperature photoluminescence spectra of β-$NaYF_4$ UCNPs doped with 4.2 mol% Er^{3+} (20 K) for the **(A)** $^4S_{3/2} \rightarrow {}^4I_{15/2}$ and **(B)** $^4S_{3/2} \rightarrow {}^4I_{13/2}$ transitions together with the calculated positions of the crystal field transitions and their oscillator strengths. λ_{ex} = 980 nm; power density = 9.6 W · cm^{-2}. The large opaque bars (16 and 14 bars in A and B, respectively) represent the averaged positions of the crystal field transitions of the respective multiplets according to the *ab initio* calculations. Their height is equal to their normalized oscillator strength. Shorter semitransparent bars indicate transitions for the individual clusters (14 clusters with each 16/14 transitions). Their labeling in the legend follows *n^{th} crystal field energy level of the initial multiplet ($^4S_{3/2}$)–n^{th} crystal field energy level of the final multiplet ($^4I_{15/2}$ / $^4I_{13/2}$)*. The height of the smaller bars represents the weighting factor of the cluster they originate from (not their oscillator strength), relative to that of all other clusters. Bars of the same height were retrieved from the same cluster.

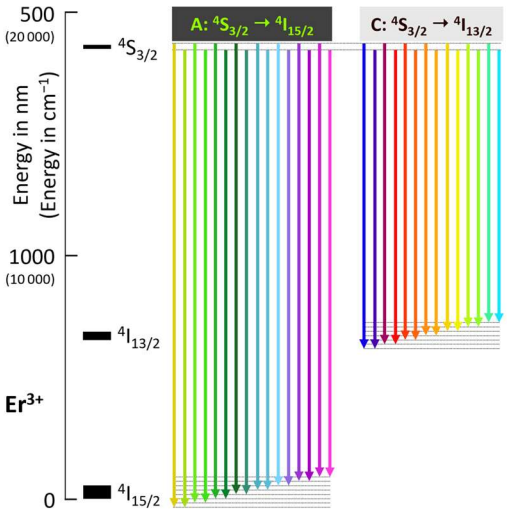

Figure S13: Energy level diagram showing individual crystal field transitions for the $^4S_{3/2} \rightarrow {}^4I_{15/2}$ and $^4S_{3/2} \rightarrow {}^4I_{13/2}$ transitions of Er^{3+}. The separation of the crystal field energy levels is not true to scale.

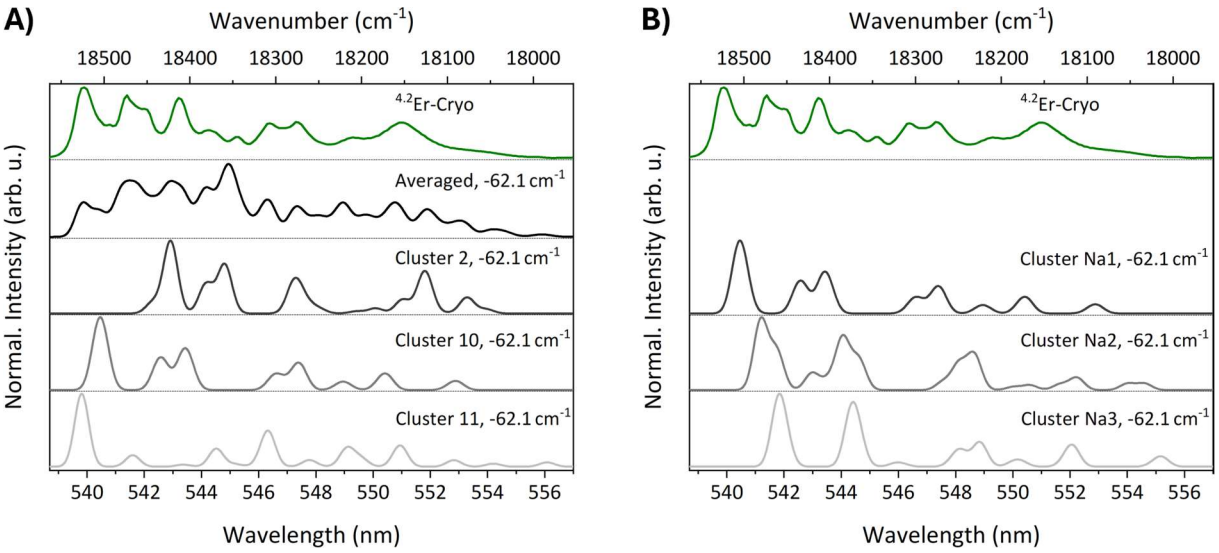

Figure 14: (A) Low-temperature photoluminescence spectrum of Er^{3+}-doped β-$NaYF_4$ for the $^4S_{3/2} \rightarrow {}^4I_{15/2}$ transition (20 K) together with the *ab initio* results for the averaged spectrum. Additionally, individual spectra of cluster 2, cluster 10, and cluster 11 (color code dark grey, grey, and light grey, respectively) are shown. **(B)** Low-temperature photoluminescence spectrum of Er^{3+}-doped β-$NaYF_4$ for the $^4S_{3/2} \rightarrow {}^4I_{15/2}$ transition (20 K). Additionally, individual spectra of cluster Na1, cluster Na2, and cluster Na3 (color code dark grey, grey, and light grey, respectively) are shown. All *ab initio* spectra were shifted by −62 cm^{-1}.

4 Env Input Files

4.1 $LiYF_4$: Ln^{3+}

```
&envin
! output format
Sortie="orca",
! prefix of the generated files and prefix of the coordinate file
Prefix="LiYF4_Er",
NFI_In="LiYF4_Er.cell",
! number of atoms in the .cell file and number of unit cells surrounding the qc
NCh=254,
NCel = 0,
! unit cell lengths and angles
a=15.596216, b=15.597938, c=10.789323,
alpha= 90.008492, beta=89.989532, gamma=89.993942,
! name and fractional coordinates of the central atom in the quantum cluster
Atom0="Er",
Pos0= 0.33317, 0.33237, 0.50056,
! number, names, and fractional coordinates of the magnetic atoms (in the qc)
NMag=1,
AtomMag="Er",
PosMag= 0.33317, 0.33237, 0.50056,
! maximum distance between the central atom and the qc, and between the qc and the ECPs
DSys = 3.0,
DPseud=6.6,
&end
```

4.2 β-$NaYF_4$: Ln^{3+}

```
&envin
! output format
Sortie="orca",
! prefix of the generated files and prefix of the coordinate file
Prefix="10-Er_Na1",
NFI_In="10-Er_Na1.cell",
! number of atoms in the .cell file and number of unit cells surrounding the qc
NCh=144,
```

```
NCel = 0,
! unit cell lengths and angles
a=12.054222, b=12.069157, c=14.151001,
alpha=90.008041, beta=89.996727, gamma=119.791977,
! name and fractional coordinates of the central atom in the quantum cluster
Atom0="Er",
Pos0= 0.498079, 0.498427, 0.499946,
! number, names, and fractional coordinates of the magnetic atoms (in the qc)
NMag=1,
AtomMag="Er",
PosMag= 0.498079, 0.498427, 0.499946,
! maximum distance between the central atom and the qc, and between the qc and the ECPs
DSys = 2.8,
DPseud=7.0,
&end
```

5 Orca Input Files

5.1 β-$NaYF_4$:Er^{3+}, Cluster 10, AVAS

```
# CASSCF+NEVPT2+QDPT calculation of 10-NaYF4_Na1: 4.3 % Er3+ (Er-F9-Na19Y22F62) with 35 quartet and 112 doublet roots

% Pal NProcs 24 end          # number of cores for parallel processing
% MaxCore 6500   # amount of RAM per core

% PointCharges "pointcharges.pc"    # file that contains all point charges
% Method
 DoEQ true                   # include interactions between point charges
 FrozenCore FC_None          # no frozencore approximation, calculates correlation effects for electrons on low-lying orbitals
end

! AVAS(valence-f)     # determines good (f-) starting orbitals for the active space
% CASSCF
 NEl 11                      # number of electrons
 NOrb 7                      # number of orbitals
 Mult 4,2             # included multiplicities
 NRoots 35,112               # number of multiplets per multiplicity
 BWeight = 0.238095, 0.761905        # weight per mutliplicity block
 MaxIter 500                 # maximum number of iterations to achieve convergence criteria
 ETol 1e-8                   # energy convergence setting (default is 1e-7)
 GTol 1e-5                   # gradient convergence setting
 ActConstraints 0 # requests natural orbital construction
 trafostep RI                # utilize the RI-MO algorithm for faster integral transformation
 ActOrbs fOrbs               # requests AILFT analysis
 PTMethod SC_NEVPT2      # strongly contracted MR approach, provides a DEC corrected total energy
 PTSettings                  # settings for the chosen perturbation theory method
  D3Tpre 1e-15               # truncation of the third-order reduced density matrix (tight setting)
  D4Tpre 1e-15               # fourth-order rdm, avoids intruder states (extremely tight setting)
 end
 DoHigherMoments true                # request the multipole expansion up to 2nd order (magnetic dipole and electric quadrupole contri-
butions), introduces origin-dependence
 Rel                         # enter into relativistic calculation
  DoSOC true                 # spin-orbit coupling via QDPT
  NInitStates 364  # number of inital SOC states to compute the transition moments from
  Temperature 1000000      # temperature for calculating the Boltzmann distribution
 end
end

% Rel                         # include relativistic effects
 Method DKH                  # (relativistic) Hamiltonian operator
 Order 2              # second-order DKH Hamiltonian
 PictureChange 2 # include the second-order DKH transformation of the SOC operator and the first order of the Zeeman operator
 FiniteNuc true              # account for the spatial extent of the nuclei (opposed to the point charges used for the elementary particles)
end

! AutoAux                    # automatic construction of a auxiliary basis set for Coulomb-, exchange-, and correlation-fitting
% Basis
 Basis "DKH-DEF2-TZVPP"# general basis set
 NewGTO
  Er "SARC2-DKH-QZVP" end
 NewECP                      # ECP per element
  Na "SDD" end
 NewECP                      # ECP per element
  Y "SDD" end
end

* xyz -6 4              # keyword, total charge, multiplicity, (file name)
 Er     0.000000000000     0.000000000000     0.000000000000
 f     -2.288293866532     0.264219131682     0.154104399356
 f     -0.764422676182    -1.236186817617     1.778695901990
 f     -0.890452277930    -1.245531670436    -1.777974200946
 f      0.901031047951    -2.118480423942    -0.149646834086
```

```
f    -0.652430405736     1.453640812048     1.774139279713
f    -0.685848639863     1.321738560667    -1.777195895899
f     1.496152743901    -0.032761847666     1.778837411999
f     1.576211860870    -0.061662684727    -1.770417566487
f     1.359225926221     1.956778621591    -0.147085502930
na>    1.000000000000    -5.837462991042    3.508160738213   -1.601765938248
 y>    3.000000000000    -6.017756529567    0.028568661062   -3.537283231759
 y>    3.000000000000     6.008547470344    0.002211016831   -0.007712295468
 y>    3.000000000000    -6.020682748207    0.022229583649    3.543764390152
 y>    3.000000000000    -2.988002297169    1.787849206282   -5.310997981446
na>    1.000000000000    -2.994288366143    1.761756782630   -1.888734084671
 y>    3.000000000000    -3.013599305164    1.801549085398    1.753592026466
na>    1.000000000000    -3.049130920577    1.761412214588    5.328644279518
 y>    3.000000000000    -3.013670802338   -5.206731368023   -3.544047410170
 y>    3.000000000000    -3.008972446713   -5.196997612085    0.002051895125
 y>    3.000000000000    -3.039232045980   -5.212022481241    3.532655854478
na>    1.000000000000    -2.892644931270   -1.728342792114   -5.269832719947
na>    1.000000000000    -3.117200553127   -1.730281064809   -1.774294940723
na>    1.000000000000    -2.946536963787   -1.728198405309    1.892130324877
na>    1.000000000000    -3.116082550569   -1.731787125482    5.271983672078
na>    1.000000000000    -0.023713871479   -3.521825753021   -5.327130122426
 y>    3.000000000000    -0.007235836938   -3.451501785362   -1.764799619146
na>    1.000000000000     0.003598316679   -3.474697776469    1.776445892853
 y>    3.000000000000     0.009563166295   -3.445531132356    5.295035652477
 y>    3.000000000000     0.029896818201    0.033492219871   -3.543184199117
 y>    3.000000000000     0.000104553872    0.059277885641    3.531113395384
na>    1.000000000000     0.188263952816    3.509323652404   -5.501074224987
na>    1.000000000000    -0.034288238537    3.506912933477   -1.834521600379
na>    1.000000000000     0.137113199849    3.507251995543    1.545190236813
na>    1.000000000000    -0.088196485810    3.505632873118    5.327271632435
na>    1.000000000000     3.032245866219    1.761980419041   -5.327158424428
 y>    3.000000000000     3.041283552673    1.781693990052   -1.766002454219
na>    1.000000000000     3.031231160018    1.760767554736    1.719714530409
 y>    3.000000000000     3.015333236939    1.781356400910    5.316092341756
 y>    3.000000000000     3.023605951204   -5.209538793396   -3.541075699989
 y>    3.000000000000     3.042402805652   -5.180467680774   -0.012679296770
na>    1.000000000000     2.909371934939   -1.729649248073   -5.616277522981
na>    1.000000000000     3.080843641767   -1.729076664134   -2.179353189315
na>    1.000000000000     2.909180898898   -1.729817205698    2.180640930393
na>    1.000000000000     3.187849876032   -1.729344891637    5.501725171026
 f>   -1.000000000000    -3.671122164266   -3.806556555007    1.771648703562  NewECP "SDD" end
 f>   -1.000000000000    -3.741142530187   -3.932132849339   -1.776884573880  NewECP "SDD" end
 f>   -1.000000000000    -4.459125978031   -0.071130010625   -5.270823290007  NewECP "SDD" end
 f>   -1.000000000000    -4.479772716203   -0.031504174524    1.772724179627  NewECP "SDD" end
 f>   -1.000000000000    -4.533999961350   -0.032250823088   -1.776346835847  NewECP "SDD" end
 f>   -1.000000000000    -4.509801361264   -0.030866936721    5.276809163371  NewECP "SDD" end
 f>   -1.000000000000    -4.720139015370    1.957568172472    0.146675123905  NewECP "SDD" end
 f>   -1.000000000000    -4.669173430926    1.954900683893   -3.695434817361  NewECP "SDD" end
 f>   -1.000000000000    -4.715982371792    1.958824134757    3.401334566505  NewECP "SDD" end
 f>   -1.000000000000    -1.686113669656   -3.312416235594   -0.147311918944  NewECP "SDD" end
 f>   -1.000000000000    -1.673889905133   -3.285140832677   -3.402650609585  NewECP "SDD" end
 f>   -1.000000000000    -1.681448470011   -3.282715545223    3.697033880458  NewECP "SDD" end
 f>   -1.000000000000     0.714516538470   -5.021332569770   -0.198793260069  NewECP "SDD" end
 f>   -1.000000000000     0.714304612173   -5.013290638932   -3.348607937304  NewECP "SDD" end
 f>   -1.000000000000     0.699328686183   -4.978095674774    3.697684826497  NewECP "SDD" end
 f>   -1.000000000000    -2.294678001002    0.261228780870   -3.702213146772  NewECP "SDD" end
 f>   -1.000000000000    -2.308427069337    0.258150794901    3.350419265414  NewECP "SDD" end
 f>   -1.000000000000    -0.718643384081   -1.250840436581   -5.281224275639  NewECP "SDD" end
 f>   -1.000000000000    -0.880974834064   -1.250270987785    5.324526338268  NewECP "SDD" end
 f>   -1.000000000000    -3.888277086848    3.987656210268    1.773092105650  NewECP "SDD" end
 f>   -1.000000000000    -3.701718139137    3.994167981914   -1.775299661784  NewECP "SDD" end
 f>   -1.000000000000    -2.016527058264    3.163527114593    0.152590242264  NewECP "SDD" end
 f>   -1.000000000000    -2.015541980621    3.159876948724   -3.704109380888  NewECP "SDD" end
 f>   -1.000000000000    -2.052866861503    3.127569580027    3.401377019508  NewECP "SDD" end
 f>   -1.000000000000     0.987428693650   -2.082539497500   -3.350886248442  NewECP "SDD" end
```

```
  f>    -1.000000000000      0.983301769528   -2.065978420748    3.699864080630   NewECP "SDD" end
  f>    -1.000000000000     -0.634719383650    1.437588079137   -5.319941413989   NewECP "SDD" end
  f>    -1.000000000000     -0.731038656733    1.320560160409    5.327285783435   NewECP "SDD" end
  f>    -1.000000000000      2.277219613995   -3.915168901290   -5.318200840884   NewECP "SDD" end
  f>    -1.000000000000      2.316825634506   -3.915958595597    1.777238348901   NewECP "SDD" end
  f>    -1.000000000000      2.370831738236   -3.801343861560   -1.774436450731   NewECP "SDD" end
  f>    -1.000000000000      2.364434482778   -3.792334083728    5.272578014114   NewECP "SDD" end
  f>    -1.000000000000     -1.427308003719    5.157280769980    1.778596844984   NewECP "SDD" end
  f>    -1.000000000000     -1.461950364017    5.205281689379   -1.781313837149   NewECP "SDD" end
  f>    -1.000000000000      1.510954696010   -0.035542885439   -5.323691429217   NewECP "SDD" end
  f>    -1.000000000000      1.547189850966   -0.036738796403    5.326408421382   NewECP "SDD" end
  f>    -1.000000000000      1.383495211951    1.921115731612   -3.403952501664   NewECP "SDD" end
  f>    -1.000000000000      1.356269752863    1.948122993079    3.700316912657   NewECP "SDD" end
  f>    -1.000000000000      4.413783044986   -3.352538011469    0.144410963768   NewECP "SDD" end
  f>    -1.000000000000      4.353005806372   -3.282861225918   -3.698463131545   NewECP "SDD" end
  f>    -1.000000000000      4.380938316307   -3.320719732142    3.406230812802   NewECP "SDD" end
  f>    -1.000000000000      3.730221715937    0.263755855370   -3.399410030388   NewECP "SDD" end
  f>    -1.000000000000      3.721598247504    0.205780860823    3.754402037941   NewECP "SDD" end
  f>    -1.000000000000      3.742965951157    0.314524088923   -0.156354408493   NewECP "SDD" end
  f>    -1.000000000000      2.308756001980    3.989646330295    1.772681726625   NewECP "SDD" end
  f>    -1.000000000000      2.170781578588    3.965898120777   -1.771931723579   NewECP "SDD" end
  f>    -1.000000000000      2.141776332332    3.988329370788    5.323479164204   NewECP "SDD" end
  f>    -1.000000000000      5.254902312094   -1.242169405883   -1.778738354992   NewECP "SDD" end
  f>    -1.000000000000      5.124110525315   -1.278355003289    1.776460043854   NewECP "SDD" end
  f>    -1.000000000000      4.023370854432    3.159465412457   -3.355725890736   NewECP "SDD" end
  f>    -1.000000000000      3.992931913190    3.125048860464    3.698816906566   NewECP "SDD" end
  f>    -1.000000000000      4.062441331257    3.171578585900   -0.148415697011   NewECP "SDD" end
  y>     2.999996911163     -6.045674529656    0.002211016831   -0.007712295468
  f>    -0.999786768100     -5.067905149161   -2.110104140388   -3.699071624582   NewECP "SDD" end
  f>    -0.999867724887     -5.035074970614   -2.075307686216    3.351070211453   NewECP "SDD" end
  f>    -0.999854341688     -5.044277648056   -2.076047081163    0.151712880211   NewECP "SDD" end
  f>    -0.999997610702     -1.525679720261   -5.260144578026    1.780394022093   NewECP "SDD" end
  f>    -0.999991545728     -1.470998509527   -5.279858780703   -1.775865701818   NewECP "SDD" end
  y>     2.999956276198     -2.954187357655    5.293569606919   -0.012679296770
  y>     2.999998520926     -2.967727962951    5.246962349714    3.542462498073
  f>    -0.999789546872      0.752179342796    5.451884062537    0.154486476379   NewECP "SDD" end
  f>    -0.999700144440      0.732075452080    5.493996898911   -3.717199056682   NewECP "SDD" end
  f>    -0.999695744888      0.731212999469    5.494959800998    3.351636251488   NewECP "SDD" end
  y>     2.999993207424      6.036465470433    0.028568661062   -3.537283231759
  y>     2.999996188746      6.033539251793    0.022229583649    3.543764390152
  f>    -0.999998859950      5.304919691119    1.293167179430    1.781172327140   NewECP "SDD" end
  f>    -0.999877882808      5.393631972057    1.435570770336   -1.780082700074   NewECP "SDD" end
  y>     2.999959228263      3.048659389980    5.277039675608    0.002051895125
*
```

5.2 β-$NaYF_4$: Er^{3+}, Cluster 12, Mergefrag

Initial Guess for Er^{3+}:

```
# CASSCF calculation with one interation of Er3+ with 35 quartet and 112 doublet roots for initial guess orbitals

% Pal NProcs 24 end          # number of cores for parallel processing
% MaxCore 6500   # amount of RAM per core

% CASSCF
  MaxIter 1                   # determines the number of CASSCF (macro) iterations
  NEl 11                      # number of electrons
  NOrb 7                      # number of orbitals
  Mult 4,2            # included multiplicities
  NRoots 35,112               # number of multiplets per multiplicity
  BWeight = 0.238095, 0.761905        # weight per mutliplicity block
  PrintWF true
end

% Method
```

```
 FrozenCore FC_None       # no frozencore approximation, calculates correlation effects for electrons on low-lying orbitals
end

% Rel                     # include relativistic effects
 Method DKH               # (relativistic) Hamiltonian operator
 Order 2            # second-order DKH Hamiltonian
 PictureChange 2 # include the second-order DKH transformation of the SOC operator and the first order of the Zeeman operator
 FiniteNuc true           # account for the spatial extent of the nuclei (opposed to the point charges used for the elementary particles)
end

% Output
 Print[p_basis] 2   # prints the basis in the input format
end

! AutoAux                # automatic construction of a auxiliary basis set for Coulomb-, exchange-, and correlation-fitting
% Basis
 Basis "DKH-DEF2-TZVPP"  # general basis set
 NewGTO                  # basis per element
  Er "SARC2-DKH-QZVP" end
end

* xyz +3 4               # keyword ; total charge ; multiplicity ; (file name)
 Er    0.0    0.0    0.0
*
```

Full Calculation for Er^{3+} after Restart:

```
# CASSCF+NEVPT2+QDPT calculation of Er3+ with 35 quartet and 112 doublet roots

% Pal NProcs 24 end       # number of cores for parallel processing
% MaxCore 6500   # amount of RAM per core

% SCF
 Guess MORead   # restart from an earlier calculation
 MOInp "input-IG.gbw"     # initial orbitals from a HF calculation
 Convergence verytight    # target precision of the energy and the wavefunction
 Rotate                   # adjust active orbitals from an initial guess
  {27,36}           # {remove, add}
  {28,37}
  {29,38}
  {30,39}
  {31,40}
  {32,41}
  {33,42}
 end
end

% Method
 FrozenCore FC_None       # no frozencore approximation, calculates correlation effects for electrons on low-lying orbitals
end

% CASSCF
 NEl 11                   # number of electrons
 NOrb 7                   # number of orbitals
 Mult 4,2           # included multiplicities
 NRoots 35,112            # number of multiplets per multiplicity
 BWeight = 0.238095, 0.761905      # weight per mutliplicity block
 MaxIter 500              # maximum number of interations to achieve convergence criteria
 ActConstraints 0
 trafostep ri             # utilize the RI-MO algorithm for faster integral transformation
 PrintWF true
 PTMethod SC_NEVPT2       # strongly contracted MR approach, provides a DEC corrected total energy
 PTSettings               # settings for the chosen perturbation theory method
  D4Tpre 1e-14            # avoids intruder states (very tight setting)
 end
```

```
 DoHigherMoments true     # request the multipole expansion up to 2nd order (magnetic dipole and electric quadrupole contributions),
introduces origin-dependence
 rel                      # enter into relativistic calculation
  DoSOC true              # spin-orbit coupling via QDPT
  NInitStates 364  # number of inital SOC states to compute the transition moments from
  Temperature 1000000     # temperature for calculating the Boltzmann distribution
 end
end

! AutoAux                 # automatic construction of a auxiliary basis set for Coulomb-, exchange-, and correlation-fitting
% Basis                   # basis per element
 Basis "DKH-DEF2-TZVPP"  # general basis set
 NewGTO                  # basis per element
  Er "SARC2-DKH-QZVP" end
end

*xyz +3 4              # keyword, total charge, multiplicity, (file name)
 Er    0.0     0.0     0.0
 *
```

DFT Calculation for Surrounding Ions and Point Charges:

```
# DFT calculation of 9 F-, ECPs, and point charges

% Pal NProcs 24 end       # number of cores for parallel processing
% MaxCore 3000   # amount of RAM per core

% SCF
 MaxIter 500             # maximum number of SCF iterations to reach convergence
 Convergence verytight   # target precision of the energy and the wavefunction
end
! PBE0                   # DFT functional

% PointCharges "pointcharges.pc"    # file that contains all point charges
% Method
 DoEQ true               # include interactions between point charges
 FrozenCore FC_None      # no frozencore approximation, calculates correlation effects for electrons on low-lying orbitals
end

! AutoAux                 # automatic construction of an auxiliary basis set for Coulomb-, exchange-, and correlation-fitting
% Basis
 Basis "DKH-DEF2-TZVPP"  # general basis set
 NewECP                  # ECP per element
  Na "SDD" end
 NewECP                  # ECP per element
  Y "SDD" end
end

* xyz -9 1              # keyword, total charge, multiplicity, (file name)
 f    -2.299492273536     0.308637372811    -0.153181543199
 f    -0.818879087031    -1.217957239365    -1.788458596217
 f    -0.749118336035    -1.180309559734     1.766083923179
 f     0.957298398847    -2.089301717118    -0.156636872453
 f    -0.624558199710     1.385730558004     1.705105858557
 f    -0.633420712704     1.448685779723    -1.731034989147
 f     1.620272740359    -0.048917365162     1.708122191061
 f     1.585444746148     0.027856445483    -1.732012110945
 f     1.501069922024     1.966620981619     0.015364886232
  f>    -1.000000000000     -3.616969752303   -3.742219477545    1.756964119738  NewECP "SDD" end
  f>    -1.000000000000     -1.483281727066   -5.213510369862    1.711011072897  NewECP "SDD" end
  f>    -1.000000000000     -4.554457480747    0.073984742263    1.759442327195  NewECP "SDD" end
  f>    -1.000000000000     -4.471358951069   -0.056232986376   -1.780330075759  NewECP "SDD" end
  f>    -1.000000000000     -4.503300747424    0.037250296028   -5.290944597836  NewECP "SDD" end
  f>    -1.000000000000     -4.431057887467   -0.071949672423    5.268853148507  NewECP "SDD" end
  f>    -1.000000000000     -4.701662530124    1.976313126456   -0.165728353523  NewECP "SDD" end
```

```
f>   -1.000000000000   -1.653017848711   -3.247327998787   -3.360760857462  NewECP "SDD" end
f>   -1.000000000000   -4.676890702508    1.985495062150   -3.357234722281  NewECP "SDD" end
f>   -1.000000000000   -4.663113037556    1.969747961160    3.690886413075  NewECP "SDD" end
f>   -1.000000000000   -1.617248029872   -3.254848963274   -0.164666264613  NewECP "SDD" end
f>   -1.000000000000   -1.638595671890   -3.230301453121    3.641605487649  NewECP "SDD" end
f>   -1.000000000000    0.749223038664   -5.006143580048   -0.210704278567  NewECP "SDD" end
f>   -1.000000000000   -2.310979368770    0.280778569443   -3.360732535091  NewECP "SDD" end
f>   -1.000000000000   -2.295118581786    0.275918003966    3.627500946924  NewECP "SDD" end
f>   -1.000000000000    0.772107127869   -4.956249997758   -3.358395939489  NewECP "SDD" end
f>   -1.000000000000    0.766493418574   -4.915732239621    3.689555261641  NewECP "SDD" end
f>   -1.000000000000   -0.817733798160   -1.228162188904    5.269065566289  NewECP "SDD" end
f>   -1.000000000000   -3.816450895798    4.008431336318   -1.781094779774  NewECP "SDD" end
f>   -1.000000000000   -0.798563277331   -1.172839559706   -5.290052443151  NewECP "SDD" end
f>   -1.000000000000   -3.833265813567    4.052240491136    1.759286554155  NewECP "SDD" end
f>   -1.000000000000   -2.058737219729    3.188307177482    3.683012793955  NewECP "SDD" end
f>   -1.000000000000    1.004145483932   -2.038644391723   -3.369781532605  NewECP "SDD" end
f>   -1.000000000000   -1.996971619225    3.185009744230   -3.361568045034  NewECP "SDD" end
f>   -1.000000000000    1.033751495854   -2.015588605525    3.636394171397  NewECP "SDD" end
f>   -1.000000000000   -1.994431917776    3.209551431044   -0.157231642243  NewECP "SDD" end
f>   -1.000000000000   -0.711936165766    1.396138800890   -5.235333622506  NewECP "SDD" end
f>   -1.000000000000    2.340946409013   -3.876635334905    1.764257130254  NewECP "SDD" end
f>   -1.000000000000    2.378521906020   -3.840575335991   -5.288508873935  NewECP "SDD" end
f>   -1.000000000000   -0.688728740098    1.483251201001    5.209815166294  NewECP "SDD" end
f>   -1.000000000000    2.407802943759   -3.744709456566   -1.783884533311  NewECP "SDD" end
f>   -1.000000000000    2.433436540495   -3.706981847047    5.268442474128  NewECP "SDD" end
f>   -1.000000000000    1.517090797101   -0.036550616726   -5.287517590953  NewECP "SDD" end
f>   -1.000000000000    1.479107813772    0.069602739607    5.268428312943  NewECP "SDD" end
f>   -1.000000000000   -1.475470844758    5.167587296065    1.767330107500  NewECP "SDD" end
f>   -1.000000000000    4.437201106207   -3.274037525842   -3.712864572920  NewECP "SDD" end
f>   -1.000000000000    1.392532127605    1.976574173895   -3.415366388624  NewECP "SDD" end
f>   -1.000000000000    4.429250373208   -3.269262433015    3.341855674863  NewECP "SDD" end
f>   -1.000000000000    1.386101387971    1.972220299282    3.336516907942  NewECP "SDD" end
f>   -1.000000000000    4.460341376552   -3.303762316061    0.190382977422  NewECP "SDD" end
f>   -1.000000000000    3.725996229721    0.283955256882   -3.419345681740  NewECP "SDD" end
f>   -1.000000000000    3.724910305357    0.266818222262    3.393359906408  NewECP "SDD" end
f>   -1.000000000000    3.738996653948    0.461249658737    0.012603455066  NewECP "SDD" end
f>   -1.000000000000    2.190011989058    3.967955283430   -1.730865054922  NewECP "SDD" end
f>   -1.000000000000    5.184453948238   -1.186394384778    1.754613362950  NewECP "SDD" end
f>   -1.000000000000    2.243909262942    3.966018355847    1.706819361998  NewECP "SDD" end
f>   -1.000000000000    5.250111275293   -1.170458331321   -1.778135092012  NewECP "SDD" end
f>   -1.000000000000    4.011660262190    3.140229669000   -0.039453062712  NewECP "SDD" end
f>   -1.000000000000    4.035485396296    3.187065114589    3.391009149620  NewECP "SDD" end
f>   -1.000000000000    4.046317139562    3.192080455337   -3.362587650387  NewECP "SDD" end
f>   -1.000000000000   -3.722048656733   -3.924665774858   -1.786773415147  NewECP "SDD" end
na>   1.000000000000   -3.062343860357   -1.804378518666   -2.076964427742
na>   1.000000000000   -3.069555754538   -1.812246470978    5.321858465711
na>   1.000000000000   -2.947545973451   -1.606851014237   -5.287503429767
na>   1.000000000000   -2.904136620751   -1.519840691063    1.882248127567
na>   1.000000000000    0.042149882197   -3.410402411246    1.823422563136
na>   1.000000000000   -2.991025551500    1.833991004062   -5.400453045054
na>   1.000000000000   -2.999516923814    1.828112942700    1.766310502146
na>   1.000000000000    0.079003550537   -3.354858013524   -5.343411789992
na>   1.000000000000    2.996384747963   -1.763228909509    2.170187511673
na>   1.000000000000   -0.015930357109    3.523022365965    1.652086380167
na>   1.000000000000    3.060192958885   -1.656433202894   -5.519987611583
na>   1.000000000000   -0.041059624125    3.674240626765   -1.674758438101
na>   1.000000000000    0.105476993763    3.435442983838   -5.458712162066
na>   1.000000000000    3.064271237285   -1.662608618084   -2.306970402101
na>   1.000000000000    0.036136765750    3.619031029899    5.437172998971
na>   1.000000000000    3.131836352550   -1.521407564485    5.437881058244
na>   1.000000000000    3.032930527372    1.823930793162    5.495517083096
na>   1.000000000000    3.076486816200    1.880198637181   -5.574904688825
 y>   3.000000000000   -2.966783394600   -5.160194478640    3.541273488613
 y>   3.000000000000   -5.990436598340    0.077223391515   -3.571974938706
 y>   3.000000000000   -5.995334522170    0.064545621600    3.552970627809
```

```
  y>     3.000000000000     -2.963709629066   -5.089549595429   -0.007505428298
  y>     3.000000000000      0.051218650999   -3.417905851849   -1.776336621457
  y>     3.000000000000     -2.996338510160    1.807209489822    5.291029564949
  y>     3.000000000000     -2.977665474977    1.817487369832   -1.777143809029
  y>     3.000000000000      0.069307304399   -3.389000090115    5.290208216191
  y>     3.000000000000      3.072635176974   -5.181828655114    3.536543652667
  y>     3.000000000000      0.021334790413    0.094965246924   -3.582411732396
  y>     3.000000000000      0.026551079810    0.097541355053    3.527069819590
  y>     3.000000000000      3.081924216514   -5.123096876113    0.003582779923
  y>     3.000000000000      3.042860219791    1.816025759712   -1.859505263707
  y>     3.000000000000      3.063326589178    1.807281083487    1.843361512274
  y>     3.000000000000     -2.963104823677   -5.176898325394   -3.580613261841
  y>     3.000000000000     -5.989407364360    0.025273006708   -0.011031563479
  f>    -0.999866027919     -5.044085023025   -2.051517651206    0.136131475897  NewECP "SDD" end
  f>    -0.999929646478     -4.997320938612   -2.048592091175    3.338796858802  NewECP "SDD" end
  f>    -0.999937704878     -4.971807286311   -2.055538839272   -3.656842923212  NewECP "SDD" end
  f>    -0.999998266478     -1.446439206195   -5.254674339321   -1.769171061611  NewECP "SDD" end
  f>    -0.999966330782     -1.541751994445    5.324484613547   -1.783077345740  NewECP "SDD" end
  f>    -0.999673930815      0.722885314723    5.504178375816    0.144316641097  NewECP "SDD" end
  f>    -0.999645101918      0.730143690463    5.519405288202   -3.712298125502  NewECP "SDD" end
  f>    -0.999662701635      0.726844167569    5.505766164915    3.288680423434  NewECP "SDD" end
  y>     2.999823058018     -3.002824854802    5.350599725562    0.003582779923
  f>    -0.999946800387      5.329685707741    1.439336365092   -1.779055569067  NewECP "SDD" end
  f>    -0.999876770699      5.360462610831    1.486925853619    1.762033824135  NewECP "SDD" end
  y>     2.999958845034      6.086591635640    0.025273006708   -0.011031563479
  y>     2.999561411107      3.027540299618    5.384147006247   -0.007505428298
*
```

Full Calculation of Merged Fragments:

```
# CASSCF+NEVPT2+QDPT calculation of 12-NaYF4: 5.0 % Er3+ (Er-F9-Na18Y19F61) with 35 quartet and 112 doublet roots

% Pal NProcs 24 end                    # number of cores for parallel processing
% MaxCore 3000               # amount of RAM per core

% SCF
  Guess MORead               # restart from an earlier calculation
  MOInp "merged.gbw"         # merged ligand and metal orbitals
end

% PointCharges "pointcharges.pc"    # file that contains all point charges
% Method
  DoEQ true                          # include interactions between point charges
  FrozenCore FC_None         # no frozencore approximation, calculates correlation effects for electrons on low-lying orbitals
end

% CASSCF
  NEl 11                             # number of electrons
  NOrb 7                             # number of orbitals
  Mult 4,2              # included multiplicities
  NRoots 35,112                      # number of multiplets per multiplicity
  BWeight = 0.238095, 0.761905       # weight per mutliplicity block
  MaxIter 500                        # maximum number of iterations to achieve convergence criteria
  ETol 1e-8                          # energy convergence setting (default is 1e-7)
  GTol 1e-5                          # gradient convergence setting
  ActConstraints 0 # requests natural orbital construction
  trafostep RI                       # utilize the RI-MO algorithm for faster integral transformation
  ActOrbs fOrbs                      # requests AILFT analysis
  PTMethod SC_NEVPT2         # strongly contracted MR approach, provides a DEC corrected total energy
  PTSettings                         # settings for the chosen perturbation theory method
    D3Tpre 1e-15                     # truncation of the third-order reduced density matrix (tight setting)
    D4Tpre 1e-15                     # fourth-order rdm, avoids intruder states (extremely tight setting)
  end
  DoHigherMoments true       # request the multipole expansion up to 2nd order (magnetic dipole and electric quadrupole contributions),
introduces origin-dependence
```

```
  rel                         # enter into relativistic calculation
   DoSOC true                 # spin-orbit coupling via QDPT
   NInitStates 364  # number of inital SOC states to compute the transition moments from
   Temperature 1000000      # temperature for calculating the Boltzmann distribution
  end
end

% Rel                         # include relativistic effects
  Method DKH                  # (relativistic) Hamiltonian operator
  Order 2             # second-order DKH Hamiltonian
  PictureChange 2 # include the second-order DKH transformation of the SOC operator and the first order of the Zeeman operator
  FiniteNuc true              # account for the spatial extent of the nuclei (opposed to the point charges used for the elementary particles)
end

! AutoAux                     # automatic construction of a auxiliary basis set for Coulomb-, exchange-, and correlation-fitting
% Basis
   Basis "DKH-DEF2-TZVPP"# general basis set
  NewGTO
   Er "SARC2-DKH-QZVP" end
  NewECP                      # ECP per element
   Na "SDD" end
  NewECP                      # ECP per element
   Y "SDD" end
end

* xyz -6 4              # keyword, total charge, multiplicity, (file name)
  f     -2.299492273536     0.308637372811     -0.153181543199
  f     -0.818879087031    -1.217957239365     -1.788458596217
  f     -0.749118336035    -1.180309559734      1.766083923179
  f      0.957298398847    -2.089301717118     -0.156636872453
  f     -0.624558199710     1.385730558004      1.705105858557
  f     -0.633420712704     1.448685779723     -1.731034989147
  f      1.620272740359    -0.048917365162      1.708122191061
  f      1.585444746148     0.027856445483     -1.732012110945
  f      1.501069922024     1.966620981619      0.015364886232
   f>    -1.000000000000     -3.616969752303   -3.742219477545    1.756964119738  NewECP "SDD" end
   f>    -1.000000000000     -1.483281727066   -5.213510369862    1.711011072897  NewECP "SDD" end
   f>    -1.000000000000     -4.554457480747    0.073984742263    1.759442327195  NewECP "SDD" end
   f>    -1.000000000000     -4.471358951069   -0.056232986376   -1.780330075759  NewECP "SDD" end
   f>    -1.000000000000     -4.503300747424    0.037250296028   -5.290944597836  NewECP "SDD" end
   f>    -1.000000000000     -4.431057887467   -0.071949672423    5.268853148507  NewECP "SDD" end
   f>    -1.000000000000     -4.701662530124    1.976313126456   -0.165728353523  NewECP "SDD" end
   f>    -1.000000000000     -1.653017848711   -3.247327998787   -3.360760857462  NewECP "SDD" end
   f>    -1.000000000000     -4.676890702508    1.985495062150   -3.357234722281  NewECP "SDD" end
   f>    -1.000000000000     -4.663113037556    1.969747961160    3.690886413075  NewECP "SDD" end
   f>    -1.000000000000     -1.617248029872   -3.254848963274   -0.164666264613  NewECP "SDD" end
   f>    -1.000000000000     -1.638595671890   -3.230301453121    3.641605487649  NewECP "SDD" end
   f>    -1.000000000000      0.749223038664   -5.006143580048   -0.210704278567  NewECP "SDD" end
   f>    -1.000000000000     -2.310979368770    0.280778569443   -3.360732535091  NewECP "SDD" end
   f>    -1.000000000000     -2.295118581786    0.275918003966    3.627500946924  NewECP "SDD" end
   f>    -1.000000000000      0.772107127869   -4.956249997758   -3.358395939489  NewECP "SDD" end
   f>    -1.000000000000      0.766493418574   -4.915732239621    3.689555261641  NewECP "SDD" end
   f>    -1.000000000000     -0.817733798160   -1.228162188904    5.269065566289  NewECP "SDD" end
   f>    -1.000000000000     -3.816450895798    4.008431336318   -1.781094779774  NewECP "SDD" end
   f>    -1.000000000000     -0.798563277331   -1.172839559706   -5.290052443151  NewECP "SDD" end
   f>    -1.000000000000     -3.833265813567    4.052240491136    1.759286554155  NewECP "SDD" end
   f>    -1.000000000000     -2.058737219729    3.188307177482    3.683012793955  NewECP "SDD" end
   f>    -1.000000000000      1.004145483932   -2.038644391723   -3.369781532605  NewECP "SDD" end
   f>    -1.000000000000     -1.996971619225    3.185009744230   -3.361568045034  NewECP "SDD" end
   f>    -1.000000000000      1.033751495854   -2.015588605525    3.636394171397  NewECP "SDD" end
   f>    -1.000000000000     -1.994431917776    3.209551431044   -0.157231642243  NewECP "SDD" end
   f>    -1.000000000000     -0.711936165766    1.396138800890   -5.235333622506  NewECP "SDD" end
   f>    -1.000000000000      2.340946409013   -3.876635334905    1.764257130254  NewECP "SDD" end
   f>    -1.000000000000      2.378521906020   -3.840575335991   -5.288508873935  NewECP "SDD" end
   f>    -1.000000000000     -0.688728740098    1.483251201001    5.209815166294  NewECP "SDD" end
```

```
f>   -1.000000000000    2.407802943759   -3.744709456566   -1.783884533311  NewECP "SDD" end
f>   -1.000000000000    2.433436540495   -3.706981847047    5.268442474128  NewECP "SDD" end
f>   -1.000000000000    1.517090797101   -0.036550616726   -5.287517590953  NewECP "SDD" end
f>   -1.000000000000    1.479107813772    0.069602739607    5.268428312943  NewECP "SDD" end
f>   -1.000000000000   -1.475470844758    5.167587296065    1.767330107500  NewECP "SDD" end
f>   -1.000000000000    4.437201106207   -3.274037525842   -3.712864572920  NewECP "SDD" end
f>   -1.000000000000    1.392532127605    1.976574173895   -3.415366388624  NewECP "SDD" end
f>   -1.000000000000    4.429250373208   -3.269262433015    3.341855674863  NewECP "SDD" end
f>   -1.000000000000    1.386101387971    1.972220299282    3.336516907942  NewECP "SDD" end
f>   -1.000000000000    4.460341376552   -3.303762316061    0.190382977422  NewECP "SDD" end
f>   -1.000000000000    3.725996229721    0.283955256882   -3.419345681740  NewECP "SDD" end
f>   -1.000000000000    3.724910305357    0.266818222262    3.393359906408  NewECP "SDD" end
f>   -1.000000000000    3.738996653948    0.461249658737    0.012603455066  NewECP "SDD" end
f>   -1.000000000000    2.190011989058    3.967955283430   -1.730865054922  NewECP "SDD" end
f>   -1.000000000000    5.184453948238   -1.186394384778    1.754613362950  NewECP "SDD" end
f>   -1.000000000000    2.243909262942    3.966018355847    1.706819361998  NewECP "SDD" end
f>   -1.000000000000    5.250111275293   -1.170458331321   -1.778135092012  NewECP "SDD" end
f>   -1.000000000000    4.011660262190    3.140229669000   -0.039453062712  NewECP "SDD" end
f>   -1.000000000000    4.035485396296    3.187065114589    3.391009149620  NewECP "SDD" end
f>   -1.000000000000    4.046317139562    3.192080455337   -3.362587650387  NewECP "SDD" end
f>   -1.000000000000   -3.722048656733   -3.924665774858   -1.786773415147  NewECP "SDD" end
na>   1.000000000000   -3.062343860357   -1.804378518666   -2.076964427742
na>   1.000000000000   -3.069555754538   -1.812246470978    5.321858465711
na>   1.000000000000   -2.947545973451   -1.606851014237   -5.287503429767
na>   1.000000000000   -2.904136620751   -1.519840691063    1.882248127567
na>   1.000000000000    0.042149882197   -3.410402411246    1.823422563136
na>   1.000000000000   -2.991025551500    1.833991004062   -5.400453045054
na>   1.000000000000   -2.999516923814    1.828112942700    1.766310502146
na>   1.000000000000    0.079003550537   -3.354858013524   -5.343411789992
na>   1.000000000000    2.996384747963   -1.763228909509    2.170187511673
na>   1.000000000000   -0.015930357109    3.523022365965    1.652086380167
na>   1.000000000000    3.060192958885   -1.656433202894   -5.519987611583
na>   1.000000000000   -0.041059624125    3.674240626765   -1.674758438101
na>   1.000000000000    0.105476993763    3.435442983838   -5.458712162066
na>   1.000000000000    3.064271237285   -1.662608618084   -2.306970402101
na>   1.000000000000    0.036136765750    3.619031029899    5.437172998971
na>   1.000000000000    3.131836352550   -1.521407564485    5.437881058244
na>   1.000000000000    3.032930527372    1.823930793162    5.495517083096
na>   1.000000000000    3.076486816200    1.880198637181   -5.574904688825
 y>   3.000000000000   -2.966783394600   -5.160194478640    3.541273488613
 y>   3.000000000000   -5.990436598340    0.077223391515   -3.571974938706
 y>   3.000000000000   -5.995334522170    0.064545621600    3.552970627809
 y>   3.000000000000   -2.963709629066   -5.089549595429   -0.007505428298
 y>   3.000000000000    0.051218650999   -3.417905851849   -1.776336621457
 y>   3.000000000000   -2.996338510160    1.807209489822    5.291029564949
 y>   3.000000000000   -2.977665474977    1.817487369832   -1.777143809029
 y>   3.000000000000    0.069307304399   -3.389000090115    5.290208216191
 y>   3.000000000000    3.072635176974   -5.181828655114    3.536543652667
 y>   3.000000000000    0.021334790413    0.094965246924   -3.582411732396
 y>   3.000000000000    0.026551079810    0.097541355053    3.527069819590
 y>   3.000000000000    3.081924216514   -5.123096876113    0.003582779923
 y>   3.000000000000    3.042860219791    1.816025759712   -1.859505263707
 y>   3.000000000000    3.063326589178    1.807281083487    1.843361512274
 y>   3.000000000000   -2.963104823677   -5.176898325394   -3.580613261841
 y>   3.000000000000   -5.989407364360    0.025273006708   -0.011031563479
f>   -0.999866027919   -5.044085023025   -2.051517651206    0.136131475897  NewECP "SDD" end
f>   -0.999929646478   -4.997320938612   -2.048592091175    3.338796858802  NewECP "SDD" end
f>   -0.999937704878   -4.971807286311   -2.055538839272   -3.656842923212  NewECP "SDD" end
f>   -0.999998266478   -1.446439206195   -5.254674339321   -1.769171061611  NewECP "SDD" end
f>   -0.999966330782   -1.541751994445    5.324484613547   -1.783077345740  NewECP "SDD" end
f>   -0.999673930815    0.722885314723    5.504178375816    0.144316641097  NewECP "SDD" end
f>   -0.999645101918    0.730143690463    5.519405288202   -3.712298125502  NewECP "SDD" end
f>   -0.999662701635    0.726844167569    5.505766164915    3.288680423434  NewECP "SDD" end
 y>   2.999823058018   -3.002824854802    5.350599725562    0.003582779923
f>   -0.999946800387    5.329685707741    1.439336365092   -1.779055569067  NewECP "SDD" end
```

```
 f>   -0.999876770699      5.360462610831   1.486925853619   1.762033824135  NewECP "SDD" end
 y>    2.999958845034      6.086591635640   0.025273006708  -0.011031563479
 y>    2.999561411107      3.027540299618   5.384147006247  -0.007505428298
 Er    0.000000000000      0.000000000000   0.000000000000
*
```

6 References

(1) Dulick, M.; Faulkner, G. E.; Cockroft, N. J.; Nguyen, D. C. Spectroscopy and Dynamics of Upconversion in Tm^{3+}: $YLiF_4$. *J. Lumin.* **1991**, *48-49*, 517–521. DOI: https://doi.org/10.1016/0022-2313(91)90183-V.

(2) Xiao, Y.; Kuang, X.; Yeung, Y.; Ju, M. Investigation of the Structure and Luminescence Mechanism of Tm^{3+}-Doped $LiYF_4$: New Theoretical Perspectives. *Inorg. Chem.* **2020**, *59* (2), 1211–1217. DOI: https://doi.org/10.1021/acs.inorgchem.9b02935.

(3) Sugiyama, A.; Katsurayama, M.; Anzai, Y.; Tsuboi, T. Spectroscopic Properties of Yb Doped YLF Grown by a Vertical Bridgman Method. *J. Alloys Compd.* **2006**, *408-412*, 780–783. DOI: https://doi.org/10.1016/j.jallcom.2005.01.094.

(4) Rinkel, T.; Nordmann, J.; Raj, A. N.; Haase, M. Ostwald-Ripening and Particle Size Focussing of Sub-10 nm $NaYF_4$ Upconversion Nanocrystals. *Nanoscale* **2014**, *6* (23), 14523–14530. DOI: https://doi.org/10.1039/C4NR03833A.

(5) Liu, N.; Gobeil, N.; Evers, P.; Gessner, I.; Rodrigues, E. M.; Hemmer, E. Water Dispersible Ligand-Free Rare Earth Fluoride Nanoparticles: Water Transfer Versus $NaREF_4$-to-REF_3 Phase Transformation. *Dalton Trans.* **2020**, *49* (45), 16204–16216. DOI: https://doi.org/10.1039/D0DT01080D.